# Fast transcranial acoustic simulations for personalized dosimetry in ultrasound brain therapy

Célestine Angla

université
PARIS-SACLAY

# Fast transcranial acoustic simulations for personalized dosimetry in ultrasound brain therapy

*Simulations acoustiques transcraniennes rapides pour la dosimétrie personnalisée en thérapie ultrasonore du cerveau*

**Thèse de doctorat de l'université Paris-Saclay**

École doctorale n° 575, electrical, optical, bio : physics and engineering (EOBE)
Spécialité de doctorat: Physique et Imagerie Médicale
Graduate School : Sciences de l'ingénierie et des systèmes. Référent : Faculté des sciences d'Orsay

Thèse préparée dans l'unité de recherche **Laboratoire d'Imagerie Biomédicale Multimodale Paris Saclay** (Université Paris-Saclay, CEA, CNRS, Inserm), sous la direction de **Jean-Luc GENNISSON**, Directeur de recherche, le co-encadrement de **Sylvain CHATILLON**, Ingénieur de recherche, et le co-encadrement de **Benoit LARRAT**, Ingénieur de recherche

**Thèse soutenue à Paris-Saclay, le 20 décembre 2023, par**

**Célestine ANGLA**

## Composition du jury

Membres du jury avec voix délibérative

| | |
|---|---|
| **Stefan CATHELINE**<br>Directeur de recherche, Université Lyon 1 | Président |
| **Guillaume HAÏAT**<br>Directeur de recherche, Université Paris-Créteil | Rapporteur & Examinateur |
| **Gianmarco PINTON**<br>Maître de conférence (HDR), University of North Carolina | Rapporteur & Examinateur |
| **Pierre GELAT**<br>Maître de conférence, University College London | Examinateur |

THESE DE DOCTORAT
NNT : 2023UPAST207

université PARIS-SACLAY
ÉCOLE DOCTORALE
Physique et ingénierie : Electrons, Photons, Sciences du vivant (EOBE)

**Titre:** Simulations acoustiques transcraniennes rapides pour la dosimétrie personnalisée en thérapie ultrasonore du cerveau.

**Mots clés:** thérapie ultrasonore, simulation rapide, modélisation du crâne, simulations transcraniennes, thérapie du cerveau, correction d'aberrations.

**Résumé :** La thérapie par ultrasons de pathologies cérébrales est très prometteuse, notamment pour son caractère non invasif lorsque la sonde ultrasonore reste externe au crâne. Cependant, la structure complexe de l'os du crâne atténue et perturbe fortement la propagation du faisceau ultrasonore, ce qui altère les dimensions, la position et l'intensité de la tâche focale. Or ces paramètres focaux doivent être parfaitement maitrisés pour assurer à la fois l'efficacité et la sureté du traitement. En raison de la grande variabilité inter et intra individus de la géométrie et des propriétés acoustiques du crâne, des simulations personnalisées sont nécessaires pour prédire les caractéristiques focales en fonction du patient et de la position de la sonde ultrasonore. La plupart des méthodes de simulations utilisées actuellement, telles que k-Wave, sont très gourmandes en temps de calcul et en espace mémoire, ce qui les limite à des outils de planning préintervention. L'objectif de cette thèse était de développer une méthode semi-analytique rapide et réaliste de calcul de champ ultrasonore au travers du crâne. Dans un premier temps, un modèle lisse et homogène du crâne, réaliste et favorable aux algorithmes de calcul de champ rapides, a été développé. Pour cela, les surfaces internes et externes du crâne ont été modélisées en utilisant une méthode appelée « Multi-level Bspline Approximation », et une méthode d'homogénéisation des propriétés acoustiques du crâne a été développée et validée numériquement. Ce modèle de crâne lisse et homogène a ensuite été utilisé en entrée de l'algorithme de calcul de champ développé. Cet algorithme, nommé SplineBeam, est basé sur une méthode de calcul des trajets ultrasonores par minimisation de la fonction temps de vol, qui est rapide et précise, et qui, combinée à la méthode des pinceaux, permet un échantillonnage régulier de la sonde ultrasonore. SplineBeam a été validé numériquement, par comparaison avec le modèle pinceau, implémenté dans la plateforme de simulation CIVA HealthCare, développée au CEA, et avec d'autres solvers numériques (dont k-Wave) sur une série de configurations, et expérimentalement, par comparaisons avec des champs de pressions acquis par hydrophone au travers d'un échantillon de crâne ex vivo. Les champs simulés avec SplineBeam se sont avérés être plus proches des champs mesurés expérimentalement que les champs simulés avec k-Wave, ce qui valide à la fois le modèle du crâne et la méthode de calcul de champ. De plus, SplineBeam peut restreindre son calcul à la tâche focale, ce qui, pour une grande sonde, lui permet de réduire drastiquement le nombre de points de calcul et d'avoir des temps de calcul de deux ordres inférieurs à ceux de k-Wave.

**Title:** Fast transcranial acoustic simulations for personalized dosimetry in ultrasound brain therapy.

**Keywords:** ultrasound therapy, fast simulation, skull modeling, transcranial simulations, brain therapy, aberration correction.

**Abstract:** Ultrasound brain therapy is a promising method, as it is non-invasive when ultrasonic waves are sent through the skull. However, the skull bone complex structure strongly attenuates and aberrates the ultrasound beam, altering the dimensions, position and intensity of the focal spot. These focal parameters must be perfectly controlled to ensure both treatment efficacy and safety. Due to the high inter/intra-individual variability of skull geometry and acoustic properties, personalized simulations are required to predict focal characteristics depending on the patient skull and the ultrasonic probe position. Most simulation methods currently in use, such as k-Wave, are very time- and memory-intensive, limiting them to pre-intervention planning tools. The aim of this thesis was to develop a fast and realistic semi-analytical method for ultrasound field computation through the skull. As a first step, we developed a smooth and homogeneous model of the skull, realistic and suited to fast field computation algorithms. To this end, we modeled the skull inner and outer surfaces using a method called "Multi-level Bspline Approximation", and we developed a skull acoustic property homogenization method, which was numerically validated. This smooth and homogeneous skull model was then used as input to the field computation algorithm developed. This algorithm, named SplineBeam, is based on an ultrasonic path computation method that minimizes the time-of-flight function, which is fast and accurate, and which, combined with the pencil method, enables a regular sampling of the ultrasound probe. SplineBeam was validated numerically, by comparison with the pencil method, embedded in the CIVA HealthCare simulation platform, developed at the CEA, and with other numerical solvers (including k-Wave) on a series of configurations, and experimentally, by comparison with hydrophone measured pressure fields through an ex vivo skull sample. SplineBeam simulated fields were found to be closer to the experimentally measured ones than those simulated with k-Wave. This validates both the skull model and the field computation method. Furthermore, SplineBeam can restrict its computation to the focal spot, which allows it to drastically reduce the number of computation points, making it faster than k-Wave by two orders of magnitude, for a large probe.

# Acknowledgments

Je tiens en premier lieu à remercier Dr Guillaume Haïat et Dr Gianmarco Pinton d'avoir accepté d'être rapporteurs de ma thèse et d'avoir eu la patience de la lire. Je vous remercie également, ainsi que Dr Stefan Catheline et Dr Pierre Gélat, d'être venus jusqu'à Saclay pour examiner ma thèse.

Je voudrais ensuite remercier profondément mon directeur de thèse Jean-Luc Gennisson et mes encadrants de thèse Sylvain Chatillon et Benoit Larrat. La complémentarité de vos compétences scientifiques et de vos qualités humaines m'a permis d'être parfaitement entourée durant ces trois années de thèse. Merci en particulier à Sylvain pour ta présence au quotidien et ton aide précieuse dans tous les domaines.

Je tiens également à remercier toutes les personnes qui m'ont aidé pendant cette thèse. En particulier, merci à Paul Mondou pour ton aide et ton infinie patience, c'était un plaisir de travailler avec toi sur la partie expérimentale, toujours dans la bonne humeur avec des discussions intéressantes (souvent tournant autour de l'escalade). Merci à Hamza Chouh pour ta grande aide sur la partie modélisation et programmation, c'est toujours très agréable de travailler avec quelqu'un d'aussi réactif et investi. Merci à Damien Kuntz, notre rencontre fut brève mais très sympathique, je suis ravie de voir que la relève est assurée et te souhaite bon courage pour les trois années à venir. Un grand merci également à chacune des personnes du DIN qui m'ont aidé à un moment ou à un autre, des collègues du LSMA (Guillaume Cousin, Alain Lhemery, Nicolas Leymarie, Edouard Demaldent...) et même des autres labos (Thibaud Fortuna, Kévyn Perlin, Gwenael Toullelan, ...). Votre patience pour m'aider et répondre à toutes sortes de questions m'a sauvée plus d'une fois. Comme ma thèse était en partenariat entre trois labos, j'ai également pu embêter des collègues à Neurospin (Pauline Agou, Gaëlle Thomas) et à Biomaps (Vincent Brûlon), un grand merci à vous.

Merci à toutes les personnes que j'ai croisé au DIN, à mes co-bureaux successifs et en particulier à la team de doctorants et "jeunes" permanents, pour avoir rendu les journées de travail plus agréables. Je garderai de très bons souvenirs des repas du midi, des pauses cafés, des afterworks (dansants ?), des sessions d'escalade, des parties de (Marie) pala et des conférences que j'ai pu faire avec certains d'entre vous. Merci également à tous les collègues de Biomaps. Je suis rarement venue à Orsay, mais à chaque fois on a passé un bon moment. Je garderai de très bons souvenirs des afterworks, des séminaires endiablés et des parties de squash avec vous !

Enfin, je voudrais remercier ceux qui m'ont aidé à rester motivée et épanouie durant ces trois années : mes amis, mes nombreux colocs successifs, ma famille, Hélène. Continuer d'avoir une vie en dehors de la thèse, faire du sport, sortir, voyager, étaient nécessaires pour moi, et sans vous cela n'aurait pas été possible, merci à vous !

# Table of contents

# Résumé en français

## Introduction

La thérapie par ultrasons de pathologies cérébrales est très prometteuse, notamment pour son caractère non invasif lorsque la sonde ultrasonore reste externe au crâne. Cependant, la structure complexe de l'os du crâne atténue et perturbe fortement la propagation du faisceau ultrasonore, ce qui altère les dimensions, la position et l'intensité de la tâche focale. Or ces paramètres focaux doivent être parfaitement maîtrisés pour assurer à la fois l'efficacité et la sûreté du traitement. En raison de la grande variabilité inter et intra individus de la géométrie et des propriétés acoustiques du crâne, des simulations personnalisées sont nécessaires pour prédire les caractéristiques focales en fonction du patient et de la position de la sonde ultrasonore. La plupart des méthodes de simulation utilisées actuellement, telles que k-Wave, sont très gourmandes en temps de calcul et en espace mémoire, ce qui les limite à des outils de planning pré-intervention. L'objectif de cette thèse est de développer une méthode semi-analytique rapide et réaliste de calcul de champ ultrasonore au travers du crâne.

Dans un premier temps, un modèle lisse et homogène du crâne, réaliste et favorable aux algorithmes de calcul de champ rapides, sera développé. Ensuite, une méthode semi-analytique de calcul de champ ultrasonore transcrânien, basé sur le modèle de crâne précédemment développé, sera implémentée. Enfin, le modèle de crâne et la méthode de calcul de champ seront validés expérimentalement par comparaison avec des champs de pression acquis par hydrophone au travers d'un échantillon de crâne ex vivo.

## Modélisation réaliste, lisse et homogène du crâne pour les algorithmes semi-analytiques de calcul de champ ultrasonore

Le modèle de crâne est construit à partir d'un scan CT du crâne du patient, fourni sous la forme d'un fichier DICOM (Digital Imaging and Communications in Medicine). Le modèle de crâne construit à partir de cette image rayons X permettra ainsi de personnaliser les simulations.

### Modélisation de la géométrie du crâne à l'aide de surfaces paramétriques lisses

Pour modéliser le crâne de manière lisse, nous avons utilisé une méthode appelée Multi-level Bspline Approximation (MBA) [1]. L'idée générale de cette méthode est d'approximer des datasets complexes par une structure hiérarchique de courbes B-Splines. Cette structure permet aux MBA de modéliser les détails des données tout en gardant une forme très lisse et en éliminant le bruit. De plus, le stockage et le temps de calcul des MBA sont plus optimisés que ceux des B-Splines. Une implémentation en C++ trouvée sur GitHub (`https://github.com/SINTEF-Geometry/MBA`) a été utilisée. Elle comprend notamment : la fonction pour construire une surface MBA à partir d'un nuage de points 3D, la fonction $z = f(x, y)$ de la surface MBA construite, les dérivées premières et secondes de $f$.

Pour construire les surfaces MBA des parois interne et externe d'un crâne à partir d'un scan CT, le protocole suivant a été défini (il est illustré en figure 1) :

- Un maillage STL (figure 1.(a)) de la surface du crâne est extrait à partir du fichier DICOM avec un logiciel tel que VG-Studio, ITK-Snap ou 3D-Slicer. Cette étape est exécutée une seule fois.
- La partie du maillage du crâne qui est sous la sonde est découpée avec un filtre "clip" avec Paraview ou MeshLab (figure 1.(a) → figure 1.(b)).
- Le maillage STL découpé est converti en maillage MSH avec Gmsh (ce maillage sera utilisé pour le tracé de rayon du first guess pour le calcul de trajets ultrasonores).

- Les surfaces interne et externe du crâne sont extraites à l'aide d'un code en C++ basé sur l'orientation des normales des faces (figure 1.(b) → figure 1.(c)).
- Les surfaces MBA sont construites à partir des sommets des maillages interne et externe (figure 1.(c) → figure 1.(d)).

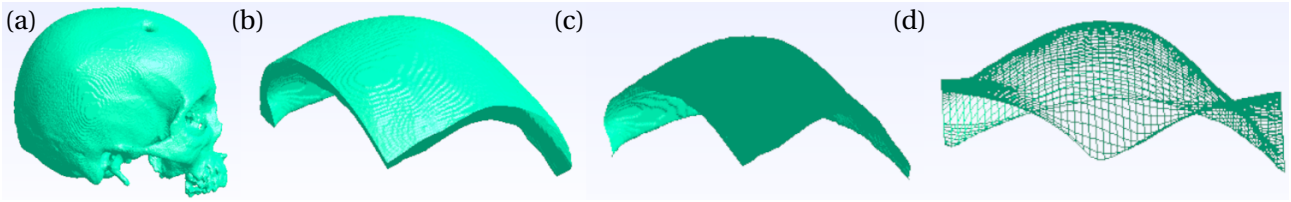


*Figure 1: Etapes de construction des surfcaes MBA : (a) maillage du crâne, (b) maillage du crâne découpé, (c) paroi interne du maillage du crâne découpé, (d) surface MBA interne*

## Modélisation homogène des propriétés acoustiques du crâne

### Extraction de la densité et de la vitesse ultrasonore à partir d'un scan CT

Les propriétés acoustiques du crâne sont également extraites à partir du scan CT. Le fichier DICOM contient une matrice 3D d'intensités, appelées unités Hounsfield (HU). Des lois empiriques reliant les HU aux propriétés acoustiques ($\rho$ la densité et $c$ la vitesse des ultrasons) ont été proposées dans la littérature. Nous avons utilisé les relations les plus génériques, proposées par Marsac et al. [2] :

$$\rho = \rho_{\text{min}} + (\rho_{\text{max}} - \rho_{\text{min}}) \frac{HU - HU_{\text{min}}}{HU_{\text{max}} - HU_{\text{min}}} \tag{1}$$

$$c = c_{\text{min}} + (c_{\text{max}} - c_{\text{min}}) \frac{\rho - \rho_{\text{min}}}{\rho_{\text{max}} - \rho_{\text{min}}} \tag{2}$$

Nous avons pris $HU_{min} = HU_{water}$ et $HU_{max}$ comme la valeur maximale sur le scan CT. Les valeurs utilisées pour $(\rho_{min}, c_{min}, \rho_{max}, c_{max})$ sont données en table 1 et sont issues de la littérature [2].

*Table 1: Densités et vitesses ultrasonores extrêmes utilisées dans les relations de Marsac*

| $\rho_{min}$ | $c_{min}$ | $\rho_{max}$ | $c_{max}$ |
|---|---|---|---|
| 1000 | 1500 | 2700 | 4000 |

### Modélisation de l'atténuation

Pour l'atténuation, nous avons utilisé un seul coefficient pour l'ensemble du crâne [3], mais avec une dépendance en fréquence. La valeur utilisée est issue de la littérature [4] et vaut :

$$\alpha_{skull} = 83 Np.m^{-1}.MHz^{-1} = 0.72 dB.mm^{-1}.MHz^{-1} \tag{3}$$

### Homogénéisation de la densité et de la vitesse ultrasonore

La première idée qui vient à l'esprit pour obtenir un modèle de crâne homogène est de calculer la moyenne des matrices 3D de propriétés acoustiques dérivées du scan CT. C'est ce qui est fait dans la plupart des études [5]. Il a été démontré que cette méthode n'influence pas beaucoup la position focale, mais qu'elle surestime l'amplitude focale par rapport au modèle hétérogène (c'est-à-dire en utilisant telles quelles les matrices 3D de propriétés acoustiques). La méthode d'homogénéisation développée ici vise à corriger ce problème de surestimation afin d'obtenir un modèle homogène du crâne plus réaliste.

La méthode est divisée en deux étapes. D'abord, le crâne est modélisé par un milieu tri-couches pour représenter les différentes couches d'os présentes dans le crâne : os cortical, os trabéculaire, os cortical. Les

voxels identifiés comme du crâne dans les matrices de densité et de vitesse sont segmentés entre os cortical et os trabéculaire à l'aide de l'algorithme de clustering K-Means [6]. Puis, les propriétés acoustiques sont moyennées pour chaque type d'os. La deuxième étape consiste à calculer les propriétés acoustiques d'un milieu homogène équivalent au milieu tri-couches. Pour cela, on cherche la vitesse et la densité équivalentes qui minimisent l'erreur entre le champ de pression au travers du milieu tri-couches et celui au travers du milieu équivalent. Pour simplifier, l'étude a été menée sur des milieux avec des interfaces planes et parallèles mais l'extension de cette méthode à des géométries plus complexes sera analysée dans les résultats.

Lorsqu'on calcule un champ ultrasonore avec une méthode de tracé de rayons, il y a trois grandeurs d'intérêt : la direction finale du rayon (donnée par l'angle de réfraction après la dernière interface), le temps de vol et le coefficient de transmission. Comme les interfaces sont supposées être planes et parallèles et que le premier et le dernier milieu sont supposés identiques, l'angle de réfraction après la dernière interface est égal à l'angle d'incidence. Comme le temps de vol ne dépend que de la vitesse des ultrasons, la vitesse équivalente a été définie de manière à minimiser l'erreur de temps de vol entre le milieu tri-couches et le milieu homogène. Enfin, étant donné la vitesse équivalente, la densité équivalente a été définie de manière à minimiser l'erreur de coefficient de transmission entre le milieu tri-couches et le milieu homogène.

Pour la vitesse équivalente, deux candidats ont été retenus :

- L'inverse de la lenteur moyenne : $c_{eq}^1 = \frac{1}{s_{mean}} = \frac{1}{\sum_{i=1}^3 \frac{1}{c_i}\frac{d_i}{d}}$, avec $d_\text{i}$ l'épaisseur de chaque couche $i$ et $d = \sum_{\text{i}=1}^3 d_\text{i}$ l'épaisseur totale du milieu.
- La vitesse moyenne : $c_{eq}^2 = c_{mean} = \sum_{i=1}^3 c_i \frac{d_i}{d}$.

En effet, à incidence normale, le temps de vol au travers d'un milieu tri-couches est égal à celui au travers d'un milieu homogène équivalent de vitesse $c_{eq}^1$. De même, à incidence normale, la matrice de propagation (de la méthode des pinceaux [7]) au travers d'un milieu tri-couches est égale à la matrice de propagation au travers d'un milieu homogène équivalent de vitesse $c_{eq}^2$.

Une fois la vitesse ultrasonore fixée, on cherche la densité équivalente qui minimise l'erreur de coefficient de transmission. Pour cela, on a modélisé un grand nombre de configurations de milieux tri-couches, avec différents angles d'incidence, propriétés acoustiques et épaisseurs. Pour chaque configuration, la vitesse équivalente est calculée et la densité qui minimise l'erreur de coefficient de transmission entre le milieu tri-couches et le milieu homogène équivalent est trouvée de manière exhaustive dans une gamme prédéfinie de densités. Ensuite, étant donné cet ensemble de configurations et de densités optimales, une régression linéaire a été effectuée pour obtenir une relation linéaire entre les paramètres des configurations et les densités optimales. Les relations obtenues, en fonction des densités d'os cortical $\rho_{cort}$ et trabéculaire $\rho_{trab}$ et de la proportion d'os trabéculaire $\frac{d_{trab}}{d}$, sont listées en table 2.

*Table 2: Résultats des régressions linéaires*

| **Vitesse** | **Relation** |
|---|---|
| $c_{eq} = c_{mean}$ | $-1441.8 + 3.6\rho_{cort} - 0.6\rho_{trab} - 708.7\frac{d_{trab}}{d} - 1.3\rho_{cort}(1 - \frac{d_{trab}}{d}) - 0.9\rho_{trab}\frac{d_{trab}}{d}$ |
| $c_{eq} = \frac{1}{s_{mean}}$ | $-1479.6 + 3.7\rho_{cort} - 0.6\rho_{trab} - 614\frac{d_{trab}}{d} - 1.3\rho_{cort}(1 - \frac{d_{trab}}{d}) - 0.9\rho_{trab}\frac{d_{trab}}{d}$ |

La méthode d'homogénéisation a été évaluée sur des configurations réalistes de crânes. Deux scans CT humains ont été obtenus grâce au Visible Human Project Data : une tête de femme et une tête d'homme. Des simulations 3D au travers de ces deux crânes ont été faites avec k-Wave, afin de pouvoir modéliser des milieux complètement hétérogènes. Une sonde focalisée opérant à $0.8$MHz a été simulée. Les champs de pression simulés au travers du milieu hétérogène (issu directement du scan CT) ont été comparés à ceux simulés au travers des milieux homogénéisés. Les erreurs de position focale $E_{pos}$, d'amplitude focale $E_{amp}$ et de volume focal $E_{dim}$, relatives au milieu hétérogène d'origine, sont listées en tables 3 et 4.

Ces tables confirment les résultats de la littérature : l'erreur de position focale est très faible (inférieure à 1mm) avec la vitesse moyenne, et le milieu moyenné surestime (de plus de $40\%$) la pression au point focal. Les deux milieux équivalents permettent de réduire l'erreur de pression focale (d'environ $30\%$), ce qui

*Table 3: Erreurs entre les champs de pression simulés au travers du crâne de femme avec les différents types de milieux homogènes (erreurs relatives au milieu hétérogène)*

| Milieu | $E_{pos}$ | $E_{amp}$ | $E_{dim}$ |
|---|---|---|---|
| Moyenné | 0.35mm | 42.10% | 12.58% |
| Équivalent ($c_{eq} = c_{mean}$) | 0.79mm | 8.44% | 3.58% |
| Équivalent ($c_{eq} = \frac{1}{s_{mean}}$) | 0.79mm | 3.66% | 2.42% |

*Table 4: Erreurs entre les champs de pression simulés au travers du crâne d'homme avec les différents types de milieux homogènes (erreurs relatives au milieu hétérogène)*

| Milieu | $E_{pos}$ | $E_{amp}$ | $E_{dim}$ |
|---|---|---|---|
| Moyenné | 0.82mm | 43.23% | 37.48% |
| Équivalent ($c_{eq} = c_{mean}$) | 0.56mm | 15.04% | 40.83% |
| Équivalent ($c_{eq} = \frac{1}{s_{mean}}$) | 0.56mm | 9.19% | 43.62% |

démontre le potentiel de cette méthode. L'erreur de volume focal est très similaire pour les trois milieux homogènes pour le crâne de femme, mais elle est plus faible avec les milieux équivalents que le milieu moyenné pour le crâne d'homme.

## Méthode semi-analytique rapide de calcul de champ ultrasonore transcranien avec calcul des trajets par minimisation du temps de vol

### Calcul des trajets ultrasonores par minimisation du temps de vol

D'après le principe de Fermat, les ultrasons prennent le trajet ayant le temps de parcours le plus court. Ainsi, on peut calculer le trajet parcouru par les ultrasons entre deux points en minimisant la fonction temps de vol. Dans le cas d'un modèle homogène du crâne, les surfaces externe $0/1$ et interne $1/2$ séparent trois milieux homogènes isotropes de lenteur $s_0$ (avant le crâne), $s_1$ (le crâne) et $s_2$ (après le crâne). Le processus de calcul de trajet est illustré en figure 2.

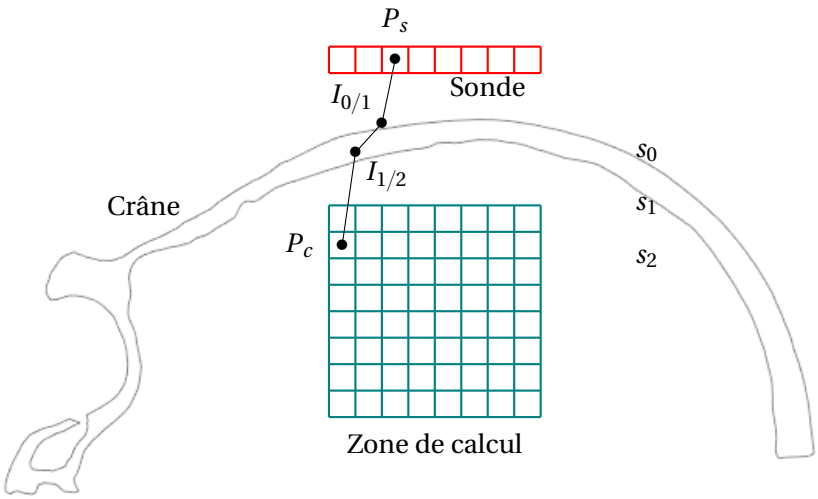


*Figure 2: Calcul d'un trajet ultrasonore au travers d'un crâne*

Ainsi, trouver le trajet ultrasonore entre un point source $P_s$ et un point de calcul $P_c$, revient à trouver les points d'intersection $I_{0/1}$ et $I_{1/2}$ minimisant la fonction temps de vol :

$$\begin{cases} \min_{I_{0/1}, I_{1/2}} t(I_{0/1}, I_{1/2}) \\ t(I_{0/1}, I_{1/2}) = ||P_s - I_{0/1}||s_0 + ||I_{0/1} - I_{1/2}||s_1 + ||I_{1/2} - P_c||s_2 \end{cases} \tag{4}$$

Comme les surfaces du crâne sont modélisées par des splines, elles sont décrites par des fonctions de la forme $f(u,v) = (x,y,z)$. Ainsi le problème d'optimisation peut s'écrire :

$$\begin{cases} \min_{(u,v),(w,x)} t((u,v),(w,x)) \\ t((u,v),(w,x)) = ||P_s - f_{0/1}(u,v)||s_0 + ||f_{0/1}(u,v) - f_{1/2}(w,x)||s_1 + ||f_{1/2}(w,x) - P_c||s_2 \end{cases} \quad (5)$$

Comme les fonctions $f_{0/1}$ and $f_{1/2}$ sont differentiables, la fonction objective $t$ l'est également et on peut calculer sont gradient.

Pour calculer un trajet ultrasonore au travers d'un crâne on résout donc ce problème d'optimisation, à l'aide de l'algorithme Limited-memory Broyden–Fletcher–Goldfarb–Shanno (L-BFGS) [8]. Une implémentation en C++ de L-BFGS trouvée sur GitHub a été utilisée (https://github.com/twesterhout/lbfgs-cpp).

Un "first guess" doit être donné à l'algorithme. Pour cela on trace un rayon tout droit entre les deux points, à l'aide de la librairy Embree, au travers des maillages triangulaires des parois interne et externe du crâne. Les coordonnées 2D des points d'intersection du rayon avec les maillages sont données en "first guess".

### Validation de la méthode de calcul de trajets par application au calcul de lois de retard pour la correction des aberrations induites par le crâne

Pour obtenir une focalisation de bonne qualité (à l'endroit désiré et avec une pression la plus élevée possible) au travers d'un crâne, on peut utiliser une sonde multi-éléments. En calculant des lois de retard qui prennent en compte le crâne et en les appliquant aux différents éléments de la sonde, des interférences constructives vont ainsi se former au focus choisi.

Étant donné la position du focus choisi $(x_f, y_f, z_f)$ et une sonde multi-éléments à $N$ éléments, on peut calculer des lois de retard de la manière suivante :

- Calcul des trajets ultrasonores par minimisation du temps de vol entre $(x_f, y_f, z_f)$ et le centre de chaque élément de la sonde $i \in \{1, ..., N\}$.
- Calcul des temps de vol associés $t_i$, $\forall i \in \{1, ..., N\}$.
- Calcul du temps de vol maximal $t_{max} = \max_{i \in \{1,...,N\}} t_i$.
- Le retard de chaque élément $i \in \{1, ..., N\}$ est donné par $\tau_i = t_{max} - t_i$.

Cette méthode de calcul de lois de retard, nommée SplineRay, a été validée en comparant des champs de pression transcrâniens simulés en utilisant différentes lois de retards :

- Les lois nominales : calcul sans prise en compte du crâne, $\forall i \in \{1, ..., N\}$, $t_i = \frac{d_i}{c_{water}}$, $\tau_i = t_{max} - t_i$, avec $d_i$ la distance entre le focus et le centre de l'élément $i$.
- Les lois par tracé de rayon : calcul par tracé de rayons droits avec prise en compte des vitesses.
- Les lois de CIVA : calcul par simulation du champ ultrasonore et corrélation croisée.

Une de sonde de $32 \times 32$ éléments opérant à 1MHz a été simulée. Deux focus ont été choisis : $F1$ (centré) et $F_2$ (décalé de 20mm selon l'axe $X$). Les simulations ont été faites avec CIVA et SplineBeam (méthode de calcul de champ développée dans la section suivante). Les métriques suivantes ont été calculées : décalage du focus $\Delta X = (x_f, y_f, z_f) - (x_{max}, y_{max}, z_{max})$, pourcentage de pression restaurée au focus comparé aux lois nominales $r_P = 100 \frac{P(x_f, y_f, z_f)}{P^{nom}(x_f, y_f, z_f)}$). Elles sont résumées en table 5.

Les lois SplineRay permettent à chaque fois de restaurer une pression au focus au moins deux fois plus élevée que sans correction d'aberration (lois nominales). De même, la pression maximale est atteinte à moins de 5mm du focus désiré, ce qui est très faible comparé aux décalages du focus supérieurs à 20mm induits par le crâne. Comme on pouvait s'y attendre, les lois CIVA donnent de meilleurs résultats que SplineRay lorsque les champs sont simulés par CIVA, et les lois SplineRay donnent de meilleurs résultats que CIVA lorsque les champs sont simulés par SplineBeam. Cependant, les lois CIVA permettent en moyenne de focaliser plus proche du focus (d'environ 0.75mm) que les lois SplineRay, tandis que les lois SplineRay permettent en moyenne de restaurer une pression plus élevée au focus (de plus de 20%) que les lois CIVA. Ainsi ces deux méthodes sont équivalentes, et donnent une meilleure focalisation que les lois obtenues par tracé de rayon qui ne prennent pas en compte la réfraction. SplineRay semble finalement être la meilleure méthode car elle permet d'obtenir une focalisation similaire à CIVA mais à moindre coût (car seuls les trajets ultrasonores sont calculés et non le champ complet).

*Table 5: Comparaison des métriques de focalisation des champs de pressions simulés (avec CIVA ou SplineBeam) au travers d'un crâne avec différentes lois de retard*

| **Focus** | | $F_1$ | | $F_2$ | |
|---|---|---|---|---|---|
| **Métrique** | **Simu** / **Loi** | **CIVA** | **SplineBeam** | **CIVA** | **SplineBeam** |
| $\Delta X$ (mm) | **Nominale** | (-4, -2, -28) | (-4.5, -1.5, -22.5) | (3.5, -0.5, -23) | (3.5, -0.5, -23.5) |
| | **Tracé de rayon** | (-2.5, -0.5, -11.5) | (-1,-0.5, -4) | (1.5, 0, -8.5) | (1.5, 0, -7.5) |
| | **CIVA** | (-0.5, 0, -3) | (-0.5, 0,-3.5) | (0, 0, -1) | (0.5, 0, -3) |
| | **SplineRay** | (0, 0, -5) | (0, 0, -3.5) | (0.5, 0, -2.5) | (0.5, 0, -2.5) |
| $r_P$ | **Nominale** | 100.00% | 100.00% | 100.00% | 100.00% |
| | **Tracé de rayon** | 163.18% | 193.46% | 194.41% | 180.98% |
| | **CIVA** | 236.65% | 232.38% | 221.05% | 188.24% |
| | **SplineRay** | 230.73 % | 310.97% | 220.67 % | 204.23% |

### SplineBeam : la méthode de calcul de champ ultrasonore

La méthode de calcul de champ développée est similaire aux méthodes de tracé de rayon, à l'exception du calcul des trajets ultrasonores. Plutôt que de lancer des rayons depuis le point de calcul, comme dans la méthode des pinceaux implémentée dans CIVA, la sonde est échantillonnée et le trajet entre chaque échantillon de la sonde et le point de calcul est calculé par minimisation du temps de vol. Dans les deux cas, les contributions temporelles de tous les trajets sont sommées pour obtenir la réponse impulsionelle du champ ultrasonore. L'avantage de la méthode développée est qu'elle permet un échantillonage régulier de la sonde, puisqu'il est défini au préalable.

La sonde, qui peut être de géométrie quelconque, est échantillonnée grâce à un code de CIVA. Ce code fournit les coordonnées du centre $C$, l'aire $dS$ et la normale $n$ de chaque échantillon. Les coordonnées des coins d'un échantillon sont calculées en approximant l'échantillon par un carré de centre $C$, d'aire $dS$ et de normale $n$. Pour chaque échantillon, cinq trajets sont calculés : un depuis le centre (rayon axial dans la méthode des pinceaux), quatre depuis les coins (rayons paraxiaux dans la méthode des pinceaux). Pour chaque échantillon, ces cinq trajets sont calculés par minimisation du temps de vol (comme détaillé dans la section précédente) entre le point de l'échantillon et le point de calcul. Ils permettent d'obtenir : les temps de vol minimal $t_{min}$ et maximal $t_{max}$ de l'échantillon, les directions des rayons paraxiaux et le coefficient de Fresnel total [9] $T_A$ du rayon central. Les directions des rayons paraxiaux permettent de calculer la divergence $DF$ du faisceau. Pour une amplitude d'entrée $A_0$, la réponse impulsionelle associée à l'échantillon de surface $dS$ est un créneau d'amplitude $A_{IR} = \frac{A_0 \times DF \times T_A \times dS}{t_{max} - t_{min}}$ entre $t_{min}$ et $t_{max}$. Les réponses impulsionnelles de tous les échantillons de la sonde sont ensuite sommées puis cette somme est convoluée avec le signal d'entrée. Le calcul de champ peut être large bande ou harmonique et peut prendre en compte des milieux avec une atténuation dépendent de la fréquence. Cet algorithme en C++ a été baptisé SplineBeam.

### Validation numérique de l'algorithme de calcul de champ

Dans un premier temps, SplineBeam a été validé numériquement par comparaison avec d'autres méthodes existantes, grâce à l'étude benchmark de Aubry et al. [10]. Cette étude compare 11 solveurs (dont k-Wave) sur 9 configurations benchmark avec 2 sondes différentes opérant à 500kHz : une focalisée (sc1) et une plane (sc2). Toutes les configurations, à l'exception de celles avec plus de trois milieux (n°4 et 6), ont été simulées par SplineBeam. Les différences de position de la focale $\Delta X_{max}$ et d'amplitude focale $\Delta P_{max}$ relatives à k-Wave sont résumées en table 6.

La comparaison entre les champs SplineBeam et k-Wave est globalement satisfaisante car les différences de position et d'amplitude focales sont toujours inférieures à 1.50mm et 8% respectivement.

### Évaluation et optimisation du temps de calcul de SplineBeam

Le temps de calcul de SplineBeam est proportionnel au nombre de trajets ultrasonores et donc au nombre de points de calcul et au nombre d'échantillons de la sonde. Ainsi pour réduire le temps de calcul, l'utilisateur peut jouer sur ces paramètres, par exemple en réduisant la taille et/ou le pas de la zone de calcul, ou en augmentant le pas d'échantillonage de la sonde.

*Table 6: Comparaison des métriques des champs simulés par SplineBeam (SB) par rapport à k-Wave, à celles moyennées sur les 10 autres solvers (Autres), sur les configurations benchmark proposées par Aubry et al. [10]*

| Config | Matériau | Forme | $\Delta X_{max}$(mm) | | $\Delta P_{max}$(%) | |
|---|---|---|---|---|---|---|
| | | | SB | Autres | SB | Autres |
| BM1-SC1 | Eau | Aucune | 0.00 | 0.10 | 0.07 | 0.39 |
| BM1-SC2 | Eau | Aucune | 0.00 | 0.00 | 1.31 | 0.22 |
| BM2-SC1 | Eau[a] | Aucune | 0.50 | 0.15 | 0.03 | 0.37 |
| BM2-SC2 | Eau[a] | Aucune | 0.00 | 0.00 | 0.42 | 0.35 |
| BM3-SC1 | Os | Plate | 0.00 | 0.50 | 4.21 | 4.77 |
| BM3-SC2 | Os | Plate | 0.00 | 0.00 | 0.27 | 5.36 |
| BM5-SC1 | Os | Sphérique | 1.00 | 0.35 | 7.29 | 3.77 |
| BM5-SC2 | Os | Sphérique | 0.50 | 0.00 | 2.58 | 6.30 |
| BM7-SC1 | Os | Crâne | 0.00 | 0.21 | 4.46 | 5.77 |
| BM7-SC2 | Os | Crâne | 0.50 | 0.15 | 5.11 | 4.48 |
| BM8-SC1 | Os[b] | Crâne | 1.50 | 0.66 | 2.80 | 5.92 |
| BM8-SC2 | Os[b] | Crâne | 1.00 | 0.19 | 4.25 | 7.80 |
| BM9-SC1 | Os[b] | Crâne | 1.00 | 0.29 | 1.37 | 5.85 |
| BM9-SC2 | Os[b] | Crâne | 1.12 | 0.48 | 3.43 | 5.87 |

[a]Eau avec atténuation.
[b]Avec cerveau dans le crâne.

Comme les calculs sont indépendants pour tous les points de calcul, le code a été parallélisé avec la librairie Intel Threading Building Blocks (TBB). Le temps de calcul a ainsi été divisé par le nombre de coeurs physiques de l'ordinateur.

Pour un même nombre de points de calcul, nous avons remarqué que k-Wave était environ 3 fois plus rapide que SplineBeam. Cependant, l'avantage principal de SplineBeam est qu'il ne nécessite pas autant de points de calcul que k-Wave. En effet, contrairement à k-Wave, SplineBeam n'a pas de contrainte de convergence sur le pas spatial, qui peut donc être augmenté pour réduire le nombre de points de calcul. De plus, la zone de calcul de SplineBeam peut être réduite à la tâche focale, ce qui peut permettre de réduire considérablement le nombre de points de calcul. Par exemple, pour les configurations expérimentales présentées dans la section suivante, la zone de calcul de k-Wave, qui doit comprendre la crâne et être aussi large que la sonde, était environ 275 fois plus grande que celle de SplineBeam. C'est pour cela que, sur ces configurations pratiques, SplineBeam (3 minutes) a été environ 120 fois plus rapide que k-Wave (6h) sur un ordinateur portable (2.3GHz, 8 coeurs).

## Validation expérimentale de l'algorithme de calcul de champ ultrasonore avec des mesures transcraniennes par hydrophone

### Set-up et protocole expérimentaux

Pour mesurer un champ de pression au travers d'un crâne, on place d'un côté du crâne la sonde qui va émettre les ultrasons, et de l'autre, un hydrophone pour mesurer le champ de pression. Le set-up détaillé est illustré en figure 3.

Un protocole très strict a été défini pour mesurer les champs de pression au travers de l'échantillon de crâne humain de manière précise, afin d'être capable de reproduire les mêmes configurations en simulation. Un cadre a été construit pour positionner le crâne dans la cuve. Le crâne (attaché au cadre) est tout d'abord dégazé puis passé au CT (pour en déduire sa géométrie et ses propriétés acoustiques). Il est ensuite placé dans la cuve. Le cadre comporte 4 points de repère qui sont repérés avec le robot, ce qui permet ensuite au robot de positionner la sonde à l'endroit voulu dans le repère du crâne. De même, le robot vient repérer de manière précise le banc cartésien auquel est fixé l'hydrophone. Ce protocole précis nous a permis d'atteindre un erreur de positionnement comprise entre 1.12mm et 1.25mm. Une fois tous les éléments mis en place, un scan en 3D est effectué par l'hydrophone attaché au banc cartésien, qui est lui même piloté par un code Python. Les signaux enregistrés en chaque point sont ensuite post-traités avec un code Python également.

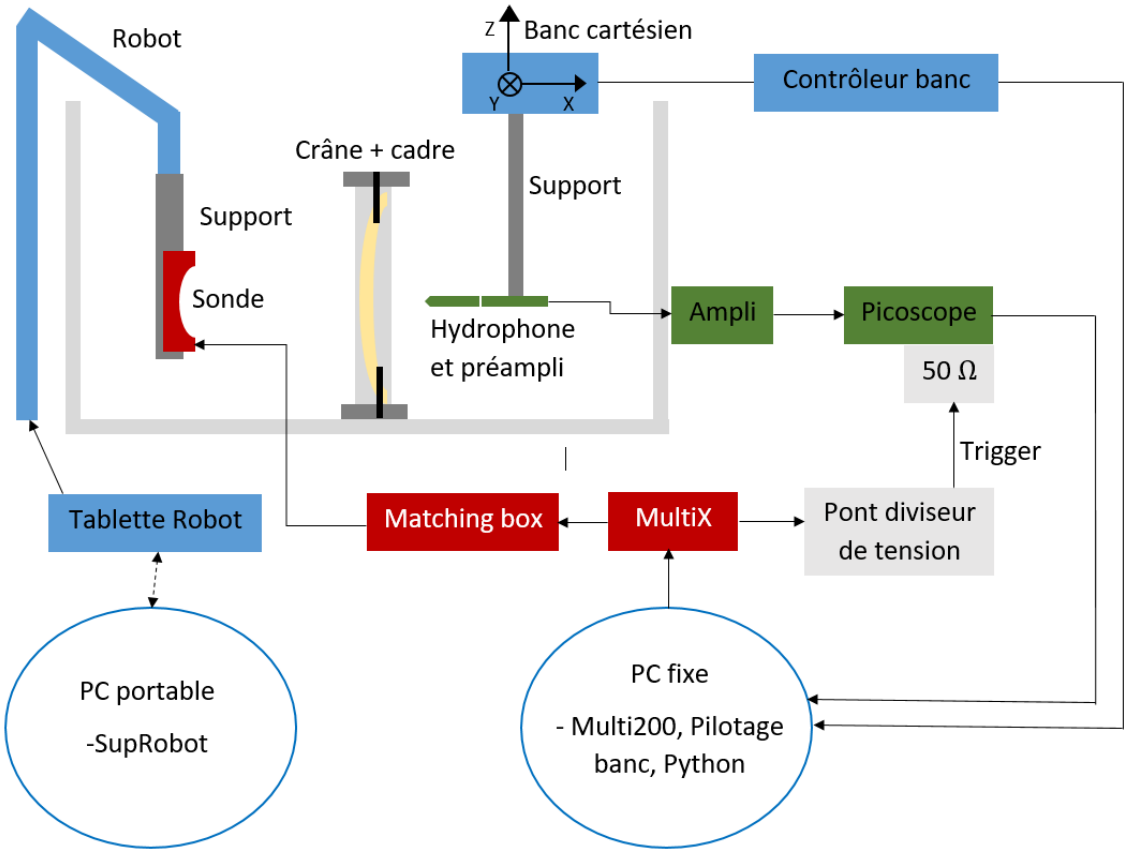


*Figure 3: Set-up pour les mesures ultrasonores transcraniens*

Le protocole a tout d'abord été validé grâce à des mesures sans crâne pour référence. Ensuite, trois champs transcrâniens ont été mesurés pour trois positions de la sonde, illustrées en figure 4.

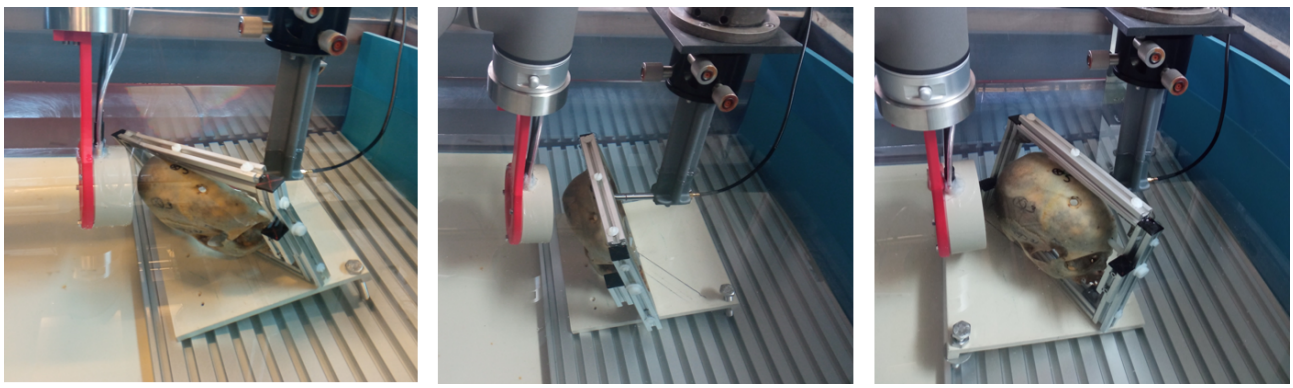

*Figure 4: Les 3 positions de la sonde*

### Comparaison des champs simulés et mesurés au travers d'un échantillon de crâne humain

Pour les 3 positions de la sonde, l'erreur de position focale $\Delta X_{max}$, l'erreur d'amplitude focale $\Delta P_{max}$ et l'erreur de volume focal $\Delta V_{focal}$ entre les champs expérimentaux et simulés (avec SplineBeam, CIVA ou k-Wave) sont présentées en table 7.

Cette table montre une bonne concordance entre les champs mesurés et simulés avec toutes les méthodes de simulation. La plupart des erreurs de position focale sont entre 1mm et 2mm, et la plupart des erreurs d'amplitude focale sont inférieures à 2dB, ce qui est très faible comparé à la différence d'amplitude focale entre les mesures avec et sans crâne qui est toujours supérieure à 13dB. Enfin, les erreurs de volume focal sont toutes inférieures à 20%.

L'erreur de position focale est plus faible pour SplineBeam que pour les autres méthodes de simulation.

*Table 7: Comparaison des champs de pression simulés et mesurés expérimentalement au travers d'un crâne*

| Pos | Comparaison | $\Delta X_{max}$ | $\Delta P_{max}$ | $\Delta V_{focal}$ |
|---|---|---|---|---|
| 1 | Avec/sans crâne | 4.64mm | −13.12dB | 2.43% |
| | SplineBeam/Exp | 1.58mm | −0.14dB | 0.28% |
| | k-Wave hétérogène/Exp | 1.58mm | −2.00dB | 6.16% |
| | k-Wave homogène/Exp | 2.55mm | −1.58dB | 1.75% |
| | CIVA/Exp | 2.06mm | +0.14dB | 3.74% |
| 2 | Avec/sans crâne | 1.73mm | −13.70dB | 6.44% |
| | SplineBeam/Exp | 1.00mm | +0.17dB | 11.70% |
| | k-Wave hétérogène/Exp | 1.12mm | −1.98dB | 18.26% |
| | k-Wave homogène/Exp | 1.50mm | −1.51dB | 16.20% |
| | CIVA/Exp | 1.50mm | +2.18dB | 11.88% |
| 3 | Avec/sans crâne | 2.12mm | −17.91dB | 48.43% |
| | SplineBeam/Exp | 1.12mm | +0.54dB | 14.82% |
| | k-Wave hétérogène/Exp | 2.60mm | −0.11dB | 15.38% |
| | k-Wave homogène/Exp | 1.87mm | −1.17dB | 11.97% |
| | CIVA/Exp | 1.22mm | +0.43dB | 6.77% |

Elle est toujours inférieure à 1.6mm, mais jamais en dessous de 1mm, ce qui pouvait être attendu sachant que l'erreur de positionnement des mesures était de l'ordre de 1mm. L'erreur d'amplitude focale de SplineBeam est très faible (<0.6dB en valeur absolue). Cette erreur est possiblement biaisée par le choix du coefficient d'atténuation qui est largement débattu dans la littérature. Cependant, les valeurs de $\Delta P_{max}$ sont plus proches les unes des autres qu'avec k-Wave hétérogène ou CIVA ce qui suggère que pour k-Wave hétérogène et CIVA il n'existe aucune valeur de coefficient d'atténuation telle que les erreurs $\Delta P_{max}$ soient faibles pour les 3 positions de la sonde. Finalement, SplineBeam est capable de simuler correctement les champs expérimentaux et de manière plus fiable que les autres méthode de simulation comparées.

Enfin, si l'on compare les erreurs entre k-Wave homogène et hétérogène, on remarque qu'elles sont en moyenne équivalentes. Ce résultat est une première validation expérimentale de la méthode d'homogénéisation développée dans la première section.

## Conclusion

Une méthode de simulation ultrasonore transcrânienne rapide, basée sur un nouveau modèle de crâne lisse et homogène personnalisé, a été développée. La capacité de cette nouvelle méthode de simulation à calculer des champs de pression réalistes au travers d'un crâne a été vérifiée expérimentalement. Dans un premier temps, un modèle lisse et homogène du crâne, réaliste et favorable aux algorithmes de calcul de champ rapides, a été développé. Pour cela, les surfaces internes et externes du crâne ont été modélisées en utilisant une méthode appelée « Multi-level Bspline Approximation », et une méthode d'homogénéisation des propriétés acoustiques du crâne a été développée et validée numériquement. Ce modèle de crâne lisse et homogène a ensuite été utilisé en entrée de l'algorithme de calcul de champ développé. Cet algorithme, nommé SplineBeam, est basé sur une méthode de calcul des trajets ultrasonores par minimisation de la fonction temps de vol, qui est rapide et précise, et qui, combinée à la méthode des pinceaux, permet un échantillonnage régulier de la sonde ultrasonore. SplineBeam a été validé numériquement, par comparaison avec des solveurs existants (dont k-Wave) sur une série de configurations, et expérimentalement, par comparaison avec des champs de pression acquis par hydrophone au travers d'un échantillon de crâne ex vivo. Les champs simulés avec SplineBeam se sont avérés être plus proches des champs mesurés expérimentalement que les champs simulés avec k-Wave, ce qui valide à la fois le modèle du crâne et la méthode de calcul de champ développés. De plus, SplineBeam peut restreindre son calcul à la tâche focale, ce qui, pour une grande sonde, lui permet de réduire drastiquement le nombre de points de calcul et d'avoir des temps de calcul de deux ordres inférieurs à ceux de k-Wave.

# List of Figures

# List of Tables

# Symbols and abbreviations

**BBB** Blood Brain Barrier

**Config** Configuration

**CT** Computed Tomography

**Exp** Experiments

**FD** Finite Differences

**FFT** Fast Fourier Transform

**FUS** Focused UltraSound

**HIFU** High Intensity Focused Ultrasound

**HU** Hounsfield Unit

**IR** Impulse response

**KW** k-Wave

**L-BFGS** Limited-memory Broyden–Fletcher–Goldfarb–Shanno

**MBA** Multi-level B-spline Approximation

**RT** Ray-Tracing

**SB** SplineBeam

**Simu** Simulation

**STL** Stereolithography

# Introduction

Most drugs are ineffective for brain diseases because of their extremely low Blood-Brain-Barrier (BBB) penetration. This barrier restricts the passage of many substances, including drugs, from the bloodstream into the brain to protect the brain from potentially harmful compounds. Focusing low intensity ultrasound waves in the brain, combined with the injection of microbubbles in the blood vessels, allows to open this barrier. The mechanical effect of ultrasound will make the microbubbles oscillate. This mechanical disruption creates temporary gaps or openings in the tight junctions between the endothelial cells that form the BBB, allowing the drugs to pass. BBB opening [11] is an example of ultrasound use for brain therapy. Other examples include thermal ablation [12] and neuro-modulation [13].

In the field of ultrasound brain therapy, one of the main challenges is to choose the right acoustic pressure dose to optimize and secure the therapy. The problem is that, to reach the brain, ultrasound has to pass through the skull. However, the skull is a complex medium which strongly attenuates and deviates the ultrasound beam, so the dose emitted will be reduced and the focal spot shifted and distorted after crossing the skull. Furthermore, the geometric and acoustic properties of the skull vary between and within individuals, so passing through different skulls, or parts of the skull, will not influence the emitted dose and the focal spot in the same way. If the ultrasound dose is not adapted to the patient, the latter risks brain damage (if the dose is too high) or lack of treatment efficacy (if the dose is too low). Dose monitoring is mostly carried out by MRI (MR-ARFI or thermometry), which is costly. To do away with the need for MRI, and thus extend the use of ultrasound brain therapy, while guaranteeing treatment safety and efficiency, it is necessary to simulate ultrasound propagation through the skull in a personalized way. Indeed, such simulations will help determine an acoustic dose according to the patient, as well as find the best transducer position to reach a given target.

In 2003, Aubry et al. [14] proposed the first personalized transcranial ultrasound simulation tool. They developed a finite difference algorithm, as well as empirical equations for computing 3D skull acoustic property matrices from a patient CT scan. Those matrices can be directly used as an input to the simulation tool, providing a highly detailed skull model, and thereby highly accurate personalized transcranial simulations. However, finite differences require the spatial step to be small enough to converge, making this method quite slow and memory demanding.

In 2012, Jing et al. [15] proposed to use a k-space method to simulate wave propagation through the skull. Like finite differences, it allows a heterogeneous description of the skull, but k-space needs less spatial resolution to achieve convergence with reasonable accuracy. It results in a computation time decrease of two orders of magnitude [15]. Thus, this method has become the reference for transcranial ultrasound simulations, especially since the development of the Matlab toolbox k-Wave [16] in 2010. However, the k-space method is still slower than ray-tracing by one order of magnitude [17], and computation speed is sometimes of crucial importance to make these simulations usable for clinical applications.

For High Intensity Focused Ultrasound (HIFU) applications, where the focus position and shape are of crucial importance, aberration correction can be performed. Aberration correction consists in using a multi-element transducer and computing emitting delays for the transducer elements, so that the ultrasound focuses at a desired location. The delays are computed by taking into account the skull effects. Several studies [5] [18] [17] [19] compared the ability of various transcranial ultrasound simulation methods to correct skull-induced aberrations to maximize the pressure on the other side of the skull as close as possible to the target point. They measured the pressure field across several human skull samples using two types of delay laws. In one case, these delay laws were computed using a numerical method (finite differences or k-space), in the other, using a semi-analytical method (ray-tracing). The results show that numerical method based phase correction outperforms ray-tracing based phase correction, but the gap between numerical methods and ray-tracing vary between the studies (ranging from a 2% difference [19] to a 50% difference [18] in restored pressure at focus). Thus, these studies show that, depending on the algorithm and skull modeling

used, semi-analytical methods can reach similar accuracies for skull aberration correction. However, they only worked on aberration correction, which means they only computed delay laws and did not simulate the whole pressure fields, which is what we are interested in for personalized dosimetry and transducer position optimization. Thus, they did not compare the fields simulated by the two types of methods with experimentally measured fields.

To sum up, over the last twenty years, numerous personalized transcranial ultrasound simulation tools for computing pressure fields have been developed, and could be used to predict the acoustic dose to be delivered in ultrasound brain therapy, depending on the patient and the target to be reached. Nevertheless, numerical simulation methods suffer from convergence constraints that forces them to have a large number of computation points and time steps, which makes them too slow for most clinical applications. On the other hand, semi-analytical methods, which are faster than numerical ones, as they do not have such convergence constraints, are mostly outperformed by numerical ones in terms of realism, which makes them not accurate enough for most clinical applications. However, a recent study [19] showed that semi-analytical methods could reach approximately the same accuracy as numerical ones for aberration correction. This suggests the potential of well-designed semi-analytical methods to combine computation speed and accuracy of results. For transcranial pressure field computation, it does not yet exist any simulation method combining these two assets. That is why the goal of this thesis is to develop a new semi-analytical ultrasound simulation method for transcranial pressure field computation, that combines computational speed and pressure field realism. This work takes parts in improving the CIVA Healthcare platform [20] developed in our team at the CEA, and is based on some of Hamza Chouh's work [21].

The first chapter presents the state of the art in transcranial ultrasound simulations [22]. First, a brief description of the application cases of such simulations are described. Then, the different skull models and simulation methods are detailed and compared. Finally, a review of the experimental validations of transcranial ultrasound simulations is given.

As transcranial simulation accuracy is highly dependent on skull modelling [23], Chapter II aimed to build a realistic skull model from a CT scan in a way suitable for semi-analytical ultrasound simulation methods. Indeed, most existing skull models are suitable for numerical methods only, and the skull models used for semi-analytical methods are often very simple. The skull model has to be built from a CT scan to make the simulation tool a personalized one. The first objective was to model the skull geometry smoothly to get closer to the real skull shape compared to a meshed representation. In addition, a smooth geometry will enable us to use a minimization algorithm in chapter III. It also avoids having sharp edges (as is the case in a mesh) which can cause numerical errors. The second objective of this chapter was to develop a new skull acoustic property homogenization method. Indeed, a homogeneous skull model is often required as input to semi-analytical simulation methods, but most homogeneous models are built by simply averaging the acoustic properties derived from the CT scan. Thus, a more realistic skull acoustic property homogenization method was developed [24].

The aim of Chapter III was to develop a new and fast semi-analytical ultrasound simulation method for computing pressure fields through the skull, using the skull model developed in Chapter I. As most semi-analytical methods are based on ray tracing, they do not ensure a regular sampling of the transducer, which results in a less realistic pressure field. Thus a new method was needed. The first objective of this chapter was to develop a method for computing ultrasonic paths by minimizing the time-of-flight function, which will allow a regular sampling of the transducer. The second objective was to validate the developed ultrasonic path computation method by applying it to the computation of delay laws for skull aberration correction. The third objective was to implement a semi-analytical pressure field computation algorithm using the ultrasonic path computation method developed. The fourth objective was to numerically validate the pressure field computation algorithm by comparison with existing algorithms in the literature. This is a second validation step that allows to validate the whole pressure field computation algorithm on standard configurations. Finally, the last objective was to evaluate and optimize the computation time of the pressure field computation algorithm developed, in order to get the fastest algorithm possible.

The aim of Chapter IV was to experimentally validate the simulation method developed in Chapter II and the skull model developed in Chapter I, by comparing transcranial hydrophone measured pressure fields with simulated ones. Indeed, comparing simulated fields with experimental ones is the only way to ensure the realism of a simulation method. In addition, there are few experimental measurements of transcranial pressure fields in the literature, and to our knowledge, no comparison between measured pressure fields and semi-analytical simulated ones. The first objective of this chapter was to define an experimental set-up for the measurements and to choose the equipment. Then, a measurement protocol was developed to achieve a

precise positioning of the transducer and hydrophone relative to the skull. Before doing the measurements, a method to simulate the same configurations as in the measurements was defined. Then, pressure fields in water (without skull) were measured to evaluate the error between the simulated and measured pressure fields, as a reference. It also helped validate the measurement protocol. Finally, the realism of the pressure fields simulated with the simulation method developed in chapter III and the skull model developed in chapter II was assessed by comparing them with those experimentally measured through a human skull sample. In addition, comparisons with other simulation methods were carried out.

# Chapter 1

# State of the art of transcranial ultrasound simulations

Transcranial ultrasound (see figure 1.1) is increasingly used for therapy and imaging of the brain. Therapeutic applications include thermal ablation [12], Blood-Brain-Barrier (BBB) opening [11] and neuro-modulation [13]. Transcranial ultrasound imaging has been used for a long time for vascular and flow imaging through the temporal windows but its generalization is still impeded by the strong image distortion and sensitivity loss at typical imaging frequencies [25].

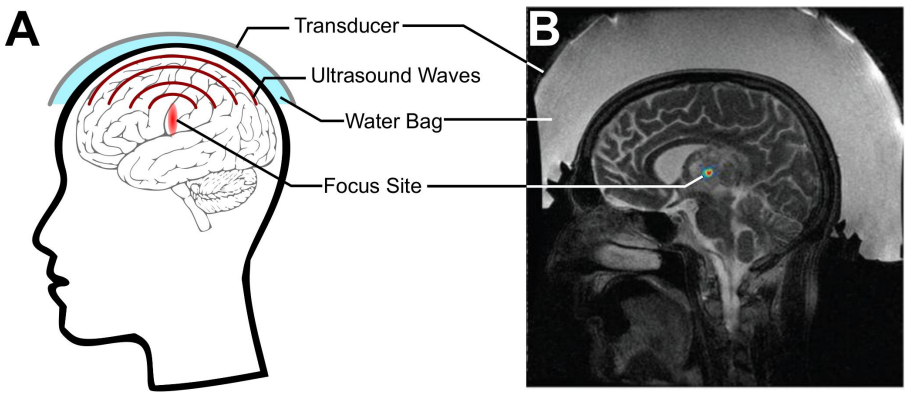


*Figure 1.1: Focused ultrasound for non invasively delivering acoustic energy to the brain. (A) Schematic of Focusing UltraSound use. (B) Simulation of energy deposited by a commercial MRI-guided FUS system through the skull, from [26]*

Making ultrasound cross the skull is of high interest but it is also a big challenge as the skull is highly attenuating and aberrating. In addition, the pores located in the trabecular bone act as scatterers for ultrasound. As a result, ultrasound beams are both spatially shifted and attenuated. As the structure and acoustic properties of the skull differ between samples and even within a sample, case-specific simulations are needed to perform transcranial focused ultrasound interventions safely.

The first issue when performing transcranial acoustic simulations is skull modelling. Due to the big variations within a skull and between specimens, most studies use images of the skull to extract its geometric description and derive acoustic properties using empirical relationships. However, these relationships are only hypothetical and the imaging resolution is often not precise enough to fully describe the porous structure of the skull. Once the skull is modelled, several simulation methods can be used, which can be divided into two main categories: numerical methods and semi-analytical ones. The type of method used usually depends on the application and the aim is to find the best balance between accuracy and computation performances. Likewise, approximations, such as neglecting shear waves and non-linear effects, can be made to speed up the simulations but the loss in accuracy has to be evaluated.

After a brief overview of a few applications of transcranial acoustic simulations in the first section, sections one and two will focus on the different skull modelling methods that were previously introduced, and on the simulation methods used for transcranial ultrasound. Finally, the methods used to compare simulations and experiments will be described in the last section. Indeed, another main issue with transcranial acoustic simulations is to evaluate their accuracy. The only way to do so is to compare the results of the simulations

with the results of experiments in a set-up as close as possible to the simulated one.

## Contents

## 1.1 Applications of transcranial simulations

Transcranial acoustic simulations have many applications. Their main goal is to optimize the ultrasound treatment, by predicting the acoustic dose, the focal characteristics, and for operation planning. When combined with a multi-element transducer or an acoustic lens [27], simulations can be used to correct the phase and amplitude (especially at high frequencies where the distortion induced by the skull is higher) of the emitted signal in order to achieve good focusing through the skull or for imaging applications [5] [28]. For thermal therapies, such as sub-thalamic nuclei ablation for the treatment of essential tremor [29], heat simulations are also often performed in order to predict whether heating occurs at the planned location and to avoid burning surrounding tissues. Acoustic simulations are thus needed in this case, as the pressure field obtained is the input of the thermal simulations. Thermal simulations are also used for non-thermal applications, in order to predict that no unwanted heating happens. Generally speaking, in addition to optimizing the treatment, acoustic simulations are often performed to ensure the safety of ultrasound therapies. Apart from heating prediction, they are used for standing waves and cavitation prediction [30] [31] [32] [33] [34] [35]. Finally, acoustic simulations can be used to optimize the positioning of the transducer [36].

### 1.1.1 Phase and amplitude correction

Transcranial simulations can be used to correct the phase difference induced by the skull in order to obtain nearly optimal focusing. To do that, several strategies can be used: classical time reversal method and cross correlation.

Time reversal consists in simulating wave propagation from a virtual source point located inside the brain at the intended focusing location and recording the signals on each element of the transducer. Then, if only time derivatives of even order are considered in the simulation equation, one can achieve focusing at the virtual source point by emitting the reversed signals received by each element of the transducer.

The cross correlation method aims to facilitate the experimental back-propagation, by using only the phase delays (and not the whole reversed signals). An element is chosen as reference, and then for each element $i$, the delay $\tau_i$ is found by maximization of the cross correlation function [37]:

$$p_{\text{ref}}.p_i(\tau_i) = \int p_{\text{ref}}(t)p_i(t+\tau_i)dt \tag{1.1}$$

where $p_{\text{ref}}$ and $p_i$ are the received signals of the reference element and element $i$.

One can find a way to distribute the emitted energy across the skull surface so that the transducer elements near the thickest parts, and thus the most absorbing parts, of the skull, emit less power than the elements in front of the thinnest locations. Doing so will ensure a better transmission of the waves while avoiding unnecessary heating of the skull in the most absorbing locations. This distribution of energy can be achieved with amplitude correction [35] [37] [14] [38] [18].

Acoustic simulations can also be combined with the emission of a cavitation bubble that reflects the ultrasound waves [39]. This method uses acoustic simulations as a first step to focus near the intended location which enables the creation of a cavitation bubble, whose signal is recorded by the transducer array. The bubble is then used an invasive source inside the brain to obtain accurate focusing. For safety reasons, the relevance of this approach for clinical applications is debatable.

### 1.1.2 Heating prediction

The pressure field computed by the transcranial acoustic simulation can be entered as input to a heat transfer equation to simulate the heating of the skull and brain, and avoid burning tissues [38] [18] [40] [41] [42] [43] [44] [45] [46]. This heat transfer equation is called the Pennes Bio-Heat equation and is given by :

$$\rho C\frac{\partial T}{\partial t} = \nabla\cdot(k\nabla T) - \rho_b w_b C_b(T-T_b) + \frac{\alpha p^2}{\rho c} \tag{1.2}$$

Where $\rho$ is the density of the tissue, $C$ is its specific heat capacity, $k$ is its thermal conductivity, $\alpha$ is its absorption coefficient, and $c$ is its speed of sound. $\rho_b$ is the blood density, $C_b$ is its specific heat capacity, $T_b$ is the temperature, $\omega_b$ is the perfusion rate, and $p$ is ultrasound pressure derived from the acoustic model.

The first term of the right side models the thermal diffusion, the second one models the effects of perfusion and the last one models the acoustic power (found with the acoustic simulation). In Kyriakou et

al. [18] and Guo et al. [44] add another term to the equation to model the body heat production. The Bio-Heat is often solved using 3D finite differences. The criteria for a safe transcranial treatment are that the temperature at the focal region is higher than 60 °C and that there are no regions under the skull whose thermal dose is higher than 90 equivalent minutes at 43 °C [38]. Using the temperature found after solving the Bio-Heat equation, the thermal dose can be computed as:

$$TD = \int_0^t R(T(t'))^{(T_{\text{ref}} - T(t'))} dt' \tag{1.3}$$

Where $T_{\text{ref}} = 43°\text{C}$ and

$$R(T) = \begin{cases} 0.50 & \text{for } T \geqslant T_{\text{ref}} \\ 0.25 & \text{for } T < T_{\text{ref}} \end{cases}$$

The thermal dose is defined as cumulative equivalent minutes at 43°C. For thermal ablation, the thermal dose can be used to compute the power required to achieve a thermal dose high enough to cause irreversible damage in the brain tissues. For instance, Pulkkinen et al. [45] perform the sonications with the power required to achieve an equivalent thermal dose of 25min at the focus. In addition to ensuring that the target location is heated enough to perform ablation, the thermal dose can also be used to check whether heating occurs at undesired locations. For example, in Pulkkinen et al. [45], target positions inducing a thermal dose of more than 5min at a location adjacent to the skull, were considered to be untreatable.

For non-thermal applications such as BBB opening, heat simulations can be performed to ensure that no undesired heating occurs during the treatment. For instance, Marquet et al. [40] estimate the maximum heat dissipation increase in the skull and find that after 60s of sonication, the temperature increase is lower than 0.03°C, which is negligible. In fact, this is due to the very short duty cycles, which let the skull bone cool enough between each pulse.

During most transcranial treatments, active cooling of the skull is performed in order to limit skull heating. Pulkkinen et al. [45] simulate the circulating water at 15°C for 15min prior to sonications using the Dirichlet boundary condition with constant temperature of 15°C around the skull. The simulated field is then used as the input temperature field for the sonications simulations. Kyriakou et al. [18] use a similar method to simulate the cooling procedure. Pulkkinen et al. [45] also simulate the active cooling of the skull base. This cooling method is based on circulating cooled water prior to sonications in a large nasal cavity at the centre of the skull-base. It is very important to apply such a method when targets are located near the skull base, as measurements have shown that the temperature in the soft tissue adjacent to the bone can exceed that of the focus [45]. In this study [45], the nasal cavity cooling was found to increase the treatment envelope for the uncorrected sonications, while for the phase corrected sonications, the nasal cavity cooling was found to sometimes have negative effect on the sonications if the focus was to close the cooled area (in those cases, the temperature also decreased at the focus).

Most thermal simulations are performed assuming that thermal tissue properties are not temperature dependant. However, the high temperature used for thermal ablation can cause vascular shutdown, which prevents the perfusion in those locations and cause the temperature to increase faster. Kyriakou et al. [18] simulate this effect by assuming that perfusion decreases linearly when the tissue temperature is above 50°C and stops above 51°C. The results show that after 20s of sonication, only 1 °C of the total additional temperature increase was observed in tissues where vascular shutdown occurred, suggesting that this effect can be neglected.

Heat simulations can also be used to predict thermal lesions. McDannold et al. [42] gathered the post-treatment images from 40 clinical TcMRgFUS treatments, including 16 for which bone marrow lesions were observed. They predicted the presence of lesions using a threshold for the acoustic energy of 18.1-21.1 kJ (maximum acoustic energy used) and 97.0-112.0 kJ (total acoustic energy applied over the whole treatment). The results show that the size of the lesions was not always predicted by the acoustic energy. However, the locations, sizes, and shapes of the heated regions estimated by the thermal simulations were qualitatively similar to those of the lesions and the lesions generally appeared in areas with high predicted temperatures.

### 1.1.3 Transcranial FUS safety assessment

Ultrasound can produce cavitation phenomenon and thus create bubbles that will oscillate with the varying pressure field. If the bubble oscillates too much and collapses, the pressure and temperature can increase very fast, and blood vessels can be damaged, causing haemorrhages. Simulations can be used to predict

cavitation phenomenon [33] [34] [35] and avoid haemorrhages in the brain. Several studies have used simulation to try to understand phenomenon that occurred during clinical trials [33] [34]. It can help avoid these effects in the future. However, simulation can also be used to prepare case-specific treatments and prevent those undesirable effects. The standard indicator to evaluate the likelihood of cavitation risks is the mechanical index (MI), defined by:

$$\mathrm{MI} = \frac{P_-}{\sqrt{f}} \tag{1.4}$$

Where $P_-$ represents the peak rarefactional pressure and $f$ is the frequency.

This equation 1.4 represents an indicator for mechanical index (MI), where $P_-$ is the peak rarefactional pressure and $f$ is the frequency. However, it should be noted that cavitation depends on other factors that are currently unknown.

To ensure the safety of diagnostic devices and avoid adverse biological effects associated with acoustic cavitation, the FDA (Food & Drug Administration - 510K Norm 1992) imposes a maximum MI value of 1.9 [33].

In particular, studies [40] and [47] have focused on the TRUMBI (transcranial low-frequency ultrasound-mediated thrombolysis in brain ischemia) clinical trial which has been stopped prematurely because haemorrhages were observed on several patients. Baron et al. [33] simulate the pressure fields used in the trial, and they compute the associated MI. They find that the peak negative pressure is higher than the cavitation threshold in large areas of the brain, which is mainly due to the presence of standing waves. Using acoustic simulations, Pinton et al. [34] find that a volume of 2.7 $\mathrm{cm}^3$ was above the MI threshold in the TRUMBI trial. They also investigate the risk of cavitation at 220kHz and 1MHz. They find that for an equivalent energy deposition rate and the same geometry, the brain volume above the MI ($0.4 \leqslant MI \leqslant 3$) is 3 to 4 orders of magnitude larger at 220kHz than at 1MHz. This high correlation between frequency and the volume with a high probability of cavitation is due to three reasons. First, the focal volume decreases with the frequency. Second, the heat deposition increases when frequency increases (as absorption increases). Third, the pressure needed to obtain a given MI decreases as the square root of the frequency. Both studies claim that unfocussed transducers (as the one used in the TRUMBI trial) should not be used, in order to avoid creating hot spots at unwanted locations due to the focusing effect of the skull. Top et al. [35] use simulation to investigate blood-brain barrier disruption that was observed in the pre-focal region during previous experiments at 220kHz. Their results are in agreement with the disruption in the pre-focal region. However, they observe side lobes in the post-focal region in the simulations that did not seem to have had any effects in the experiments. They suggest this difference might be due to shielding of the ultrasound field due to microbubble activity in the focal region. They also simulate the field produced by the Passive Cavitation Detector (PCD) at its resonant frequency (610 kHz) and at the subharmonic of the transducer (110 kHz), as the sensitivity pattern is proportional to the transmitted field. Transcranial acoustic simulations can also help predicting standing waves, which are contributors to undesired cavitation effects. Deffieux and Konofagou [30] and Mueller et al [31] estimate standing waves using a filter that detects their characteristic pattern. First, the fast oscillations of the field are extracted along each dimension using a high-pass spatial filter. Second, a Hilbert transform is applied to obtain the envelope of this signal. Third, only the maximum of the three dimensions is kept so as to have a unique map. The resulting field estimates the maximum of the spatial modulation pattern which is often associated with the presence of standing waves. Zhang et al. [32] use what they call the standing-wave ratio to predict the intensity of standing waves. It is defined as:

$$R_a = \frac{P_{\mathrm{max}} - P_{\mathrm{min}}}{P_{\mathrm{avg}}} \tag{1.5}$$

Where $P_{\mathrm{max}}$, $P_{\mathrm{min}}$, and $P_{\mathrm{avg}}$ represent the maximum, minimum, and average pressures, respectively.

Methods for reducing standing waves have also been developed and verified thanks to simulations. Baron et al. [33] suggest using higher frequencies (more absorption so less interferences), reducing the duration of the pulses (to avoid interferences) and applying modulation. Deffieux and Konofagou [30] propose to use fast periodic linear chirps to reduce standing waves. Chirps are signals with a varying frequency over time. It induces a time-dependent phase difference between the incident and reflected waves which ensures that, even if interferences occur, their position will change over time and thus, after some time, the effects of constructive and destructive interference will even out. When using a chirp with a period of 23µs and a frequency oscillating between 450 and 550 kHz, they manage to reduce the peak amplitude of standing waves (as a percentage of the peak pressure) from 19% to 12%, and to reduce the standing wave volume

(that is to say the volume with standing wave amplitude higher than 5% of the peak pressure) from 0.87% to 0.17%. While the standing wave volume reduction is quite satisfying (5 times reduction), the standing wave amplitude reduction is not as significant (1.5 times reduction). The authors suggest it may be due to interferences occurring close to the skull surface, because the time delay between the incident and reflected waves is too small compared to the frequency shift. Zhang et al. [32] use the Randi function to generate a random phase between 0 and $\pi$, which is added to the original signal at regular intervals to break the standing wave formation condition.

## 1.2 Skull modeling

Skull modelling is an important factor for accurate simulations. As the shape and acoustic properties of the skull vary between individuals, and even within one individual (across the years and among the whole surface of the skull), it is very tricky to create good skull models. Most skull models are based on skull imaging of the considered individual, as for example X-rays.

### 1.2.1 Shape

When finite differences or other voxel-based simulation algorithms are used, the skull shape does not need to be extracted. However, for geometrical based simulation algorithm, one needs to model the skull shape. Hayner and Hynynen [48] model the skull as a medium contained between two flat, but not necessarily parallel, interfaces, as in the frequency range considered, the minimum radius of curvature of a skull is greater than the wavelength. However, in most studies, the skull is segmented from either computed tomography (CT) scans or magnetic resonance (MR) images, in order to have a more accurate modelling of the geometry. To obtain the shape of the skull from a tensor of intensity voxels, two steps are usually needed: a segmentation step and a mesh-making step. Segmentation of the bone voxels is often performed using a threshold method. Clement and Hynynen [49], Clement et al. [50] and Yin and Hynynen [51] identify the inner and outer surfaces of the skull by searching for the innermost and outermost densities greater than $1400$ kg.m$^{-3}$ along each line of a CT slice. Pichardo and Hynynen [52] perform the segmentation with the FMRIB Software Library [53]. Mesh-making is often performed using an iso-surface algorithm [52] [54] [55] [56] [57]. In some cases, a condition is imposed so that no surface area element is greater than $\frac{\lambda}{2}^2$, with $\lambda$ the acoustic wavelength in water [55] [56]. For skull segmentation from MRI, two UTE (ultra-short echo time) images are generally combined (using simple arithmetic operations) to separate skull voxels from other tissues using various thresholds [44] [58]. In Miller et al. [58], after thresholding, a spatial connectivity requirement is applied to the pixels in the bone class, to eliminate isolated pixels or groups of pixels that are clearly not part of the skull.

### 1.2.2 Acoustic properties

Several studies have measured skull acoustic properties (density, speed of sound and attenuation) [48] [59] [60]. However, as the skull acoustic properties are very different depending on the patient and the skull part considered, these values are good orders of magnitude but not reusable. Thus, most recent studies try to deduce the acoustic properties of a given skull from images acquired with either CT or MR.

#### 1.2.2.1 Density

**Linear relationship between density and Hounsfield Units (HU)** In Rho et al. [61], ultrasonic measurements show a linear relationship between density and HU. HU are arbitrary units that depend on the CT scanner used. It is thus necessary to have a specific conversion from HU to any physical measure for each sample.

Connor et al. [62] introduce a method to compute the skull density from HU. Assuming that the relation between HU and density is linear, and ensuring that a sample of both water and air (which have known densities) appear in the CT scan, one has:

$$\rho = \kappa_1 H + \kappa_0 \tag{1.6}$$

With $\kappa_1 = \frac{1}{H_{\text{water}} - H_{\text{air}}}$ and $\kappa_0 = \frac{-H_{\text{air}}}{H_{\text{water}} - H_{\text{air}}}$.
This method is used in [5] [46] [54] [55] [56] [63] [23] [64].

To confirm the linear relationship obtained, they make the hypothesis that density and HU are related by a second-order polynomial. They use the relationship relating the total mass of the skull $M$ with the volume $v$ of a voxel and the sum of all densities across the skull: $M = v\sum_{\text{skull}}\rho$. Using this additional relationship, they are able to fit a second-order polynomial for density, but they find that the quadratic term is negligible in front of the others (by five orders of magnitude). Thus, their linear approximation seems correct.

**Porosity-based and equivalent relationships** Aubry et al. [14] propose a different method based on the bone porosity. HU is defined by:

$$H = 1000\left(\frac{\mu_x - \mu_{\text{water}}}{\mu_{\text{bone}} - \mu_{\text{water}}}\right) \tag{1.7}$$

where $\mu_x$, $\mu_{\text{water}}$, and $\mu_{\text{bone}}$ denote the photoelectric linear attenuation of the explored tissue, water, and bone. They propose a linear relationship:

$$\mu_x = \Psi\mu_{\text{water}} + (1-\Psi)\mu_{\text{bone}} \tag{1.8}$$

with $\Psi$ being the bone porosity. Thus, they have:

$$\psi = 1 - \frac{H}{1000} \tag{1.9}$$

The density can be computed from the porosity with:

$$\rho = \psi\rho_{\text{water}} + (1-\psi)\rho_{\text{bone}} \tag{1.10}$$

A density map extracted from a skull CT scan is shown in figure 1.2. This method is used in [31] [32] [17], [33] [35] [38] [18] [39], [65] [66] [15].

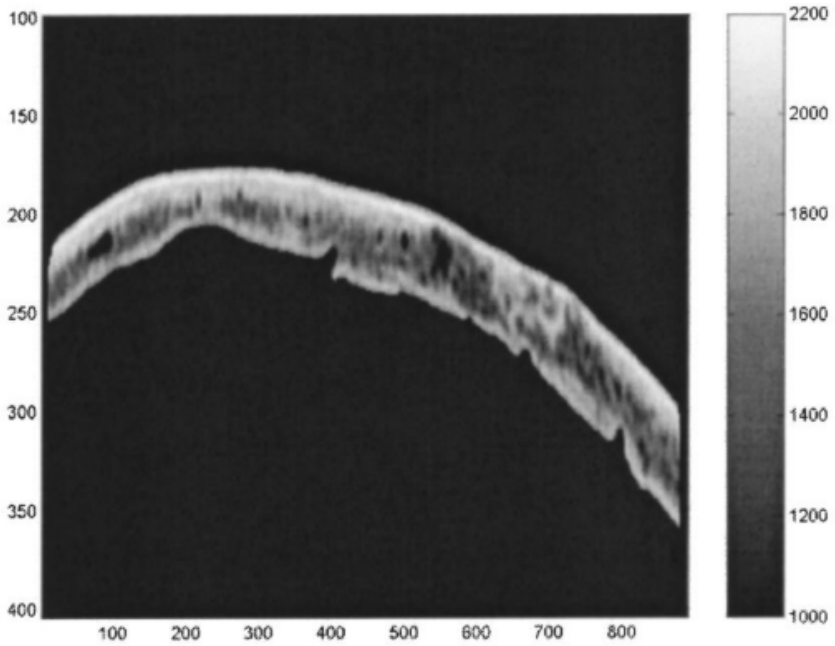


*Figure 1.2: Slice of the 3-D mass density map deduced from CT scans (in kg.m$^{-3}$), from [14]*

This relationship implies a linear relationship between the bone density and the Hounsfield Units (HU), as it was assumed in the previous section. However, instead of building the linear fit from $H_{\text{water}}$ and $H_{\text{air}}$, they build it from $\rho_{\text{water}}$ and $\rho_{\text{bone}}$. In the first case, $H_{\text{water}}$ and $H_{\text{air}}$ are derived from direct measurements on the CT scans. Thus, they are more reliable than the values of $\rho_{\text{water}}$ and $\rho_{\text{bone}}$, which are taken from measurements from the literature that were probably not conducted in the exact same conditions as the experiments conducted in the study. On the other hand, if the density is assumed to be linearly related to HU in the range corresponding to bone, it is probably not the case for all values of HU. Thus, building the linear fit from values in water and cortical bone (which are the lower and upper bounds for HU in the skull) seems more accurate than using values from air and water.

Guo et al. [44] use the same equations as before, but they change the definition of porosity:

$$\psi = 1 - \frac{H}{\max(H)} \tag{1.11}$$

Indeed, with Aubry's definition of Hounsfield Units, one has $0 \leqslant H \leqslant 1000$. In this study, they generalize Aubry's formulas for raw CT data, where the maximum value of $H$ is not necessarily 1000.

Deffieux and Konofagou [30] normalize the apparent CT density to have $0 \leqslant \rho_{\text{CT}} \leqslant 1$, and then the density is given by:

$$\rho = \rho_{\text{min}} + (\rho_{\text{max}} - \rho_{\text{min}})\rho_{\text{CT}} \tag{1.12}$$

This is, in fact, equivalent to the previous equation based on porosity as $\rho_{\text{CT}} = \frac{H}{max(H)} = 1 - \psi$.

Marsac et al. [2] introduce a new relationship for density:

$$\rho = \rho_{\text{min}} + (\rho_{\text{max}} - \rho_{\text{min}})\frac{H - H_{\text{min}}}{H_{\text{max}} - H_{\text{min}}} \tag{1.13}$$

This equation is similar to the porosity-based equation 1.10 and is equivalent to it when $H_{\text{min}} = 0$. Indeed, if $H_{\text{min}} = 0$, one has $1 - \psi = \frac{H - H_{\text{min}}}{H_{\text{max}} - H_{\text{min}}}$. Thus, this equation is the more general form of the porosity-based equation. This equation is used in [27], [19].

**Bone fraction based relationship** Vyas et al. [47] propose a method based on the fraction of bone in the voxel, which is defined by:

$$f = \frac{(H/1000) \times (\mu/\rho)_{\text{water\_eff}}}{\rho_{\text{bone}} \times (\mu/\rho)_{\text{bone\_eff}} - (\mu/\rho)_{\text{water\_eff}}} \tag{1.14}$$

where $(\mu/\rho)_{\text{eff}} = \frac{\sum S(E) \times (\mu/\rho)(E)_{\text{water}}}{\sum S(E)}$, and $S(E)$ is the beam spectrum as a function of energy. Then the density is defined by:

$$\rho = f \times \rho_{\text{bone}} + (1 - f)\rho_{\text{water}} \tag{1.15}$$

This method is similar to the porosity-based equation 1.10. However, bone fraction is computed in a more complicated way than porosity, and equation 1.14 seems not to be homogeneous.

#### 1.2.2.2 Speed of sound

**Linear relationships between speed of sound and Hounsfield Units** Fry and Barger [67] and Vyas et al. [47] use an empirical linear relationship linking directly the speed of sound to Hounsfield Units:

$$c = 1460 + 0.7096H \tag{1.16}$$

Clement and Hynynen [49] use a relationship between the average speed of sound in a skull and the average density of that same skull, obtained experimentally from 1000 measurements with 10 skulls at 0.51 MHz:

$$c = 2.06\rho - 1540 \tag{1.17}$$

With $c$ in m/s and densities $\rho$ between 1820 kg/m$^3$ and 2450 kg/m$^3$. Thus, $c \in [2209, 3507]$ m/s. This roughly corresponds to the range of values found in the literature.

As a linear relationship is assumed between density and HU, this relationship is similar to equation 1.16 as it implies a linear relationship between speed of sound and HU.

**Porosity-based and equivalent relationships** Similarly to the porosity-based relationship for density, Aubry et al. [14] propose a sound speed relationship based on porosity:

$$c = c_{\text{min}} + (1 - \psi)(c_{\text{max}} - c_{\text{min}}) \tag{1.18}$$

The linear relationship between velocity and porosity is justified by Carter and Hayes, who showed that the elastic modulus of bone is proportional to the apparent density cubed. This method is used in [31] [32] [15] [17], [33] [35] [38] [18] [39] [44] [65] [66]. This relationship is similar to equations 1.16 and 1.17 as it implies a linear fit between speed of sound and HU. However, equation 1.18 is more general as porosity does not depend on the CT scanner while HU do.

In the same way as for the density equations, other studies have improved the porosity-based equation for speed of sound to make it more general. To account for CT scans where HU are not normalized, Deffieux and Konofagou [30] propose:

$$c = c_{\text{min}} + (c_{\text{max}} - c_{\text{min}})\rho_{\text{CT}} \tag{1.19}$$

Which is equivalent to the equation introduced by Marsac et al. [2]:

$$c = c_{\text{min}} + (c_{\text{max}} - c_{\text{min}})\frac{\rho - \rho_{\text{min}}}{\rho_{\text{max}} - \rho_{\text{min}}} \tag{1.20}$$

These equations are also used in [27] [19]. Marsac et al. [2] search for the best value of $c_{\text{max}}$ such that the simulations fit the experiments.

**Relationships obtained with genetic algorithms** Connor et al. [62] use a genetic algorithm to find the optimal relationship between density and speed of sound at 0.74MHz, using a success function that compares the phase difference between simulation and experiment. They compare their result function with what could be expected for a cellular solid, as they approximate the skull bone as one. The speed of sound in a solid is given by $c = \sqrt{\frac{E}{\rho}}$ where $E$ is the Young's modulus of the material and $\rho$ its density. For open-pore cellular materials, it can be shown that $E \propto \rho^2$, while for closed-pore materials $E \propto \rho^3$. The curve of speed of sound against bone density obtained in this study agrees with these models. Indeed, it initially has a form similar to that of a square root function (as it would be for an open-celled porous solid), then the model transitions into a linear function (as it would be for a closed-celled porous solid). In addition, the transitional density region is located between the density of trabecular bone and that of cortical bone.

Pichardo et al. [54] use a similar method, but they investigate the sound speed relationships at various frequencies as they have found from measurements that the skull is a dispersive medium. They perform a two-step optimization (to speed up the process while maintaining a good simulation accuracy) at several frequencies: 0.27, 0.836, 1.402, 1.965, and 2.525 MHz. The sound speed functions found in this study were used (either directly or interpolated to fit the needed frequency) in [5] [46] [55] [56] [63] [23].

**Polynomial relationship** McDannold et al. [41] [42] assume that the relationship between the inverse of the speed of sound and the skull density can be approximated by a series of polynomials:

$$\frac{1}{c} = \sum_m B_m \rho^m \tag{1.21}$$

The advantage of this formulation is that they can estimate the phase shifts resulting from a change in speed of sound with:

$$\Delta\phi_k(x_i, y_i) \approx 2\pi f \sum_{j=0}^{i} \frac{\Delta z}{c(x_i, y_i, z_j)} = 2\pi f \Delta z \sum_m B_m \sum_{j=0}^{i} \rho^m(x_i, y_i, z_j) \tag{1.22}$$

Indeed, when thermal therapy is performed with ultrasound, they observe changes in the speed of sound inside the skull due to temperature changes. Thus, this formula allows adapting the phase shift during therapy. However, this polynomial relationship seems to go against all previous models that proposed a relationship proportional to density.

#### 1.2.2.3 Attenuation

**Constant attenuation** Deffieux and Konofagou [30] consider a constant attenuation across the whole skull as they claim that more complex models for attenuation can be inconsistent.

**Porosity-based and normalized density-based relationships** Similarly to their density and sound speed relationships, Aubry et al. [14] propose a bone porosity-based relationship for attenuation:

$$\alpha = \alpha_{\text{min}} + (\alpha_{\text{max}} - \alpha_{\text{min}})\psi^{\beta} \tag{1.23}$$

The constants were adjusted by comparing simulations with measurements. This method is used in [31] [32], [17] [33] [35] [38] [18] [39] [65] [66] [15].

Yoon et al. [68] use a method based on the normalized density, as was done by Deffieux and Konofagou [30] for density and speed of sound:

$$\alpha = \alpha_{\text{min}} + (\alpha_{\text{max}} - \alpha_{\text{min}})\rho_{\text{CT}} \tag{1.24}$$

Unlike the relationships for density and speed of sound proposed with the normalized apparent density, this formula is not equivalent to the porosity-based attenuation formula. Indeed, this is a linear relationship and not a power law, and $\rho_{\text{CT}} = \frac{H}{\max(H)} = 1 - \Psi \neq \Psi$.

**Bone fraction-based relationship** Vyas et al. [47] propose a method based on the fraction of bone in the voxel, which is defined by:

$$f = \frac{\frac{H}{1000} \times \frac{\mu}{\rho_{\text{water\_eff}}}}{\rho_{\text{bone}} \times \frac{\mu}{\rho_{\text{bone\_eff}}} - \frac{\mu}{\rho_{\text{water\_eff}}}} \tag{1.25}$$

With $\frac{\mu}{\rho_{\text{eff}}} = \frac{\Sigma S(E) \times \frac{\mu}{\rho_{\text{water}}(E)}}{\Sigma S(E)}$, where $S(E)$ is the beam spectrum as a function of energy. Then the absorption component of attenuation is defined by:

$$\alpha_a = f \times \alpha_{\text{bone}} + (1-f)\alpha_{\text{soft tissue}} \tag{1.26}$$

For the scattering component of the attenuation, they use data found experimentally by Tavakoli [69]. This data consists of experimental values of attenuation for various porosity values. They fit the data to linear curves and obtain four linear equations (for four ranges of porosity) relating the scattering component of attenuation with porosity. Then they use those equations to compute the scattering component of attenuation, and they use the voxel bone fraction to compute porosity:

$$\psi = \frac{f_{\text{maxsubject}} - f}{f_{\text{maxsubject}}} + 0.05 \tag{1.27}$$

**Relationships obtained with genetic algorithms** Pichardo et al. [54] use a genetic algorithm to find a relationship between attenuation and density at several frequencies: 0.27, 0.836, 1.402, 1.965, and 2.525 MHz. Like in 1.2.2.3, they find the relationship that minimizes the phase difference between simulation and experiment. The attenuation functions found in this study were used (either directly or interpolated to fit the needed frequency) in [5] [46] [55] [56] [63] [23].

**Polynomial relationship** McDannold et al. [41] [42] assume that the relationship between the attenuation and the skull density can be approximated by a series of polynomials:

$$\alpha = \sum_m A_m \rho^m \tag{1.28}$$

The advantage of such a formulation is that, assuming that attenuation mainly occurs along the propagation axis $z$, one can compute the pressure field without attenuation and deduce an approximation of the pressure field with a given attenuation model without having to run the whole simulation. Indeed, if attenuation mainly occurs along the $z$ direction, the pressure distribution for element $k$ is approximately:

$$P_k(x_i, y_i, z_i) \approx P_{k0}(x_i, y_i, z_i) \times \exp\left(-\sum_{j=0}^{i} \alpha(x_i, y_i, z_j)\Delta z\right) \tag{1.29}$$

Where $P_{k0}$ is the pressure computed without attenuation for transducer element number $k$. This formula shows that the pressure field without attenuation can be computed separately from the attenuation contribution with this method, allowing to compare several attenuation models without any loss of computation time.

**Frequency dependency of attenuation** In Pichardo et al. [54], the relationships between density and attenuation found at several frequencies suggest that attenuation generally increases with frequency. Several studies have focused on the relationship between attenuation and frequency.

**Linear relationships** Connor et al. [62] use a linear increase of attenuation with frequency with various coefficients, one for cortical bone:

$$\alpha = 167 \times f \times 10^{-6}\,\text{Np.m}^{-1} \tag{1.30}$$

And one for trabecular bone:

$$\alpha = 300 \times f \times 10^{-6}\,\text{Np.m}^{-1} \tag{1.31}$$

Where trabecular bone voxels are identified as those containing less than 70% of bone.

Bossy et al. [70] perform acoustic simulations through trabecular bone at 0.4–1.2 MHz. They find that the attenuation linearly increases with frequency and can thus be modeled by:

$$\alpha = \alpha_0 + nBUA \times f \tag{1.32}$$

They also find that nBUA values are strongly and positively correlated with the bone volume fraction (BV/TV) and that the speed of sound is positively correlated with the bone volume fraction.

Haïat et al. [71] confirm that both Broadband Ultrasonic Attenuation (BUA) and speed of sound exhibit

**Power laws** Attenuation is a combination of absorption and scattering. According to Pinton et al. [72], 86% of attenuation is due to scattering (and thus only 14% is due to absorption) in skull bone at 1 MHz. Thus, a more efficient model of attenuation could be defined by separating the effects of absorption and scattering. That is what is done in Yousefian et al. [73], where they numerically study attenuation in porous media (mimicking cortical bone). They claim that total attenuation is not described by a linear combination of scattering and absorption anymore in the presence of multiple scattering. Thus, they propose a non-linear formula for total attenuation:

$$\alpha_{\text{tot}} = \alpha_{\text{scat}} + c f^{\beta_{\text{app}}} \tag{1.33}$$

Where $\beta_{\text{app}}$ and $c$ are to be determined and depend on pore diameter and pore density.

Webb et al. [74] compare CT and MR images as predictors of attenuation. They measure the acoustic attenuation at 0.5, 1, and 2.25 MHz in 89 samples taken from two ex-vivo human skulls and find the best parameters to fit the equation:

$$\alpha = \alpha_0 f^{\beta} e^{cp} \tag{1.34}$$

Where $f$ is the frequency, $p$ is the imaging parameter (HU value, UTE and ZTE magnitude, or $T_{2*}$ value), and $\alpha_0$, $\beta$, $c$ are the model parameters. This equation assumes the traditional power law between frequency and attenuation and that the imaging parameter provides a rough estimate of the pore structure in each sample. HU provides the best prediction of attenuation with a minimum standard error of 1.7 Np/cm. The ZTE, UTE, and $T_{2*}$ values had standard errors of 2.0, 2.0, and 2.1, respectively.

#### 1.2.2.4 Virtual CT datasets built from MRI

While acoustic properties are most often derived from CT scans, several studies have investigated the possibility of using MR images (as MR is often used to guide focused ultrasound therapy) to reduce the whole procedure and to avoid the patient's exposure to X-rays. These methods consist of building a virtual CT data from MRI.

Wintermark et al. [75] compare three MRI pulse sequences: $T_1$ weighted 3D Volumetric Interpolated Breath-hold Examination (VIBE), proton density weighted 3D Sampling Perfection with Application-optimized Contrasts using different flip-angle Evolution (SPACE), and 3D true Fast Imaging with Steady-state Precession (FISP) $T_2$-weighted imaging. The MR modality giving a total thickness closest to the CT-based total thickness was identified. Random coefficient regression was used to predict CT total skull thickness based on the optimal MRI sequence. The same method was used for the thickness of each of the three layers (inner table, diploe, outer table). Similarly, a regression model was used to predict reference standard CT average density based on the optimal MRI sequence average intensity. Virtual CT datasets derived from the MRI datasets were built using the models described before. The $T_1$ 3D VIBE sequence was the MRI sequence coming closest to the reference standard CT in terms of measuring total skull thickness, and was thus selected for the rest. In experiments made with a human skull, the mean absolute difference between the phase shifts calculated with standard CT and virtual CT was 0.8 $\pm$ 0.6 rad. Miller et al. [58] investigate the feasibility of using ultrashort echo-time magnetic resonance imaging (UTE MRI) instead of CT to calculate and apply aberration corrections on a clinical TcMRgFUS system. A 3D map of the skull is created from the MR images by applying a segmentation algorithm, and is used to construct virtual CT

data, by assigning 1000 Hounsfield units to bone pixels and -1000 Hounsfield units to all other pixels. The virtual CT data was entered in the planning software of a MRgFUS system to calculate aberration correction phases. There was no significant difference between the sonication results achieved using CT-based and MR-based aberration correction.

#### 1.2.2.5 Shear waves parameters

As the acoustic parameters of shear waves in bone have not been studied extensively, most studies that account for the presence of shear waves assume that the shear wave speed is half that of the longitudinal waves, as is a typical assumption for solids. However, a few studies have looked more into shear wave parameters.

White et al. [59] measure an average speed of sound for a 1.0 MHz longitudinal wave of $2820 \pm 40$ m/s and $1500 \pm 140$ m/s for shear waves. They find that the shear attenuation coefficient in skull bone is on average higher by 115 Np/m than the longitudinal one for the frequency range studied. So, although the speed of sound of shear waves in the skull is closer to that of the surrounding media (brain and tissues), which allows for more efficient transmission through the boundaries, the high shear attenuation coefficient tends to restrict this beneficial effect.

Pichardo et al. [64] use a genetic algorithm method (similar to their approach for compressional wave parameters) to establish the relationship between the apparent density calculated from CT scans and shear speed of sound and attenuation at 270 kHz and 836 kHz. They assume a linear relationship for the speed of sound and a constant attenuation.

#### 1.2.2.6 Comparison of the methods and discussion

**Comparison of a few methods for acoustic parameter modeling** McDannold et al. [41] compare Pichardo's relationships [54] for the speed of sound and attenuation to their polynomial formulas at 660 kHz. While there was no significant difference between their relationships and Pichardo's in the resulting dimensions or obliquity of the simulated focal region, the temperatures simulated using Pichardo's relationships were less accurate (less close to the experiments) than those simulated using their relationships.

Bancel et al. [19] use Marsac's density relationship [2] and compare the speed of sound relationships given by Pichardo [54], Marsac [2], and McDannold [41]. Marsac's relationships seem to perform slightly better for aberration correction simulations, with a restored pressure of 85% (compared to 81% with Pichardo's relationship and 82.5% with McDannold's relationship) and a peak-to-side lobe ratio of 45.5% (compared to 51.5% with Pichardo or McDannold's relationship).

**Impact of the error in skull modeling** In Robertson et al.'s paper [65], the impact of changes in bone layer geometry and the speed of sound, density, and acoustic absorption values is quantified through a numerical sensitivity analysis. The errors in the field resulting from noisy variations (around a mean value) in medium properties are smaller than those from linear changes (variations of the mean value). Noisy variations for absorption have almost no effect: homogeneous maps of absorption are good. Linear variations in Hounsfield unit (HU) values resulted in errors lower than the errors for individual changes in assigned medium properties, thus suggesting that the primary concern should be the robustness of any method for the conversion of CT images to acoustic properties. Speed of sound is shown to be the most influential acoustic property and must be defined with less than 4% error. Changes in the skull thickness of as little as 0.1 mm can cause an error in peak pressure of greater than 5%, while smoothing with a 1 $mm^3$ kernel (skull maps obtained from low-resolution images) causes an increase of over 50% in peak pressure.

**Considering X-ray energy** While many studies have investigated the relationship between acoustic properties and Hounsfield Units, they have ignored the impact of X-ray energy (HU is a function of the linear attenuation coefficient which itself depends on the X-ray energy), reconstruction method, and reconstruction kernel on the measured HU. Webb et al. [76] imaged 91 human skull fragments by 80 CT scans with a variety of energies and reconstruction methods. The average HU from each fragment is found for each scan and correlated with the speed of sound measured. The results show that both the energy and the reconstruction method have a significant influence on the relationship between velocity and HU. The main issue is that it is difficult to have an estimate of the real X-ray energy except in dual-energy CT. Aubry and Marsac relationships are based on porosity, which depends on the linear attenuation and thus accounts for X-ray energy. So these formulas work well when the energy is known. Pichardo and Connor relationships

do not account for X-ray energy. Considering CT parameters can be obtained with dual-energy CT, by obtaining calibration measurements or by working with the vendor to obtain accurate estimates of the X-ray spectrum of a given scan. The results provide estimates of the relationship between HU and velocity for a variety of different CT parameters. They also show that the relationship between HU and velocity is patient-specific. The measurements show that CT is able to capture only about one-half of the variation in acoustic velocity within the skull. Some of the remaining variation is likely due to errors in the measured velocity, but it is also likely an indication that some of the variation in velocity is not well modelled by HUs. This could be because the variation in velocity results from changes in the chemical composition of the skull, a variation not necessarily captured by the measured HU.

### 1.2.3 Levels of heterogeneity

The skull is made of two types of bone: cortical bone and trabecular bone. The inner and outer tables are made of cortical bone, which is a dense and nearly homogeneous medium, whereas the middle layer is made of trabecular bone, which is a complex porous structure, highly scattering. Thus, the skull is very heterogeneous. However the imaging modalities, be it CT or MR, cannot capture heterogeneities below their resolution. Thus, when modelling the skull, one can use levels of heterogeneity (figure 1.4) going from assigning different acoustic properties to each voxel, to assigning the same acoustic properties to the whole skull.

#### 1.2.3.1 Fully heterogeneous

In this model, each voxel has a given density, sound speed and attenuation. It is used in [27],[5] [42] [43] [44] [46] [54] [62] [63] [23] [65] [66] [30] [15] [17] [2] [68] [77] [31] [65] [78] [33] [35] [14] [38] [18] [39] [41].

#### 1.2.3.2 Heterogeneous but binary

The skull is assumed to be a complex porous structure made of bone and with pores filled with marrow (whose acoustic properties are close to those of water). Simple image thresholding allows labelling voxels as either being bone or marrow and constant acoustic properties are assigned to bone or marrow. It is used in [72],[37],[34],[70],[71],[3]. However, this method requires high resolution scans, as the structure of the diploe is not visible at the millimeter scale.

#### 1.2.3.3 N layers

In this model [54], the skull is divided into N homogeneous layers. Density along the acoustic axis (only normal incidence is considered) was computed by averaging the density from the voxel on the acoustic axis and the one of its four neighbours in the plane perpendicular to the acoustic axis. In a given layer, the acoustic properties are averaged from the CT scans. Each layer thickness is set to $\frac{1}{4}$ of the voxel spacing to allow a smooth variation.

#### 1.2.3.4 Three layers

The skull is often described as a three-layer medium where the inner and outer layers are made of cortical bone and the middle layer is made of trabecular bone. A CT scan of high resolution ($10\mu$m), where the three layers can be seen in the transverse and coronal planes, is displayed in figure 1.3. In each layer, the acoustic properties are averaged from the CT scans [48],[75].

#### 1.2.3.5 One layer

The simplest assumption that can be made is considering the skull as a homogeneous and isotropic medium. The acoustic properties are either averaged from CT scans, or taken from measurements from the literature. This model is used in [5], [18],[49] [50] [51] [52],[58],[65],[17]. In Jiang et al. [17], the velocity on the skull surface is taken to be that in cortical bone (which influences refraction computations) and the velocity inside the skull is taken as being the averaged value on the ray paths (which influences the time of flight computations). The density is taken as being the maximum density as it influences the refraction computations. The main issue with those methods is that if the transducer has a large aperture, the acoustic properties may vary quite a lot along the surface intersected by the ultrasound beam. In Jones et al. [56]

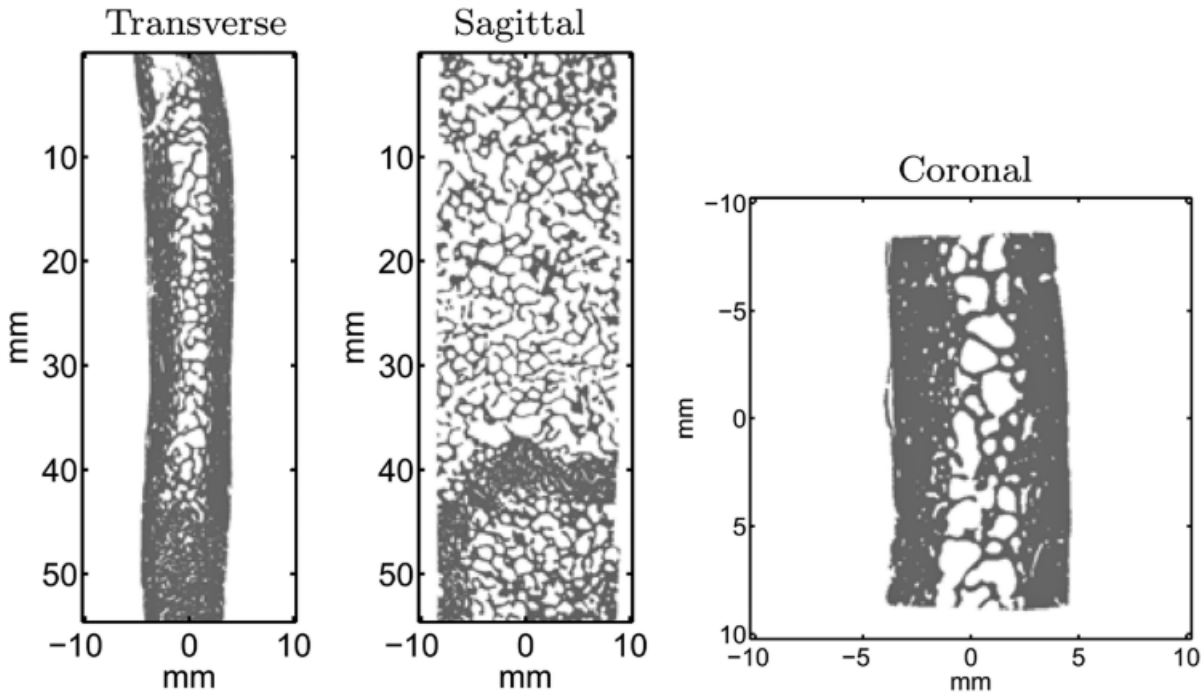


*Figure 1.3: Three planes of a 10µm CT scan, illustrating the distribution of cortical and trabecular bone in a human skull sample from [72]*

and Pajek and Hynynen [55], a locally averaging method was proposed. It consists in spatially averaging the acoustic properties independently for each ray path going through the skull.

#### 1.2.3.6 Comparison of the levels of heterogeneity

Jones and Hynynen [5] experimentally compare CT-based aberration corrections with two skull models : one homogeneous layer and a fully heterogeneous model. For both models, they compare the corrections computed using a full-wave method and using a ray-tracing method. By averaging the metrics on the two methods, the homogeneous model increases the peak pressure shift error (compared to the hydrophone-based shift) by 4%, the -3dB volume error by 27.5% and the peak-to-side-lobe ratio error by 22%, compared to the heterogeneous model. Thus, the heterogeneous model performs better, as the homogeneous one underestimate attenuation and the focal spot spreading. Kyriakou et al. [18] find similar results when comparing heterogeneous and homogeneous skull modelling with a full-wave simulation. Indeed, the prediction of the focusing (shift and volume) seems unaffected by skull inhomogeneity while the peak pressure is reduced by 25% with the heterogeneous model. Jiang et al. [17] compare the performances of two homogenous models : one with the average properties of the skull, and one the properties of the cortical bone on the surface (as refraction computations are influenced only by the properties on the surface on the skull) and with the average properties of the skull on the inside (for the time-of-flight computations). Shifts of 9.5 mm in the axial direction and 1.5 mm in the focal plane compared with the virtual source were observed with the first one, compared to 0.5 mm in the axial direction and 0.5 mm in the focal plane with the optimized model. Robertson et al. [3] study the influence of homogenization of CT maps. Progressive homogenization of acoustic property maps leads to an overestimation in the amplitude of transmitted US, an underestimation of time-of-flight, and a loss of fine spatial detail in the intracranial field. Inflating the simulated attenuation coefficient of the skull layer reduces the error in transmitted pressure amplitude to around 40%, however this is unable to correct fully for errors in time of flight and the pressure distribution of the transmitted field. One must also take into account that the frequency will influence the level on heterogeneity needed. Indeed, at lower frequencies, heterogeneities much smaller than the wavelength do not need to be taken into account and parameters at those scales can be homogenised.

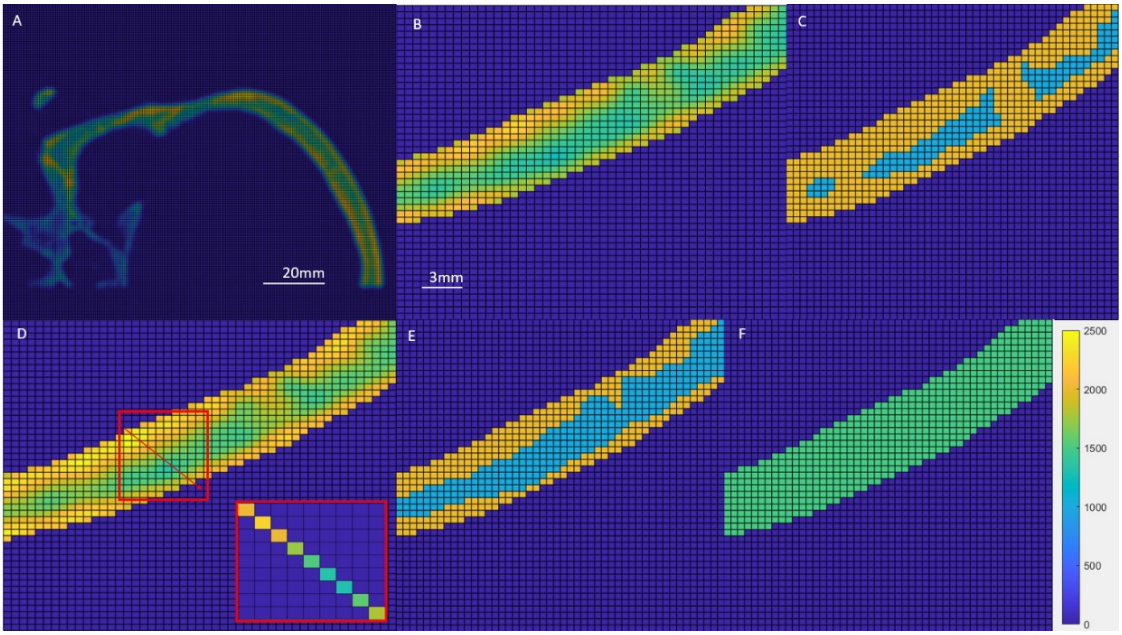


*Figure 1.4: The different level of homogenization. A: original skull, B: heterogeneous model, C: binary model, D: N-layers model, E: three-layers model, F: one layer model*

## 1.3 Simulation methods

### 1.3.1 Semi-analytical methods

#### 1.3.1.1 Ray tracing

A fast common method to simulate wave propagation is ray tracing [50] [51] [52],[55],[56] [59] [17] [20]. It considers reflection, refraction and mode conversion at each interface. The ray paths are obtained using Snell-Descartes' laws of a three-layer model, composed of water, skull and brain. This method is illustrated by figure 1.5.

In general, possible reflections from inside the skull are not considered due to the high attenuation of the skull [52]. Moreover, as the skull thickness varies across its surface, it acts as a random phase aberration to the transmitted waves, thus making constructive interferences less probable. Clement et al. [50] compute the amplitudes of the reflected wave, the transmitted longitudinal wave, and the transmitted shear wave, with respect to the incident wave amplitude using the fact that the normal component of the particle displacement, the normal stress and the shear stress must be continuous at the boundary.

In White et al. [59], the skull interfaces are supposed to be parallel, and the pressure (longitudinal and shear) transmission coefficients are computed with:

$$T_L = \frac{\rho_f}{\rho_S} \frac{2Z_L \cos(2\theta_S)}{Z_L \cos^2(2\theta_S) + Z_S \sin^2(2\theta_S) + Z_f} \tag{1.35}$$

$$T_S = -\frac{\rho_f}{\rho_S} \frac{2Z_S \cos(2\theta_S)}{Z_L \cos^2(2\theta_S) + Z_S \sin^2(2\theta_S) + Z_f} \tag{1.36}$$

Where $\rho_f$ and $\rho_S$ are the densities of the fluid and the solid, $Z_L$ and $Z_S$ are the longitudinal and shear impedances of the solid, and $Z_f$ is the fluid impedance. The ultrasound beam is approximated as a one-dimensional ray. The values obtained after the first interface are then used as the input for the second interface.

Yin and Hynynen [51] divide each skull interface into small rectangular planar patches. The plane-wave theory is then applied to each patch, and the contribution of each patch is summed using the Rayleigh-Sommerfeld integral. The computations are made for each interface successively: once the computations are obtained for an interface, this interface is considered as the new source for the next interface. As the patch surfaces are small (about a quarter wavelength), the acoustic pressure in the tissue can be computed as the product of the particle normal velocity and the specific acoustic impedance of the tissue.

Pichardo et al. [52] also divide the interfaces into small elements, but the amplitude computations are different. The contribution coefficients due to the longitudinal propagation from the transducer surface to

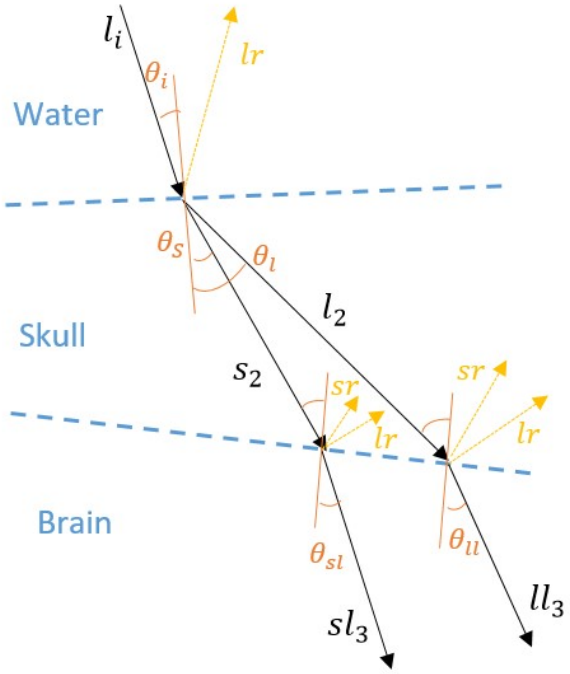


*Figure 1.5: three-layer model of wave of transmission through the skull*

the outer face of the skull $U_{LL,1\to2}$, from the outer face to the inner face $U_{LL,2\to3}$, and from the inner face to a point $q$ inside the brain $U_{LL,3}$ are computed with:

$$U_{LL,m\to n} = \frac{jk^*_{l_m}\rho_m c_{l_m}}{2\pi}\frac{e^{-jk^*_{l_m}R_{i_m\to i_n}}}{R_{i_m\to i_n}}\left(1-\frac{j}{k^*_{l_m}R_{i_m\to i_n}}\right)T_{l_{i_m\to i_n}}\cos(\theta_{i_m\to i_n})ds_{i_m} \tag{1.37}$$

$$U_{LL,3} = \frac{jk^*_{l_3}\rho_3 c_{l_3}}{2\pi}\frac{e^{-jk^*_{l_3}R_{i_3\to q}}}{R_{i_3\to q}}ds_{i_3} \tag{1.38}$$

Where $c_{l_m}$ and $k^*_{l_m} = k_{l_m} + j\alpha_{l_m}$ are the longitudinal speed of sound and wave number ($\alpha_{l_m}$ being the attenuation coefficient), $\rho_m$ is the density, $R_{i_m\to i_n}$ is the distance between the surface elements $i_m$ and $i_n$, $\theta_{i_m\to i_n}$ is the incident angle, $ds_{i_m}$ is the surface area of element $i_m$, and $T_{l_{i_m\to i_n}}$ is the transmission coefficient. Similarly, the contribution coefficients due to shear-mode conversion are computed. The pressure amplitude of the transmitted wave is then obtained using the Rayleigh-Sommerfeld integral for a multilayer case:

$$p(q) = p_{LL}(q) + p_{SL}(q) \tag{1.39}$$

with $p_{LL}(q) = \sum_{i_1=1}^{N_1} u_{i_1}U_{LL,1\to2}U_{LL,2\to3}U_{LL,3}$ and $p_{SL}(q) = \sum_{i_1=1}^{N_1} u_{i_1}U_{LS,1\to2}U_{LS,2\to3}U_{LL,3}$, where $N_1$, $N_2$, and $N_3$ correspond to the number of elements of each interface (transducer, outer and inner surfaces of the skull), and $u_{i_1}$ is the amplitude of the particle displacement of element $i_1$.

Pajek and Hynynen [55] use the same method, but shear waves are not taken into account due to their high attenuation at the high frequencies used (higher than 1 MHz). Jones et al. [56] also use this method, but with spatially averaged acoustic properties for each ray path going through the skull.

In Jiang et al. [17], the frequency deviation caused by the acoustic attenuation is calculated in the frequency domain, and the ultrasound amplitude after refraction is computed using the transmission coefficient at each interface. After the first interface, the amplitude of the velocity potential is given by:

$$Q_2 = Q_s T_r \frac{l'_2}{l'_2 + l_{2r}} \tag{1.40}$$

where $Q_s$ is the velocity potential of the source, $T_r$ is the plane-wave transmission coefficient, $l_1$ is the length of the incident ray, $l_{2r}$ is the length of the refracted ray, and $l'_2 = \frac{l_1 \sin\alpha\cos^2\beta}{\sin\beta\cos^2\alpha}$ represents the divergence of

the beam. Then, after propagation through the medium layer, the velocity potential at the second interface is considered as a new source to compute the velocity potential after crossing the second interface.

CIVA Healthcare [20], which is simulation platform developed in our team at the CEA, is also based on ray-tracing. The interfaces between the media can be modeled either with analytical shape or with meshes. Ultrasonic fields can be computed through homogeneous or heterogeneous tissues, made of isotropic and anisotropic media. This models takes into account the propagation of bulk waves in each medium and the various reflections and refractions, with and without mode conversion at each interface. It is based on the pencil method [7] which consists in dividing the wavefront into pencils. A pencil being an entity composed of an axial ray, following the geometrical path, and paraxial rays, belonging to the envelope of the pencil, diverging slightly. More details about this method can be found in section 3.3.1.

#### 1.3.1.2 Transfer function methods

**Transfer matrix method for transmission coefficient computation** In Pichardo et al. [54], as the skull is divided into $N$ layers and is surrounded by water, the transmission coefficient $T$, at normal incidence, is computed using:

$$T = \frac{2Z_w}{(m_{2,2} + m_{3,3} + Z_w m_{2,3})Z_w + m_{3,2}} \tag{1.41}$$

where $Z_w = \rho_w c_w$ is the acoustic impedance of water, $m_{j,k} = A_{j,k} - \frac{A_{j,1}A_{4,k}}{A_{4,1}}$ ($A_{j,k}$ is the coefficient of the transfer matrix $A$ giving the stress and particle velocity at the last interface from the stress and particle velocity at the first interface). $A$ is obtained by the product of the matrices of the sound transmission coefficients of the $N$ skull layers.

**Projection algorithm in the wavevector-frequency domain** Clement and Hynynen [49] propose a projection algorithm in the wavevector-frequency domain that works for normal incidence or any angle of incidence. By taking the Fourier transform of the linearized Stoke's equation, they obtain a simple equation whose solution is given by:

$$\tilde{p}(k,z) = \tilde{p}(k,z_0)e^{ik(z-z_0)} \tag{1.42}$$

Thus, the field recorded in a plane $z = z_0$ is related to the field at any other plane by a transfer function. The pressure field is then obtained by taking the inverse Fourier transform. For non-normal incidence, a rotation of the planar field at $z = z_0$ is performed in the wavevector-frequency domain.

**Hybrid Angular Spectrum (HAS) method** The traditional angular spectrum method assumes that the medium is homogeneous. The pressure in the initial plane is encoded into a spectrum of traveling plane waves in the spatial-frequency domain using Fast Fourier Transform. Then, the propagation of the waves to the next plane is calculated in the spatial-frequency domain by multiplying the initial spectrum by a propagation transfer function. Finally, IFFT is performed to obtain the pressure in the final plane.

Vyas and Christensen [79] extend this method to calculate linear ultrasound wave propagation in inhomogeneous tissue geometries. In this new method, wave propagation through each plane is calculated in two steps: one in the space domain and one in the spatial-frequency domain.

The transmission from one plane to another is computed using:

$$p_n(x,y) = p_{n-1}(x,y)e^{jb_n(x,y)r' - a_n(x,y)r} \tag{1.43}$$

where $b_n(x,y) = \frac{2\pi f}{c_n(x,y)}$ is the propagation constant at a given voxel $(x,y)$ with a speed of sound $c_n(x,y)$, and $a_n(x,y)$ is the pressure attenuation coefficient of a given voxel. $r'$ is the effective path length between two wavefronts, and $r$ is the entire propagation path.

By dividing the phase change into an average phase shift $b'_n r'$ inside a plane and the difference $\Delta b_n(x,y)r'$ from this average phase shift for each voxel of the plane, the transmission equation can be re-written as:

$$p_n(x,y) = p_{n-1}(x,y)e^{jb'_n r' + j\Delta b_n(x,y)r' - a_n(x,y)r} \tag{1.44}$$

Propagation from one plane to another is then achieved in the space domain using:

$$\tilde{p}_n(x,y) = p_{n-1}(x,y)e^{j\Delta b_n(x,y)r' - a_n(x,y)r} \tag{1.45}$$

And propagation across a given plane is performed in the spatial-frequency domain using:

$$p_n(x,y) = \mathscr{F}^{-1}\left[\mathscr{F}\left[p'_n(x,y)\right] e^{jb'_n\sqrt{1-\alpha^2-\beta^2}\Delta z}\right] \tag{1.46}$$

with $\alpha = \lambda f_x$ and $\beta = \lambda f_y$.

This method is used in studies [43], [23], and [47].

### 1.3.2 Numerical methods

#### 1.3.2.1 Finite differences

Many studies use finite difference methods to simulate wave propagation. This allows modeling the skull as a heterogeneous medium, but it is computationally intensive. Unlike semi-analytical methods, finite difference methods require a fine spatial step in order to converge, as the pressure field at a given position depends on the pressure field at previous positions.

Several wave equations can be considered when using finite differences, depending on which effects one wants to take into account or neglect, such as linearity, shear mode conversion, absorption, etc. The effects taken into account by several studies are listed in table 1.1. All those equations are derivatives of the Westervelt equation, which is given by:

$$\frac{\partial^2 p}{\partial z^2} - \frac{1}{c^2}\frac{\partial^2 p}{\partial t^2} + \frac{\mu}{c^4}\frac{\partial^3 p}{\partial t^3} + \frac{2\beta}{\rho c^4}\left[p\frac{\partial^2 p}{\partial t^2} + \left(\frac{\partial p}{\partial t}\right)^2\right] - \frac{\partial p}{\partial z}\cdot p\frac{\partial}{\partial z}(\ln p) = 0 \tag{1.47}$$

where $p$ is the wave pressure, $c$ is the local speed of sound, $\rho$ is the local density, $\mu = 2\alpha c^3 (2\pi f)^{-2}$ is the local diffusivity parameter ($\alpha$ is the local attenuation coefficient), and $\beta$ is the non-linearity parameter.

*Table 1.1: Effects taken into account in the equations used in finite differences studies*

| Reference | Non-linearity | Shear waves | Absorption |
|---|---|---|---|
| [18],[44],[38],[34],[54] | × | | × |
| [5],[30],[80],[33],[14],[18],[46],[62],[63],[2],[68] | | | × |
| [39] | | | |
| [70] | | × | |
| [72] | | × | × |
| [37] | × | × | × |

#### 1.3.2.2 K-space

In 2012, Jing et al. [15] proposed using a k-space method to simulate wave propagation inside the skull. Like finite differences, it allows a heterogeneous description of the skull, but k-space is faster as it needs less spatial resolution to achieve convergence with reasonable accuracy.

The k-space methods are part of the bigger family of Pseudo-Spectral Finite Difference Time Domain methods (PSTD). The PSTD methods transform the fields to the spectral domain at each time step to compute the spatial derivatives more easily. These methods are called global methods because the entire simulation domain is used in approximating the derivative of a single point. They are more accurate than standard finite difference methods and theoretically allow discretizing the domain as low as two points per wavelength. However, the standard PSTD methods only improve efficiency in the spatial domain, as finite difference schemes are still needed in the time domain, requiring fine time steps to avoid dispersion. The k-space method aims to allow larger time steps without significantly reducing accuracy. It consists of multiplying the time step by the k-space operator $\kappa = \text{sinc}\left(\frac{c_{\text{ref}} k \Delta t}{2}\right)$, which is derived from the exact solution of the homogeneous and lossless wave equation.

The k-space method has been used in other studies [30] [35] [41] [42] [65] [19] [31] [65] [78] [3], thanks to the development of the Matlab toolbox *k-Wave* [16], although some studies have developed their own k-space algorithm [17].

### 1.3.3 Hybrid methods

A good balance is to combine numerical methods and analytical ones. For instance, one can use an analytical method to compute wave propagation before and after the skull (as those media can reasonably be assumed homogeneous) and then use a numerical method only within the skull.

When simulations are used for phase correction computations, the waves are propagating from a virtual source inside the brain towards the transducer outside the skull. In a few papers [2] [19] [80] [27] [81], the finite difference or k-space algorithms are only performed from an arbitrary plane or spherical surface as close as possible to the inner surface of the skull, and propagation in brain tissues is modeled by a ray-tracing code to save time. In [66] [19] [81], the numerical simulations are only performed to an arbitrary plane or a receiving surface just in front of the skull, and the propagation from there to the transducer is realized by a ray tracing code.

In direct simulations (from the transducer to the brain), hybrid methods are also used. In Wu et al. [78], they developed a method that combines the k-space corrected PSTD method with an acoustic holography approach based on the Rayleigh integral. The k-Wave stage is used to calculate the sound field in the skull, which is divided into multiple sound paths (one per array element). The propagation in each sound path is simulated with k-Wave from the element to a virtual sensor located near the skull-brain interface. The simulations in all sound paths are run in parallel. The relative amplitude and phase of each discrete point in the sensors are extracted by taking an FFT of an integer number of cycles of the signal after it reaches steady state. Propagation from the virtual sensors is then performed with the Rayleigh integral based method. In Pulkkinen et al. [45], the propagation from the phased-array element through the water to a parallel plane near the skull is simulated with the Rayleigh integral. Then the propagation through the skull is performed with a finite element code and propagation in the brain is simulated using the angular spectrum method.

### 1.3.4 Artificial Intelligence based methods

AI (Artificial Intelligence) based methods have emerged during the course of this PhD. Stanziola et al. [82] developed the first Physics-Informed Neural Network to solve the Helmholtz equation and used it to simulate transcranial ultrasonic fields. They used a physics-based loss function, which means the training data does not need to contain ground truth wavefields. The neural network, which has a modified U-Net architecture, is trained on a dataset of sound speed distributions containing idealized skulls. The network appeared to generalize very well to 2D sound speed distributions derived from a skull CT scan, with a $l_\infty$ error compared to k-Wave of less $1\%$.

### 1.3.5 Comparison of the methods

All these methods simulate wave propagation through the skull with a variable degree of realism, depending on the acoustic effects taken into account or neglected. Most of the time analytical methods are faster but less accurate than numerical ones. A few papers have compared some of these methods.

In Jing et al. [15], the k-space and the Finite Differences Time Domain (FDTD) methods are compared. It was found that for very fine spatial resolution (more than 10 grid points per wavelength), these two methods match very well. However, at a low spatial resolution, the k-space method was observed to produce considerably less numerical error. The computation time at a fine spatial resolution (7.68 grid points per wavelength) can be reduced by a factor of around 80 using 2.56 grid points per wavelength, without altering too much the resulting field.

Jones et al. [5] compare full-wave finite difference phase correction with analytical phase correction. The results show that the finite difference method outperforms the analytical one for every metrics : shift decrease of 25%, -3dB volume decrease of 20%, peak-to-side-lobe ratio increase of 26%, signal-to-noise ratio increase of 37% with the full-wave method compared to the analytical one. However, the FDTD method took 7.8h while the analytical phase correction took only 27s.

Kyriakou et al. [18] compare distance based phase correction, ray-tracing based phase correction and finite difference based phase correction. The ray-tracing based phase correction only performs a bit better than the distance based one, and gives much worse results than the finite difference based phase correction (shift x6, peak pressure /2, focal volume x5).

Robertson et al. [65] compare FDTD and k-space methods for phase aberration correction. Numerical dispersion has a serious effect on the accuracy of FDTD scheme, resulting in high temporal sampling requirements to reduce positional error, while for the k-space scheme, only 3 Pixel Per Wavelength (PPW)

will serve to limit dispersion sufficiently for transcranial transmission for any stable Courant-Friedrichs-Lewy (CFL) value. To reduce error in the intensity below 10% following transcranial transmission, k-space scheme requires 4.3 PPW, while FDTD requires 5.9 PPW. Jiang et al. [17] compare FDTD, k-space and ray-tracing methods, for phase and amplitude correction. The k-space method (4 PPW) has a 0.7% phase error compared with the FDTD method (16 PPW). The ray-tracing method has an amplitude error of 5.35% and a phase error of 1.2% compared to the FDTD method. The k-space method took 23h35 while the ray-tracing method took 37min.

Bancel et al. [19] compare k-space and ray-tracing methods. The restored pressure compared to the hydrophone-based correction is 85% for the k-space method and 83.5% for the ray-tracing method. Similarly, the other metrics show results a bit better with the k-space method but the differences are not as big as other studies have shown before.

Aubry et al. [10] recently proposed a set of 9 benchmark configurations with increasing geometric complexity for transcranial ultrasound simulation tools to be compared. They compared 11 solvers (mostly numerical methods and HAS methods) and obtained a good agreement between them all, with median values for the difference in focal pressure and focal position of less than 10% and 1mm for all configurations. This numerical study does not aim to determine which solver is the best as no experimental comparisons were carried out. However, it shows that all the methods compared are able to simulate very similar transcranial ultrasonic fields.

In terms of computation speed, it is quite hard to compare the methods from various papers as the conditions (CPUs, GPUs, parallel computing, ...) differ from one paper to another and relevant information (such as domain size, time step) are not always available. Table 1.2 is an attempt to compare the computation times of several studies.

*Table 1.2: Comparison of the computation time of several simulation methods*

| Ref | Simulation Method | Skull Modeling | Computer | Domain size ($mm^3$) | Number of points | Time | Time for 1e9 points |
|---|---|---|---|---|---|---|---|
| [49] | Layered wavenumber | Homogeneous | 1GHz | | | 5h | |
| [14] | FD | Heterogeneous | 500MHz | 70x10x30 | 2.1e7 | 20h | 950h |
| [50] | RT | Homogeneous | 1GHz | | 1.6e4 | 30s | 521h |
| [52] | RT | Homogeneous | | 160x160x160 | 3.2e7 | 106min | 55h |
| [39] | FD | Heterogeneous | | 180x180x150 | 1.5e9 | 90min | 60min |
| [77] | FD | Heterogeneous | | | 2.2e9 | 120min | 54min |
| [72] | FD | Binary | 2.8GHz | | 1.0e8 | 12h | 120h |
| [83] | FD | Heterogeneous | | | 1.3e9 | 3h | 2h18 |
| [55] | RT | Homogeneous | | | | 24h | |
| [15] | k-space | Heterogeneous | 2.6GHz | 47x100x31 | 7.5e5 | 17s | 6h20 |
| [5] | FD | Heterogeneous Homogeneous | | 100x130x40 | 2.1e7 | 7h48 | 371h |
| [47] | HAS | Heterogeneous | 2.7GHz | | | 20min | |
| [35] | k-space | Heterogeneous | 2.5GHz | | 1.9e6 | 15min | 131h30 |
| [23] | HAS | Heterogeneous | | | 4.6e7 | 45min | 16h |
| [31] | k-space | Heterogeneous | | | 1.2e8 | 30h | 250h |
| [65] | k-space | Heterogeneous | 3.3GHz | | 2.7e8 | 19h53 | 74h |
| [3] | k-space | Binary | 3.3GHz | | 4.2e6 | 9h | 2143h |
| [68] | FD | Heterogeneous | 3.6GHz | 180x200x175 | 6.3e7 | 150s | 40min |
| [43] | HAS | Heterogeneous | 1.4GHz | | 1.4e9 | 180s | 128s |
| [17] | k-space | Heterogeneous | | | 1.3e8 | 23h | 177h |
| [17] | RT | Homogeneous | | | 1.3e8 | 37min | 4h40 |

FD: Finite Differences.
RT: Ray-Tracing.

## 1.4 Experimental validation of the simulations

Experiments are the only way to evaluate the accuracy of simulations. They are most of the time considered as gold standards or references even though they can also be enticed with errors as discussed below. In this section, the classical set-ups for experimental validation of transcranial acoustic simulations are described and the experiments versus simulation results are compared.

### 1.4.1 Experimental set-ups

The typical set-up for transcranial acoustic measurements is composed of an emitting transducer and an hydrophone mounted on a three axis positioning system, as illustrated by figure 1.6. A first scan, without skull is often performed as a reference result. Then, a skull or a phantom is placed between the transducer and the hydrophone. Prior to the experiments, the skulls are put in water and degassed (typically for 24h) in order to remove all the air trapped inside and to ensure the skull pores are filled with water to mimic in vivo conditions. When the skull modelling is deduced from CT scan, CT-scans of the skulls should be performed under water as well. Likewise, the experiments are made in a tank filled with degassed water.

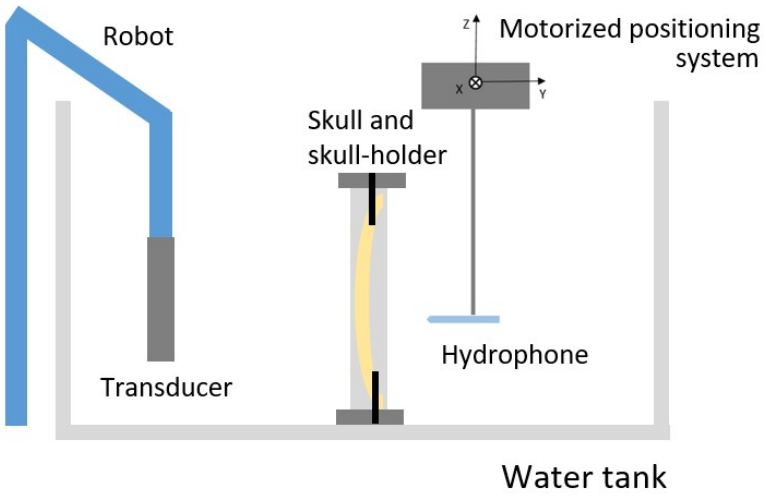


*Figure 1.6: Typical set-up for transcranial acoustic measurements*

Most of the time, accurate positioning of the skull is performed using a stereotactic frame, or a homemade frame, which contains fiducial markers. The CT scans of the skulls are acquired with the positioning frame and the position of the fiducial markers is determined from the CT images. Likewise, the fiducial marker positions are recorded with the three axis positioning system [14] [63], or with an optical-based position tracking system [68]. From this, a rigid transformation matrix representing the rotation and translation between the experimental and simulation frames can be computed [49]. Otherwise, the transducer can be attached to the skull positioning frame [30] [49] [54] [66] [78] [80] [81] in order to obtain accurate relative positioning more easily. On the other hand, this method does not allow for different positions of the transducer. When experiments are performed under MR guidance, MR tracking coils can be used to find the transducer location within the MR frame [42]. MR images can also be used to find the relative position of the transducer with respect to the skull frame [23]. A few studies have estimated the positioning error between their experiments and their simulations. Those errors are displayed in table 1.3.

O'Reilly et al. [84] use high frequency ultrasound measurements to localize the skull surface and register CT data to the ultrasound treatment space. The results show on an average sub-millimetre ($0.9 \pm 0.2$ mm) displacement and sub-degree ($0.8° \pm 0.4°$) rotation registration errors.

### 1.4.2 Comparison of simulations and experiments

Though many studies have checked their simulation results through experiments, only a few of them have directly compared the pressure field obtained with experiments with the simulated one. Indeed, most studies have compared simulations and experiments through their application. For instance, many studies experimentally compared the field produced by a phased-array transducer with a simulated phase correction with

*Table 1.3: Positioning method and error for measurements in several studies*

| Reference | Positioning method | Positioning error (mm) |
|---|---|---|
| [49] | Skull attached to the transducer | 0.5 |
| [14] | Position of the skull markers recorded by the three-axis system | 1 |
| [66] | Skull attached to the transducer | "a few" |
| [80] | Skull attached to the transducer | 0.7 |
| [23] | Relative position between transducer and skull measured with MRI | 0.25 |
| [68] | Position of the skull markers recorded by an optical-based position tracking | 0.41 |
| [78] | Skull attached to the transducer | 0.02 |

the field produced by a multi-element transducer with a hydrophone based correction (which is considered as the optimal phase correction) [30], [37], [14], [49], [23],[2], [19], [78], [80], [81]. Another way to assess the accuracy of transcranial acoustic simulations is to compare the results of heat simulations with MR thermometry data [43] or with lesion locations [42]. In Bouchoux et al. [63], Yoon et al. [68] and Bancel et al. [19], they directly compare the acoustic field obtained with experiments with the simulated one. The results are summed up in table 1.4.

*Table 1.4: Comparison between experimental and simulated acoustic fields in different studies*

| Ref | Focus shift | Pressure metric | Pressure value |
|---|---|---|---|
| [63] | $< 2.5$mm | $\frac{\sum_{(x,y,z)}(\max_t \lvert p_{\text{simu}}\rvert - \max_t \lvert p_{\text{meas}}\rvert)}{\max_t \lvert p_{\text{meas}}\rvert}$ | -9.17% $\pm$ 4.55%, 4 skulls (120kHz) |
| [68] | 1.43mm $\pm$ 0.8mm | $\frac{(R^{XY}-\overline{R^{XY}})}{R^{XY}} + \frac{(R^{XZ}-\overline{R^{XZ}})}{R^{XZ}} + \frac{(R^{ZY}-\overline{R^{ZY}})}{R^{ZY}}$ | 5.8% $\pm$ 6.4%, 3 skulls (250kHz) |
| [19] | 0.3mm $\pm$ 0.1mm | $\frac{1}{Nel}\sum_{i=1}^{Nel}(p_i^{\text{simu}} - p_i^{\text{meas}})$ | -0.9% $\pm$ 5.4%, 5 skulls (800kHz) |

The phase correction results obtained in several studies are displayed in the table 1.5.

*Table 1.5: Comparison of simulation-based and invasive aberration correction in several studies*

| Ref | Shift | | | Percentage of peak pressure compared to the uncorrected case | |
|---|---|---|---|---|---|
| | Without correction | Simulation correction | Hydrophone correction | Simulation correction | Hydrophone correction |
| [49] | 1.1mm | 0.48mm | | 135% | 294% |
| [37] | | 0mm | | | |
| [23] | 1.77mm | 0.71mm | 0.25mm | 151% | 217% |
| [2] | 1.05mm | 0.54mm | | 190% | 220% |
| [78] | 0.5mm | 0mm | | 137% | 147% |
| [19] | 0.9mm | 0.2mm | 0mm | 130% | 153% |
| [81] | | 0.63mm | | 149% | 165% |

Almquist et al. [23] perform experiments with phantoms and human skulls in order to separate the errors coming from the simulation algorithm from the errors coming from the skull modelling (as the acoustic properties of the phantoms are known). The results are presented in table 1.6.

Simulation based correction is able to reach 94% of the optimal correction (hydrophone-based correction) when the acoustic properties are known (phantom experiments) while only 70% when they are unknown and deduced from CT-scans with empirical relationships (skull experiments). In a few studies [41],[43] [44] [45], MR thermometry data was compared with the results of thermal simulations. Qualitatively speaking, the predicted and measured temperature fields agree well in all those studies. In Pulkkinen et al. [45], for the seven sonications performed on a single skull, the error between the simulated and measured temperatures at the two locations of interest (focus and tissue near the skull base) is on average 1°C and never exceeds 3°C. The other studies collected data from several patients (at least 9) who had undergone several sonications, and were thus able to make statistical analysis of the results, as shown in table 1.7.

*Table 1.6: Comparison of simulated-based and invasive aberration correction for a phantom and for a human skull*

| Metric | Shift | | | Percentage of peak pressure compared to the uncorrected case | | |
|---|---|---|---|---|---|---|
| | Without correction | Simu-based correction | Hydro-based correction | Without correction | Simu-based correction | Hydro-based correction |
| Phantom | 1.9mm | 0.56mm | 0.25mm | 100% | 141% | 150% |
| Skull | 1.77mm | 0.71mm | 0.25mm | 100% | 151% | 217% |

*Table 1.7: Correlation between simulated and measured temperature in several studies*

| Reference | Metric | Correlation between simulated and measured |
|---|---|---|
| [41] | Peak temperature rise | $r^2 = 0.71$ |
| [44] | Peak temperature | $r^2 = 0.75$ |
| [43] | Focal spot temperature rise | $0.613 \leqslant r^2 \leqslant 0.947$ |

McDannold et al. [41] also compare the dimensions and obliquity of the heating. The found that the predicted and measured dimensions ($R^2 = 0.62$) and obliquity ($R^2 = 0.74$) of the heating are correlated.

### 1.4.3 Sources of errors between experiments and simulations

On the simulation side, as shown by Almquist et al. [23], imprecise skull modelling based on CT scans is an important source of mismatch between simulations and experiments. In addition, many approximations, such as neglecting shear waves (especially if the incidence angles are greater than 30° [50]), attenuation and non-linearity, degrade the accuracy of the results. For instance, in Ding et al. study [38], the thermal dose at the focus computed with non-linear wave propagation was almost twice the linear thermal dose, suggesting that non-linearity effects have to be taken into account. Jiang et al. [17] compare simulations with and without shear waves for incident angles smaller than 20°. They found a shift of 0.5mm of the focus when shear waves are neglected, while perfect focusing is reached when shear waves are included. The maximum pressure reached with shear waves is approximately 3.65 Pa, while that when shear waves are not considered is approximately 4.85 Pa. On the experimental side, very close positioning of the experiments relatively to the simulations is crucial in order to be sure to be able to compare them. One also needs to keep in mind that hydrophones are generally not very precise (up to 10% errors) and need to be well calibrated.

## 1.5 Discussion

Almquist et al. [23] showed that transcranial acoustic simulations accuracy is highly dependent on skull modelling, which can be divided into two steps: the geometric description and the acoustic properties. The shape is not needed for numerical methods and is usually segmented from CT or MR images for semi-analytical methods. Over the years, image-derived acoustic properties have replaced measured ones, because of their case-specific adaptability. Most studies agree that both density and speed of sound depend linearly on HU values, but various empirical relationships have been proposed and improved. Marsac et al. [2] seem to have reached the more general porosity-based relationships and their accuracy is demonstrated by Bancel et al. [19]. The main issue with these relationships remains to choose the constants $(\rho_{max}, \rho_{min}, c_{max}, c_{min})$. While $\rho_{min}$ and $c_{min}$ are often taken as the values of water, $\rho_{max}$ and $c_{max}$ are sample-dependant and thus hard to choose. Marsac et al. [2] tried to find the best $c_{max}$ such that simulations fit the experiments, but this kind of approach is hard to generalize as it depends mostly on the samples used, the frequency and the experimental conditions. Indeed, Pichardo et al. [54] showed that the speed of sound relationships are frequency dependent. A polynomial relationship has been proposed by McDannold et al. [41] for the speed of sound, with constants found by comparing simulations with experiments. Once again, the problem of such strategies is that the relationships are case specific to the experimental conditions of the study and are not always well generalizable. To avoid any bias, the relationships need to be compared in a different study, such as the one from Bancel et al. [19], who showed that Marsac relationships were more accurate than Pichardo's and McDannold's. But more comparison studies are needed. Finally, attenuation is the parameter that is the hardest to determine since it is not well understood. Various empirical relationships

have been proposed, relating attenuation to HU values with a linear or a power law. Robertson et al. [65] showed that attenuation can be defined by a constant across the whole skull, but of course this constant is skull specific. Linear and power laws relating attenuation with frequency have also been investigated. In particular, in trabecular bone, where most of the scattering occurs, linear relationships have been established with a slope that varies quasi linearly with the bone fraction volume. However, Yousefian et al. [73] claim that total attenuation is not described by a linear combination of scattering and absorption anymore in the presence of multiple scattering. They propose a relationship for attenuation, which is the sum of a constant absorption and a frequency dependent power law for scattering. However, to our knowledge, no comparison studies have shown that any attenuation relationship is better than the others. While most studies derived the acoustic properties of the skull from CT scans, Webb et al. [76] warned that X-ray energy, reconstruction method, and reconstruction kernel should also be taken into account. After computing the acoustic properties of the skull, one can consider several levels of heterogeneity, going from global properties for the whole skull to individual properties for each voxel. Comparisons of these levels of heterogeneity is complicated as it is closely linked to the kind of simulation method used. Indeed, numerical methods tend to use fully heterogeneous skull model while semi-analytical methods (in particular ray-tracing) often use fully homogeneous ones. Jones and Hynynen [5] and Kyriakou et al. [18] both compared homogeneous and heterogeneous models with a same simulation method for correction aberration and found that, as can be expected, the heterogeneous performs better, especially in terms of predicted pressure amplitude, while both models seem nearly equivalent in terms of predicted shift. This is in agreement with Robertson et al. study [3], who shows that homogenization of acoustic property maps leads to an overestimation in the amplitude of ultrasound and an underestimation of time-of-flight. However, smarter homogeneous models can be used to improve computation time without losing too much accuracy. For example, Jiang et al. [85] showed that taking different averaged properties for the refraction computations and for the time-of-flight computations significantly improves the accuracy without increasing the computation time. In terms of simulation methods, the most used ones are ray-tracing, Hybrid Angular Spectrum, FDTD and k-space. The k-space method seems to have replaced FDTD, as it produces less numerical errors at low spatial resolution [15]. Thus, the k-space method can be used with quite coarse meshes without losing to much accuracy, which results in a computation time decrease (by a factor of around 80 [15]). Several studies compare finite difference based [5] [18] and k-space based [17] [19] phase correction with ray-tracing based phase correction. The results show that both FDTD and k-space based phase correction outperforms ray-tracing based phase correction, but the gap between numerical methods and ray-tracing vary between the studies (going from a 2% difference [19] to a 50% difference [18] in restored pressure at focus). In terms of computation time, FDTD is slower than ray-tracing by three orders of magnitude [5], while the k-space method is slower than ray-tracing by one order of magnitude [17].

## 1.6 Conclusion

Transcranial focused ultrasound is a promising method for several therapeutic applications. Simulations are needed to optimize such treatments and to assess their safety. The main challenge of such simulations is to determine the skull acoustic properties. Then, depending on level of precision of the skull modelling, different types of simulation methods can be used. Another big challenge is to make measurements precise enough to be able to compare them with simulation results and thereby to assess the accuracy of the simulations.

# Chapter 2

# Smooth and homogeneous realistic skull model for semi-analytical ultrasonic field computation

As shown by Almquist et al. [23], transcranial simulations accuracy is highly dependent on skull modelling. Indeed, they compared simulation based skull aberration correction through phantoms (with known acoustic properties and geometry) and through real skulls (with unknown acoustic properties and geometry, derived from the CT scan), and reached 94% of the optimal correction (hydrophone-based correction) in the phantom experiments, while only 70% in the skull experiments. Thus, the objective of this chapter was to develop realistic skull model from a CT scan, designed for semi-analytical ultrasonic field computation algorithms. Indeed, as numerical methods are widely used, skull modeling is achieved only by computing the acoustic property (density, sound speed and attenuation) matrices from the skull CT scan. In the case of our method, both the geometry and the acoustic properties have to be modeled. That is why, in the first section of this chapter, we will explain how we modeled the skull geometry from a CT scan. We modeled the skull with smooth surfaces, to get closer to the real skull shape, compared to the staircase modeling (due to the computation grid) used for numerical methods, or to mesh models. In addition, this will enable us to use a minimization algorithm in chapter 3. It also avoid having sharp edges (as is the case in a mesh) which can cause numerical errors. In the second part of this chapter, we will explain how we modeled the skull acoustic properties from a CT scan. After extracting the acoustic properties from a CT scan, we developed a new skull homogenization method to obtain a single equivalent value for each one of these properties (density and sound speed). Indeed, a homogeneous model is often required for semi-analytical ultrasonic field computation algorithms, and very few homogenization methods have been proposed in the literature. In addition, using a heterogeneous model seems too precise compared to the uncertainty on the acoustic properties derived from the CT scan. Thus a homogeneous skull model might be enough, especially when working at lower frequencies where the skull heterogeneities can be neglected. Besides, most homogeneous models are built by simply averaging the acoustic properties derived from the CT scan, but Jiang et al. [17] showed that a more sophisticated homogeneous model can reach similar aberration correction results as a heterogeneous model. The fact that the whole (geometric and acoustic) skull model is derived from a CT scan is what makes it patient specific and will thus make the simulation tool a personalized one.

## Contents

## 2.1 Skull geometry modeling using smooth parametric surfaces

To build a smooth model of the skull we used splines. More precisely, we used a method called Multi-level Bspline Approximation (MBA), which is more robust than interpolation methods.

### 2.1.1 Smooth and robust surface modeling using MBA

Splines are an interpolation method. They are a piecewise-defined polynomial functions that consist of several polynomial segments, joined together at specific points called knots. These segments are continuous at the knots, ensuring the smoothness of the overall curve.

Basis-Splines (B-Splines) are a specific type of splines that use a basis function approach. In B-Spline representation, the overall curve is defined as a linear combination of basis functions, each associated with a specific knot. The basis functions are typically piecewise polynomials of a fixed degree (often 3). The main property of B-Splines is local support, which means each basis function is only nonzero over a limited range of knots. This property enables B-Splines to be efficiently computed. B-Splines also offer local control over the shape of the curve, as each control point affects only a limited region of the curve. This concept is illustrated in figure 2.1 where only part of the data points is used as control points.

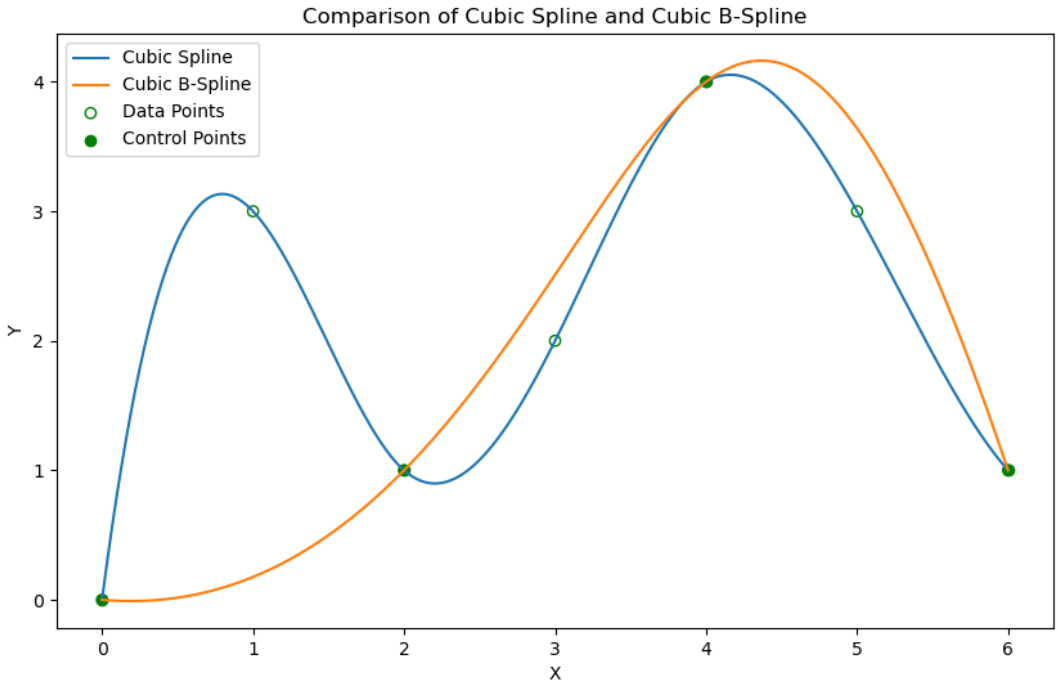


*Figure 2.1: Spline and B-Spline cubic curves with the same number of data points, but only half of them are used as control points for B-Spline construction*

The main drawback of B-Splines is that the user has to make a trade-off between the shape smoothness and the accuracy of the interpolation function generated. Multi-level B-Spline approximation (MBA) circumvent this trade-off. The resulting function simultaneously achieves a smooth shape while closely approximating the given data. The idea behind MBA is to approximate complex datasets with a hierarchical structure of B-Spline curves. Instead of representing the entire dataset with a single high-degree B-Spline, MBA decomposes the data into multiple lower-degree B-Splines, organized in a hierarchical manner. The lower-degree B-Splines capture the coarse features of the data, while higher-degree B-Splines are used to refine the approximation and capture finer details. This approach significantly reduces the number of control points required to represent the data accurately, leading to efficient data storage and faster computation, while maintaining a good level of accuracy. At the same time, MBA helps to eliminate noise and unwanted fluctuations in the data by approximating the underlying smooth curve. Another advantage of MBA is its adaptability: its hierarchical nature allows for easy control over the level of detail in the approximation. Different levels of approximation can be achieved by adjusting the number of levels or the degree of B-Splines in

the hierarchy. More details about MBA can be found in [1]. A C++ implementation of the MBA algorithm found on GitHub was used (https://github.com/SINTEF-Geometry/MBA). This algorithm includes:

- The function to build an MBA surface from a set of 3D points.
- The function $z = f(x, y)$ of the parametric surface.
- The first and second order derivatives of $f$.

### 2.1.2 Protocol to model the skull surfaces with MBA from a CT scan

#### 2.1.2.1 General protocol

The CT scan is an X-ray image of the skull. It is obtained as a DICOM (Digital imaging and communications in medicine) file, which is the standard file format used in medical imaging.

As we model the skull as a homogeneous medium, only the external (inner and outer) surfaces of the skull need to be modeled. The inner and outer surfaces are each modeled with MBA, but only for a portion of the skull. Indeed, as a MBA surface is described by a function $z = f(x, y)$, the surface needs to have a single value for every pair $(x, y)$, which is not possible if we consider the whole skull. Thus, for a given transducer position, only the part of the skull located below the transducer is modeled as MBA surfaces. In addition, the transducer, the skull and the computation zone are rotated so that the $z$ axis is oriented along the transducer normal vector, so that the MBA surfaces are well defined.

To model a skull from a CT scan using MBA, the surface of the skull is first extracted as a STL file (figure 2.2.(a)) from the DICOM file, with a software such as VG-Studio, ITK-Snap or 3D-Slicer. This is only done once. Then, for a given transducer position, the following steps need to be followed:

- Cut the skull mesh part located below the transducer using a clip filter with Paraview or MeshLab (figure 2.2.(a) → figure 2.2.(b)).
- Convert the cut STL mesh to a MSH mesh using Gmsh (to be used for ray-tracing to find the first guess of the path computation in the next chapter).
- Extract the inner and outer surfaces of the skull from the cut mesh using a C++ code explained in the next paragraph (figure 2.2.(b) → figure 2.2.(c)).
- Build the MBA surfaces from the inner and outer mesh vertices (figure 2.2.(c) → figure 2.2.(d)).

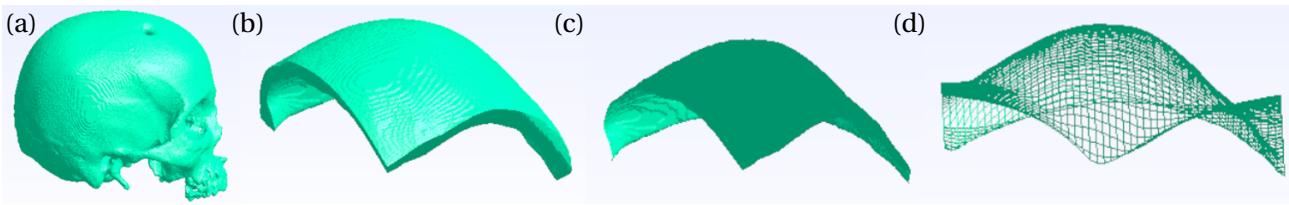


*Figure 2.2: Steps for MBA construction: (a) skull mesh, (b) cut skull mesh, (c) inner cut skull mesh, (d) inner MBA surface*

#### 2.1.2.2 Inner and outer skull surfaces extraction

To extract the inner and outer surfaces of the cut skull mesh, two methods can be used.

The first method we thought of, was to go through all the faces and cast a ray from the skull "center" towards the barycenter of the face, and keep only the first hit for the inner surface extraction, or the last hit for the outer surface extraction. Unfortunately, this method does not work very well, as the ray casting is not precise enough. That is why we thought of another method.

The second method works only if the face normals are conform. In that case, we go through all the faces and compute the dot product $\vec{BC}.\vec{n}$ where $\vec{BC} = \text{center} - \text{barycenter}$ and $\vec{n} = ((v_1 - v_0) \times (v_2 - v_0))$ is the face normal, with $(v_0, v_1, v_2)$ the face vertices. If this dot product is greater than 0 than the face belongs to the inner surface, otherwise it belongs to the outer surface. This method works very well, but cannot be used if the face normals are not conform.

Both methods are illustrated in figure 2.3.

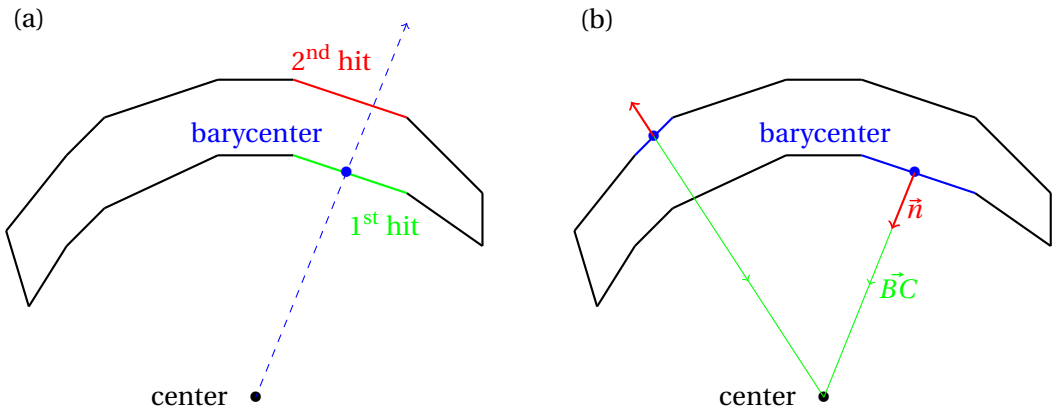


*Figure 2.3: Inner and outer surfaces extraction: (a) first method, (b) second method*

## 2.2 Skull acoustic property homogeneous modeling

### 2.2.1 Skull acoustic property extraction from a CT scan

#### 2.2.1.1 Hounsfield Unit matrix extraction from a CT scan

A CT scan DICOM file contains a 3D matrix of intensities, called Hounsfield Units (HU), divided into 2D slices. Each one of these slices is saved in a different file, that contains the 2D matrix of HU and information about the slice (such as the number of rows and columns or the slice position). To compute the skull acoustic properties, the 3D HU matrix needs first to be extracted.

To extract the 3D HU matrix from a CT scan we used the pydicom Python library. We wrote a simple Python script that reads all the slice files in a DICOM directory. As the file numbering does not always corresponds to the slice numbering, special care has to be taken (by using the InstanceNumber attribute). For a given slice, the 2D array of HU values is obtained thanks to the pixel_array attribute. This 2D array is then inserted in the 3D matrix at the location given by the InstanceNumber attribute.

At the same time, the position and orientation of the patient, as well as the voxel spacing in all three directions are retrieved from the DICOM file using pydicom. The patient position, obtained thanks to the ImagePositionPatient, gives the (x, y, z) coordinates of the upper left hand corner (center of the first voxel transmitted) of the image, in millimeters. The patient orientation, given by the ImageOrientationPatient attribute, contains the direction cosines of the first row and the first column with respect to the patient. Only the position and orientation of the first slice are kept. The voxel spacing is obtained in the first two directions by the pixelSpacing attribute. The voxel spacing in the third direction is given by the difference of the z coordinates of the positions of two consecutive slices.

The Python script is given in section A.1.

#### 2.2.1.2 Skull segmentation

Once the 3D HU matrix is extracted, the skull needs to be segmented. First, we compute $HU_{water}$ by taking the average HU value over a few voxels identified as water. Then, the skull is segmented using a user chosen threshold. All voxels with a HU value below this threshold are given the value of $HU_{water}$. To remove potential artefacts, we only keep the biggest connected component identified as non-water, with the code written in section A.2.

#### 2.2.1.3 Computation zone creation

To obtain a local homogeneous skull model, the homogenization method is performed only on the pressure field computation zone. Thus, the HU values at each point of this zone need to be computed. In addition, this computation zone can also be used directly to extract heterogeneous acoustic properties for k-Wave computations.

First, the position of the HU matrix voxels in the CT scan coordinate system needs to be computed. To determine the position $(x, y, z)$, in the CT scan coordinate system, of a given voxel of indexes $(i, j, k)$, a Python script was written. It creates a change of basis matrix to go from the coordinate system to the indexing system. It allows thus to do the backward operation. The Python script is given in section A.3.

Then, given the change-of-basis matrix between the skull coordinate system and the computation zone coordinate system, as well as the zone spacing and dimensions in all 3 directions, the computation zone is created. To do so, all points of the computation zone are computed in the skull coordinate system. Then, the corresponding voxel indices are computed. Finally, the HU values from the 8 neighbours voxels are interpolated to give the HU value of the computation point. The Python code is given in A.4.

Once the zone is created, because of the interpolation, voxels at the border between bone and water, might have HU values that are greater than $HU_{water}$ but lower than the skull threshold. Thus voxels with HU values lower than the skull threshold are assigned the value of $HU_{water}$.

The whole process to obtain a computation zone from a CT scan is illustrated in figure 2.4.

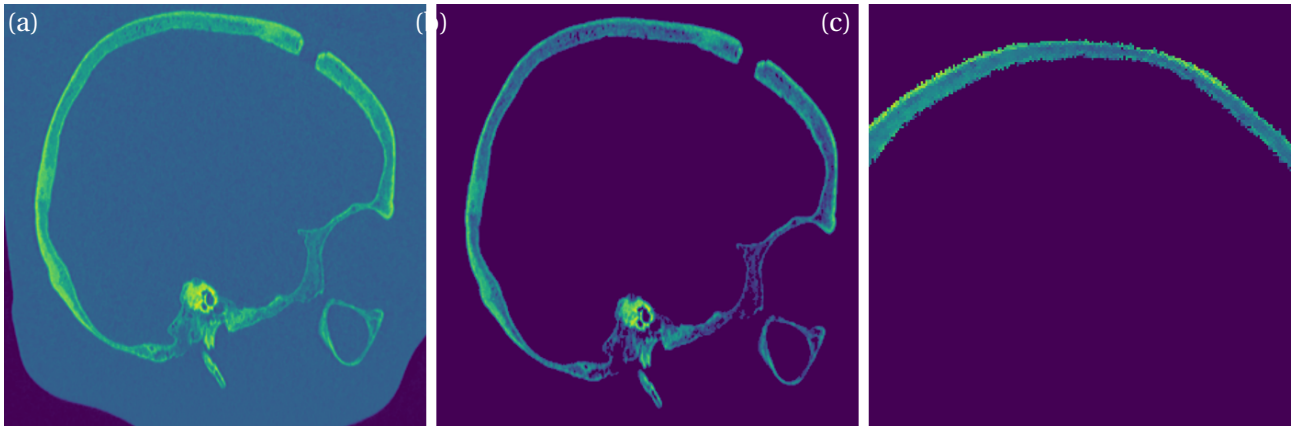


*Figure 2.4: Process to obtain a computation zone from a HU matrix: (a) HU matrix, (b) Skull segmented, (c) Computation zone*

#### 2.2.1.4 Acoustic properties computation from Hounsfield Units

Once a HU value is associated with each point of the computation zone, the acoustic properties can be computed. Indeed, several empirical formulas to compute the density and sound speed from HU were proposed in the literature, as detailed in chapter 1.

**Density and sound speed** To compute the density $\rho$ and sound speed $c$ from HU values, we chose to use the empirical formulas proposed by Marsac et al. [2] as they are the most general:

$$\rho = \rho_{\text{min}} + (\rho_{\text{max}} - \rho_{\text{min}}) \frac{HU - HU_{\text{min}}}{HU_{\text{max}} - HU_{\text{min}}} \tag{2.1}$$

$$c = c_{\text{min}} + (c_{\text{max}} - c_{\text{min}}) \frac{\rho - \rho_{\text{min}}}{\rho_{\text{max}} - \rho_{\text{min}}} \tag{2.2}$$

To use these formulas, values for $(HU_{min}, \rho_{min}, c_{min})$ and $(HU_{max}, \rho_{max}, c_{max})$ have to be chosen.

Instead of using values from the literature, we wanted to use two samples of materials of known densities and sound speeds and to put them inside the CT scanner (with the same CT parameters as for the skull [76]). As the CT scan is performed in water, the sample for $(\rho_{min}, c_{min})$ was chosen as water. For $(\rho_{max}, c_{max})$, we wanted to use the values of a plexiglas sample, as we have transducer wedges made of plexiglas in our laboratory, with precisely measured sound speed, and easily measurable density. $HU_{max}$ was not the maximum value on the CT scan, but we only wanted two points in the range of the skull values, and sufficiently spread, to be able to build the affine functions described in equations 2.1 and 2.2. However, the density of plexiglas is too close to that of water even if its sound speed is not. This means that the empirical relationships to compute the acoustic properties of the skull from HU values cannot be seen as an affine regression in the range of HU values of the CT scan. They must be seen as a way to express the proportion of pure bone and pure water (or marrow) in a voxel of the CT scan. The problem is that, given the spatial resolution of a CT scan (typically of the order of 0.5mm), it is unsure whether there exist a single voxel of pure bone in the whole CT scan. That is why $HU_{max}$ can be very approximate. In addition, the values of density and sound speed of pure bone are not well known. An idea would be to take a small (and as homogeneous and flat as possible) sample of skull bone (temporal bone) and to measure its sound speed and density. However, because of a lack of time, we used values from the literature for $(\rho_{max}, c_{max})$. We

thus used $HU_{min} = HU_{water}$. Then, $HU_{max}$ was computed as the maximal value on the whole CT scan. Special care has to be taken to remove the part containing the teeth (if there are some in the skull sample) for the computation, as they can have a very high HU value. The values used for $(\rho_{min}, c_{min}, \rho_{max}, c_{max})$ are given in table 2.1 and were taken from the literature [2].

*Table 2.1: Extreme densities and sound speeds used in Marsac's relationships*

| $\rho_{min}$ | $c_{min}$ | $\rho_{max}$ | $c_{max}$ |
|---|---|---|---|
| 1000 | 1500 | 2700 | 4000 |

**Attenuation** Attenuation is a key parameter to obtain realistic transcranial simulations. However there is no consensus in the literature on an attenuation coefficient or a formula for the human skull. Several studies [64] [74] [4] have measured attenuation through human skull samples at several frequencies. They obtain the total attenuation, which is a combination of scattering and absorption. The problem is that, depending on the simulation method and skull model used, part of this attenuation is already simulated. That is also why formulas with parameters tuned so that experiments fit with a given simulation method [14] [42] are unusable for studies using a different simulation method. Indeed, with another simulation method, different physical phenomenons will be taken into account, and thus a different proportion of attenuation will be included in the simulations. In addition, such formulas are often tuned at a given frequency, but skull attenuation depends on frequency, thus such formulas are all the more unusable.

As our simulation algorithm is based on a new method, we can not use any simulation-tuned formula from the literature. Instead, we used a frequency-dependent attenuation coefficient used in a study [4] comparing experimental data with an analytical transmission model taking into account skull absorption:

$$\alpha_{skull} = 83\text{Np.m}^{-1}.\text{MHz}^{-1} = 0.72\text{dB.mm}^{-1}.\text{MHz}^{-1} \tag{2.3}$$

### 2.2.2 Skull acoustic property homogenization

The first idea that comes to one's mind to obtain a homogeneous skull model is to average the acoustic property maps derived from the CT scan, and that is what is done in most studies [5]. It was shown that this method does not influence much the focal spot position, but it overestimates the amplitude, compared to the heterogeneous model. This amplitude overestimation is due to two main reasons. First, the averaged model underestimate the impedance difference between the skull and its surrounding medium. Indeed, as the densest bone (cortical bone) is located at the skull borders, the averaged medium is necessarily less dense and thus closer to the surrounding medium in terms of impedance. Second, the averaged model does not take the internal heterogeneity into account. A more sophisticated method has been proposed in a recent study [17]. The idea is to use the mean acoustic properties for the time of flight computations and to use the maximum acoustic properties for the transmission coefficient. As using the averaged properties results in a focal position near the one using the heterogeneous properties, the averaged properties are a good candidate to compute the time of flight. On the other hand, using the maximum properties to compute the transmission coefficients allows to keep approximately the same impedance difference (between the skull and its surrounding medium) as the heterogeneous model. This homogenization method gives a better focusing than the classic averaging method when applied to aberration correction. However, it suffers from two drawbacks. First, the amplitude overestimation is not entirely fixed, as the internal heterogeneity is still not taken into account. Second, this method is not compatible with all simulation tools. Indeed, it is not always possible to use different properties for different computations. In fact, it is almost always impossible when using a simulation tool as a user. That is why we developed a new skull homogenization method that compensates for these two drawbacks.

The method is divided into two parts: modeling the skull as a three-layer medium and then homogenizing this three layer medium. The first step aims to model the skull based on the different types of bone inside the skull, which are trabecular bone and cortical bone (see figure 1.3). Indeed, the skull is composed of a layer of trabecular bone, which is a porous medium, located between two plates of cortical bone, which is a much denser bone (by around 10% [10]). This step assumes that these two types of bone can be modeled as homogeneous media [67] [48]. The second step, on the other hand, models a non-realistic medium, with

acoustic properties found so as to minimize the error between the field computed through the three layer medium and the field computed through the homogeneous one. The media located on either side of the skull are supposed to have the same acoustic properties. In the case of realistic simulations, this medium can have the properties of soft tissues (skin and brain), but it can also have the properties of water for ex vivo simulations.

#### 2.2.2.1 Modeling the skull as a three-layer medium (cortical bone - trabecular bone - cortical bone)

The goal of this step is to segment the skull into two media: cortical bone and trabecular bone. We chose to do the segmentation on the Hounsfield Units (HU) intensity matrix directly and to derive the acoustic properties afterwards. First, a threshold for skull segmentation has to be chosen. Then the intensity of the background $HU_{min}$ is computed by taking the average intensity over a few background voxels (the background can be either water in case of an ex vivo skull surrounded by water, either soft tissue for a real head). Then all values under the skull threshold are given the value of $HU_{min}$.

The voxels identified as skull (or non-background) are then segmented into trabecular bone and cortical bone with the K-Means clustering algorithm [6]. The K-Means algorithm aims to separate data into clusters, by allocating each observation to the cluster with the nearest mean. After that, a few post-processing tasks, described below, are applied. To remove any bone parts isolated, we labeled as background all connected components of skull, except from the biggest one (using the method "regionprops" from the skimage.measure Python package). Because of the averaging effect of CT-scans with low resolution, there are voxels located between cortical bone and the background that are labeled as trabecular bone even though they are only voxels at the border of the skull that have the value of the averaged intensity of cortical bone and background. It is quite easy to detect such voxels with the human eye as they appear as a thin region (one voxel width) located at the border between skull and background. To remove them with a simple code, we just set as background the voxels labeled as trabecular bone that have both cortical and background neighbours, as well as small trabecular regions that have a background neighbour. Finally, all voxels identified as trabecular bone are averaged, and all voxels identified as cortical bone are averaged.

Then, the acoustic property maps are extracted from this new HU map. The empirical relationships used in the present manuscript, previously proposed by Marsac et al [2], computes the density $\rho$ and sound speed $c$ at a given voxel of intensity $HU$ using:

$$\rho = \rho_{min} + (\rho_{max} - \rho_{min}) \frac{HU - HU_{min}}{HU_{max} - HU_{min}} \tag{2.4}$$

$$c = c_{min} + (c_{max} - c_{min}) \frac{\rho - \rho_{min}}{\rho_{max} - \rho_{min}} \tag{2.5}$$

With $HU_{min}$ and $HU_{max}$ the minimal and maximal intensities on the CT scan ($HU_{min}$ is computed as explained previously and $HU_{max}$ is the maximal value on the original CT scan), and $(\rho_{min}, c_{min})$ and $(\rho_{max}, c_{max})$ their associated densities and sound speeds. Usually, the CT scan is performed in water so $\rho_{min} = 1000$ kg.m$^{-3}$ and $c_{min} = 1480$ m.s$^{-1}$. The maximal properties are taken as those of pure bone, on which there is no scientific agreement, but for instance Marsac et al. took $\rho_{max} = 2700$ kg.m$^{-3}$ and $c_{max} = 4000$ m.s$^{-1}$.

#### 2.2.2.2 Homogenization of the three-layer medium

The second step consists of computing the acoustic properties of an equivalent homogeneous medium from those of the three layers. For the sake of simplicity, the study has been carried out for planar parallel layers, but the extension of this method to more complex geometries will be analyzed in the result section. The three-layer medium and equivalent medium are illustrated in figure 2.5. When computing an ultrasonic field with a ray-tracing method, three values are of interest: the final direction of the ray (given by the refraction angle after the last interface), the time of flight and the transmission coefficient. As the interfaces are supposed to be planar and parallel and as the first and last media are the same, the refraction angle after the last interface is equal to the incidence angle. As the time of flight only depends on the speed of sound, the equivalent speed of sound has been defined so as to minimize the time of flight error between the three-layer medium and the homogeneous one. Finally, given the equivalent speed of sound, the equivalent density has been defined so as to minimize the transmission coefficient error between the three-layer medium and the homogeneous one.

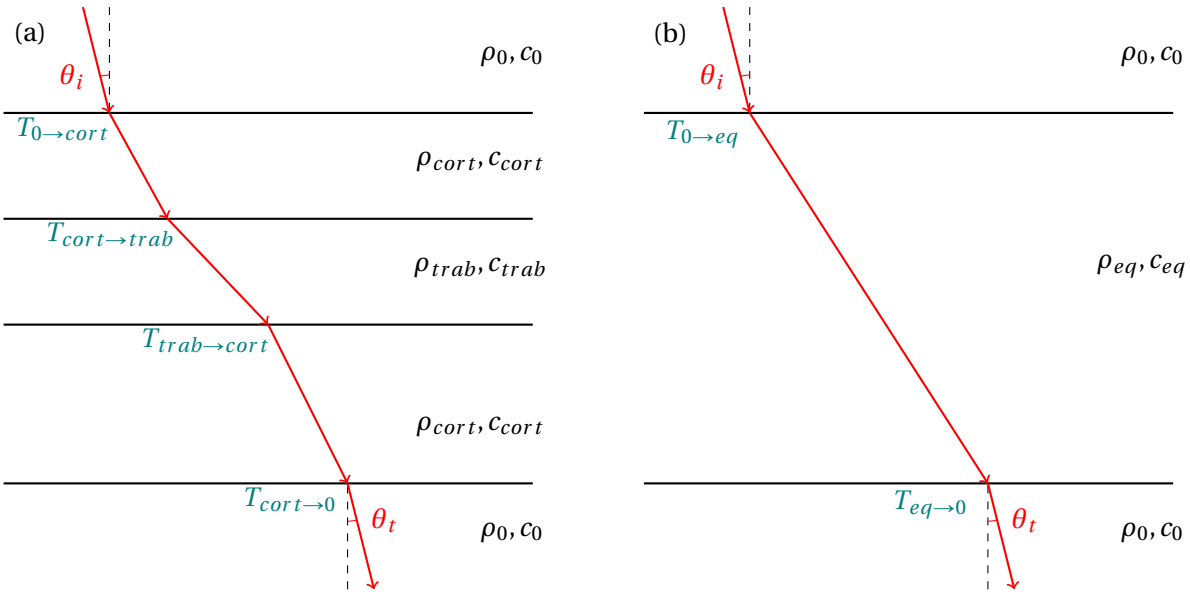


*Figure 2.5: Three layer medium (a) versus equivalent medium (b)*

**Equivalent speed of sound** Let us consider the slowness of a medium: $s = 1/c$, with $c$ the sound speed of the medium. Let us define the average slowness of 3 media: $s_{\text{mean}} = \sum_{i=1}^{3} s_i \frac{d_i}{d}$, where $d_i$ is the thickness of medium $i$, $d = \sum_{i=1}^{3} d_i$ the total thickness, and thus $\frac{d_i}{d}$ the proportion of medium $i$. It is quite easy to show that, at normal incidence, the time of flight through an equivalent medium of sound speed $1/s_{\text{mean}}$, is equal to the time of flight through the three layer medium:

$$\begin{aligned} t_{eq} &= d\, s_{eq} \\ &= d \sum_{i=1}^{3} s_i \frac{d_i}{d} \\ &= \sum_{i=1}^{3} d_i s_i \\ &= t_{3layers} \end{aligned} \tag{2.6}$$

Thus the inverse of the average slowness is good candidate for the equivalent sound speed. However, as the average sound speed $c_{mean} = \sum_{i=1}^{3} c_i \frac{d_i}{d}$ is always used in the literature, we investigated a little bit more.

Let us the consider the propagation through the three media using the pencil method, introduced by Nicolas Gengembre [7]. It is a ray tracing method considering an axial ray, as well as a paraxial ray, which is a first order approximation, that accounts for the beam divergence. At normal incidence, the propagation through the three layer medium is expressed by three propagation matrices:

$$\begin{aligned} L_1 L_2 L_3 &= \begin{bmatrix} 1 & 0 & d_1 c_1 & 0 \\ 0 & 1 & 0 & d_1 c_1 \\ 0 & 0 & 1 & 0 \\ 0 & 0 & 0 & 1 \end{bmatrix} \begin{bmatrix} 1 & 0 & d_2 c_2 & 0 \\ 0 & 1 & 0 & d_2 c_2 \\ 0 & 0 & 1 & 0 \\ 0 & 0 & 0 & 1 \end{bmatrix} \begin{bmatrix} 1 & 0 & d_3 c_3 & 0 \\ 0 & 1 & 0 & d_3 c_3 \\ 0 & 0 & 1 & 0 \\ 0 & 0 & 0 & 1 \end{bmatrix} \\ &= \begin{bmatrix} 1 & 0 & \sum_{i=1}^{3} d_i c_i & 0 \\ 0 & 1 & 0 & \sum_{i=1}^{3} d_i c_i \\ 0 & 0 & 1 & 0 \\ 0 & 0 & 0 & 1 \end{bmatrix} \end{aligned} \tag{2.7}$$

It is easy to see, that by taking $c_{eq} = c_{mean} = \sum_{i=1}^{3} c_i \frac{d_i}{d}$, the last matrix is a propagation matrix through an equivalent medium of thickness $d$ and of sound speed $c_{eq}$.

Thus, the average speed of sound is also a good candidate for the equivalent sound speed. In the following, all computations and tests have been made with both candidates:

- $c_{eq}^1 = \frac{1}{s_{mean}} = \frac{1}{\sum_{i=1}^{3} \frac{1}{c_i} \frac{d_i}{d}}$

- $c_{eq}^2 = c_{mean} = \sum_{i=1}^{3} c_i \frac{d_i}{d}$

The time of flight error between the three layer medium and the equivalent homogeneous medium was then evaluated for different configurations with different angles of incidence, medium properties and thicknesses.

In order to evaluate what the error would be for a realistic configuration, we computed the angle distribution on a skull mesh with a transducer pointing to a realistic target inside the skull. To do so, a small code goes through all the facets of the skull mesh that are in the ultrasonic beam of the transducer, and computes the angle between the main ray and the facet normal. A realistic angle distribution is thereby obtained, and displayed in figure 2.6. It shows that most angles (more than 97% of them) are lower than 30°. The time of flight error weighted by this angle distribution was then computed. This error takes into account all contributions equally, even though contributions with higher angles of incidence have a smaller transmission coefficient, so this is actually an upper bound of what the error would be.

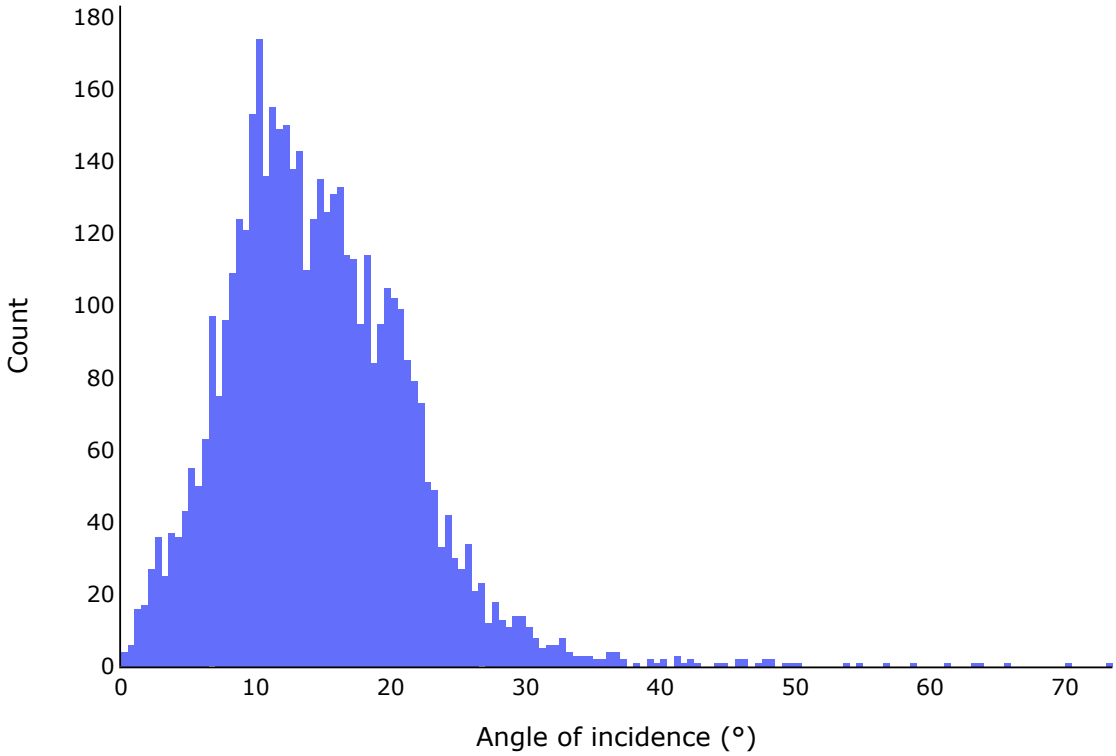


*Figure 2.6: Realistic angle distribution*

**Equivalent density** Once the equivalent sound speed is set, the goal is to find the equivalent density so as to minimize the transmission coefficient error between the three layer medium and the equivalent homogeneous medium.

A preliminary study was carried out in order to determine whether the reflections inside the skull could be neglected or not. If they are negligible, classical transmission coefficients can be used, otherwise transmission coefficients can be derived using the transfer matrix formalism [86]. Thus, CIVA Healthcare simulations with and without internal reflections taken into account were compared for several configurations of three-layer medium with planar interfaces. The configurations and the results are detailed in appendix B. Table B.1 shows that when the skull attenuation is taken into account, reflections are negligible. Thus, classical transmission coefficients, taking shear waves into account, were used [9].

Then, the strategy was to model a lot of three layer medium configurations, with different incidence angles, medium properties and thicknesses. For each configuration, the equivalent sound speed is computed and the density that minimizes the transmission coefficient error between the three layer medium and the equivalent homogeneous medium is found exhaustively in a predefined range of densities. Then, given

this set of configurations and optimal densities, a linear regression has been performed to obtain a linear relationship between the configuration parameters and the optimal densities.

A few assumptions were made to simplify the problem (mostly to lower the number of parameters) and to make it more accurate:

- Media 1 and 3 were assumed to be the same as they represent cortical bone.
- The thicknesses were represented as proportions $\frac{d_i}{d}$, as the transmission coefficients do not depend directly on the thicknesses. They however depend on the equivalent sound speed which depends on the proportions rather than the thicknesses.
- To reduce the number of parameters, the densities and sound speeds were derived from the CT scan using the relationships proposed by Marsac (equations 2.4 and 2.5). Doing so, the sound speed linearly depends on the density (equation 2.5). We therefore only needed to vary the densities.
- The acoustic properties of the surrounding medium were fixed.
- $\rho_{\text{min}}$, $\rho_{\text{max}}$, $c_{\text{min}}$, $c_{\text{max}}$ (from equations 2.4 and 2.5) were fixed.
- The shear wave sound speed was taken as half the longitudinal sound speed, for both trabecular and cortical bones, as is often done for solid materials.

This aim of this approach is more to show a proof of concept rather than to give formulas that can be applied to every use case. That is why, anyone can use this method with different acoustic properties of the surrounding medium, different $\rho_{min}$, $\rho_{max}$, $c_{min}$, $c_{max}$, different ranges of the varying parameters, so as to have relationships best fitted to his use case or more accurate depending on the new discoveries that will be made about bone properties.

The properties of the surrounding medium were taken as these of water. The ranges for trabecular and cortical bone densities were centered around values from the literature [48] [10]. Table 2.2 summarizes the properties used (all densities are in kg.m$^{-3}$ and all sound speeds are in m.s$^{-1}$).

*Table 2.2: Acoustic properties*

| $\rho_0$ | $c_0$ | $p_{trabecular}$ | $\rho_{cortical}$ | $\rho_{trabecular}$ | $\rho_{min}$ | $\rho_{max}$ | $c_{min}$ | $c_{max}$ |
|---|---|---|---|---|---|---|---|---|
| 1000 | 1480 | [0.0, 0.9] | [1800, 1950] | [1600, 1750] | 1000 | 2700 | 1480 | 4000 |

#### 2.2.2.3 Evaluation of the homogenization method

**Test configurations and metrics** The whole homogenization method was tested on several configurations. To begin with, the first step was tested on planar configurations, then both steps were tested on realistic configurations. For both types of test configurations,we modeled a spherically curved transducer with a 50mm radius of curvature and a 30mm aperture diameter. For the sake of simplicity, shear waves were neglected in the simulations, based on a study on the influence of shear waves whose results are presented in appendix B. The first round of simulations was performed with CIVA, and the second round with k-Wave to be able to model heterogeneous media. To evaluate the method, that is to say to compare the field through the equivalent media with the field through the original medium, we used the metrics presented in table 2.3. The -3dB volume is computed as the volume of an ellipsoid of axis $(l_x, l_y, l_z)$, which are the -3dB distances along each axis. As the volume of an ellipsoid is $\frac{4\pi}{3} l_x \times l_y \times l_z$, the error in focal volume is $E_{dim} = \frac{|\frac{4\pi}{3} l_x^{ref} \times l_y^{ref} \times l_z^{ref} - \frac{4\pi}{3} l_x \times l_y \times l_z|}{|\frac{4\pi}{3} l_x^{ref} \times l_y^{ref} \times l_z^{ref}|} = \frac{|l_x^{ref} \times l_y^{ref} \times l_z^{ref} - l_x \times l_y \times l_z|}{|l_x^{ref} \times l_y^{ref} \times l_z^{ref}|}$

*Table 2.3: Metrics*

| **Focal spot position error** | **Maximum pressure error** | **-3dB volume error** |
|---|---|---|
| $E_{pos} = \|\|X_0^{ref} - X_0\|\|$ | $E_{amp} = \frac{\|P_{max}^{ref} - P_{max}\|}{\|P_{max}^{ref}\|}$ | $E_{dim} = \frac{\|l_x^{ref} \times l_y^{ref} \times l_z^{ref} - l_x \times l_y \times l_z\|}{\|l_x^{ref} \times l_y^{ref} \times l_z^{ref}\|}$ |

**Time of flight** The time of flight error between the three layer medium and the equivalent homogeneous medium was evaluated for different configurations (properties given in table 2.2). The mean and maximal errors, either for all incidence angles in $[0,\theta_{lim}[$ (with $\theta_{lim} = \sin^{-1}(\frac{c_0}{max(c_{cort})})$), either for the realistic angle distribution $D$, are showed in table 2.4.

*Table 2.4: Time of flight errors relative to the three layer medium*

| Sound speed | Mean error | Maximal error |
|---|---|---|
| $c_{eq} = c_{mean}$ and $\theta \in [0,\theta_{lim}[$ | 4.29% | 208.58% |
| $c_{eq} = \frac{1}{s_{mean}}$ and $\theta \in [0,\theta_{lim}[$ | 4.08% | 192.91% |
| $c_{eq} = c_{mean}$ and $\theta \in D$ | 0.27% | 0.39% |
| $c_{eq} = \frac{1}{s_{mean}}$ and $\theta \in D$ | 0.12% | 0.17% |

The mean and maximal errors as a function of the incidence angle for the uniform distribution are plotted in figure 2.7.

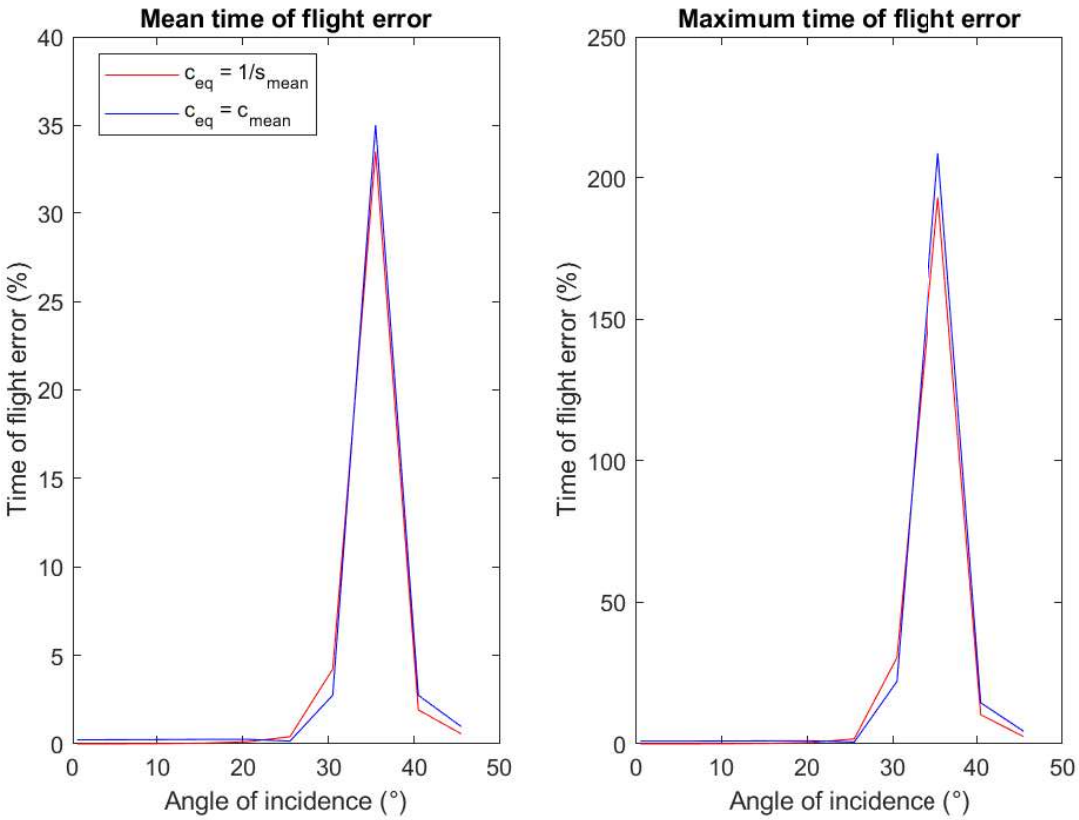


*Figure 2.7: Mean and maximal time of flight error for the uniform distribution*

As expected the inverse of the average slowness gives better results for the time of flight computations, but the difference is not significant. The maximal errors for a uniform distribution of the incidence angles ($\theta \in [0,\theta_{lim}[$ are very high (around 200%). These high errors are entirely due to angles between $30°$ and $40°$, as shown by figure 2.7. However, the realistic angle distribution in figure 2.6 does not contain a lot of angles within this range. That is why, the errors are much more reasonable for the realistic angle distribution. They all are below 1%, which is very acceptable, all the more so as it is a upper bound of the error, as explained in the previous section. The average sound speed performs very well as well, with mean and maximum errors both lower than 1% for the realistic angle distribution. It is thus kept as a candidate, all the more so as it is expected to perform a bit better than the inverse of the average slowness for the transmission computations.

**Transmission coefficient** Different combinations of variables were tested for the linear regression model. Finally, the best set of variables appeared to be $(\rho_{cort}, \rho_{trab}, \frac{d_{trab}}{d}, \rho_{cort}(1-\frac{d_{trab}}{d}), \rho_{trab}\frac{d_{trab}}{d})$.

The linear relationships and Root Mean-Square Error (RMSE) obtained depending on which $c_{eq}$ was chosen are displayed in table 2.5. The RMSE is given by: $\sqrt{(\frac{\sum_{i=1}^{N}(T^i_{3layers}-T^i_{eq})}{N}}$. The added variable plots of the two linear regression models are showed in figures 2.8 and 2.9.

*Table 2.5: Linear regression results*

| Sound speed | Relationship | RMSE |
|---|---|---|
| $c_{eq} = c_{mean}$ | $-1441.8 + 3.6\rho_{cort} - 0.6\rho_{trab} - 708.7\frac{d_{trab}}{d} - 1.3\rho_{cort}(1-\frac{d_{trab}}{d}) - 0.9\rho_{trab}\frac{d_{trab}}{d}$ | 22.5 |
| $c_{eq} = \frac{1}{s_{mean}}$ | $-1479.6 + 3.7\rho_{cort} - 0.6\rho_{trab} - 614\frac{d_{trab}}{d} - 1.3\rho_{cort}(1-\frac{d_{trab}}{d}) - 0.9\rho_{trab}\frac{d_{trab}}{d}$ | 23.3 |

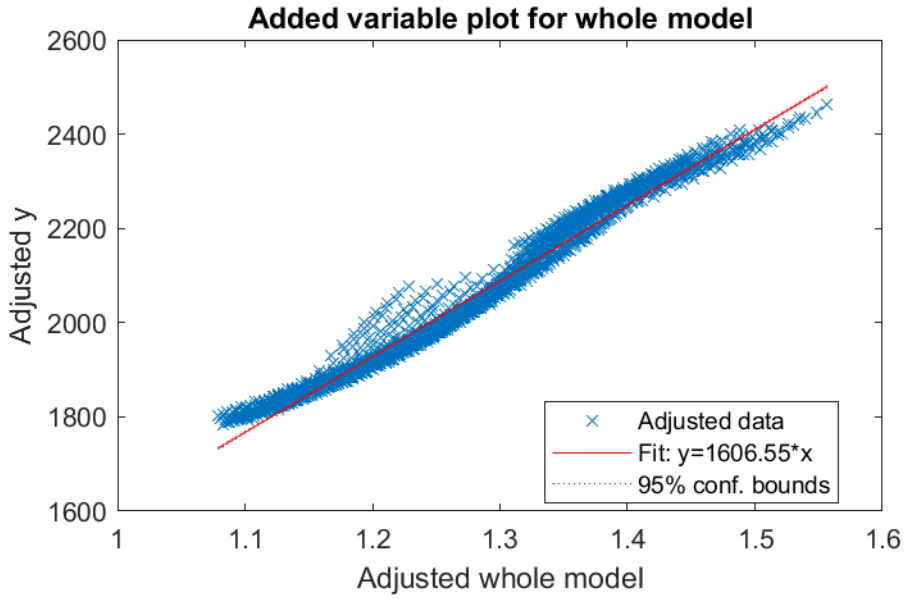


*Figure 2.8: Added variable plot of the linear regression model obtained with $c_{eq} = c_{mean}$*

The relationships obtained with the linear regressions show that the equivalent density does not depend on the incidence angle. The RMSE show that the linear regression performed a bit better with the average sound speed than with the inverse of the average slowness, as expected. Both added variable plots show a good fitting of the data with the models.

**Planar configurations** The second step of the homogenization method (from a three layer medium to a homogeneous medium) was tested for planar parallel interfaces with different frequencies, incidence angles, bone densities and thicknesses. The test configuration parameters are given in table 2.6, all combinations of parameters were tested, resulting in total of 32 configurations. The 3D simulations were performed using CIVA Healthcare. Shear waves were neglected.

*Table 2.6: Test configuration parameters*

| $f$ | $\theta_i$ | $\rho_{cort}$ | $\rho_{trab}$ | $\frac{d_{trab}}{d}$ |
|---|---|---|---|---|
| 0.5 MHz | 0° | 1850 kg.m$^{-3}$ | 1600 kg.m$^{-3}$ | 0.3 |
| 0.8 MHz | 15° | 1950 kg.m$^{-3}$ | 1700 kg.m$^{-3}$ | 0.7 |

The second step (from a three layer medium to a homogeneous medium) of the homogenization method was tested on 32 three-layer medium with planar parallel interfaces configurations, with parameters as listed

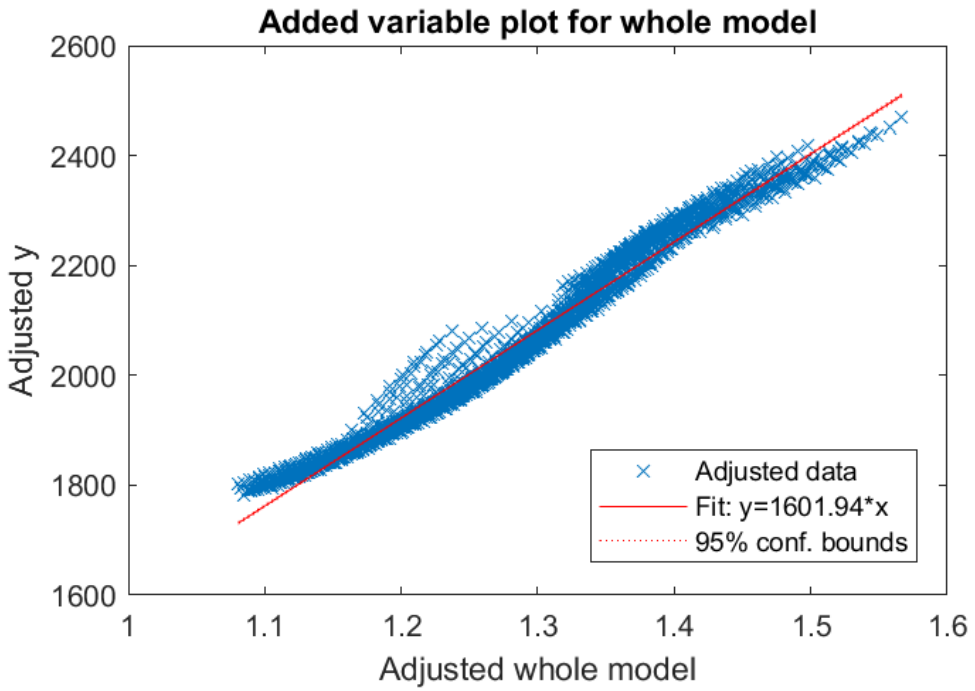


*Figure 2.9: Added variable plot of the linear regression model obtained with* $c_{eq} = \frac{1}{s_{mean}}$

in table 2.6. The pressure field through the three layer medium and through three homogeneous medium (one with the averaged properties, and the two others with the properties given by the homogenization method, one with $c_{eq} = c_{mean}$ and one with $c_{eq} = \frac{1}{c_{mean}}$) were simulated and compared using the metrics described in table 2.3. The errors, relative to the original three layer media, averaged over all 32 configurations are shown in table 2.7.

*Table 2.7: Pressure field results through planar configurations*

| Medium | $E_{pos}$ | $E_{amp}$ | $E_{dim}$ |
|---|---|---|---|
| Averaged | 1.20mm | 13.47% | 5.94% |
| Equivalent ($c_{eq} = c_{mean}$) | 1.20mm | 4.30% | 5.99% |
| Equivalent ($c_{eq} = \frac{1}{s_{mean}}$) | 1.07mm | 1.89% | 5.23% |

The pressure fields along each axis (x,y,z) through the different media are displayed in figure 2.10, for a configuration taken randomly from the set ($f = 0.5$ MHz, $\theta_i = 15°$, $\frac{d_{trab}}{d} = 0.3$, $\rho_{cort} = 1950$ kg.m$^{-3}$, $\rho_{trab} = 1600$ kg.m$^{-3}$).

As shown in the literature, the focal spot position error is very low (1.20mm) using the average sound speed. Using the inverse of the average slowness performs a bit better for the focal spot position (the focal spot position error is reduced by 0.13mm), as could be expected from the time of flight results in section 3.1. The pressure at the focal spot with the averaged medium is much higher (by more than 13%) than those obtained with the original medium, as we can see from table 2.7 and figure 2.10. This confirms what was described in the literature. In addition, the focal spot pressure error is much lower (by around 10%) with both equivalent media than with the averaged medium. Thus, most of the amplitude overestimation was corrected with our method, and especially using the inverse of the average slowness. It is quite surprising at first glance that the inverse of the average slowness performs better than the average sound speed in terms of focal pressure, as the transmission coefficient error was lower with the average sound speed than with the inverse of the average slowness. But, it seems logical that the time of flights should be the first concern when computing a pressure field, because if the ultrasonic paths are wrong, the pressure will be even more wrong, even if the transmission coefficients are right. The -3dB volume errors are equivalent for all media. The focal volume error is very similar for all three homogeneous media.

**Realistic configurations** Both steps of the homogenization method were evaluated on realistic skull geometries, using human heads CT-scans. The CT scans were obtained thanks to the Visible Human Project

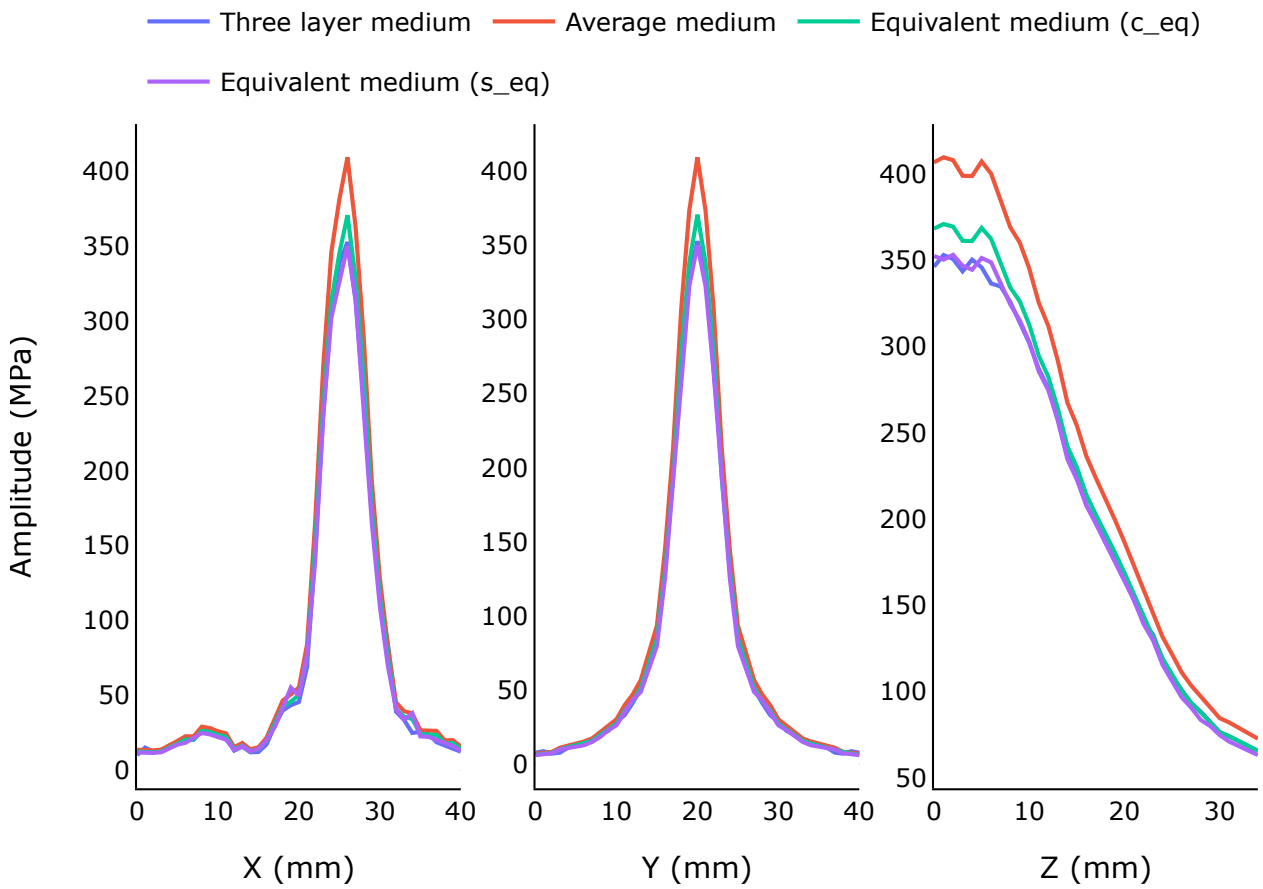


*Figure 2.10: Pressure field profiles through the different media for a planar configuration*

Data, by the courtesy of the U.S. National Library of Medicine. The female head CT and male head CT datasets were used. The acoustic property maps were derived from the CT scans using relationships (2.4) and (2.5). The three layer medium was then modeled using the method presented in section 2.1. $HU_{max}$ was computed as the maximal value on the CT scan, excluding the mouth, otherwise the maximum value would correspond to the teeth location and we want the maximal value to correspond to the densest bone voxel. The HU maps obtained for the female skull are displayed in figure 2.11. Finally, the average and equivalent media were computed, and the field through each one of these media were computed. All simulations for these configurations were performed using k-Wave, to be able to model a fully heterogeneous medium. The same transducer as for the planar configurations was used, driven at 0.8MHz. These 3D simulations were broadband with parameters as listed in 2.8. Shear waves were not taken into account.

*Table 2.8: K-Wave simulation parameters for the realistic configurations*

| $\Delta x$ | $\Delta t$ | $Nt$ | PML size |
|---|---|---|---|
| 0.25mm | 33ns | $60\mu$s | $3\Delta x$ |

The whole homogenization method was then tested on two realistic configurations: a female skull and a male skull. The errors relative to the original heterogeneous media are summarized in tables 2.9 and 2.10.

The pressure fields along each axis (x,y,z) and through all media are displayed in figure 2.12.

Tables 2.9 and 2.10 and figure 2.12 confirm, once again, the results from the literature: the focal spot position error is very low (below 1mm) using the average sound speed, and the averaged medium

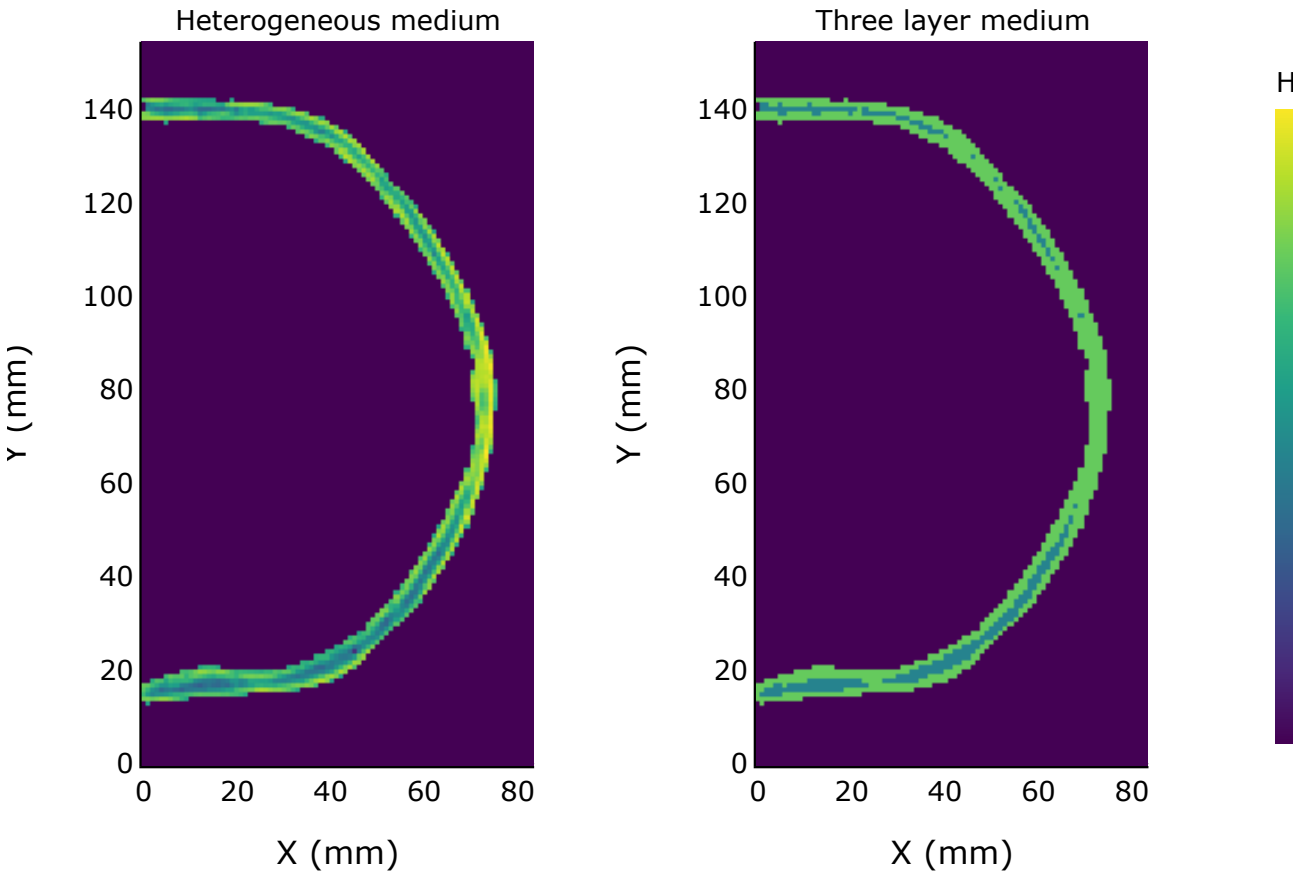


*Figure 2.11: HU maps at a given slice of the female skull*

*Table 2.9: Pressure field results through the female skull (errors relative to the heterogeneous medium)*

| Medium | $E_{pos}$ | $E_{amp}$ | $E_{dim}$ |
|---|---|---|---|
| Three-layer | 0mm | 8.24% | 14.19% |
| Averaged | 0.35mm | 42.10% | 12.58% |
| Equivalent ($c_{eq} = c_{mean}$) | 0.79mm | 8.44% | 3.58% |
| Equivalent ($c_{eq} = \frac{1}{s_{mean}}$) | 0.79mm | 3.66% | 2.42% |

overestimates a lot (by more than 40%) the pressure at the focal spot. The equivalent media both allow to reduce the focal pressure error (by around 30%) compared to averaged medium, which once again shows the potential of this homogenization method. Once again, the inverse of the average slowness performs better (by around 5%) in focal pressure. The focal volume error is very similar for all three homogeneous media for the female skull, but for the male skull, it is lower with the equivalent media than with the averaged medium.

These tables also allow us to evaluate the first step of the homogenization method, that is to say approximating the skull as a three layer medium. Approximating the heterogeneous medium by the three-layer one is quite realistic as the focal spot position errors are below 0.6mm, the focal pressure errors below 11% and the focal volume errors below 33%. However, these errors are not negligible. This is probably due to the fact that the impedance discontinuities are more brutal within the three-layer medium than within the heterogeneous medium, due to the blurring effects on the CT scans that tends to smooth the boundaries between the different media. This raises the question of whether the heterogeneous medium is more realistic than the three layer one. Without any experimental validation, the answer to this question is unknown. That is why, it might be more relevant to validate numerically only the second step of the homogenization method, that is to say approximating a three layer medium as a homogeneous medium. To do so, the focal position, pressure and volume errors relative to the three layer medium are displayed in tables 2.12 and 2.11.

*Table 2.10: Pressure field results through the male skull (errors relative to the heterogeneous medium)*

| Medium | $E_{pos}$ | $E_{amp}$ | $E_{dim}$ |
|---|---|---|---|
| Three-layer | 0.56mm | 10.28% | 32.12% |
| Averaged | 0.82mm | 43.23% | 37.48% |
| Equivalent ($c_{eq} = c_{mean}$) | 0.56mm | 15.04% | 40.83% |
| Equivalent ($c_{eq} = \frac{1}{s_{mean}}$) | 0.56mm | 9.19% | 43.62% |

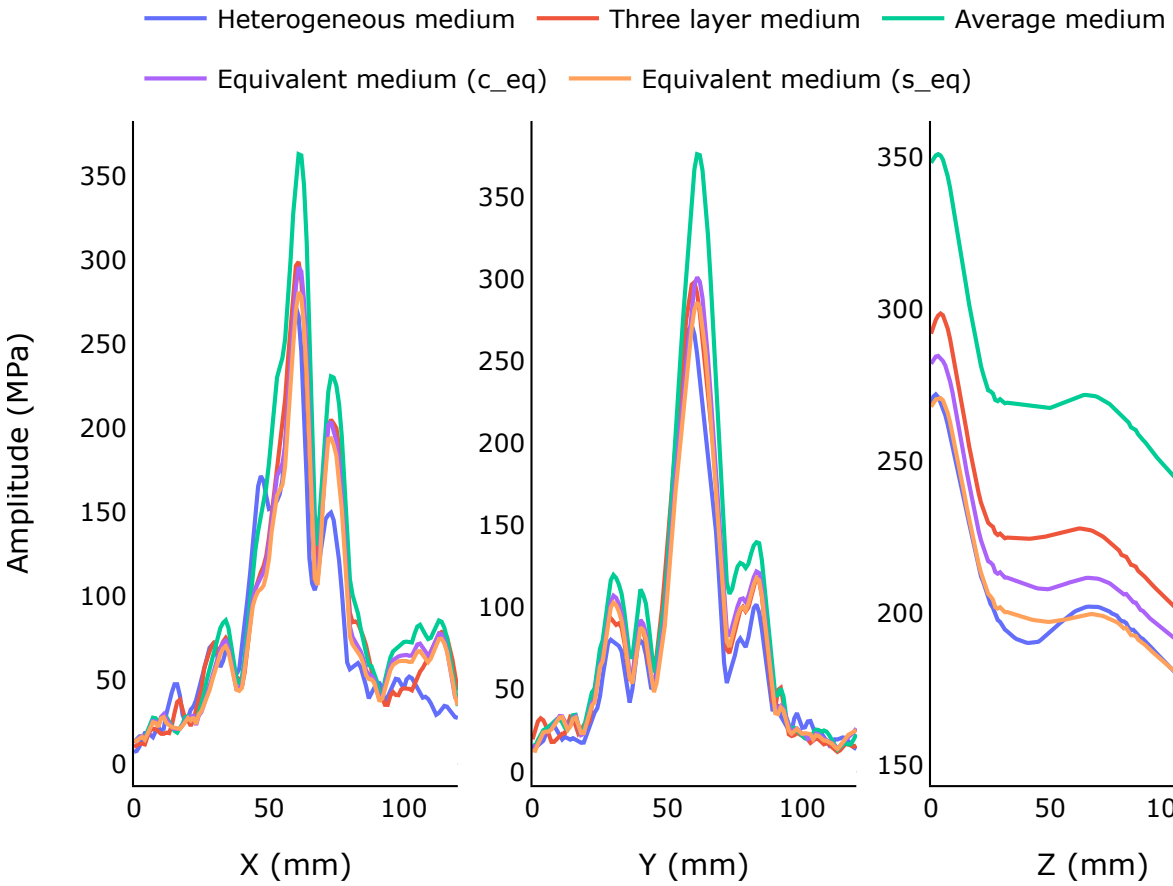


*Figure 2.12: Pressure field through the different media for the realistic configuration*

Taking the male and female skull results into account, the equivalent media are overall as close to the three layer medium as the averaged medium in terms of focal position and volume. In terms of maximum pressure, the equivalent media are always closer (by at least 25%) to the three layer medium than the averaged medium. This shows the potential of this homogenization method over the standard averaging method. However, even if for the male skull, the maximum pressure error can be small enough for some applications, for the female skull, the error is too high. This suggests that the method developed is promising but needs improvement.

#### 2.2.2.4 Discussion

The results obtained in this study confirm observations from the literature: averaging the skull acoustic properties does not have much impact on the focal spot position but leads to an overestimation of the amplitude. That is why we kept the average sound speed and tried to compensate the amplitude overestimation by tuning the equivalent density. The results are pretty satisfying, as the maximum pressure obtained with the equivalent media is always closer to the heterogeneous medium (by more than 40%) or the three layer medium (by more than 25%) than with the averaged medium, on realistic configurations. However, there is still room for improvement, as the maximum pressure error compared to the heterogeneous medium and

*Table 2.11: Pressure field results through the female skull (errors relative to the three layer medium)*

| Medium | $E_{pos}$ | $E_{amp}$ | $E_{dim}$ |
|---|---|---|---|
| Averaged | 0.35mm | 54.87% | 23.45% |
| Equivalent ($c_{eq}$) = $c_{mean}$) | 0.79mm | 18.18% | 15.57% |
| Equivalent ($c_{eq}$) = $\frac{1}{s_{mean}}$) | 0.79mm | 12.97% | 14.55% |

*Table 2.12: Pressure field results through the male skull (errors relative to the three layer medium)*

| Medium | $E_{pos}$ | $E_{amp}$ | $E_{dim}$ |
|---|---|---|---|
| Averaged | 0.94mm | 29.88% | 7.90% |
| Equivalent ($c_{eq} = c_{mean}$) | 0.61mm | 4.32% | 12.82% |
| Equivalent ($c_{eq} = \frac{1}{s_{\text{mean}}}$) | 0.61mm | 0.99% | 16.94% |

to the three layer medium is sometimes higher than 10%. An idea to improve the method would be to find the equivalent density using tools much more sophisticated than a linear regression. Another relevant point shown in this study is that the inverse of the average slowness is also a good candidate for the equivalent sound speed, and possibly better than the average sound speed. To better evaluate the homogenization method developed in this study, experiments through real skulls and through phantoms (of known geometry and acoustic properties) are needed to provide a ground truth. Such experiments would also allow to determine whether the three layer medium is a good approximation of the skull, and maybe whether it is a better approximation than the heterogeneous medium. If so, the three layer could be directly used as a skull model for semi analytical transcranial simulation methods.

## 2.3 Conclusion

We developed a realistic smooth and homogeneous skull model from a CT scan, designed for semi-analytical ultrasonic field computation algorithms. Indeed, we chose MBA to model the skull surfaces, as it ensures their smoothness while being able to capture the details of the skull geometry. We then developed a protocol to obtain these smooth and realistic surfaces from the skull CT scan. After explaining in details how to extract the skull acoustic properties from a CT scan, we developed a homogenization method. This skull acoustic property homogenization method is, to our knowledge, the first one that proposes an equivalent homogeneous skull model, other than an averaged model. This method is based on a realistic modeling of the skull as a three layer medium, taking into account the different types of skull bone (trabecular and cortical). The second step of this method builds a simple and strong surrogate model. We evaluated the homogenization method by comparing the pressure fields simulated by CIVA through the original heterogeneous media and through the homogenized one, for planar and realistic (derived from skull CT scans) configurations. Our homogenization method gives focal spot position errors similar to the averaged medium, that is to say negligible errors. In addition, it gives much lower errors, in terms of focal spot pressure, than the averaged medium. Thus, this new homogenization method provides a realistic homogeneous skull model for semi-analytical transcranial ultrasound simulation methods that will probably help them be more accurate. Besides, it could also be used by numerical methods that rely on piecewise homogeneous domains, such as the boundary element method [87].

# Chapter 3

# Fast semi-analytical transcranial ultrasonic field computation method based on time-of-flight minimization

The aim of this chapter was to develop a fast and realistic semi-analytical method to compute transcranial ultrasonic fields, using the skull model developed in chapter 2. A main drawback of semi-analytical methods, such as ray-tracing, is the bad sampling of the transducer. Indeed, in ray-tracing methods, the rays are usually cast from the computation point towards the transducer. In the case of a complex geometry such as the skull one, it may result in an unequal sampling of the transducer, due to ray arrivals being gathered in some parts of it, while other parts are shadowed. Our method, based on time-of-flight minimization to compute the ray paths aims to solve this problem. The first objective of this chapter was to develop an ultrasonic path computation method based on time of flight minimization. This method aims to resolve the unequal transducer sampling problem by imposing a regular sampling prior to the path computation. This method was then validated by applying it to compute delay laws for skull aberration correction. While this allows to validate the path computation method, it allows at the same time to show the potential of this method for skull aberration correction. The second objective of this chapter was to implement a semi analytical ultrasonic field computation algorithm using the path computation method developed. To do so, the pencil method used in CIVA had to adapted so that the ultrasonic paths are computed by time-of-flight minimization. This algorithm was then numerically validated by comparison with other solvers from the literature. Although only an experimental validation will assess the realism of our algorithm, this first validation step allows to compare our method to existing ones, among which some have already been experimentally validated, on benchmark configurations free from measurement errors. Finally, the computation time of the ultrasonic computation field algorithm was evaluated and improved.

## Contents

## 3.1 Ultrasonic path computation by time-of-flight minimization

### 3.1.1 Fermat's principle

The ultrasonic path computation method developed in this chapter is based on Fermat's principle. Fermat's principle states that the path taken by an ultrasonic ray between two given points is the path that can be traveled in the least time. Using this principle, the ultrasonic path between a source point and a computation point can be found by minimizing the time of flight. Supposing that all media are isotropic homogeneous, it comes down to finding the intersection points on each interface such that the time of flight function is minimal. Finally, the path respects, at each interface, the Snell-Descartes law.

To better understand this principle, let's think about a simple 2D example where a lifeguard standing in the sand at a point $L$ needs to save a swimmer who is drowning in the sea at a point $S$. The question is, what is the optimal trajectory for the lifeguard to save the swimmer in the least time. In each medium (air and water), the quickest path will obviously be straight on, but how to find the optimal point $I$ on the interface sand/water where the lifeguard needs to jump in the water ?

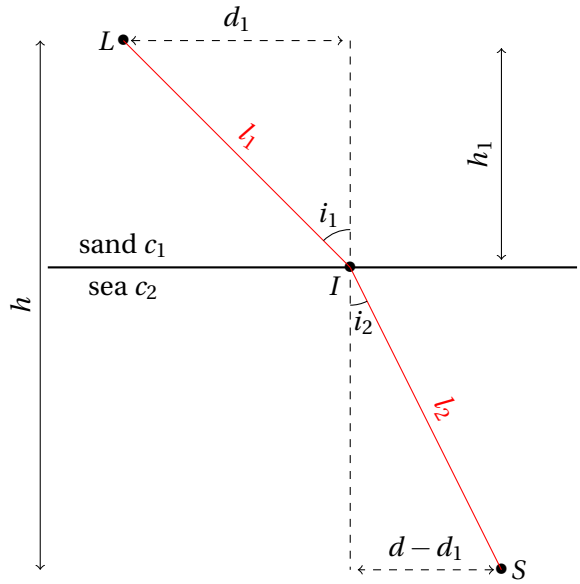


*Figure 3.1: Lifeguard problem*

Mathematically, solving this problem comes down to minimizing the time of flight function $t$, which is the sum of the flight times in medium 1 and 2:

$$t(d_1) = \frac{l_1}{c_1} + \frac{l_2}{c_2} \tag{3.1}$$

Writing $l_1$ and $l_2$ as:

$$\begin{cases} l_1 = \sqrt{d_1^2 + h_1^2} \\ l_2 = \sqrt{(d-d_1)^2 + (h-h_1)^2} \end{cases} \tag{3.2}$$

We can differentiate the time of flight function $t$ with respect to $d_1$:

$$\begin{aligned} \frac{\partial t}{\partial d_1} &= \frac{1}{c_1}\frac{\partial l_1}{\partial d_1} + \frac{1}{c_2}\frac{\partial l_2}{\partial d_1} \\ &= \frac{d_1}{l_1 c_1} - \frac{d-d_1}{l_2 c_2} \\ &= \frac{\sin(i_1)}{c_1} - \frac{\sin(i_2)}{c_2} \end{aligned} \tag{3.3}$$

$\frac{\partial t}{\partial d_1} = 0$ when $\sin(i_1)c_2 = \sin(i_2)c_1$. We recognize Snell's law. Thus, this shows, on a simple 2D example, that finding the path by minimizing the time of flight function is equivalent to applying Snell's law.

### 3.1.2 Optimization problem

In the case of an arbitrary 3D shape, the problem is very similar to the lifeguard one, but the interfaces are not planar. Modeling the interfaces using splines (or similar objects) allows to describe complex shapes and has the advantage of being a smooth geometry, unlike meshes for example which can have sharp edges. A smooth geometry is highly important to be able to use an optimization algorithm.

In the case of a homogeneous skull model, illustrated by figure 3.2, there are only two interfaces $0/1$ and $1/2$ separating three isotropic homogeneous media of slownesses $s_0$, $s_1$ and $s_2$. Thus, finding the ultrasonic path between a source point $P_s$ and a computation point $P_c$, comes down to finding the intersection points $I_{0/1}$ and $I_{1/2}$ that minimize the time of flight function:

$$\begin{cases} \min_{I_{0/1},I_{1/2}} t(I_{0/1},I_{1/2}) \\ t(I_{0/1},I_{1/2}) = ||P_s - I_{0/1}||s_0 + ||I_{0/1} - I_{1/2}||s_1 + ||I_{1/2} - P_c||s_2 \end{cases} \tag{3.4}$$

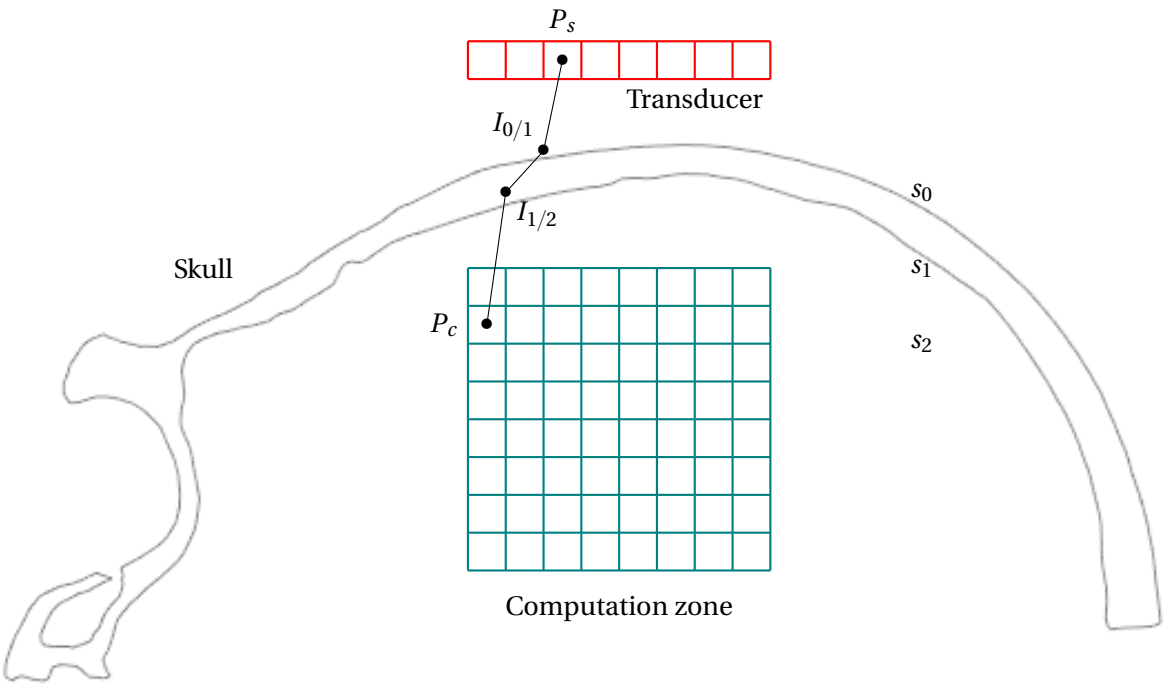


*Figure 3.2: Path computation through a skull*

As the skull is modeled with splines, the two interface surfaces can be described by a function $f(u,v) = (x,y,z)$. In our case, we use MBA surfaces (section 2.1) so we have $(u,v) = (x,y)$). Using these functions, the optimization problem can be rewritten as:

$$\begin{cases} \min_{(u,v),(w,x)} t((u,v),(w,x)) \\ t((u,v),(w,x)) = ||P_s - f_{0/1}(u,v)||s_0 + ||f_{0/1}(u,v) - f_{1/2}(w,x)||s_1 + ||f_{1/2}(w,x) - P_c||s_2 \end{cases} \tag{3.5}$$

As the functions $f_{0/1}$ and $f_{1/2}$ are differentiable, the objective function $t$ is differentiable. The gradient of the objective function is given by:

$$\nabla t = \begin{bmatrix} \frac{\partial t}{\partial u} \\ \frac{\partial t}{\partial v} \\ \frac{\partial t}{\partial w} \\ \frac{\partial t}{\partial x} \end{bmatrix} = \begin{bmatrix} s_0 \frac{\frac{\partial f_{0/1}}{\partial u}.(P_s - f_{0/1}(u,v))}{||P_s - f_{0/1}(u,v)||} + s_1 \frac{\frac{\partial f_{0/1}}{\partial u}.(f_{0/1}(u,v) - f_{1/2}(w,x))}{||f_{0/1}(u,v) - f_{1/2}(w,x)||} \\ s_0 \frac{\frac{\partial f_{0/1}}{\partial v}.(P_s - f_{0/1}(u,v))}{||P_s - f_{0/1}(u,v)||} + s_1 \frac{\frac{\partial f_{0/1}}{\partial v}.(f_{0/1}(u,v) - f_{1/2}(w,x))}{||f_{0/1}(u,v) - f_{1/2}(w,x)||} \\ s_1 \frac{\frac{\partial f_{1/2}}{\partial w}.(f_{0/1}(u,v) - f_{1/2}(w,x))}{||f_{0/1}(u,v) - f_{1/2}(w,x)||} + s_2 \frac{\frac{\partial f_{1/2}}{\partial w}.(f_{1/2}(w,x) - P_c))}{||f_{1/2}(w,x) - P_c||} \\ s_1 \frac{\frac{\partial f_{1/2}}{\partial x}.(f_{0/1}(u,v) - f_{1/2}(w,x))}{||f_{0/1}(u,v) - f_{1/2}(w,x)||} + s_2 \frac{\frac{\partial f_{1/2}}{\partial x}.(f_{1/2}(w,x) - P_c)}{||f_{1/2}(w,x) - P_c||} \end{bmatrix} \tag{3.6}$$

Computing the ultrasonic path through a skull can thus be done by solving this optimization problem.

### 3.1.3 Optimization algorithm

To solve this optimization problem, Limited-memory Broyden–Fletcher–Goldfarb–Shanno (L-BFGS) algorithm was chosen. L-BFGS is an optimization algorithm in the family of quasi-Newton methods that approximates the BFGS algorithm using a limited amount of computer memory. The advantage of L-BFGS over BFGS is its "limited-memory" feature which allows it to approximate the Hessian using a limited amount of memory. More details on this optimization method can be found in [8].

Newton and quasi Newton optimization algorithms are well suited for non-linear unconstrained problems with a smooth and differentiable objective function, which is the case here. Newton and quasi Newton methods are second order optimization methods, as they use the Hessian matrix (second order derivatives) instead of the gradient (first order derivatives), and converge thereby faster compared to first-order optimization algorithms like gradient descent. Their use of curvature information allows for more direct progress towards the optimum. Unlike Newton's method, quasi Newton methods use an approximation of the Hessian matrix, as using the exact one can be computationally expensive and may introduce numerical instability. Thus, the interest of quasi-Newton methods is that they benefit from second-order information (Hessian approximations) without the computational cost of explicitly calculating the Hessian. In addition, instead of storing the full Hessian matrix ($O(n^2)$), quasi Newton methods only need to store a few vectors ($O(nm)$) in memory, where $n$ is the number of parameters and $m$ is the number of previous iterations used to approximate the Hessian.

A C++ implementation of L-BFGS found on GitHub was used (https://github.com/twesterhout/lbfgs-cpp). The minimization algorithm takes as input an evaluation function that gives the value of the objective function and the gradient, parameters for the stopping criteria and a first guess.

### 3.1.4 First guess

As every optimization algorithm, L-BFGS needs to be provided a first guess to start the optimization. In our case, the straight path is taken as an initial guess path. To obtain the intersection points of the straight path, we cast a ray from the computation point in the direction of the transducer point using Embree C++ library. The ray is cast on the triangular meshes of the inner and outer surfaces of the skull. The ray casting function gives us, for each one of the two meshes, the intersected triangle and the local 2D coordinates $(u_{local}, v_{local})$ of the hit. This data is used to compute the global 2D coordinates $(u_{global}, v_{global})$ of the hit by interpolation using:

$$(u_{global}, v_{global}) = (1. - u_{local} - v_{local})v_0 + u_{local}v_1 + v_{local}v_2; \tag{3.7}$$

where $(v_0, v_1, v_2)$ are the 2D coordinates of the intersected triangle vertices.
The pair of 2D coordinates $(u_{global}, v_{global}, w_{global}, x_{global})$ is the initial guess given to L-BFGS.

## 3.2 Validation of the path computation method by application to delay laws computation for skull aberration correction

The path computation method developed was first validated alone by using it to compute delay laws to correct skull aberrations.

### 3.2.1 Aberration correction using delay laws

Some transducers are naturally focused because of their shape. For instance, on a hemispherical transducer, every point of the transducer is at the same distance to the center of curvature. Thus, if the medium is isotropic homogeneous, all the ultrasonic contributions will arrive at the same time at this point and will induce constructive interferences. Alternatively, a planar phased array transducer can be used to focus at a given point, by choosing emitting delays for each element, so that all the ultrasonic contributions arrive at this point at the same time. This is called a delay law. In the case of a isotropic homogeneous medium, delay laws can be easily geometrically computed. However, when there is an aberrating medium between the chosen focus and the transducer, the delay law computation is a bit more complex, as the delays have to take into account the real acoustic path between the center of each element and the focal point, accounting for the geometry and the sound speeds of the propagating media. Usually, delay law computations are based on simulation. The desired focus point is used as a virtual source and the field emitted by this source is

computed on the transducer surface. Then, two methods can be used: time reversal or cross-correlation. Time reversal theory states that if the medium is approximately linear (not too lossy or noisy), given a solution to the wave equation, then the time reversal of that solution is also a solution. This is due to the fact that the standard wave equation only contains even order derivatives. Thus, the time-reversed received signals can be back-propagated to focus at the desired location. The other method takes a reference element and finds the delays $\tau_i$ for all other elements $i$ that maximize the cross correlation function:

$$p_{\text{ref}}.p_i(\tau_i) = \int p_{\text{ref}}(t)p_i(t+\tau_i)dt \tag{3.8}$$

where $p_{\text{ref}}$ and $p_i$ are the received signals of the reference element and element $i$. A similar method is used in CIVA for the computation of delay laws in complex configurations. These simulation based methods are very precise, yet quite computation time expensive. Alternatively, methods such as ray-tracing are used to compute delay laws. The rays are assumed to be straight (refraction effects are neglected), but the various sound speeds of the media crossed by the ray are taken into account in the delay computation. This method is less precise but way faster. The path computation method described in section 3.1 can be used to compute delay laws, in a precise yet fast way. Indeed, the exact paths can be computed without computing the whole acoustic field. We called this method SplineRay.

### 3.2.2 Delay law computation by time-of-flight minimization (SplineRay)

Given a focus position $(x_f, y_f, z_f)$, and a multi-element transducer with $N$ elements, the delay laws are computed this way:

- Compute the ultrasonic paths by time-of-flight minimization between $(x_f, y_f, z_f)$ and the center of each transducer element $i \in \{1, ..., N\}$.
- Compute the associated flight times $t_i$, $\forall i \in \{1, ..., N\}$.
- Compute the maximum flight time $t_{max} = \max_{i\in\{1,...,N\}} t_i$.
- The delay of each element $i \in \{1, ..., N\}$ is given by $\tau_i = t_{max} - t_i$.

### 3.2.3 Numerical evaluation of SplineRay by comparison with other methods

SplineRay was evaluated by comparison of simulated pressure fields through a skull sample using different delay laws:

- Nominal delay laws: as if there was no aberrating medium, $\forall i \in \{1, ..., N\}$, $t_i = \frac{d_i}{c_{water}}$, $\tau_i = t_{max} - t_i$, with $d_i$ the distance between the focus position and the center of element $i$.
- Ray-tracing delay laws: computed by straight ray tracing.
- SplineRay delay laws: computed by time-of-flight minimization.
- CIVA delay laws: computed by CIVA field computation and cross correlation.

A transducer of $32 \times 32$ elements operating at 1MHz was used for the simulations. The skull mesh was taken from [10], as well as the properties of cortical bone. The transducer position of configuration BM7 [10] was simulated. Two focus positions were simulated. The first one $F1$ was around 30mm away along the transducer normal (the $Z$ axis) and centered. The other one $F_2$ was shifted by 20mm along the $X$ axis (direction parallel to the transducer). The simulations were performed with both CIVA and SplineBeam (which is the field computation method developed in section 3.3). We used these two simulation methods to be more objective. Indeed, CIVA pressure fields and laws are computed with the same method and use a skull mesh. Likewise, SplineBeam pressure fields and SplineRay laws are based on the same path computation method and use smooth skull surfaces. Thus, it is expected that CIVA laws will perform better than SplineRay laws when the pressure fields are simulated with CIVA, and that SplineRay laws will perform better than CIVA laws when the pressure fields are simulated with SplineBeam.

For the sake of brevity, only SplineBeam simulated fields are displayed, but metrics for the two simulation methods (CIVA and SplineBeam) will be compared. The pressure field profiles simulated by SplineBeam for

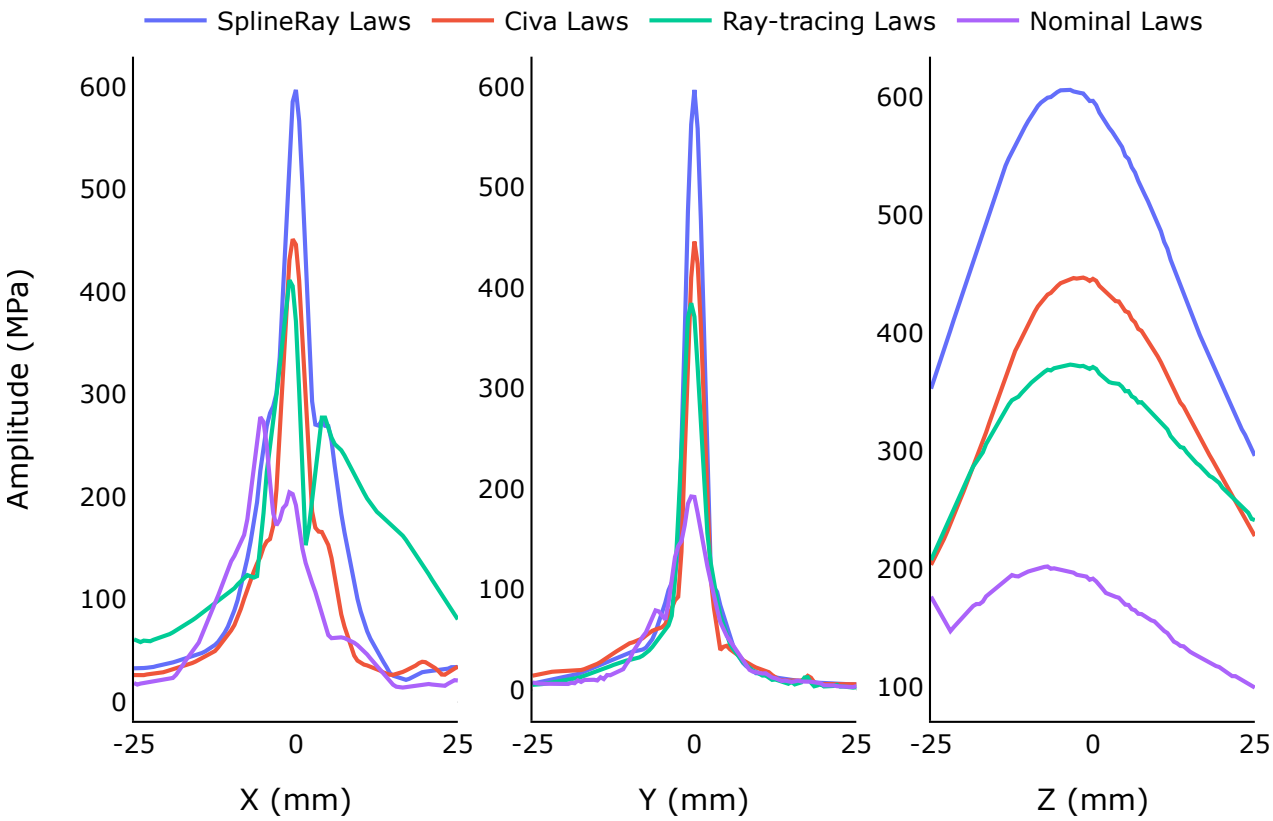


*Figure 3.3: SplineBeam pressure field profiles obtained with several delay law methods for focus position $F_1$*

each delay law method are displayed in figure 3.3 for focus position $F_1$ and in figure 3.4 for focus position $F_2$.

The plots show that all delay laws (Ray-tracing, CIVA and SplineRay) allow to focus near the desired location, unlike the default Nominal law. All delay law methods also allow to restored much more pressure at the focus than the Nominal law. SplineRay and CIVA laws manage to remove the side lobes for focus position $F_1$. The highest pressure at the focus is obtained with SplineRay laws, followed by CIVA laws. It provides a first confirmation to the hypothesis that SplineRay laws perform better than CIVA laws when the pressure fields are simulated with SplineBeam.

For all these simulations (with SplineBeam and CIVA), we computed the following metrics:

- The shift of maximum pressure compared to the desired focus location:

$$\Delta X = (x_f, y_f, z_f) - (x_{max}, y_{max}, z_{max}) \tag{3.9}$$

  where $(x_{max}, y_{max}, z_{max})$ is the position of the maximum pressure.

- The percentage of pressure at focus with method $m \in \{\text{Ray-tracing}, \text{CIVA}, \text{SplineRay}\}$ compared to nominal laws:

$$r_P = 100 \frac{P^m(x_f, y_f, z_f)}{P^n(x_f, y_f, z_f)} \tag{3.10}$$

  where $P^n$ is the pressure obtained with the nominal law and $P^m$ obtained with method $m \in \{\text{Ray-tracing}, \text{CIVA}, \text{SplineRay}\}$.

The metrics obtained for all simulations are summarized in table 3.1.

The results are very satisfying as SplineRay laws always allow to restore a pressure at the focus that is at least two times higher than the one without aberration correction (Nominal laws). Likewise, the maximum pressure is always reached at a distance to the focus point lower than 5mm, which is very low compared to the focus shifts which are higher than 20mm without aberration correction. In addition, the focus is mainly shifted in the ultrasound propagation direction (along the $Z$ axis).

As expected, CIVA laws perform better than SplineRay laws when the pressure fields are simulated with CIVA, and SplineRay laws perform better than CIVA laws when the pressure fields are simulated with

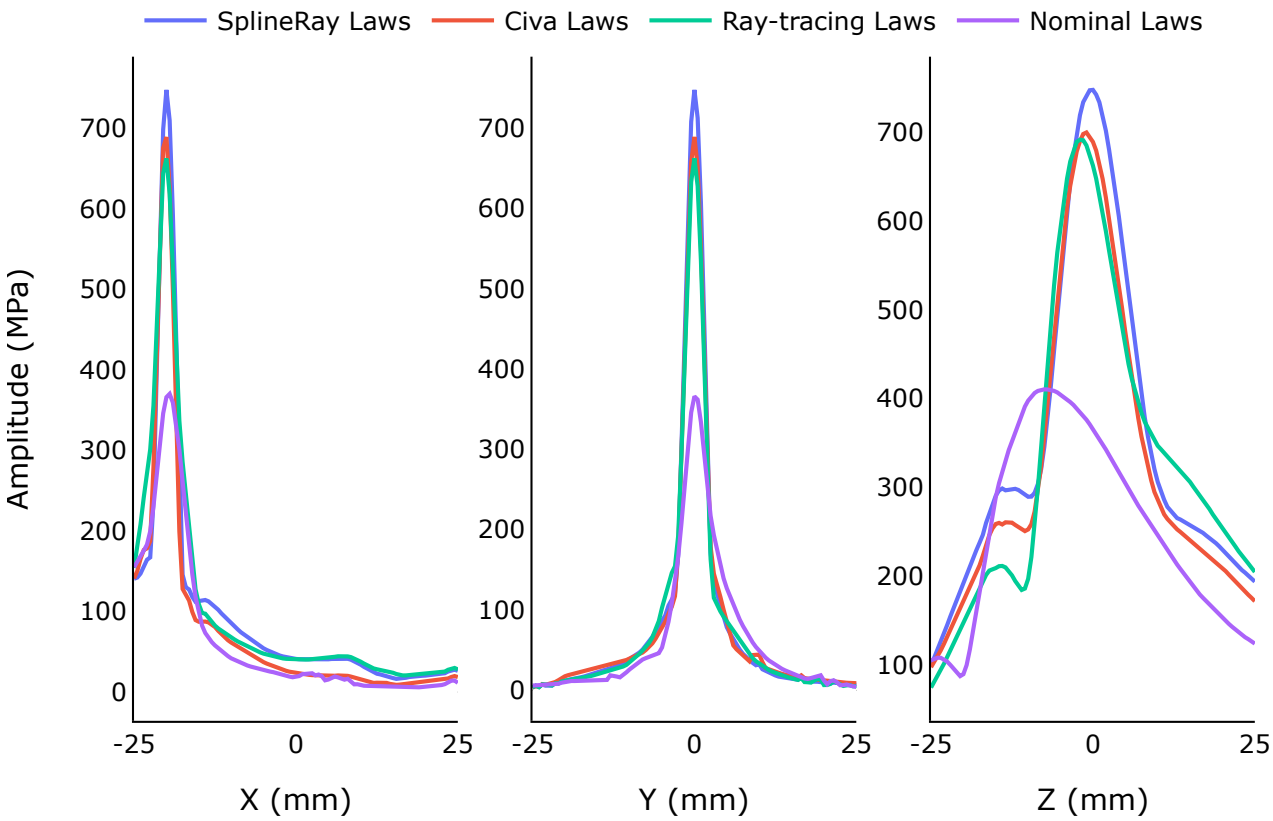


*Figure 3.4: SplineBeam pressure field profiles obtained with several delay law methods for focus position $F_2$*

SplineBeam. This is true both in terms of restored pressure and focus shift. However, CIVA laws allow to focus in average (on both simulation methods and focus positions) closer to the desired focus than SplineRay laws (by around 0.75mm), while SplineRay laws allows to restore more pressure at the desired focus than CIVA laws (by more than 20%). Thus both methods can be considered equivalent, but depending on the use case, one of them would be more appropriate. Indeed, if the main concern is the restored pressure at focus, SplineRay laws would be the best choice, whereas if the main concern is the maximum pressure position, CIVA laws would be the best choice. When both metrics are important, SplineRay would be the best choice as it provides equivalent focusing to CIVA laws, but at a lower cost. Indeed, CIVA laws require a whole field computation to be performed while SplineRay laws only compute the ultrasonic paths.

Ray-tracing laws are always outperformed by SplineRay and CIVA laws, both in terms of maximum pressure position (by in average around 5mm) and in terms of restored pressure at focus (by in average around 50%). It shows the importance of taking refraction effects into account for aberration correction.

## 3.3 SplineBeam: ultrasonic field computation method

We developed a new ultrasonic field computation method, based on the path computation method developed in section 3.1. This field computation method is very similar to a ray-tracing method, apart from the path computation. Instead of casting rays from the computation point and keeping the ones that reach the transducer surface, like what is done is CIVA for example, here the transducer is sampled and the path between each transducer source point and the computation point is found by time of flight minimization. In both cases, the temporal contributions of all considered ray paths are summed up to obtain the impulse response of the acoustic field. The advantage of such a method is that it allows a regular sampling of the transducer. It is defined before the path computations and the same number of paths is computed for each sample, which is not the case with ray-tracing.

### 3.3.1 From the pencil method to SplineBeam

The pencil method, which is the method used in CIVA, was first introduced by Nicolas Gengembre [7] to compute ultrasonic fields for non-destructive testing applications. In this method, the wavefront is cut into pencils. A pencil is a collection of rays travelling from a source point and diverging slightly. It is composed

*Table 3.1: Comparison of focusing metrics of simulated (with CIVA or SplineBeam) pressure fields through a skull with different delay laws*

| **Focus** | | $F_1$ | | $F_2$ | |
|---|---|---|---|---|---|
| **Metric** | **Simu** / **Law** | **CIVA** | **SplineBeam** | **CIVA** | **SplineBeam** |
| $\Delta X$ (mm) | **Nominal** | (-4, -2, -28) | (-4.5, -1.5, -22.5) | (3.5, -0.5, -23) | (3.5, -0.5, -23.5) |
| | **Ray-tracing** | (-2.5, -0.5, -11.5) | (-1,-0.5, -4) | (1.5, 0, -8.5) | (1.5, 0, -7.5) |
| | **CIVA** | (-0.5, 0, -3) | (-0.5, 0,-3.5) | (0, 0, -1) | (0.5, 0, -3) |
| | **SplineRay** | (0, 0, -5) | (0, 0, -3.5) | (0.5, 0, -2.5) | (0.5, 0, -2.5) |
| $r_P$ | **Nominal** | 100.00% | 100.00% | 100.00% | 100.00% |
| | **Ray-tracing** | 163.18% | 193.46% | 194.41% | 180.98% |
| | **CIVA** | 236.65% | 232.38% | 221.05% | 188.24% |
| | **SplineRay** | 230.73 % | 310.97% | 220.67 % | 204.23% |

of an axial ray, following the geometrical path, and the paraxial rays, belonging to the envelope of the pencil. The pencil method allows to compute the divergence factor $DF$, by computing the cross-section $dS$ of the pencil as a function of the initial solid angle $d\Omega$. The propagation of the pencils is done by computing propagation and interaction matrices for every material and interface encountered by the pencils. The propagation of a pencil is illustrated in figure 3.5.

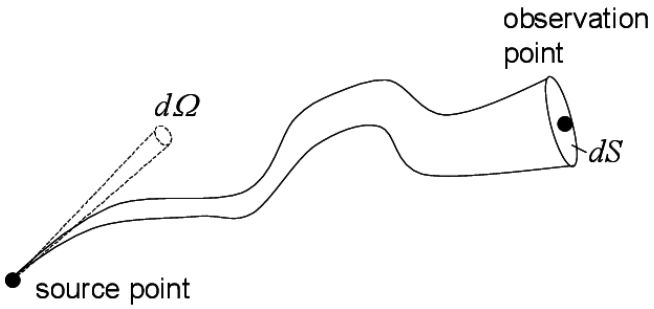


*Figure 3.5: Propagation of a pencil from [88]*

The pencil method was later adapted by Hamza Chouh [21], during his PhD at CEA List (Saclay, France), for performance purposes, to avoid computing the propagation and interaction matrices. Instead, the paraxial rays of every pencil are cast, using Intel Embree ray-tracing library, so as to reconstitute their contribution. The axial ray and paraxial rays of a pencil are illustrated in figure 3.6.

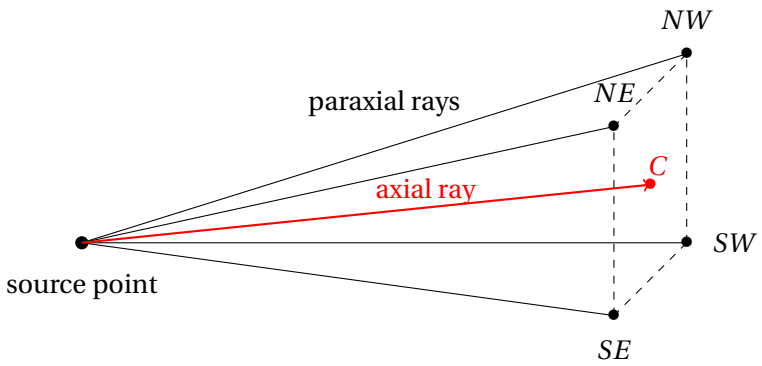


*Figure 3.6: A pencil with its axial ray and paraxial rays*

We adapted the pencil method to our path computation method. The principle is very similar to the one proposed by Hamza Chouh, but instead of casting rays to compute the paths, they are found by time of flight minimization. The advantage of computing the ultrasonic paths by time-of-flight minimization over using ray-tracing, is that each path is defined between two points and not from a point. Thus, the transducer can be sampled into small squared surfaces, and we can compute a pencil and an impulse response for each sample.

### 3.3.2 Transducer sampling

A code from CIVA is used to sample any shape of transducer. It gives, for each sample, the coordinates of its center $C$, its area $dS$ and its normal vector $n = (n_x, n_y, n_z)$.

For each sample, 5 paths are computed: 1 for the sample center (axial ray in the pencil method) and 4 for the sample corners (paraxial rays in the pencil method). The transmission coefficient is computed for the axial ray, and the paraxial rays help computing the divergence coefficient and the time spread of the impulse response.

To be able to compute the paraxial rays, the corner coordinates need to be computed. They are approximated as the corners of a square of center $C$, of area $dS$ and in the plane of normal vector $(n_x, n_y, n_z)$.

To do so, an arbitrary orthonormal basis $(u, v, n)$ is build using:

$$\begin{cases} u = \begin{cases} (n_y, -n_x, 0) \text{ if } n_y \neq n_x \neq 0 \\ (1,0,0) \end{cases} \\ v = n \times u \end{cases} \tag{3.11}$$

Then, the corner points $NE$, $NW$, $SW$, $SE$ are computed with the following equations:

$$\begin{cases} NE = C + \frac{\sqrt{dS}}{2}\frac{u}{||u||} + \frac{\sqrt{dS}}{2}\frac{v}{||v||} \\ NW = C - \frac{\sqrt{dS}}{2}\frac{u}{||u||} + \frac{\sqrt{dS}}{2}\frac{v}{||v||} \\ SW = C - \frac{\sqrt{dS}}{2}\frac{u}{||u||} - \frac{\sqrt{dS}}{2}\frac{v}{||v||} \\ SE = C + \frac{\sqrt{dS}}{2}\frac{u}{||u||} - \frac{\sqrt{dS}}{2}\frac{v}{||v||} \end{cases} \tag{3.12}$$

This approximation is exact in the case of a planar rectangular transducer whose sides are colinear with $u$ and $v$, as illustrated in figure 3.7.

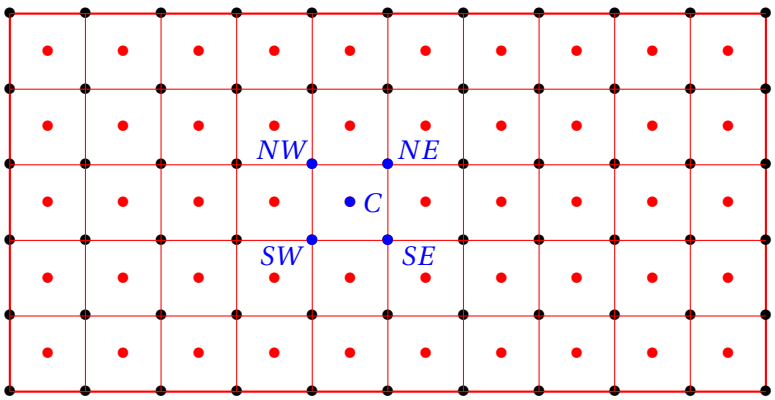


*Figure 3.7: Example of the sampling of a rectangular planar transducer*

### 3.3.3 Computing impulse response

For each transducer sample, the axial $C$ and paraxial ($NW$, $NE$, $SE$, $SW$) rays are computed by minimizing the time of flight function. From these path computations, the following is computed:

- The minimum $t_{min}$ and maximum $t_{max}$ times of flight over the five pencil rays.
- The initial directions of the paraxial rays ($R_{NW}$.dir, $R_{NE}$.dir, $R_{SE}$.dir, $R_{SW}$.dir).
- The initial polarization of the axial ray $R_c$.pol.
- The total Fresnel transmission coefficient $T_A$ of the axial ray [9].

The paraxial ray initial directions are used to compute the surface $d_\Omega$ of the unitary pencil:

$$\begin{cases} E_n = R_{NW}.\text{dir} - R_{NE}.\text{dir} \\ E_w = R_{NW}.\text{dir} - R_{SW}.\text{dir} \\ E_s = R_{SE}.\text{dir} - R_{SW}.\text{dir} \\ E_e = R_{SE}.\text{dir} - R_{NE}.\text{dir} \\ d\Omega = \frac{1}{2}||E_n \times E_e + E_s \times E_w|| \end{cases} \tag{3.13}$$

Which is itself used to compute the beam divergence factor $DF$:

$$DF = \frac{s_0}{2\pi\sqrt{\frac{dS}{d\Omega}}} \tag{3.14}$$

Finally, the impulse response parameters are computed:

- The minimum and maximum times of flight of the impulse response:

$$\begin{cases} t_{min\_samp} = (\tau_{el} + t_{min}) * Fs \\ t_{max\_samp} = (\tau_{el} + t_{max}) * Fs \end{cases} \tag{3.15}$$

  where $\tau_{el}$ is the delay of the transducer element containing this sample and $F_s$ is the sampling frequency.

- The amplitude $A_{IR}$ of the impulse response:

$$A_{IR} = \frac{A_0 \times DF \times T_A \times dS \times A_{el}}{t_{max\_samp} - t_{min\_samp}} \tag{3.16}$$

  where $A_0$ is the input amplitude, $dS$ is the sample surface and $A_{el}$ is the amplitude law of the transducer element containing this sample.

- The polarization $p$:

$$p = R_c.\text{pol} \tag{3.17}$$

### 3.3.4 Computing signal size

Before actually summing the impulse responses, the signal size is computed. To do so, the minimum and maximum times of flight $\min(t_{min})$ and $\max(t_{max})$ over all transducer samples are computed. Then the maximum delay $\tau_{max}$, over all transducer elements is computed. Finally the size of the output signal $s_{out}$ is computed as the next power of 2 of the sum of the input signal size and the spread of all impulse responses:

$$\text{size}(s_{out}) = 2^{\lceil \log_2(\text{size}(s_{in}) + (\max(t_{max}) + \tau_{max} - \min(t_{min}))F_s) \rceil} \tag{3.18}$$

where $F_s$ is the sampling frequency and "size" is a function that gives the number of elements of an array.

This allows to allocate the needed memory for the output signal. The FFT of the input signal is also computed and stored for later use.

### 3.3.5 Summing impulse responses

The impulse responses of all transducer samples are then summed. They are summed separately for the real and imaginary part of the 3 components of the displacement or pressure field. An example code is given in appendix D.

To know at which index the impulse response needs to be added, the minimum and maximum time sample indices $n_1$ and $n_2$ are computed:

$$\begin{cases} n_1 = \lfloor t_{min\_samp} \rfloor - \min(t_{min})F_s \\ n_2 = \lfloor t_{max\_samp} \rfloor - \min(t_{min})F_s \end{cases} \tag{3.19}$$

The delay $d_1$ between $n_1$ and the start of the impulse response, and the delay $d_2$ between $n_2$ and the end of the impulse response are computed:

$$\begin{cases} d_1 = t_{min\_samp} - (n_1 + \min(t_{min})F_s)) \\ d_2 = t_{max\_samp} - (n_2 + \min(t_{min})F_s) \end{cases} \tag{3.20}$$

If the impulse response is longer than a time sample, i.e. $n_1 < n_2$ et $t_{max\_samp} - t_{min\_samp} > \epsilon$, then:

- The impulse response of amplitude $A_{IR}$ is added to all time samples between $n_1$ and $n_2$.

- The impulse response of amplitude $(1 - d_1)A_{IR}$ is added to the $n_1$ sample.

- The impulse response of amplitude $d_2 A_{IR}$ is added to the $n_2$ sample.

Otherwise, the impulse response is considered as a Dirac, thus the amplitude is multiplied by $(t_{max\_samp} - t_{min\_samp})$ to avoid the division by a number close to zero:

- The impulse response of amplitude $(1-d_{moy})A_{IR}(t_{max\_samp} - t_{min\_samp})$ is added to the $n_1$ sample.
- The impulse response of amplitude $d_{moy}A_{IR}(t_{max\_samp} - t_{min\_samp})$ is added to the $n_2$ sample.

where $d_{moy} = (d_1 + d_2)/2$

The various variables are illustrated by figure 3.8.

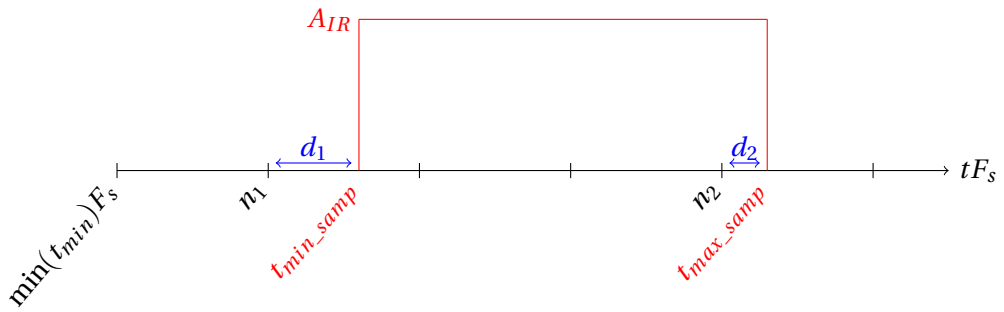


*Figure 3.8: Impulse response of amplitude $A_{IR}$ between $t_{min\_samp}$ and $t_{max\_samp}$*

### 3.3.6 Signal convolution and output signal computation

For each transducer element, the impulse response of the transmitted field is obtained by summing the impulse responses of all its samples. Then, it can be convoluted, in the Fourier domain, with the input signal to obtain the various components of the acoustic field. Finally, the contributions of all the elements are summed up, applying the delay and amplitude laws, to obtain the total field transmitted by the whole transducer. The final output signal is then computed.

- For a displacement field, the output signal sig_dis is computed as:

$$\text{sig\_dis} = \sqrt{\text{sig\_dis\_x}^2 + \text{sig\_dis\_y}^2 + \text{sig\_dis\_z}^2} \tag{3.21}$$

  where (sig_dis_x, sig_dis_y, sig_dis_z) are the three components of the displacement field.

- For a pressure field, the output signal sig_pres is computed as:

$$\text{sig\_pres} = (\text{sig\_pres\_S1} + \text{sig\_pres\_S2} + \text{sig\_pres\_S3})/3 \tag{3.22}$$

  where (sig_pres_S1, sig_pres_S2, sig_pres_S3) are the three components of the pressure field.

To compute the maximum of the output signal, the maximum of the envelope is computed.

### 3.3.7 Attenuation computation

The algorithm allows to model media with frequency dependent attenuation.

For each medium $k$, the frequency dependent attenuation is given by:

$$\alpha_k(f) = \alpha_k^0 d_k \left(\frac{f}{f_k^0}\right)^{\beta_k} \tag{3.23}$$

where $\beta_k \geqslant 0$, $d_k$ is the distance traveled by the ray in medium $k$, and $(f_k^0, \alpha_k^0) \in \mathbf{R}^2$ are the constants such that $\alpha_k(f_k^0) = \alpha_k^0$.

The total attenuation of a ray traveling through $N \geqslant 1$ media is given by:

$$\alpha(f) = \sum_{k=1}^{N} \alpha_k d_k \left( \frac{f}{f_k^0} \right)^{\beta_k} \tag{3.24}$$

When no attenuation is taken into account, the impulse responses are summed in the temporal domain and the FFT is performed afterwards. To include frequency dependant attenuation without shooting up the computation time, the FFT of each impulse response is computed and the attenuation is applied at the same time, then, by linearity of the Fourier transform, these frequency signals are summed.

As the impulse responses are rectangular signals, the analytical Fourier transform is computed using the sinc function. Indeed, the Fourier transform of a unitary rectangular signal centered at $0$ and of duration $\Delta t$ is given by:

$$\mathscr{F}(\mathbb{1}_{[-\frac{\Delta t}{2}, \frac{\Delta t}{2}]}) = \mathrm{sinc}(\pi f \Delta t) = \frac{\sin(\pi f \Delta t)}{\pi f \Delta t} \tag{3.25}$$

Taking into account the shift of $T_0$ and the amplitude $A_{IR}$ of the impulse response:

$$\mathscr{F}(A_{IR}\mathbb{1}_{[T_0-\frac{\Delta t}{2}, T_0+\frac{\Delta t}{2}]}) = \mathrm{sinc}(\pi f \Delta t) exp(-2\pi f T_0) \tag{3.26}$$

with $T_0 = \frac{(t_{max} - \min(t_{min})) + (t_{min} - \min(t_{min}))}{2}$ and $\Delta t = t_{max} - t_{min}$.

Then, a multiplication by $exp(-\frac{ln(10)}{20}\alpha(f))$ is performed to apply attenuation,

Instead of computing the frequency signals for each frequency $f \in [0, \frac{F_s}{2}[$, they are computed only in the bandwidth of the input signal. The bandwidth is computed by finding highest index $id_{min}$ and the lowest index $id_{max}$ such that:

$$\begin{cases} \forall i \in [0, id_{min}], |\mathscr{F}(s_{in})[i]| < 0.01 \max_i |\mathscr{F}(s_{in})| \\ \forall i \in [id_{max}, N], |\mathscr{F}(s_{in})[i]| < 0.01 \max_i |\mathscr{F}(s_{in})| \end{cases} \tag{3.27}$$

Doing so, the frequencies for which the input frequency signal module is lower than $1\%$ of its maximum, are not taken into account.

### 3.3.8 Harmonic computation

The algorithm also allows harmonic computations. For harmonic computations, the code is very similar except that only one frequency is considered. Thus the computation is much quicker than for the broadband case.

## 3.4 Numerical validation of the field computation algorithm

### 3.4.1 Benchmark configurations

The field computation algorithm, called SplineBeam, was first numerically validated by comparison with other solvers from the literature, thanks to the very useful benchmark study by Aubry et al. [10]. This study compares $11$ solvers (including k-Wave) on $9$ benchmark configurations with $2$ different transducers: a focused bowl (sc1) and a plane piston (sc2). Both transducers operate at $500$kHz. In the first two configurations, pressure fields in water (with and without artificial attenuation) are simulated. In configurations n°3 to 6, pressure fields through bone layers of analytical shapes (flat layers or spherical layers) are simulated. Finally, in configurations n°7 to 9, pressure fields through skull samples, whose meshes are provided, are computed. All media are considered homogeneous or piecewise homogeneous. All computations are harmonic and neglect non linear effects and elastic waves.

SplineBeam was run on all benchmark configurations, except on the ones with more than $3$ media, that is to say the ones including a layer of skin or trabecular bone: benchmark n°$4$ and $6$. Indeed, SplineBeam is so far unable to compute a pressure field through more than two surfaces and thus through more than three media. In addition, as SplineBeam can so far only compute the field in the third medium, the computation zones were reduced to the focal spot.

### 3.4.2 General results

For all benchmark configurations on which SplineBeam was run, the focus position difference $\Delta X_{max}$ and maximum amplitude difference $\Delta P_{max}$ relative to k-Wave are displayed in table 3.2. k-Wave was chosen for the comparison, as it is considered as the reference in this study. The average differences, on the ten other solvers (other than k-Wave) relative to k-Wave, are also displayed for reference.

*Table 3.2: Comparison of SplineBeam (SB) errors relative to k-Wave and other solvers (Others) average errors on the benchmark configurations proposed by Aubry et al. [10]*

| Config | Material | Shape | $\Delta X_{max}$(mm) | | $\Delta P_{max}$(%) | |
|---|---|---|---|---|---|---|
| | | | SB | Others | SB | Others |
| BM1-SC1 | Water | None | 0.00 | 0.10 | 0.07 | 0.39 |
| BM1-SC2 | Water | None | 0.00 | 0.00 | 1.31 | 0.22 |
| BM2-SC1 | Water[a] | None | 0.50 | 0.15 | 0.03 | 0.37 |
| BM2-SC2 | Water[a] | None | 0.00 | 0.00 | 0.42 | 0.35 |
| BM3-SC1 | Bone | Flat | 0.00 | 0.50 | 4.21 | 4.77 |
| BM3-SC2 | Bone | Flat | 0.00 | 0.00 | 0.27 | 5.36 |
| BM5-SC1 | Bone | Sphere | 1.00 | 0.35 | 7.29 | 3.77 |
| BM5-SC2 | Bone | Sphere | 0.50 | 0.00 | 2.58 | 6.30 |
| BM7-SC1 | Bone | Skull | 0.00 | 0.21 | 4.46 | 5.77 |
| BM7-SC2 | Bone | Skull | 0.50 | 0.15 | 5.11 | 4.48 |
| BM8-SC1 | Bone[b] | Skull | 1.50 | 0.66 | 2.80 | 5.92 |
| BM8-SC2 | Bone[b] | Skull | 1.00 | 0.19 | 4.25 | 7.80 |
| BM9-SC1 | Bone[b] | Skull | 1.00 | 0.29 | 1.37 | 5.85 |
| BM9-SC2 | Bone[b] | Skull | 1.12 | 0.48 | 3.43 | 5.87 |

[a]Water with attenuation.
[b]With brain inside the skull.

The comparison of SplineBeam with other solvers (table 3.2) is overall satisfying. The focus position difference between SplineBeam and k-Wave is always less than 1.50mm and the maximum pressure difference is always less than 8%.

The comparison of SplineBeam and k-Wave pressure fields for all configurations (BM1-SC1, BM1-SC2,BM2-SC1, BM2-SC2,BM3-SC1, BM3-SC2,BM5-SC1, BM5-SC2,BM7-SC1, BM7-SC2,BM8-SC1, BM8-SC2,BM9-SC1, BM9-SC2) are plotted in appendix E. A few of these comparison plots are displayed below for the reader to visualize the results while reading the interpretation.

In addition boxplots are displayed in appendix E, to show SplineBeam field characteristics compared to all other solvers. These boxplots show that SplineBeam maximum pressure position error relative to k-Wave is as low as half of the solvers for the flat geometries (configurations n°1 to 3), but higher than half of the solvers for more complex geometries (sphere and skull). This is due to the fact that the smooth skull model used by SplineBeam is different to the "grid model" used by most models for these geometries. Because of this, SplineBeam is one of the solvers that gives the biggest focal position error relative to k-Wave, together with CIVA and HAS. When all solvers are compared to SplineBeam on the maximum pressure position, we notice that the differences are bigger for source sc1, probably because of its non-flat geometry, which is thus modeled differently depending on the simulation method. The maximum pressure position difference is the lowest when SplineBeam is compared to MSOUND and j-Wave (but this is biased as j-Wave was not run on the configurations through skull samples). For the maximum pressure error compared to k-Wave, SplineBeam is almost always "in the box" that is to say that its error compared to k-Wave is lower than half of the other solvers, for all benchmarks.

### 3.4.3 Water configuration results

The comparison of k-Wave and SplineBeam pressure fields for configuration BM1-SC1 is shown as an example in figures 3.9 and 3.10.

Qualitatively, the pressure fields seem very similar. For the 4 configurations in water, both metrics are very low ($\Delta X_{max} \leqslant 0.5$mm and $\Delta P_{max} \leqslant 1.31\%$), which shows that SplineBeam simulates well the ultrasound

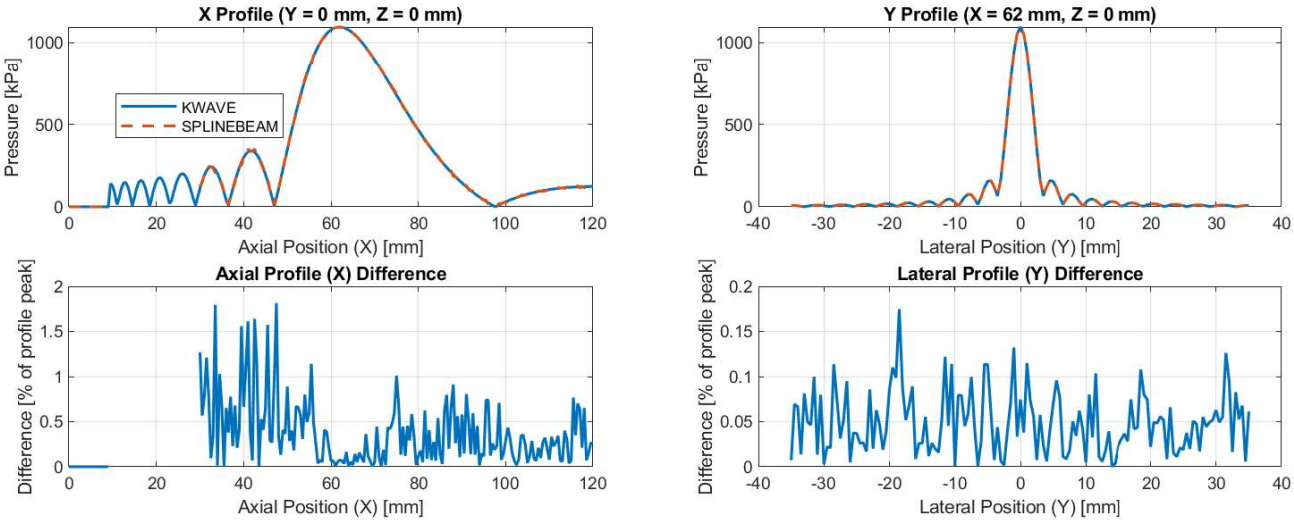


*Figure 3.9: Comparison of SplineBeam and k-Wave pressure field profiles for configuration BM1-SC1*

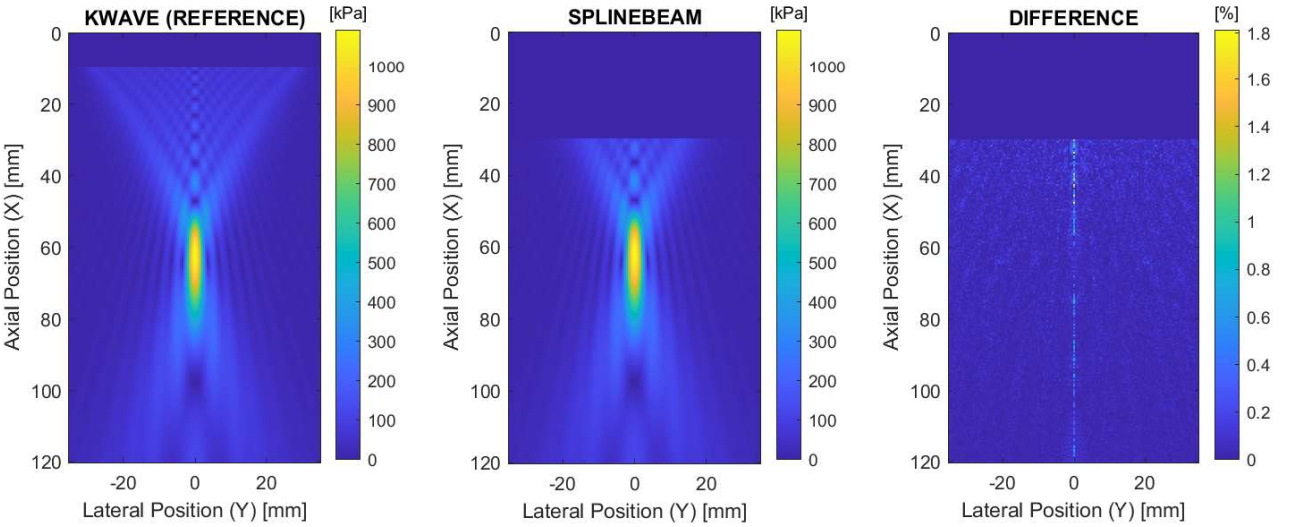


*Figure 3.10: Comparison of SplineBeam and k-Wave pressure field XY planes for configuration BM1-SC1*

propagation in very simple media. There is only a focus position difference of 0.5mm for configuration BM2-SC1, which is equal to the spatial step of the computation zone used for SplineBeam. The error could be due to the difference of geometry of the source n°1, which is analytic with SplineBeam and grid projected with k-Wave.

### 3.4.4 Analytical shape configuration results

The comparison of k-Wave and SplineBeam pressure fields for configuration BM3-SC1 is shown as an example in figures 3.11 and 3.12.

Qualitatively, the pressure fields are similar but SplineBeam seems to underestimate the maximum pressure, compared to k-Wave. For the 4 configurations through bone with analytical shapes (flat and sphere), the focus position differences are quite low ($\Delta X_{max} \leqslant 1$mm) whereas the maximal pressure differences are a bit higher ($\Delta P_{max} \leqslant 7.29\%$), especially for BM3-SC1 and BM5-SC1. We thought this difference in amplitude was due to the fact that SplineBeam neglects internal reflections, whose influence can be important for such regular geometries. Thus, we ran CIVA simulations with and without reflections and compared them with SplineBeam and k-Wave. The maximum pressure value $P_{max}$ and position $X_{max}$ of the pressure fields simulated by k-Wave, CIVA (with and without reflections) and SplineBeam for configurations n°3 and 5 are displayed in table 3.3.

For configurations BM3-SC1 and BM5-SC1, the maximum pressure of CIVA-with-reflections fields and k-Wave fields are very close ($< 0.8\%$), and the maximum pressure of CIVA-without-reflections fields and SplineBeam fields are very close ($< 1.1\%$). This confirms that, at least part of the maximum pressure

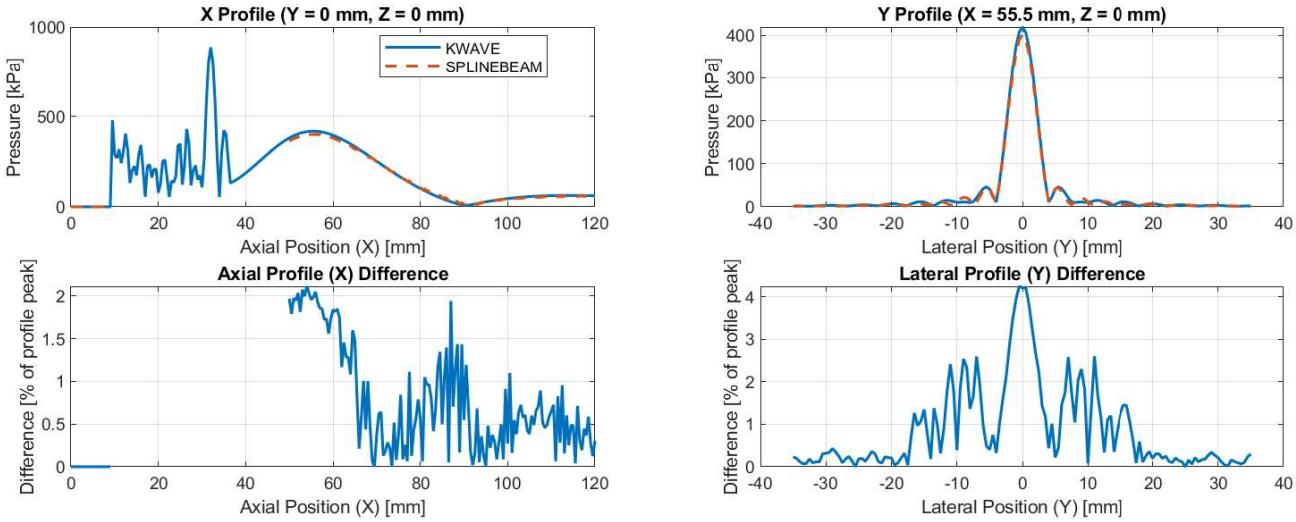


*Figure 3.11: Comparison of SplineBeam and k-Wave pressure field profiles for configuration BM3-SC1*

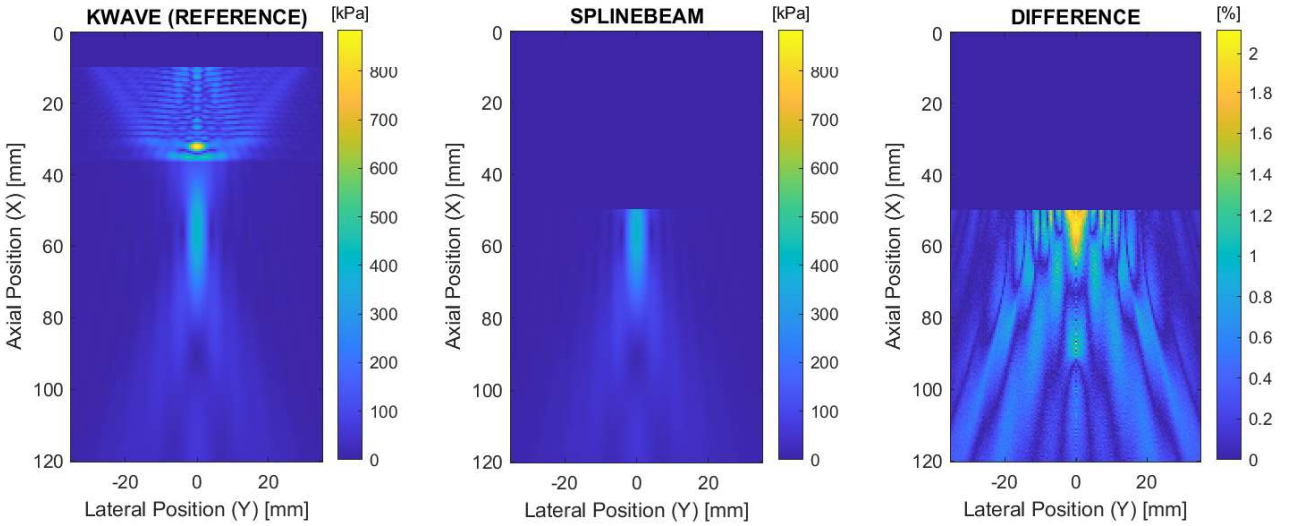


*Figure 3.12: Comparison of SplineBeam and k-Wave pressure field XY planes for configuration BM3-SC1*

difference between SplineBeam and k-Wave is due to the fact that SplineBeam does not take reflections into account.

### 3.4.5 Skull configuration results

The comparison of k-Wave and SplineBeam pressure fields for configuration BM7-SC2 is shown as an example in figures 3.13, 3.15, 3.14 and 3.16.

Qualitatively, the pressure fields are similar but the shape of the profiles are different. For the 6 configurations through skulls, the differences in focus position are a bit higher than for the previous configurations but still reasonable ($\Delta X_{max} \leqslant 1.5$mm). The differences in focus amplitude are a bit lower than for the analytical configurations ($\Delta P_{max} \leqslant 5.11\%$), which shows that the influence of internal reflections is decreased for more complex geometries. These comparisons show that SplineBeam is able to simulate correctly the ultrasound propagation through skull samples. We believe the small differences are probably due to the skull geometry modeling which is very different between k-Wave and SplineBeam. We think that the spline model is closer to the skull real shape than the stair-like geometry imposed by k-Wave grid which depends on the grid step.

We thought of using different MBA parameters to refine the geometry and see if the pressure fields got closer to k-Wave's. However, it only improved the maximum pressure error compared to k-Wave, but not the positioning error nor the profile shape differences. The fact that the other errors did not change much suggests that the skull shape did not get closer to the one used by k-Wave simulations. In fact, the maximum pressure probably only dropped because the skull surfaces became less smooth when increasing

*Table 3.3: Comparison of SplineBeam, k-Wave, CIVA (with and without reflections) maximum pressure values and position for configurations n°3 and 5*

| Config | Metric | k-Wave | CIVA (with ref) | CIVA (without ref) | SplineBeam |
|---|---|---|---|---|---|
| BM3-SC1 | $X_{max}(mm)$ | (112,71) | (111,71) | (113,71) | (112,71) |
| | $P_{max}(Pa)$ | 419140 | 416120 | 402350 | 401483 |
| BM3-SC2 | $X_{max}(mm)$ | (121,71) | (121,71) | (121,71) | (121,71) |
| | $P_{max}(Pa)$ | 423200 | 420720 | 430800 | 424360 |
| BM5-SC1 | $X_{max}(mm)$ | (121,71) | (120,71) | (123,71) | (123,71) |
| | $P_{max}(Pa)$ | 527310 | 524277 | 495230 | 488856 |
| BM5-SC2 | $X_{max}(mm)$ | (121,71) | (121,71) | (121,71) | (121,72) |
| | $P_{max}(Pa)$ | 420120 | 413930 | 435410 | 430980 |

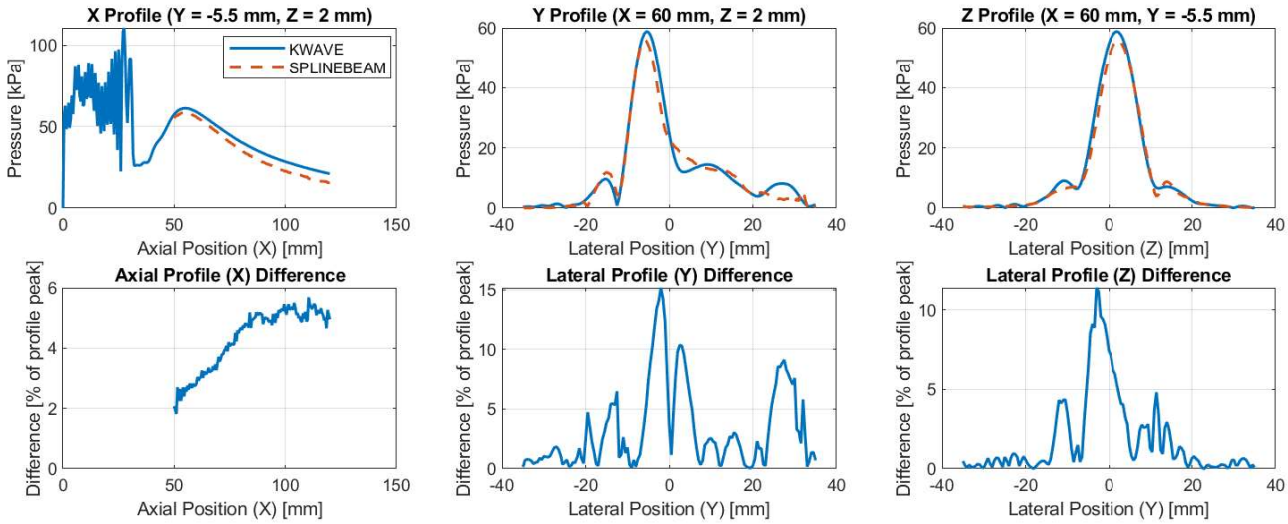


*Figure 3.13: Comparison of SplineBeam and k-Wave pressure field profiles for configuration BM7-SC2*

the MBA level.

## 3.5 Evaluation and optimization of SplineBeam computation time

### 3.5.1 Parameters influencing the computation time

SplineBeam computation time is proportional to the number of ultrasonic paths computed, and thereby to the number of computation points, and to the number of transducer samples. Thus, to reduce the computation time, the user can play with these parameters: he can reduce the computation zone size and step, and increase the transducer sampling step.

### 3.5.2 Parallel computation

As written above, the computation time is proportional to the number of computation points. As the computations are independent for all computation points, SplineBeam is very suitable for code parallelization. Thus, we used Intel library Threading Building Blocks (TBB) "parallel_for" which breaks the computation points into chunks, and runs each chunk on a separate thread. Ideally, this should reduce the computation time by the number of physical cores of the computer.

We then evaluated SplineBeam, CIVA and k-Wave computation times for different thread numbers. To do that, we used a desktop computer (with a cooling system allowing it to have a stable frequency), with Intel SpeedStep, TurboBoost and hyper-threading disabled. The configuration used for this evaluation was BM7-SC1, but the computation was broadband. The conifguration was run with and without attenuation for all simulation methods. As k-Wave C++ code does not allow to disable dispersion, attenuation with an odd power law coefficient cannot be computed. For the benchmark study [10], as the computations

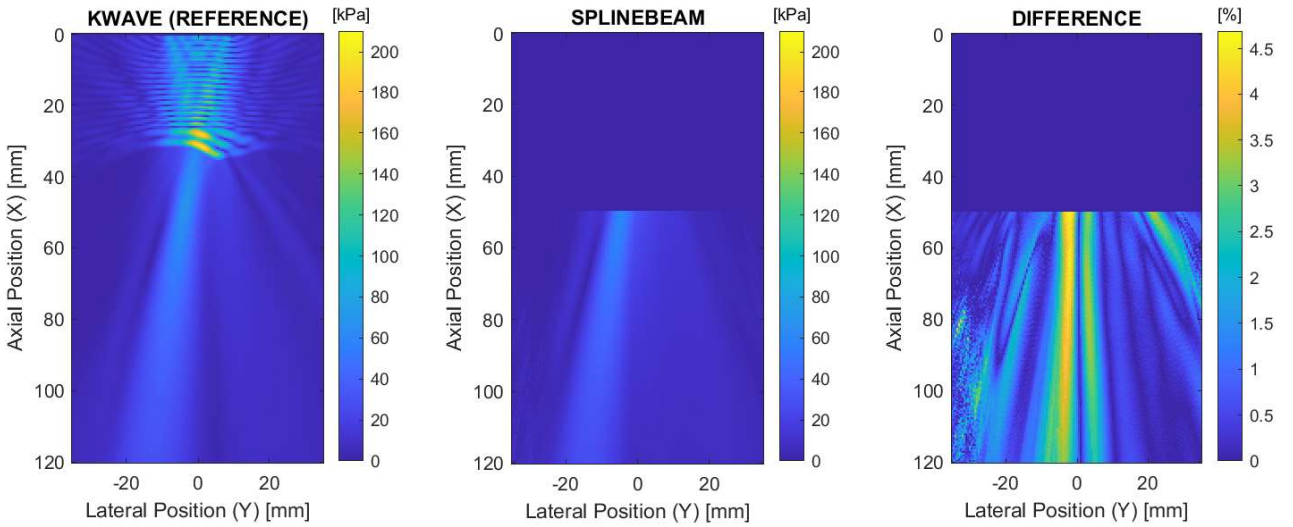


*Figure 3.14: Comparison of SplineBeam and k-Wave pressure field XY planes for configuration BM7-SC2*

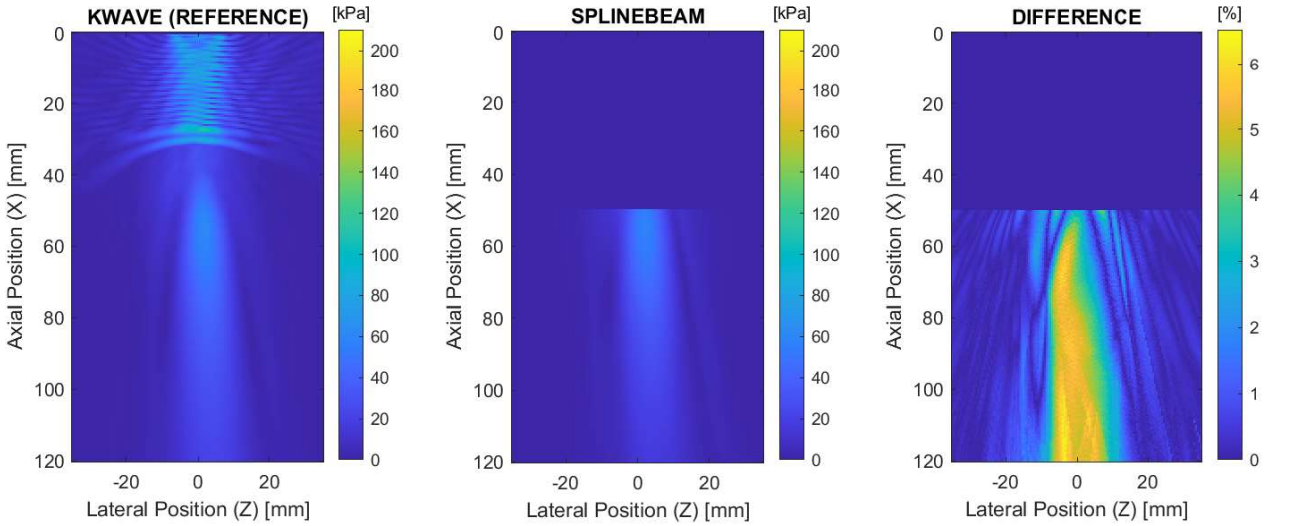


*Figure 3.15: Comparison of SplineBeam and k-Wave pressure field XZ planes for configuration BM7-SC2*

were harmonic, the power law coefficient was set to 2 and the coefficient was adjusted to give the correct attenuation in dB/cm. However, in the broadband case, it is not possible to model bone attenuation with the C++ code. Thus, for the computations with attenuation, k-Wave Matlab code was used. The computations were run for different numbers of computation points as SplineBeam computation zone must be in the third medium while k-Wave zone needs to include the skull and be at least as wide as the transducer as shown in figure 3.17.

Thus, the computation times, normalized for a same number of computation points, of CIVA, SplineBeam and k-Wave for 1, 4 and 8 threads are displayed in table 3.4.

We notice that CIVA and k-Wave computation times are approximately doubled when adding attenuation, while SplineBeam computation time remains the same. This was of course expected for k-Wave, as the C++ code, which is faster, is used for the computations without attenuation, while the Matlab code is used for the computations with attenuation.

We also ran a linear regression model for each simulation type (CIVA with attenuation, CIVA without attenuation, SplineBeam with attenuation, SplineBeam without attenuation, k-Wave with attenuation, k-Wave without attenuation) to find whether the computation time had an affine relation with the number of threads. The coefficients of determination for these linear regressions were higher than 95% for SplineBeam with and without attenuation and for k-Wave without attenuation, the others were lower than 80%. This means that SplineBeam code and k-Wave C++ code are well parallelized.

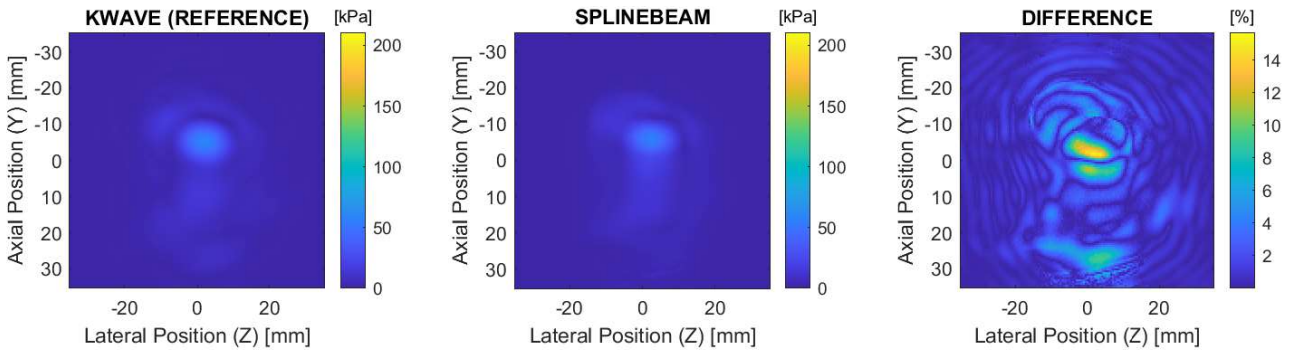


*Figure 3.16: Comparison of SplineBeam and k-Wave pressure field YZ planes for configuration BM7-SC2*

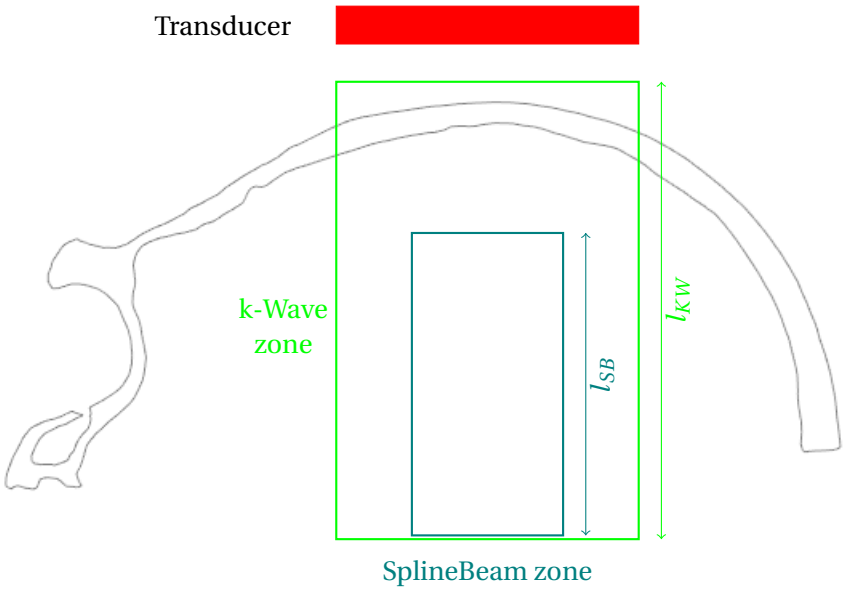


*Figure 3.17: Comparison of computation zone sizes needed for k-Wave and SplineBeam*

### 3.5.3 Comparison of SplineBeam and k-Wave computation time

Table 3.4 shows that, with 8 threads, k-Wave is 7 times faster than SplineBeam for computations without attenuation and 3 times faster than SplineBeam for computations with attenuation. However, this is for a same number of computation points, and SplineBeam has many advantages that allows it to reduce the number of computation points. First, unlike k-Wave, there is no convergence condition on SplineBeam spatial step, thus the computation zone step can be increased. Taking a spatial step two times larger in the 3 directions would result in a reduction by 8 of the computation time. Second, SplineBeam computation zone can be reduced to the focal spot, allowing to reduce the computation time a lot depending on the configuration. Finally, for computations with attenuation, k-Wave Matlab code is not well parallelized, which means that SplineBeam would probably be faster on a computer with more than 8 cores, for a same number of computation points.

To show the potential of computing the field only at the focal spot, let us study the computation times of the experimental configurations from chapter 4. The computation time for each one of the 3 experimental configurations was around 3 minutes for SplineBeam and 6 hours for k-Wave (the Matlab code was used as frequency dependent attenuation was modeled) on a laptop (2.3GHz, 8 cores). This means that SplineBeam was around 120 times faster than k-Wave. This was mainly due to the fact that k-Wave computation zone was much bigger as it needs to include the skull and the whole transducer width, as shown in figure 3.17. k-Wave computation zone was approximately 275 times bigger than SplineBeam's. Thus, for a same number of computation points, k-Wave would have had a computation time of around 1.3min, so around 3 times faster than SplineBeam as already shown from table 3.4. However, for these configurations, k-Wave computation zone cannot be smaller, and SplineBeam does not need to have a bigger computation zone. This shows a practical example where SplineBeam is much faster (120 times) than k-Wave, thank to its capacity to compute the field only at the focal spot.

*Table 3.4: Comparison of SplineBeam, k-Wave, CIVA computation time for broadband BM7-SC1 with and without attenuation and for a same number of computation points for various number of threads*

| **Simulation** | **CIVA** | | **SplineBeam** | | **k-Wave** | |
|---|---|---|---|---|---|---|
| Attenuation | With | Without | With | Without | With | Without |
| 1 thread | 6540s | 3240s | 1573s | 1530s | 239s | 106s |
| 4 threads | 780s | 660s | 720s | 660s | 54s | 54s |
| 8 threads | 600s | 300s | 120s | 120s | 41s | 18s |

### 3.5.4 Performance profiling and future optimizations

Visual Studio performance profiler was used to evaluate which parts of the code take the most time. It was found, as expected, that the minimization was taking the most time (around 65% of the time). In second position, the first guess computation is taking around 10% of the time. Given the percentage of time taken by these two tasks, the other ones are not worth investigating as it would not improve a lot the computation time.

For the two tasks cited before, an external function is called (L-BFGS, Intel ray-casting function). Thus, there are only two ways of improving the computation time: reducing the number of calls to this function, or using another implementation of the function. For both tasks, reducing the number of function calls can be done by reducing the number of ultrasonic paths to be computed. To achieve this, a smarter sampling of the transducer could be made, so that the corner paths are common for neighbour transducer samples. For example, for a planar rectangular transducer, as the one illustrated in figure 3.7, the $NE$ point of one sample could be the $NW$ point of the sample on its right, and so on. Thus, with $N$ the number of transducer samples, this method would allow to compute $2N+n+m+1$ paths (with $n \times m = N$ the number of samples in the two directions of the transducer), instead of $5N$. This is straightforward for rectangular transducers, as the samples are rectangular. However, it is a bit more complex for other transducer shapes, and a different algorithm would probably be needed for every shape. That is why we decided this was not the priority of this work. For the second task, reducing the number of function calls can be done by reducing the number of first guess computations. An idea to do this was to use the axial ray optimum as a first guess for the paraxial rays. By doing that, we obtain a 20% gain of time, but the results were a bit affected, meaning that L-BGFS was not always able to find the optimum from these first guesses. Finally, we did not have the time to test other implementations of L-BFGS nor the ray casting function, but we found several GPU implementations of L-BFGS on Github that could be used. As for the ray casting function, we think it would be difficult to find a faster function than Intel's.

## 3.6 Conclusion

We developed a new semi-analytical method to compute transcranial ultrasonic fields based on time of flight minimization, which requires a smooth and homogeneous skull model as the one developed in chapter 2. First, we developed a new ultrasonic path computation method based on time-of-flight minimization. This method allows a regular transducer sampling unlike ray-tracing methods, and is based on the smooth skull model developed in chapter 2. This path computation method was numerically validated by using it to compute delay laws for skull aberration correction. We showed that the delay laws computed with this method, called SplineRay, gave a way better focusing than straight ray-tracing laws and a similar focusing to simulated laws, but at a lower cost, as only the ultrasonic paths are computed. Then, the pencil method from CIVA was adapted so that the ultrasonic paths are computed by time-of-flight minimization. The ultrasonic field computation C++ algorithm thereby developed, called SplineBeam, can perform harmonic and broadband pressure and displacement field computations, with and without frequency dependent attenuation. The steps of the algorithm are summed up in a diagram in appendix C. SplineBeam was then numerically validated by comparison with other solvers from the literature, including k-Wave, on several benchmark configurations: in water, through bone layers of analytical shape and through skull samples. The pressure fields computed by SplineBeam were very similar to the ones simulated by the other solvers for all configurations. For example, the focus position difference between SplineBeam and k-Wave was always less than 1.50mm and the maximal pressure difference was always less than 8%. However, on

the configurations through analytical shapes, SplineBeam under-performed a little bit ($\Delta X_{max} \leqslant 1$mm and $\Delta P_{max} \leqslant 7.29\%$), as it is not able to simulate the internal reflections. On the configurations through skulls, the focus metric differences between SplineBeam and the other solvers were not that low ($\Delta X_{max} \leqslant 1.5$mm and $\Delta P_{max} \leqslant 5.11\%$). We think this is due to the smooth skull model used by SplineBeam, which we believe to be closer to the real skull shape. We then evaluated SplineBeam computation time and showed that for a computation including attenuation, k-Wave is $3$ times faster than SplineBeam for a same number of computation points. However, the advantage of SplineBeam is that it can reduce its computation zone to the focal spot, and thus reduce its computation point number. Thus, on practical configurations, SplineBeam is more than $100$ faster than k-Wave. To sum up, this new semi-analytical transcranial ultrasound simulation algorithm is fast and computes pressure fields similar to other solvers from the literature. The next chapter will show whether the pressure fields computed by SplineBeam are closer to experimentally measured ones than these other solvers.

# Chapter 4

# Experimental validation of the ultrasonic field computation algorithm by transcranial hydrophone measurements

The aim of this chapter was to validate the simulation method developed in chapter 3, by comparing hydrophone measured transcranial pressure fields with SplineBeam simulated ones. Indeed, the comparison between simulated and experimental fields is the only way to evaluate the realism of a simulation method. In addition, because of the complexity to measure transcranial pressure fields, there are few experimental validations in the literature, and to our knowledge no comparison between measured pressure fields and semi-analytical simulated ones. The first objective was to define an experimental set-up and to choose the equipment. Then, the measurement protocol had to be defined in details to reach a precise positioning of the skull, transducer and hydrophone. Before actually comparing the measured and simulated pressure fields, a method to simulate the same configurations as in the experiments had to be defined. In addition, various metrics were chosen to compare the measured and simulated fields. Then, pressure fields in water (without the skull) were measured to evaluate the error between the simulated and measured pressure fields in water, as a reference. It also allowed us to validate the measurement protocol and to improve it when needed. Finally, the realism of the pressure fields simulated with the method developed in chapter 3 and the skull model developed in chapter 2 was assessed by comparing them with those measured with the hydrophone through the skull. In addition, comparisons with other simulation methods, such as k-Wave and CIVA, were carried out. The homogenization method (developed in section 2.2.2) was also evaluated alone by comparing k-Wave simulated fields, with a heterogeneous skull model and a homogeneous one, with the measured ones.

## Contents

## 4.1 Experimental set-up and equipment used

### 4.1.1 Set-up

Basically, to measure a pressure field through a skull, one needs to position the emitting transducer on one side of the skull and a hydrophone to measure the pressure field on the other side. The detailed set-up is shown in figure 4.1.

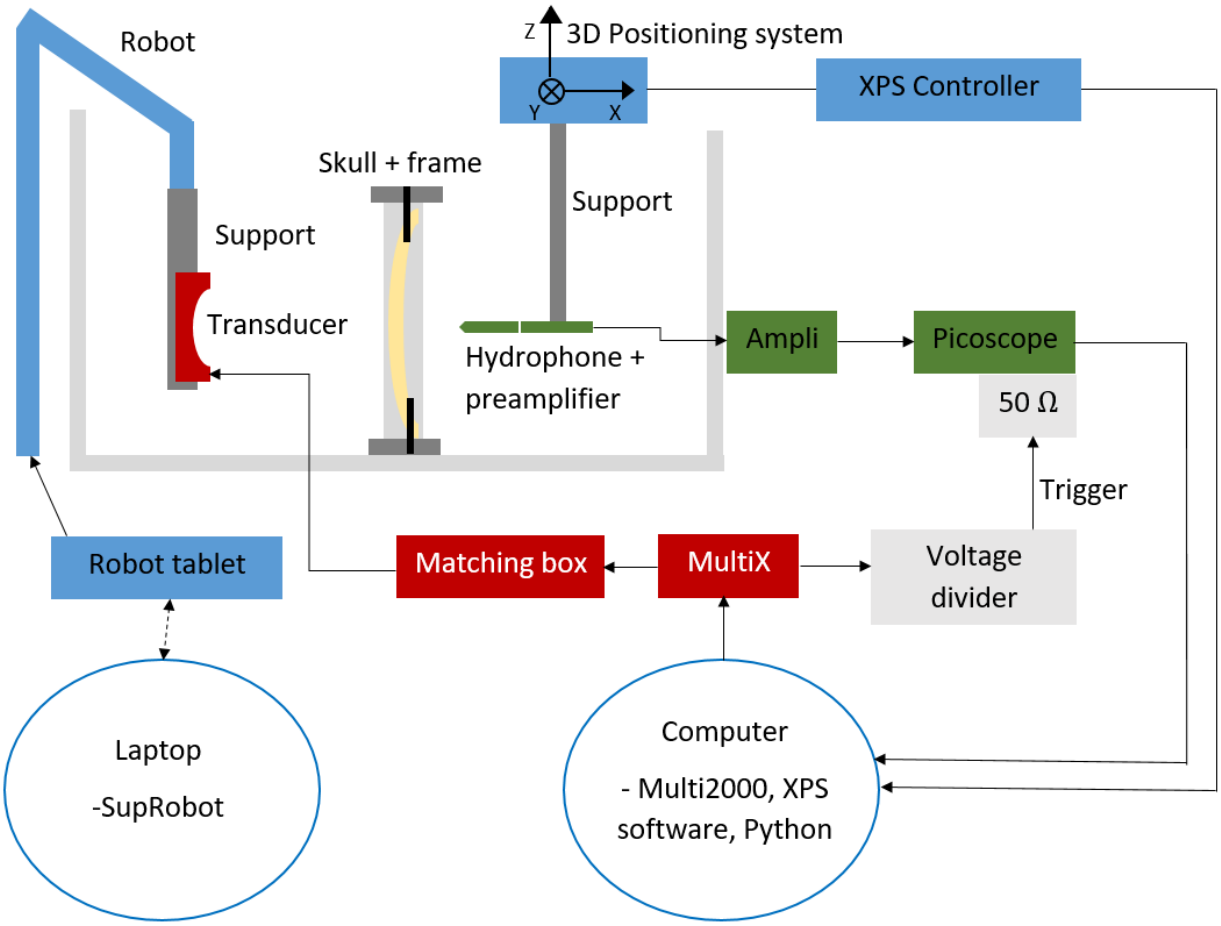


*Figure 4.1: Set-up for the transcranial ultrasound measurements*

### 4.1.2 Emitting part

The emitting part (in red in figure 4.1) is composed of a transducer, emitting at a central frequency of 0.4MHz, a matching box and a M2M MultiX++ signal generator. The generator is driven by a computer with the Multi2000 software. The transducer used was designed within the framework of Pauline Agou's PhD [89] in the BAOBAB team at Neurospin (CEA, Saclay, France) for Blood-Brain Barrier (BBB) opening on humans. It is spherically curved and has a natural focal length of 110.65 mm, which is close to the skull curvature radius to allow maximal ultrasound transmission. The transducer is composed of 16 annular elements, which, with delay laws, can be used to focus at different depths behind the skull. This transducer does not allow to correct skull aberrations. Indeed, as the elements are not many and with a ring shape (so with a strong symmetry), there are not enough degrees of freedom to correct phase distortions which are randomly spatially distributed. This was a design choice, as for BBB opening, skull aberration correction is not needed, as the focus shape is not crucial, and the skull effects are less important as the frequencies are lower. Pulses of $10\mu$s at a frequency of 0.4MHz are emitted.

### 4.1.3 Receiving part

The receiving part (in green in figure 4.1) is composed of a hydrophone Onda HGL-0400 combined with a preamplifier Onda AG-2010 and a Picoscope 5000A. The picoscope is connected to the computer, and a Python code is used to register the measured signals. The hydrophone and preamplifier are attached, thanks to a 3D printed support, to a 3D positioning system that can move in the directions (x,y,z). The positioning system is driven by a Newport XPS controller, which can be either controlled by the XPS software (to move the hydrophone "manually", to find the focal spot for example) or by a Python code (to automate the pressure scan).

## 4.2 Measurement protocol for precise positioning

### 4.2.1 Skull preparation

The skull sample used in the experiments is a half human skull, cut in the sagittal plane. It was provided by Grenoble-Alpes CHU atonomic pathology laboratory, in collaboration with Dr. De Schlichting and Prof. Chaffangon. The skull is attached to an aluminum positioning frame with nylon screws (to avoid artefacts on the CT scan). The positioning frame has four landmarks used to locate the skull coordinate system. To put the skull inside the water tank, the positioning frame is attached to a plastic board which is put down on the bottom of the water tank. To orientate the skull as needed, the plastic board has two screws on two corners that can be sank to elevate one side of the board and thus provide an angle around the $y$ axis. To get a rotation around $z$, the skull positioning frame can be rotated relative to the board around the attaching screw. The rotation angles are illustrated in figure 4.2.

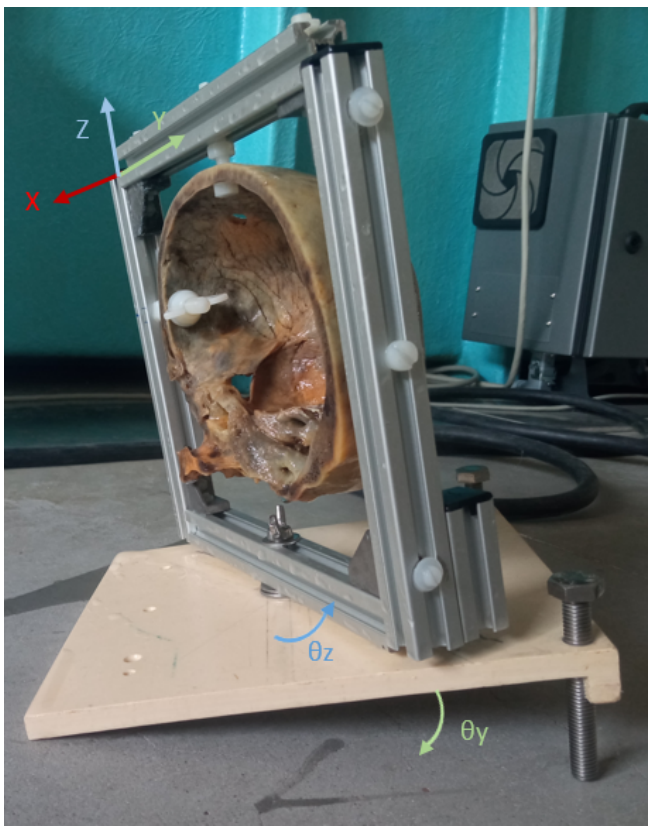


*Figure 4.2: Skull sample and its positioning frame attached to the plastic board that allows the skull to be rotated of $\theta_z$ and $\theta_y$ around the z and y axis*

The skull, together with the positioning frame, is immersed in water and degassed for at least 48h to mimic in vivo conditions. The degassing duration is based on previous experience acquired during Pauline Agou's PhD. Doing so, the air trapped in the skull pores is removed and filled with water instead. In vivo, the pores are filled with marrow, whose acoustic properties are similar to those of water. In addition, ultrasound transmission is improved by filling these pores with water instead of air. The degassing set-up, shown in figure 4.3, is composed of a vacuum bell and a vacuum pump, provided by the BAOBAB team at Neurospin (CEA, Saclay, France). The skull is transferred to the water tank so that it does not spend more

than 5 seconds in the air. The most important thing is not to allow air to re-enter the smallest interstices of the bone, which, thanks to capillarity, should not happen within 5 seconds. The water tank was not degassed because the water volume ($\approx 0.15\text{m}^3$) and the interface air/water ($\approx 0.65\text{m}^2$) were too large.

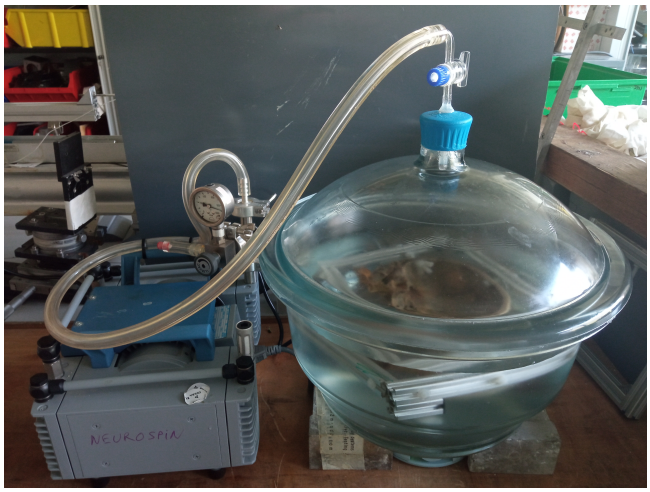


*Figure 4.3: Set-up to degas the skull*

To obtain the skull shape and acoustic properties as explained in chapter 2, two CT scans of the skull were performed. The first one was made with the skull attached to its positioning frame to have a precise positioning in the simulations. The problem with this scan, is that it contained too many artefacts because of the aluminium positioning frame. Thus, after all experiments were done, another CT scan was performed with the skull alone (degassed in water), to obtain a cleaner scan to be able to obtain the skull geometry and acoustic properties. The meshes extracted from the two scans were registered with the "align tool" of MeshLab. Both scans were performed with a SIEMENS Biograph Horizon scanner at Service Hospitalier Frédéric Joliot (Orsay, France), thanks to Vincent Brulon. The CT scan parameters are given in table 4.1.

*Table 4.1: CT scan parameters*

| **Voxel spacing** | **Slice thickness** | **Reconstruction kernel** | **Peak voltage** |
|---|---|---|---|
| $0.59\text{mm} \times 0.59\text{mm} \times 0.50\text{mm}$ | 0.75mm | J80s | 130kVp |

### 4.2.2 Transducer positioning

The transducer is attached to a UR5 (Universal Robots) robot thanks to a homemade 3D printed support which is shown in figure 4.4. The robot allows a precise positioning of the probe with respect to the skull. Indeed, the robot can be calibrated to register the skull coordinate system and then execute precise trajectories (with a repeatability of $\pm 0.1\text{mm}$) in that coordinate system.

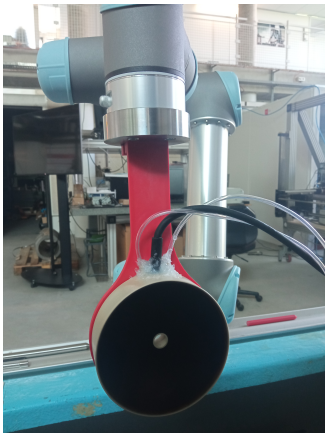

*Figure 4.4: Transducer attached to the robot with the support*

Three transducer positions, relative to the skull, were chosen. For the first one, a target was chosen at the center of the skull, and an algorithm developed by Gaelle Thomas during her PhD [90] at ICube laboratory (Strasbourg, France) was run to find the best transducer positions to reach this target. For every possible position (such that the transducer does not touch the skull), the algorithm computes the angle between the ultrasonic beam and the normal of the triangular elements of the skull mesh. The transducer position with the highest percentage of facets for which this angle is below a given threshold, was chosen. That is to say the position with the most orthogonal incidence. The two other positions were chosen so that the ultrasound crosses different parts of the skull for the three positions. These two positions were adjusted using CIVA simulations. All three positions did not target the same point. The three transducer positions are displayed in figure 4.5.

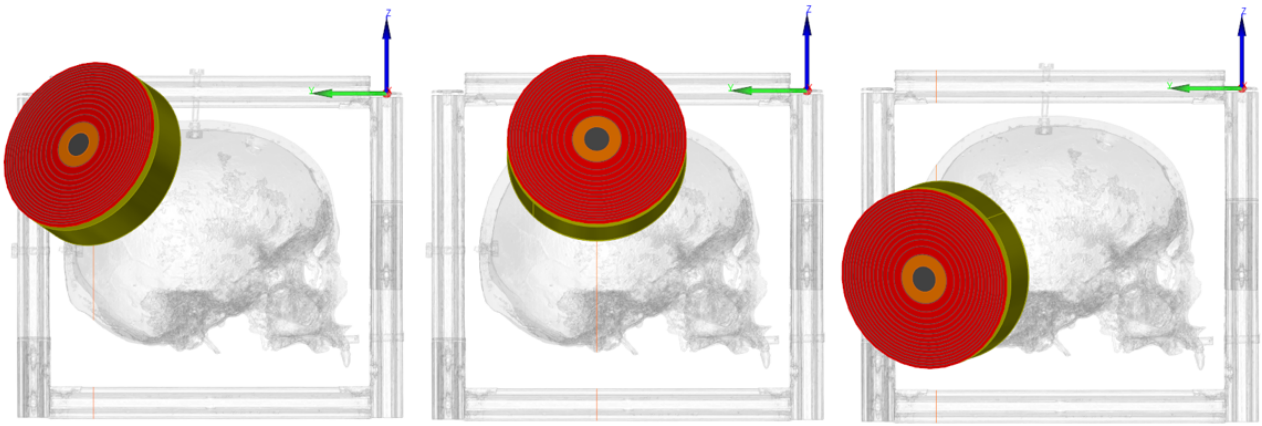

*Figure 4.5: The 3 transducer positions displayed in CIVA*

To maximize the received signal, the transducer needs to be approximately aligned with the hydrophone. As the skull is initially placed in the water tank and aligned with its main axis, and as the tank is itself approximately aligned with the 3D positioning system and thus with the hydrophone coordinate system, any angle between the transducer and the skull will induce an angle between the transducer and the hydrophone. To avoid such a situation, the skull was rotated so that the transducer is aligned with the hydrophone.

Given the rotation matrix $R_{probe}$ associated with a given transducer position (in the skull coordinate system), the projected angles around the $y$ and $z$ axis are needed. Indeed, because of the axial symmetry of the transducer, there is no need to rotate the skull around the $x$ axis. First, assuming that the transducer orientation in the probe frame is $u_z = (0,0,1)$, the transducer orientation in the skull frame is given by:

$$u_{skull} = R_{skull \to probe} u_z \tag{4.1}$$

Then, the projected angles $\theta_y$ and $\theta_z$ around the $y$ and $z$ axis are given by:

$$\begin{cases} \theta_y = \arcsin \frac{p_y(u_{skull}).z}{||p_y(u_{skull})||||z||} = \arcsin \frac{u_{skull}.z}{\sqrt{(u_{skull}.x^2 + u_{skull}.z^2)}} \\ \theta_z = \arcsin \frac{p_z(u_{skull}).y}{||p_z(u_{skull})||||y||} = \arcsin \frac{u_{skull}.y}{\sqrt{(u_{skull}.x^2 + u_{skull}.y^2)}} \end{cases} \tag{4.2}$$

The skull positioning frame is thus rotated around the screw attaching it to the board of $-\theta_z$ and the board is rotated of $-\theta_y$. The 3 experimental transducer positions, with the skull rotated so that the transducer is approximately aligned with the hydrophone, are shown in figure 4.6.

### 4.2.3 Calibration protocol

As explained before, the skull coordinate system can be registered using the robot. The coordinates of the four landmark points (on the skull positioning frame) in the skull coordinate system are given to the robot software. Then, the position of the landmarks in the robot coordinate system are recorded. To do so, a spike (of very well-known geometry) is attached to the robot, and the latter is move manually so that the spike hits each one of the four landmarks, as shown in figure 4.7. The robot software is then able to localize the robot in the skull coordinate system.

To precisely put the computation zone in the simulations at the same position as the hydrophone, one needs to find the change of basis matrix between the hydrophone coordinate system and the skull system. To

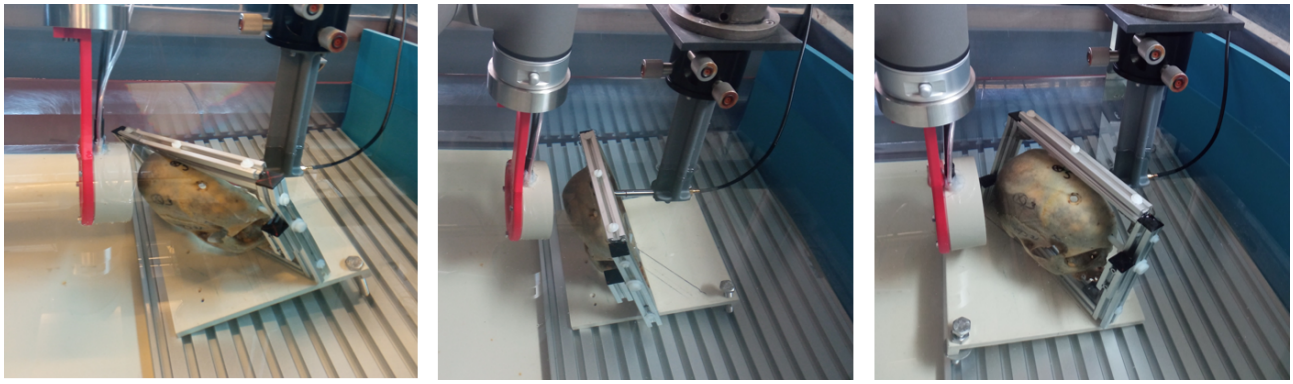

*Figure 4.6: The 3 experimental transducer positions*

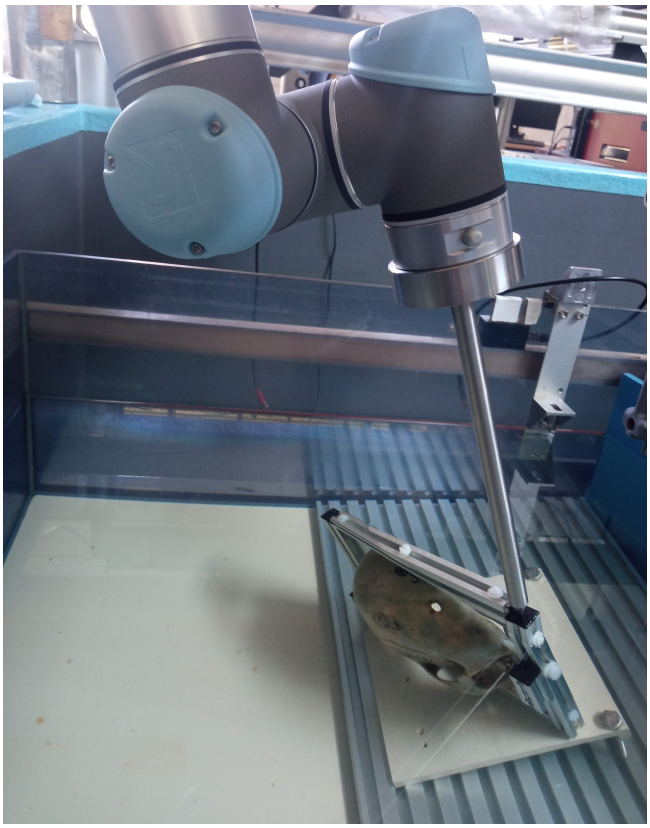

*Figure 4.7: Skull calibration process*

do so, four points are chosen in the hydrophone coordinate system and the robot is moved manually so that the spike hits each one of those points, as shown in figure 4.8. When a point is hit with the spike, the robot software displays the corresponding coordinate in the skull system. In order not to damage the hydrophone tip, a plastic copy of the hydrophone, with the same dimensions as the real one, was 3D printed and used instead. This can add some error due to small changes between the two mechanical pieces and repeatability of the exact positioning of the real hydrophone compared to the copy. The hydrophone coordinate system is defined by a central point $(0,0,0)$ chosen at an arbitrary position and the three other points are defined by moving along each one of the three axis of the positioning system.

To find the change of basis matrix between the hydrophone coordinate system and the skull system, a Python script was developed. From the four points in the hydrophone system $(X^1_{hydro}, X^2_{hydro}, X^3_{hydro}, X^4_{hydro})$ and the four points in the skull system $(X^1_{skull}, X^2_{skull}, X^3_{skull}, X^4_{skull})$, the goal is to find the best matrix $M_{skull \to hydro}$ such that:

$$\forall i \in \{1,2,3,4\}, \begin{bmatrix} X^i_{skull} \\ 1 \end{bmatrix} \approx M_{skull \to hydro} \begin{bmatrix} X^i_{hydro} \\ 1 \end{bmatrix} \tag{4.3}$$

with $M_{skull \to hydro}$ defined from a rotation matrix $R_{skull \to hydro} \in \mathbb{R}^3 \times \mathbb{R}^3$ and a translation vector

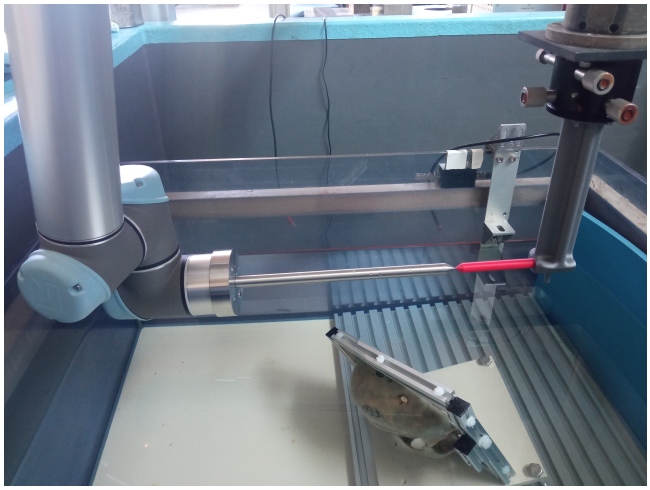

*Figure 4.8: Hydrophone calibration process*

$t_{skull \to hydro} \in \mathbb{R}^3$:

$$M_{skull \to hydro} = \begin{bmatrix} R_{skull \to hydro} & t_{skull \to hydro} \\ 0 & 1 \end{bmatrix} \tag{4.4}$$

To ensure that $R_{skull \to hydro}$ is a rotation matrix, it is decomposed as a product of three rotation matrices along each axis:

$$R_{skull \to hydro} = R_z(\theta_z^{skull \to hydro}) R_y(\theta_y^{skull \to hydro}) R_x(\theta_x^{skull \to hydro}) \tag{4.5}$$

with $R_i$ the rotation matrix around axis $i \in \{x, y, z\}$ and $\theta_i^{skull \to hydro}$ the rotation angle around the same axis.

Thus the minimization problem is:

$$\begin{cases} \min_{(t_{skull \to hydro} \in \mathbb{R}^3, (\theta_x^{skull \to hydro}, \theta_y^{skull \to hydro}, \theta_z^{skull \to hydro}) \in \mathbb{R}^3)} f_{skull \to hydro} \\ f_{skull \to hydro} = R_{skull \to hydro} X_{hydro}^i + t_{skull \to hydro} - X_{skull}^i \end{cases} \tag{4.6}$$

The objective function is minimized with Scipy least_squares function. The change of basis matrix $M_{skull \to hydro}$ is thereby obtained.

Knowing the center of the scanned zone in the hydrophone coordinate system $C_z^{hydro}$, the position of the computation zone in the skull coordinate system is:

$$C_z^{skull} = M_{skull \to hydro} C_z^{hydro} \tag{4.7}$$

### 4.2.4 Positioning error

To evaluate the positioning error, we computed the maximum pressure position difference between measured and simulated fields without skull (in water). The positioning error was around 1-1.5mm. Part of this error is of course due to the calibration process, which is complicated due the fact that the skull positioning frame is not totally rigid because of the nylon screws (a trade off had to be found between rigidity and CT scan artefacts reduction). In addition, as the skull is underwater, it is quite difficult to position the robot spike on the skull positioning frame landmarks with precision, because of the refraction of water. The hydrophone position calibration also adds some uncertainty. However, SupRobot software always indicated a calibration error of less than 1mm, thus, part of the positioning error was not due to the calibration process. We did a lot of experiments to try and understand where this remaining part of the positioning error came from. We repeated multiple times the same experiment with only one parameter changing to try and isolate the problem. We found out that even for a same calibration, a difference of nearly 1mm could be reached. We investigated and found that detaching and attaching back the transducer support to the robot was responsible for this error. We tried to use a torque wrench to ensure all screws of the transducer support were screwed equally onto the robot, it did not reduce the positioning error. By lack of time, we decided to abandon this investigation and try to correct the positioning error artificially afterwards. To do so, for each one of the measurements through the skull sample, after the scan through the skull, a additional

scan without skull was performed while keeping the transducer and hydrophone at the same position. The positioning error was then evaluated by computing the maximum pressure position difference between the measured field without skull and the simulated field without skull. This allowed to correct the transducer position in the simulations with skull. This correction is not optimal, as the transducer position is corrected by translation only, and the error could be due to a rotation error. In addition, this method only corrects the positioning error between the transducer and the skull, but not between the hydrophone and the other two elements. However, as explained previously, the biggest error is probably due to the transducer positioning and especially to the transducer support.

### 4.2.5 Scanning protocol

As explained before, the hydrophone is attached to a 3D positioning system. The positioning system is driven by a Newport XPS controller. Once the skull and probe are in position, the hydrophone is moved along each axis until the maximum pressure is found, using the Picoscope desktop application.

Once the location of the maximum is found and the scanning volume is chosen, two Python scripts, written by Paul Mondou (CEA/Neurospin/BAOBAB, Saclay, France), are used to perform the scan, that is to say to record the pressure at every point of the 3D volume. The first code moves the hydrophone thanks to the XPS controller. The second one saves the signals recorded with the Picoscope. A trigger signal is sent by the signal generator to the Picoscope, so that the Picoscope knows when to record the signals.

The scanning trajectory in a vertical plane is shown in figure 4.9. The speed of the motors of the 3D positioning system is $5$ mm/s, and the scan is done continuously in a plane parallel to the transducer, which is possible because the displacement is orthogonal to the ultrasound propagation. For the transcranial measurements, the scans lasted around 2h for a scanning zone of $40 \times 10 \times 10$ mm$^3$, with a step of $0.5$ mm in each direction.

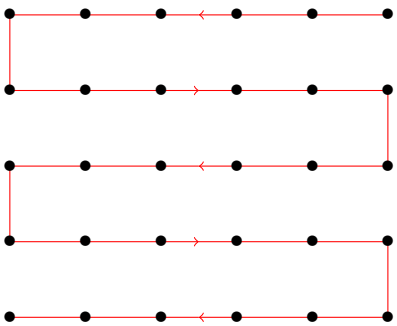

*Figure 4.9: Scan trajectory in a plane*

### 4.2.6 Post-processing of the experimental signals

Three Python codes, also written by Paul Mondou, are used for the post-processing of the signals acquired with the hydrophone.

The first one determines whether signals are missing by looking at the recording delays of the signals. The recording delays of the signals are saved in a file during the scan for this reason. Sometimes, for experimental random reasons, the recording of a signal takes longer than the displacement of the hydrophone between two scanning points. In that case, which is very occasional, empty signals have to be added at those precise locations so that there is no shift within the scan. Those signals will later be interpolated.

The second script allows to visualize a representative sample of the signals (it would be far too heavy to plot them all). This visualization helps choosing the window of processing of the signals.

The last and most important script does the main post processing tasks. It takes as input the dimensions of the scan, as well as the window of signal processing given by the second code, and the potentially missing signals locations given by the first code. For each signal, a finite impulse response filter is applied to clean the data, then the Hilbert transform is applied to get the envelope of the absolute value of the signal. An example of raw and post-processed signal is plotted in figure 4.10. Finally, the maximum of the envelope is saved in a 3D matrix containing the whole scan. The missing signal maxima can be interpolated. The lines of the scan along the y direction need to be flipped one time in two, because in a plane, one line in two is scanned in direction, and one line in two is scanned in the other direction, as illustrated in figure

4.9. A method was developed by Paul Mondou to determine a law to apply to the data to compensate for the motor speed. Indeed, as the scan is done continuously, while the ultrasonic waves propagate from the transducer to the hydrophone, the hydrophone has already moved a little by the time it records the signal. Thus, Paul determined a law that gives the optimal shift to apply to the data as a function of the motor speed and the distance between the hydrophone and the transducer. The data is then interpolated to get the values at the matrix points.

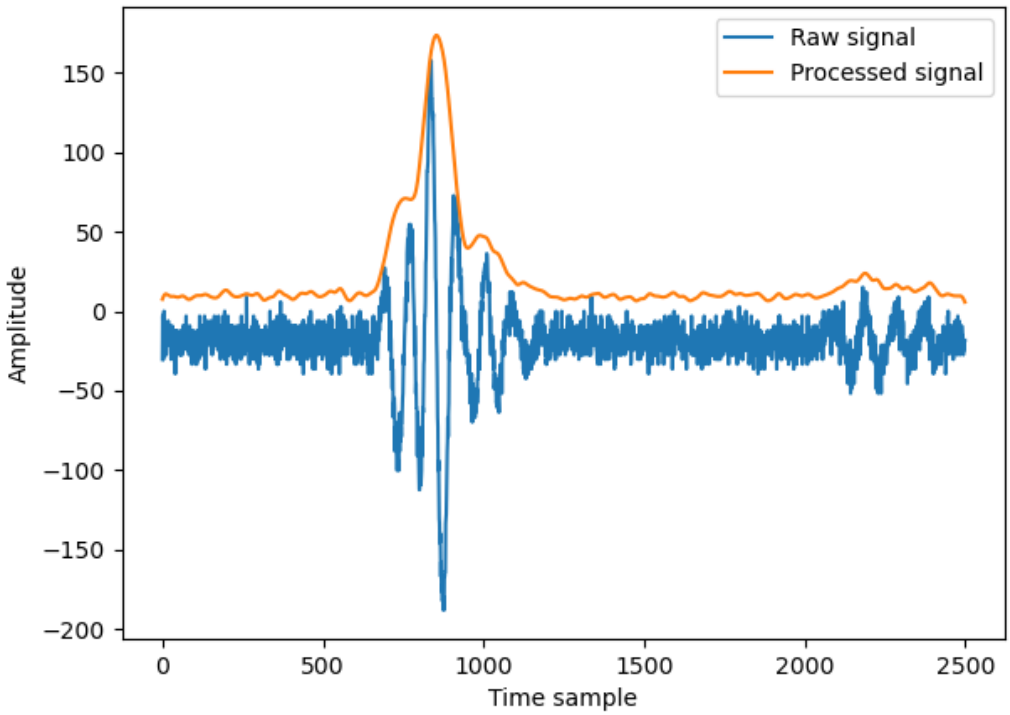


*Figure 4.10: Experimental signal post-processing*

The matrix containing the maximum of the envelope at each point of the scan is saved in a .mat format. A CIVA plug-in was coded by Sylvain Chatillon to put the experimental scans in a CIVA result format, to be able to read them and compare them to simulation results thanks to the visualization and analysis tools embedded in the CIVA platform.

## 4.3 Simulation of the experimental configurations

SplineBeam, k-Wave and CIVA simulations were run to compare the resulting pressure fields with the experimental ones. SplineBeam and k-Wave simulations were run from the CIVA interface, thanks to two plug-ins, coded by Sylvain Chatillon and me.

### 4.3.1 SplineBeam and k-Wave plug-in

The CIVA plug-in for SplineBeam works like this:

- it takes the computation field parameters from CIVA interface,
- it writes those parameters in an input file for SplineBeam,
- it runs SplineBeam executable,
- it transforms SplineBeam result as a CIVA result (readable with CIVA interface).

The plug-in for k-Wave is similar but a bit different as the input parameters between CIVA and k-Wave are quite different. Indeed, k-Wave needs as input the pressure field in an initial plane. Thus the pressure field in a plane parallel to the transducer is first computed with CIVA and given as input to k-Wave. The "kspaceFirstOrder3D" solver was used for k-Wave simulations.

### 4.3.2 Transducer modeling

To model the transducer within CIVA, the internal and external diameters of the element chords were given to CIVA. To allow a non-equal spacing of the elements, the inter-element spaces were modeled as non active elements. Given the curvature radius and the diameter of the transducer, CIVA is then able to project the elements on the spherical surface.

The signal used as input of the simulations was obtained from the measurements in water. The signal at the focal spot was taken.

### 4.3.3 Computation zone modeling

The computation zone for all three simulation methods (SplineBeam, k-Wave and CIVA) had the same spatial step (in all three directions) of $0.5$mm which is the same as the experimental one. The computation zone position for SplineBeam and CIVA was computed from equation 4.7 and the zone dimensions were the same as the experimental ones. For k-Wave simulations, the skull needs to be included in the computation zone and the zone must be as wide as the transducer width. Thus, the zone dimensions were bigger and the zone position is different, as illustrated by figure 3.17. As shown in this figure, both zones end at the same position. Thus, given the length $l_{SB}$ of SplineBeam zone and the length $l_{KW}$ of k-Wave zone, k-Wave computation zone position $C_{z,KW}^{skull}$ is given by:

$$C_{z,KW}^{skull} = M_{skull \to hydro}(C_z^{hydro} + l_{SB}/2 - l_{KW}/2) \tag{4.8}$$

The zone orientation is the same for all three simulation methods and the same as in the experiments, as computed in equation 4.7.

### 4.3.4 Material modeling

The density of water was taken as $\rho_{water} = 1000 kg.m^{-3}$ and the sound speed of water as $c_{water} = 1480 m.s^{-1}$.

For SplineBeam simulations, the skull model developed in chapter 2 was used. For CIVA simulations, the homogenized properties were used as well, but the geometry was modeled by the STL skull mesh extracted from the CT scan. Finally, for k-Wave simulations, a homogeneous skull model and a heterogeneous skull model were both tested. The heterogeneous model was build as explained in section 2.2.1.3. The homogeneous model was the same but all voxels identified as bone were given the acoustic properties given by the homogenization method developed in section 2.2.2.

## 4.4 Metrics used for the comparison of the measured and simulated fields

Different metrics were used to compare the measured and simulated pressure fields for the configurations with and without skull. For the measurements through the skull sample, the focal position error, maximum pressure error and focal spot volume error were computed. The maximum pressure error was computed from the pressure difference between the measurements/simulations with and without the skull. Indeed, only relative pressure values were computed. Computing the absolute pressure values would make the simulations more complex as we would also need to take into account the electrical power, the hydrophone and amplifier capacitance. Thus, for the configurations without skull, we only computed the focal volume and position errors. In order to compute these errors, we needed to find the focal depth, length and width errors, which we therefore also compared.

### 4.4.1 Metrics for the comparison without skull

#### 4.4.1.1 Focal depth and position error of the pressure fields

**Focal depth of the simulated pressure fields** For the simulated focal depth $d_{focal}^{simu,}$, we identify the computation point with the maximum pressure value. Then, we compute the time of flight $t_{max}$ of the maximum of the signal envelop at this point. Using this time of flight it is straightforward to compute the focal depth with:

$$d_{focal}^{water,simu} = t_{max} \times c_{water} \tag{4.9}$$

**Focal depth of the experimental pressure fields** For the experimental focal depth $d_{focal}^{water,exp}$, we also identify the acquisition point with the maximal pressure value. However, as we do not have the time of flight of the emitted signal maximum, we can not compute the time of flight $t_{max}$ of the maximum of signal envelop at this point. But, we do have the start of the emitted signal $t_{start}^{E}$. Indeed, as the emitted signal is sent at the same time as the trigger signal, and the hydrophone starts receiving when the trigger is emitted, the start of every received signal corresponds to the start of the emitted signal. Thus, we can measure the time of flight difference between the start of the emitted signal $t_{start}^{E}$ and the start of the received signal $t_{start}^{R}$. To compute the start of the received signal, we use the following procedure (illustrated by figure 4.11):

- We identify the maximum of the signal envelop $(t_{max}^{R}, A_{max}^{R})$.
- From $t_{max}^{R}$, we go through the signal in the $t_{start}^{E}$ direction until we reach the third of this maximum: $(t_{max/3}^{R}, \frac{A_{max}^{R}}{3})$.
- We compute the mean of the noise $N = \text{mean}(s^{R}[:100])$, with $s^{R}$ the received signal.
- From $t_{max/3}^{R}$, we go through the signal in the $t_{start}^{E}$ direction until we reach the first $t_{start}^{R}$ such that, $A(t_{start}^{R}) \leqslant N + 0.1(\frac{A_{max}^{R}}{3} - N)$.

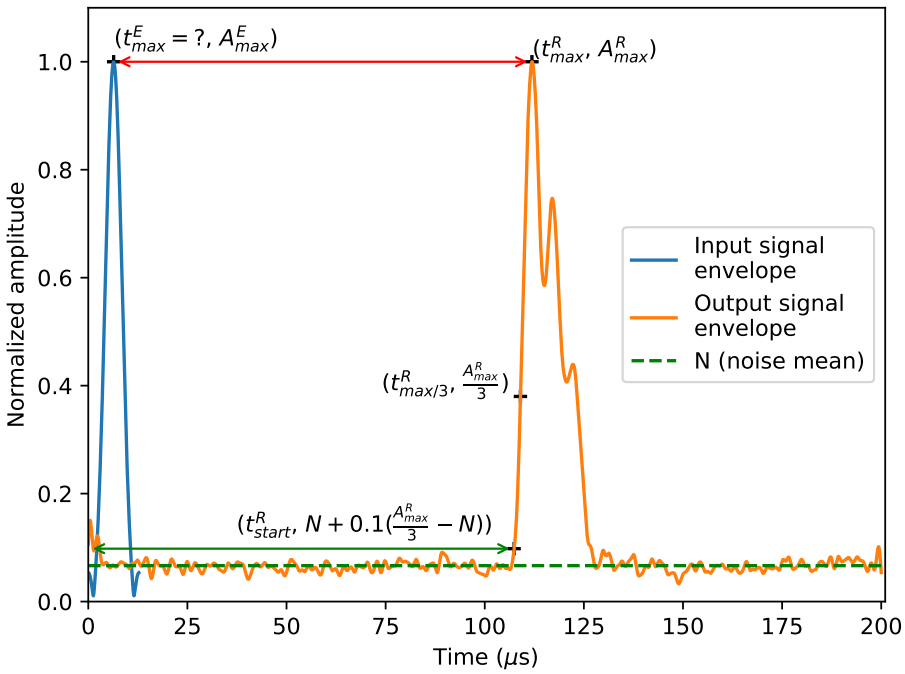


*Figure 4.11: Procedure to compute the experimental focal depth*

Finally, we compute the focal depth using (green arrow on the figure 4.11):

$$d_{focal}^{water,exp} = (t_{start}^{R} - t_{start}^{E}) \times c_{water} \tag{4.10}$$

**Focal depth and position errors** From the simulated focal depth $d_{focal}^{water,simu}$ and the experimental one $d_{focal}^{water,exp}$, we can compute the focal depth error:

$$\Delta d_{focal}^{water} = \frac{|d_{focal}^{water,exp} - d_{focal}^{water,simu}|}{d_{focal}^{water,exp}} \tag{4.11}$$

The focal position error for the configurations without skull can directly be deduced from the focal depths:

$$\Delta X_{max}^{water} = |d_{focal}^{water,exp} - d_{focal}^{water,simu}| \tag{4.12}$$

#### 4.4.1.2 Focal length, width and volume errors of the pressure fields

The focal length $l_{focal}^{water}$ is computed as the -3dB distance along the axis parallel to the transducer normal. The focal width $w_{focal}^{water}$ is computed as the -3dB distance along an axis perpendicular to the transducer normal. The focal length and focal width errors $\Delta l_{focal}^{water}$ and $\Delta w_{focal}^{water}$ are computed as:

$$\Delta l_{focal}^{water} = \frac{|l_{focal}^{water,exp} - l_{focal}^{water,simu}|}{l_{focal}^{water,exp}} \tag{4.13}$$

$$\Delta w_{focal}^{water} = \frac{|w_{focal}^{water,exp} - w_{focal}^{water,simu}|}{w_{focal}^{water,exp}} \tag{4.14}$$

Finally, the focal volume error $\Delta V_{focal}^{water}$ is computed as:

$$\Delta V_{focal}^{water} = \frac{|V_{focal}^{water,exp} - V_{focal}^{water,simu}|}{V_{focal}^{water,exp}} \tag{4.15}$$

where $V_{focal}^{water,exp}$ and $V_{focal}^{water,simu}$ are the focal volumes of the experimental and simulated fields for the configurations with skull, with $V_{focal} = l_{focal} \times w_{focal} \times w'_{focal}$ ($w'_{focal}$ being the -3dB distance along the third axis).

### 4.4.2 Metrics for the comparison with skull

#### 4.4.2.1 Focal spot position error

The focal spot position error $\Delta X_{max}^{skull}$ is computed after correction of the positioning error (as explained in section 4.2.4) and is defined by:

$$\Delta X_{max}^{skull} = ||X_{max}^{skull,exp} - X_{max}^{skull,simu}|| \tag{4.16}$$

where $X_{max}^{skull,exp}$ and $X_{max}^{skull,simu}$ are the maximum pressure positions of the experimental and simulated fields for the configurations with skull.

#### 4.4.2.2 Maximum pressure error

The focus amplitude error $\Delta P_{max}$ is computed in dB as:

$$\Delta P_{max}^{skull} = 20\log\frac{P_{max}^{skull,exp}}{P_{max}^{water,exp}} - 20\log\frac{P_{max}^{skull,simu}}{P_{max}^{water,simu}} \tag{4.17}$$

where $P_{max}^{skull,exp}$ and $P_{max}^{skull,simu}$ are the maximum pressure values of the experimental and simulated fields for the configurations with skull, and $P_{max}^{water,exp}$ and $P_{max}^{water,simu}$ are the maximum pressure values of the experimental and simulated fields for the configurations with skull but with the skull removed.

#### 4.4.2.3 Focal volume error

Finally, the focal volume error $\Delta V_{focal}^{skull}$ is computed as:

$$\Delta V_{focal}^{skull} = \frac{|V_{focal}^{skull,exp} - V_{focal}^{skull,simu}|}{V_{focal}^{skull,exp}} \tag{4.18}$$

where $V_{focal}^{exp,skull}$ and $V_{focal}^{simu,skull}$ are the focal volumes of the experimental and simulated fields for the configurations with skull.

## 4.5 Comparison of the simulated and measured pressure fields in water (without skull) for reference

Hydrophone measurements of the acoustic pressure field in water were first performed to validate the protocol and to obtain reference errors. The focal properties of the pressure fields obtained with seven different steering of the transducer ($-30$mm, $-20$mm, $-10$mm, 0mm, $+10$mm, $+20$mm, $+30$mm, relative to the natural focusing of the transducer) were computed and compared with the ones of the corresponding simulations. The delay laws used for the steerings were computed with CIVA, and the simulations were run with SplineBeam, CIVA and k-Wave. The relative focal metrics errors, compared to the experimental fields, of the simulated fields are summed up in table 4.2.

*Table 4.2: Comparison of the simulated pressure fields with the experimental ones for the configurations without skull*

| Steering | Comparison | $\Delta l_{focal}^{water}$ | $\Delta w_{focal}^{water}$ | $\Delta V_{focal}^{water}$ | $\Delta d_{focal}^{water}$ | $\Delta X_{max}^{water}$ |
|---|---|---|---|---|---|---|
| $-30$ | SplineBeam/Exp | 4.90% | 5.26% | 14.64% | 0.15% | 0.12mm |
| | k-Wave/Exp | 4.86% | 5.22% | 14.76% | 0.53% | 0.42mm |
| | CIVA/Exp | 5.01% | 5.60% | 15.36% | 0.62% | 0.50mm |
| $-20$ | SplineBeam/Exp | 3.27% | 2.87% | 8.75% | 0.61% | 0.55mm |
| | k-Wave/Exp | 3.68% | 3.16% | 9.76% | 0.76% | 0.69mm |
| | CIVA/Exp | 3.81% | 3.36% | 10.16% | 0.68% | 0.61mm |
| $-10$ | SplineBeam/Exp | 1.94% | 1.53% | 4.91% | 2.42% | 2.46mm |
| | k-Wave/Exp | 2.06% | 1.44% | 5.27% | 2.10% | 2.13mm |
| | CIVA/Exp | 2.46% | 1.93% | 6.19% | 2.46% | 2.50mm |
| 0 | SplineBeam/Exp | 4.70% | 0.06% | 4.82% | 0.47% | 0.52mm |
| | k-Wave/Exp | 1.89% | 0.38% | 1.01% | 0.61% | 0.66mm |
| | CIVA/Exp | 4.48% | 0.71% | 3.01% | 0.88% | 0.96mm |
| $+10$ | SplineBeam/Exp | 0.67% | 2.52% | 5.82% | 0.98% | 1.17mm |
| | k-Wave/Exp | 0.87% | 2.14% | 4.49% | 0.71% | 0.85mm |
| | CIVA/Exp | 1.03% | 1.33% | 3.72% | 0.96% | 1.15mm |
| $+20$ | SplineBeam/Exp | 1.24% | 3.24% | 7.90% | 0.22% | 0.28mm |
| | k-Wave/Exp | 1.93% | 2.75% | 7.69% | 0.04% | 0.05mm |
| | CIVA/Exp | 1.58% | 2.04% | 5.77% | 0.60% | 0.77mm |
| $+30$ | SplineBeam/Exp | 1.89% | 3.53% | 9.21% | 0.62% | 0.85mm |
| | k-Wave/Exp | 0.36% | 2.48% | 6.54% | 0.38% | 0.52mm |
| | CIVA/Exp | 1.92% | 2.66% | 7.41% | 0.27% | 0.37mm |

The focal depth, length and width errors are quite reasonable (below 6%), and they are very close to each other for the three simulation methods (the error difference is almost always under 1%). The highest errors (higher than 5%) are obtained with steering $-30$mm. Overall, the errors get bigger when the steering decreases. In addition, the focal width errors are bigger than the other ones. We think this is due to the fact that when the dimensions are smaller (the focal spot is smaller for lower steerings and the focal width is smaller than the focal length and depth), a small error of the order of the zone step (0.5mm) gives a high percentage of error. We notice that the focal volume errors are proportional to the focal length and width errors: $\Delta V_{focal} \approx \Delta l_{focal} + 2\Delta w_{focal}$. The focal spot position errors are quite low, almost always under 1mm, but not that low, which suggests that we can not hope focal spot position errors to be lower than 1mm for the configurations with skull. For steerings $-10$mm and $+10$mm, the focal spot position errors are bigger than 1mm and go up to 2.5mm. We think this could be due to an error in the measurements. Indeed, in earlier experiments, we measured the pressure fields with the same steerings and found focal spot positions closer to the simulated ones ($DeltaX_{max}^{water} < 1$mm). However, these measurements were made with a different hydrophone (Onda HGL-0200); so for the consistency of the results, these errors are not presented here.

The measured and SplineBeam simulated pressure fields for steering 0 (transducer natural focal) are displayed in figures 4.12 and 4.13.

The simulated and measured pressure fields are very similar, except at the beginning of the $X$ axis, which

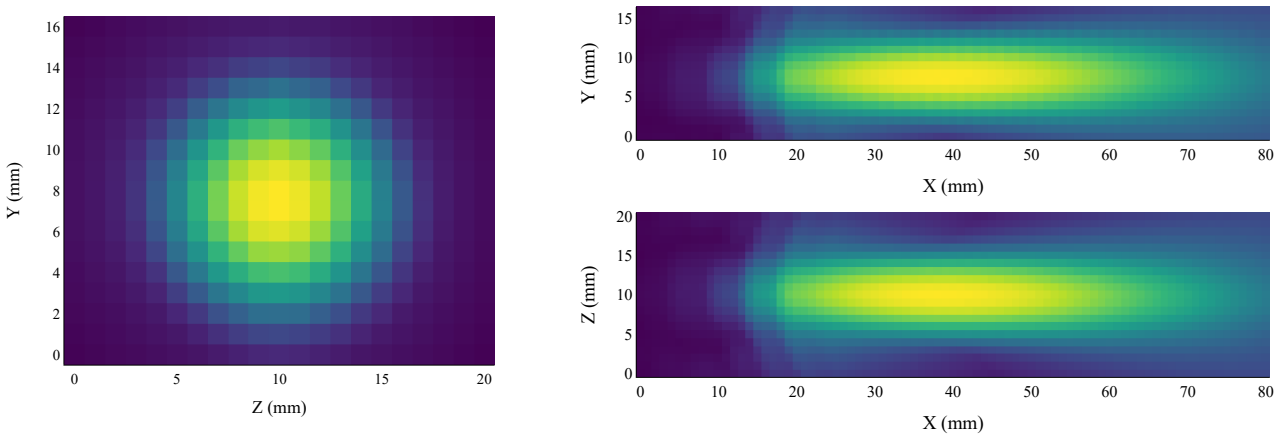


*Figure 4.12: Experimental pressure field planes with no electronic steering*

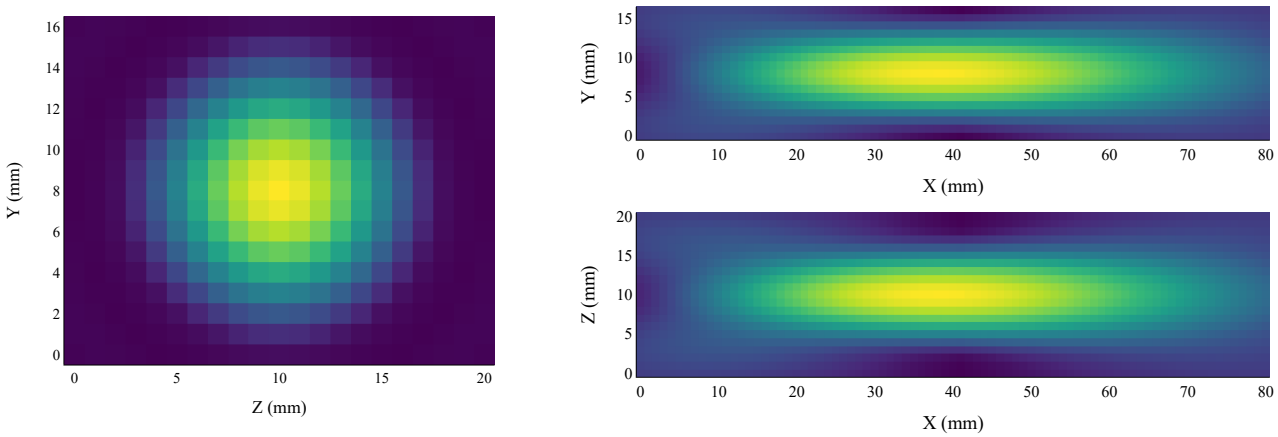


*Figure 4.13: SplineBeam simulated pressure field planes with no electronic steering*

is near the transducer.

## 4.6 Evaluation of SplineBeam realism by comparison of simulated and measured pressure fields through a human skull sample

### 4.6.1 Measurement positioning error

For all 3 transducer positions, the positioning error $\Delta X_{err}$ of the measurements is computed as:

$$\Delta X_{err} = ||X_{max}^{exp,water} - X_{max}^{simu,water}|| \tag{4.19}$$

where $X_{max}^{exp,water}$ and $X_{max}^{simu,water}$ are the maximum pressure positions of the experimental and simulated fields for the configurations with the skull removed.

All simulations are run with the transducer moved so that the simulated pressure field without skull matches the measured pressure field without skull. The positioning errors for the 3 transducer positions are given in table 4.3.

*Table 4.3: Positioning errors of the measurements*

| Position n°1 | Position n°2 | Position n°3 |
|---|---|---|
| 1.25mm | 1.12mm | 1.12mm |

### 4.6.2 Comparison of the measured and simulated pressure fields through the human skull sample

The measured and SplineBeam simulated pressure field planes for all 3 transducer positions are displayed in figures 4.14, 4.15 and 4.16. The difference between the simulated and experimental fields is also plotted for better analysis. All fields are in percentage of the maximum pressure of the fields without skull (the simulated pressure fields with skull are normalized with respect to the simulated pressure fields without skull and the experimental pressure fields with skull are normalized with respect to the experimental pressure fields without skull).

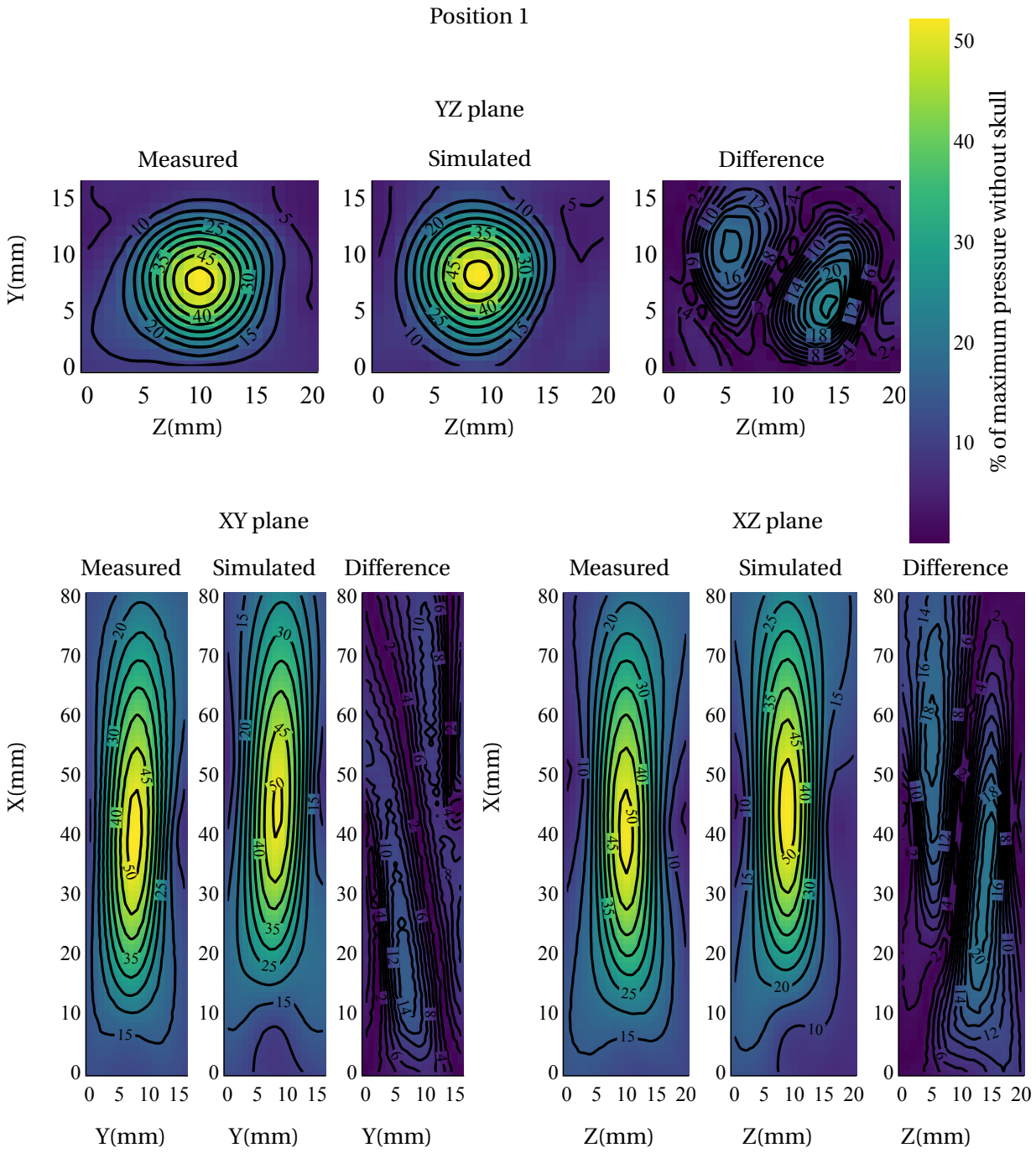


*Figure 4.14: Experimental and simulated pressure field planes for transducer position n°1.*

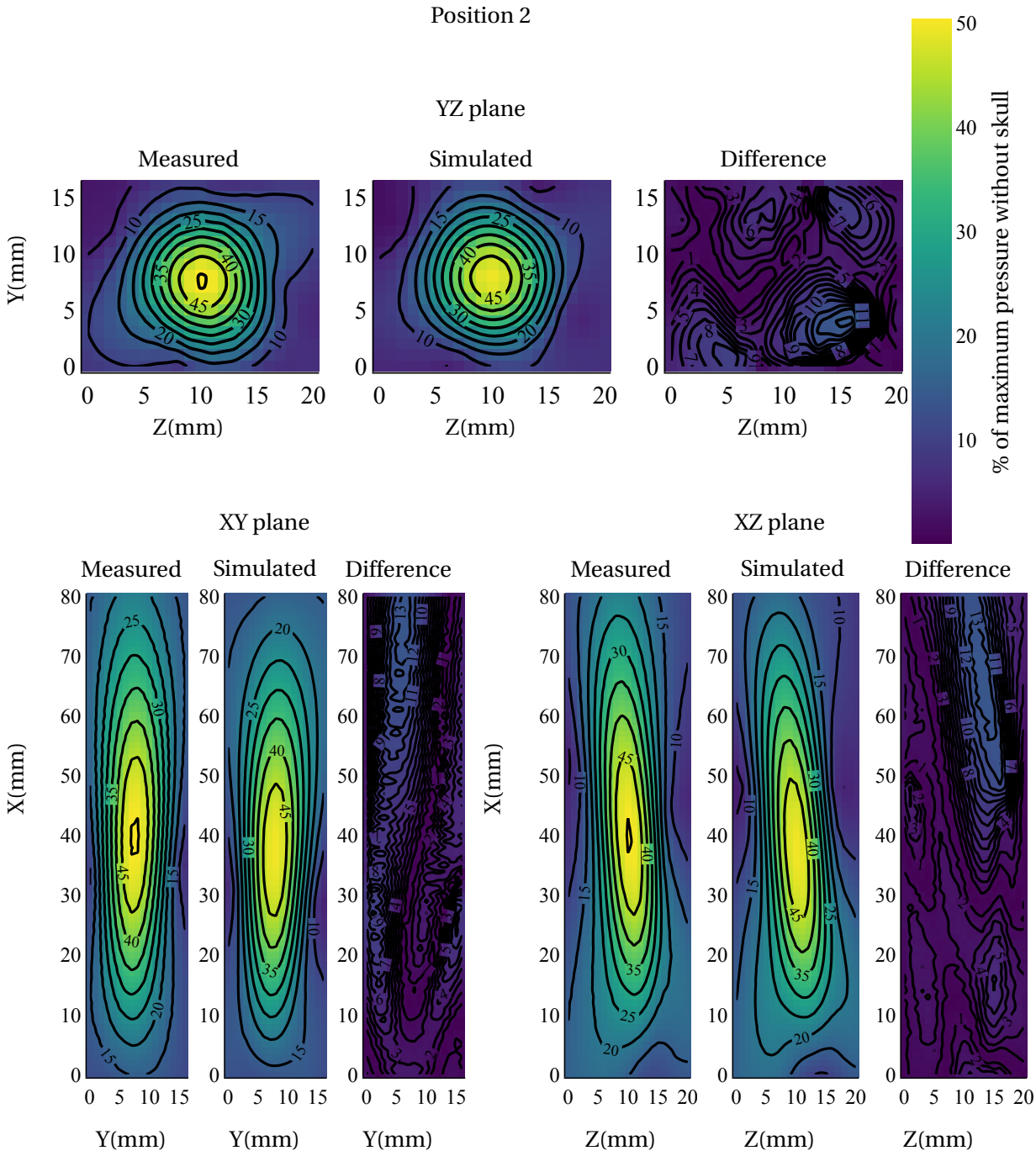


*Figure 4.15: Experimental and simulated pressure field planes for transducer position n°2.*

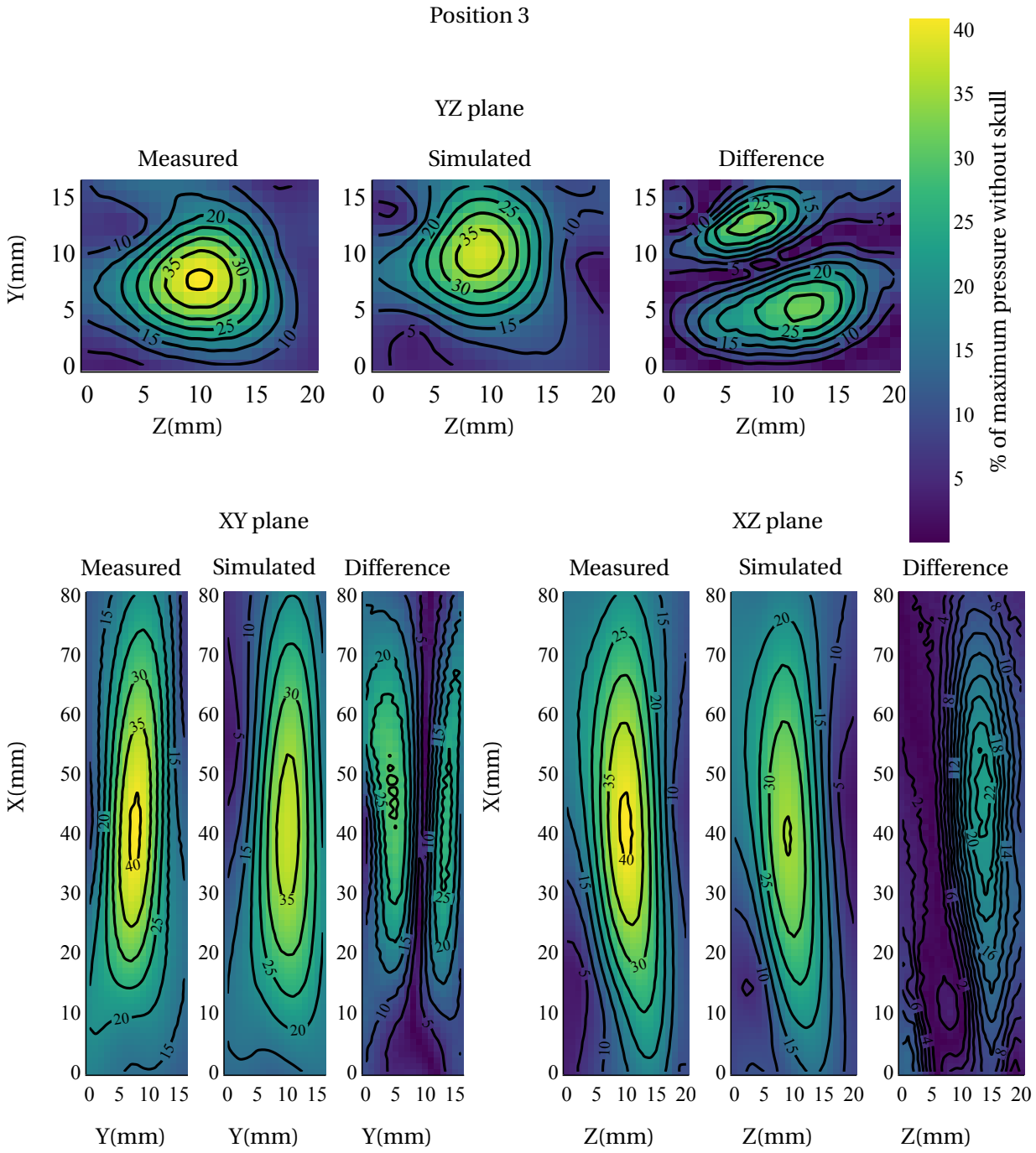


*Figure 4.16: Experimental and simulated pressure field planes for transducer position n°3.*

These figures show that, qualitatively, SplineBeam simulated pressure fields are close to the measured ones, for all transducer positions.

For all 3 transducer positions, the focus position error $\Delta X_{max}$, focus amplitude error $\Delta P_{max}$ and focal volume error $\Delta V_{focal}$ between the experimental and simulated (either with SplineBeam, CIVA or k-Wave) fields are displayed in table 4.4. k-Wave is run with a homogeneous skull model and a heterogeneous one. The relative differences of focus position, amplitude and volume, of the measured pressure fields with and without skull, are also displayed for reference.

Table 4.4 shows overall a good agreement between the measured pressure fields and the simulated ones with all simulation methods. Most focus position errors are between 1mm and 2mm. Most maximum pressure errors are lower than 2dB, which is very low compared to the difference of maximum pressure between the measurements with and without skull (which is always higher than 13dB). The focal volume errors are all lower than 20%, which corresponds approximately to a one dimensional error of 7% (as observed in 4.5), which is reasonable. In addition, the focal volume errors sometimes reached 15% for the configurations

*Table 4.4: Comparison of the simulated pressure fields with the experimental ones for the configurations through the skull sample*

| Pos | Comparison | $\Delta X_{max}$ | $\Delta P_{max}$ | $\Delta V_{focal}$ |
|---|---|---|---|---|
| 1 | With/without skull | 4.64mm | −13.12dB | 2.43% |
| | SplineBeam/Exp | 1.58mm | −0.14dB | 0.28% |
| | k-Wave heterogeneous/Exp | 1.58mm | −2.00dB | 6.16% |
| | k-Wave homogeneous/Exp | 2.55mm | −1.58dB | 1.75% |
| | CIVA/Exp | 2.06mm | +0.14dB | 3.74% |
| 2 | With/without skull | 1.73mm | −13.70dB | 6.44% |
| | SplineBeam/Exp | 1.00mm | +0.17dB | 11.70% |
| | k-Wave heterogeneous/Exp | 1.12mm | −1.98dB | 18.26% |
| | k-Wave homogeneous/Exp | 1.50mm | −1.51dB | 16.20% |
| | CIVA/Exp | 1.50mm | +2.18dB | 11.88% |
| 3 | With/without skull | 2.12mm | −17.91dB | 48.43% |
| | SplineBeam/Exp | 1.12mm | +0.54dB | 14.82% |
| | k-Wave heterogeneous/Exp | 2.60mm | −0.11dB | 15.38% |
| | k-Wave homogeneous/Exp | 1.87mm | −1.17dB | 11.97% |
| | CIVA/Exp | 1.22mm | +0.43dB | 6.77% |

without skull, which shows that the focal volume errors for the configurations with skull are not that high.

The maximum pressure position error is lower for SplineBeam than for the other simulation methods for all 3 positions. It is always under 1.6mm, but never drops below 1mm, which was expected given that the measurement positioning errors are around 1mm and that the focal position errors for the configurations without skull sometimes reached 1mm. k-Wave with a heterogeneous skull model also gives small maximum pressure position errors (<1.6mm), except for position n°3, where the error is even bigger than the difference with/without skull by 0.5mm.

The maximum pressure error for SplineBeam is very low (<0.6dB in absolute value) for all 3 configurations. It is possibly biased by the choice of the attenuation coefficient which is widely debated in the literature. However, the values of $\Delta P_{max}$ are closer to each other than with k-Wave heterogeneous or with CIVA, which suggests that for k-Wave heterogeneous and CIVA there does not exist any value of attenuation coefficient such that all $\Delta P_{max}$ are low. With k-Wave homogeneous, the values of $\Delta P_{max}$ are also close to each other, which suggests that with another attenuation coefficient value, this simulation method could give realistic results in terms of maximum pressure.

In terms of focal volume, CIVA gives overall the lowest errors (in average 7.46%), while k-Wave heterogeneous gives the highest ones (in average 13.27%). Taking the three metrics into account, k-Wave and CIVA are approximately equivalent in terms of simulating pressure fields close to the measured ones.

Overall, SplineBeam has quite low errors and lower than the other simulation methods. SplineBeam highest error is the focal volume error for position n°3 of 14.82%, which corresponds to a one dimensional error of less than 5% which is reasonable. In addition, for all metrics, SplineBeam errors are approximately proportional to the difference with/without skull. This shows that SplineBeam is always able to simulate part of the ultrasound beam attenuation, shift and distortion, but not all of it.

### 4.6.3 Experimental validation of the homogenization method

When comparing k-Wave simulations with a homogeneous skull model versus with a heterogeneous skull model, we notice that the homogeneous skull model gives better results in terms of focal volume for the 3 configurations, by in average 3%. For the first two positions, the homogeneous model gives better results in terms of maximum pressure value (by in average 0.45dB) while the heterogeneous one gives better results in terms of maximum pressure position (by in average 0.67mm), except for transducer position n°3 for which it is the opposite: the heterogeneous model gives better results in terms of maximum pressure value (by 1.06dB) while the homogeneous one gives better results in terms of maximum pressure position (by 0.73mm). It is quite surprising that the homogeneous model gives in average focus position errors higher than the heterogeneous model as both models were expected to be close to each other in terms of focus

position, as explained in section 2.2.2. Thus, we investigated by looking at the focus position differences $X_{max}^{simu,skull} - X_{max}^{exp,skull}$ along the 3 axis of the computation zone. These differences are displayed in table 4.5.

*Table 4.5: Focus position difference along $X$, $Y$ and $Z$ axis between the measured pressure fields and the k-Wave simulated ones*

| Skull model | Position n°1 | Position n°2 | Position n°3 |
|---|---|---|---|
| Heterogeneous | $(1.5, 0, -0.5)$mm | $(-1, 0, -0.5)$mm | $(2.5, 0.5, -0.5)$mm |
| Homogeneous | $(2.5, 0.5, 0)$mm | $(-1.5, 0, 0)$mm | $(1.5, 0.5, 1)$mm |

We notice that the heterogeneous skull model and the homogeneous skull model are equivalent in terms of perpendicular (to the ultrasound beam) shift, as the differences along the $Y$ and $Z$ axis are similar (the perpendicular shift error difference between the heterogeneous model and the homogeneous one is 0mm for the first position and around 0.5mm for the two last positions). It is for the parallel shift (along the $X$ axis) that the heterogeneous skull model is better than the homogeneous one (by 0.83mm in average).

## 4.7 Conclusion

In this last chapter, SplineBeam was experimentally validated by comparing simulated pressure fields with hydrophone measured ones through a human skull sample. We built an experimental set-up and defined a precise protocol for these transcranial hydrophone measurements. Measurements in water allowed to validate the protocol. Then, we defined methods to simulate the same configurations as in the measurements with several simulation tools: SplineBeam, k-Wave and CIVA. Finally, we carried out these experiments and reached a positioning error lower than 1.5mm. We then compared the measured pressure fields with those simulated with SplineBeam, as well with pressure fields simulated by other methods (k-Wave and CIVA). The pressure fields simulated with SplineBeam were very similar to the measured ones ($\Delta X_{max} \leqslant 1.58$mm, $|\Delta P_{max}| \leqslant 0.54$dB, $\Delta V_{focal} \leqslant 14.82\%$), which shows the reliability of both the simulation method developed in chapter 3 and the skull model developed in chapter 2. Besides comparing, for the first time, measured and semi-analytical simulated pressure fields, we also compared, for the first time to our knowledge, the pressure fields computed by a numerical method (k-Wave) and by semi-analytical methods (SplineBeam and CIVA) with a "ground truth" (measured pressure fields). We showed that SplineBeam simulated pressure fields were closer to the measured ones than k-Wave simulated ones, and that CIVA simulated pressure fields were approximately equivalent to those simulated with k-Wave. This confirms the potential of semi-analytical methods for transcranial ultrasound simulations as was shown by Bancel et al. [19] for aberration correction. It also confirms the advantage of the new path computation method (SplineBeam) over ray-tracing (CIVA) and of the smooth skull model (SplineBeam) over the mesh model (CIVA). In addition, the measurements also allowed to evaluate the homogenization method alone, by comparing the pressure fields computed with k-Wave with a homogeneous skull model versus with a heterogeneous one. The pressure fields simulated through both models were quite equivalent in terms of focal spot metrics, which suggests that a homogeneous assumption can be enough to model the skull, with a good homogenization method. Due to a lack of time, we did not compare the measured and simulated pressure fields through several skull samples. In addition, we did not have enough time to work more on reducing the positioning error of the measurements, which is still a bit too high compared to the skull induced focus shift. However, we know it would be hard to have a positioning error below the focus spot position errors for the configurations without skull. Thus, reaching a positioning error below 1mm seems a realistic objective. Finally, one of the next steps would be to measure absolute (and not relative) pressure values.

# Discussion

This PhD work consisted in developing a fast transcranial ultrasound simulation method based on a new personalized smooth and homogeneous skull model. The ability of this new simulation method to compute realistic pressure fields through the skull was verified experimentally.

To develop a personalized skull model, the skull geometry and acoustic properties were derived from a CT scan. First, we proposed a method to model the skull surfaces in a smooth way, to avoid having sharp edges that can generate numerical problems, and also to get closer to the real skull geometry. We chose to use MBA to model the skull external surfaces, and we defined a protocol to build these MBA surfaces from the meshes extracted from the CT scan. Then, we developed a new method for skull acoustic property homogenization. First, this method models the skull as a three-layer medium (cortical bone - trabecular bone - cortical bone). Then, it computes an equivalent density and an equivalent sound speed, from formulas derived previously by minimizing the time-of-flight and transmission coefficient errors. CIVA simulations were performed to compare the pressure fields through the original heterogeneous media (derived from skull CT scans) with those through the averaged media (densities and sound speeds computed by averaging those of the heterogeneous media) and the proposed equivalent media (densities and sound speeds computed with the new homogenization method). The simulated pressure fields through the equivalent media gave focal spot position and volume similar to the heterogeneous media and the averaged one, but focal spot pressure much closer to the original heterogeneous media than the averaged media. Thus, this homogenization method provides a promising new homogeneous skull model for semi-analytical simulations.

We also developed a new transcranial ultrasound simulation method based on time-of-flight minimization, that requires a smooth and homogeneous skull model as the one developed in chapter 2. First, we developed a path computation method based on time of flight minimization, to overcome the unequal transducer sampling problem that can occur with standard ray-tracing methods such as the one used in CIVA. We applied this new path computation method to compute delay laws for skull aberration correction. We showed that the delay laws computed with this method, called SplineRay, gave a way better focusing than straight ray-tracing laws and a similar focusing to CIVA simulated laws but with a lower computation time. Then, the pencil method for ultrasonic field computation (used in CIVA) was adapted so that the ultrasonic paths are computed by time of flight minimization. The new ultrasound simulation algorithm thereby developed was called SplineBeam. It was validated numerically by comparison with other solvers on several benchmark configurations: in water, through bone layers of analytical shapes and through skull samples. The pressure fields computed by SplineBeam were very similar to the ones simulated with the other solvers for all configurations. SplineBeam computation time was evaluated and is lower than CIVA and a bit higher than k-Wave for a same number of computation points. However, the advantage of SplineBeam is that, unlike k-Wave, it has no constraints on the spatial step nor the computation zone size, which allows it to reduce drastically the number of computation points, and thus be faster than k-Wave by two orders of magnitude for some practical cases.

Finally, SplineBeam was experimentally validated by comparing simulated pressure fields with hydrophone measured ones through a human skull sample. SplineBeam simulated pressure fields simulated were very similar to the measured ones, for all focal metrics (position, amplitude and volume). It shows that the simulation method developed in chapter 3, as well as the skull model developed in chapter 2, are realistic. This is the first time measured and semi-analytical simulated transcranial pressure fields were compared. It is also the first time, to our knowledge, that pressure fields computed by a numerical method (k-Wave) and by semi-analytical methods (SplineBeam and CIVA) were compared with measured pressure fields. SplineBeam simulated pressure fields were closer to the measured ones than k-Wave simulated ones. This confirms the potential of semi-analytical methods for transcranial ultrasound simulations. In addition, SplineBeam simulated pressure fields were closer to the measured ones than CIVA simulated ones. This confirms the advantage of the new path computation method and the smooth skull model developed in SplineBeam, over

ray-tracing and the mesh model used in CIVA. The measurements also allowed evaluating the homogenization method alone, by comparing the pressure fields computed with k-Wave with a homogeneous skull model and with a heterogeneous one. The pressure fields simulated through both models were approximately equivalent in terms of focal spot metrics. This shows that a homogeneous description of the skull can be enough, with a homogenization method more realistic than the averaging method.

As mentioned in chapter 2, the homogenization method developed is a proof of concept and could thus be improved. For instance, the equivalent density could be computed using a machine learning tool more sophisticated than a linear regression. In addition, even if chapter 4 provides a first promising experimental validation of the skull model developed in chapter 2, measurements through phantoms, of known geometry and acoustic properties, would allow to properly validate the method. The three-layer model obtained after the first step of the homogenization method also appears as a promising skull model, but two difficulties must be overcome to use it with SplineBeam. First, a method to properly extract the interfaces between cortical and trabecular bone layers must be defined. Second, SplineBeam must be extended to compute pressure fields through more than two interfaces.

Regarding the simulation method developed, the next upgrades would be to generalize the path computation algorithm so that SplineBeam can compute pressure fields or delay laws through any number of interfaces. It will allow, for transcranial simulations or aberration correction, to include a layer of skin, or to model the skull as a three layer medium (cortical bone - trabecular bone - cortical bone), or even as a multi-layer medium as is done in [54]. In addition, it will allow to compute the field in the first and second layers. Finally, it will allow to include reflections inside the layers. In terms of computation time, SplineBeam is quite fast (3 minutes for the experimental configurations) but still not enough to reach real time computations. The main limitation in terms of computation time is the optimization algorithm L-BFGS used to compute the ultrasonic paths. Thus, a GPU version of L-BFGS could be used or a faster optimization algorithm could be used. In the meantime, samplings specific to each transducer shape could be developed to reduce the number of paths that need to be computed. In addition, this would probably also improve the field computation accuracy.

To further validate SplineBeam and the skull model, more experimental measurements could be carried out. Indeed, more transducer positions could be performed, several skull samples and transducers could be used. Comparing the measured and simulated pressure fields through several skull samples would allow to confirm the value of the attenuation coefficient (specific to our simulation method and skull model), or to determine a more complicated attenuation law. Besides, the positioning error of the measurements is still too high compared to the skull induced focus shift. Thus, the positioning protocol needs to be further improved, for example by using a new material for the skull positioning frame, that could combine rigidity and CT scan compatibility. However, we know it would be hard to have a positioning error below the standard CT scan resolution of around $0.6$mm. Finally, the hydrophone measured fields can not be considered as an absolute truth as the hydrophone measurements are not always repeatable. This is probably due to the hydrophone finite precision that we have not quantified here.

# Appendix A

# Python codes for skull acoustic property modeling

## A.1 Read DICOM files

```
import numpy as np
import os

def readDicom(directory):
    files = os.listdir(directory)
    nbSlices = len(files)
    first = True

    for f in files:
        dicom_file = pydicom.dcmread(directory + f)
        array = dicom_file.pixel_array

        if first:
            nbRows, nbCols = array.shape
            dicomMat = np.zeros((nbRows, nbCols, nbSlices))
            first = False

        if dicom_file.InstanceNumber == 1:
            orientation = np.array(dicom_file.ImageOrientationPatient)
            position = np.array(dicom_file.ImagePositionPatient)
            pixelSpacing = np.array(dicom_file.PixelSpacing)

        if dicom_file.InstanceNumber == 2:
            position2 = np.array(dicom_file.ImagePositionPatient)

        dicomMat[:, :, dicom_file.InstanceNumber - offset - 1] = array

    pixelSpacing = np.append(pixelSpacing, abs(position[2] - position2[2]))
    return dicomMat, position, orientation, pixelSpacing
```

## A.2 Skull segmentation

```
    from copy import deepcopy
    from skimage.measure import label, regionprops
    import numpy as np

    dicomMat[dicomMat < threshold] = HUwater
```

```
    dicomMat_bin = deepcopy(dicomMat)
    dicomMat_bin[dicomMat < threshold] = 0
    dicomMat_bin[dicomMat >= threshold] = 1

    labeled_matrix_bis = label(dicomMat_bin, connectivity=1)
    max_region = None
    max_area = -1
    for region in regionprops(labeled_matrix_bis):
        if max_area != -1:
            if region.area > max_area:
                max_area = region.area
                max_region = region
        else:
            max_area = region.area
            max_region = region

    dicomMat[np.where((labeled_matrix_bis != max_region.label) &
    (dicomMat_bin != 0))] = HUwater
```

## A.3 Index/coordinate conversion

```
import numpy as np

def idx2coord(point, toCoord, origin, orientation, spacing):
    """
        - point is the point we search the equivalent matrix index /
        coordinate
        - toCoord is a boolean equal to True if it's a conversion matrix
        index -> coord and False if it's a conversion coord - > matrix
        index
        - origin gives the coordinates of the center of the upper left voxel of
        the first slice
        - orientation gives the direction cosines of the first row (j) and
        first column (i)
        - spacing gives the spacing along the axes (i,j,k)
    """

    # Create rotation matrix
    uj = orientation[:3]
    ui = orientation[3:6]
    uk = np.cross(ui,uj)
    Rt = np.array([ui[:], uj[:], uk[:]])
    R = deepcopy(np.transpose(Rt)) #so that R and Rt can be modified independently

    # Translates the origin at the corner of the first voxel
    t = origin - 0.5*spacing

    # Takes voxel spacing into account
    R[0,:] *= spacing[0]
    R[1,:] *= spacing[1]
    R[2,:] *= spacing[2]
    Rt[:,0] /= spacing[0]
    Rt[:,1] /= spacing[1]
    Rt[:,2] /= spacing[2]

    # Fill matrix M
```

```
    M = np.zeros((4, 4))
    M[:3, :3] = R
    M[:3, 3] = t
    M[3, :3] = [0,0,0]
    M[3, 3] = 1

    # Fill matrix M_inv
    M_inv = np.zeros((4, 4))
    M_inv[:3, :3] = Rt
    M_inv[:3, 3] = np.dot(-Rt, t)
    M_inv[3, :3] = [0,0,0]
    M_inv[3, 3] = 1

    point4 = np.append(point, 1)

    # From matrix index to coord
    if toCoord:
        return np.dot(M, point4)[:3]
    # From coord to matrix index
    else:
        return np.dot(M_inv, point4)[:3]
```

## A.4 Zone creation

```
import numpy as np

def createZone(dicomMat, origin, orientation, spacing, Mzone, zone_spacing,
zone_dim):

    Nx, Ny, Nz = np.divide(zone_dim, zone_spacing).astype(int)
    res = np.zeros((Nx+1, Ny+1, Nz+1))

    for k in range(Nz+1):
        for j in range(Nx+1):
            for i in range(Ny+1):
                x = -0.5*zone_dim[0] + j*zone_spacing[0]
                y = -0.5*zone_dim[1] + i*zone_spacing[1]
                z = -0.5*zone_dim[2] + k*zone_spacing[2]
                pnt = np.array([x, y, z])

                # point in CT coordinate
                pnt_ref_CT = np.dot(M_zone, np.append(pnt, 1))[:3]
                # floating index of the point
                pnt_mat = mat2coord(pnt_ref_CT, False, origin, orientation,
                spacing)
                # interpolate the values from its 8 neighbours
                res[i,j,k] = interpolate(pnt_mat, dicomMat)

    return res
```

# Appendix B

# Evaluation of the influence of internal reflections and shear waves

## B.1 Evaluation of the influence of internal reflections

The influence of internal reflections was assessed in the case of a three layer medium with planar parallel interfaces, which is the case where their influence should be the biggest because of the parallel interfaces. CIVA Healthcare simulated fields with and without reflections taken into account were compared. 32 configurations were simulated, with different thicknesses, frequencies and acoustic properties, as detailed in table 2.6. The transducer described in section 2.2.2.3 was used. The focal position, pressure and volume errors between the fields with and without reflections (computed using the metrics displayed in table 2.3), averaged on the 32 configurations, are shown in table B.1.

*Table B.1: Average relative errors between simulated pressure fields with and without reflections taken into account*

| **Attenuation** | $E_{\mathbf{pos}}$ | $E_{\mathbf{amp}}$ | $E_{\mathbf{dim}}$ |
|---|---|---|---|
| Without attenuation | 0.28mm | 1.04% | 1.30% |
| With attenuation | 0.06mm | 0.51% | 0.46% |

The results show that, even without attenuation, the internal reflections are quasi negligible with average focal pressure and volume errors between 1% and 1.5% and a focal position error of 0.28mm which is close to the spatial step used for k-Wave simulations at those frequencies. When attenuation is taken into account in the simulations, The focal pressure error is divided by 2, the focal volume error by 3 and the focal position error by approximately 5.

## B.2 Evaluation of the influence of shear waves

The influence of shear waves was assessed in the case of a three layer medium with planar parallel interfaces. CIVA Healthcare simulated fields with and without shear waves taken into account were compared. The same 32 configurations as in appendix A were simulated, with thicknesses, frequencies and acoustic properties, as detailed in table 2.6. The transducer described in section 2.2.2.3 was used. The focal position, pressure and volume errors between the fields with and without shear waves (computed using the metrics displayed in table 2.3), averaged on the 32 configurations, are shown in table B.2.

*Table B.2: Average relative errors between simulated pressure fields with and without shear waves taken into account*

| $E_{\mathbf{pos}}$ | $E_{\mathbf{amp}}$ | $E_{\mathbf{dim}}$ |
|---|---|---|
| 0mm | 0.62% | 3.27% |

The results show that shear waves are negligible if we are interested in focal position and pressure, as the errors are respectively of 0mm and $0.62\%$. The focal volume error is a bit higher ($3.37\%$). However, an error of around $3\%$ in volume corresponds to an error in length of around $1\%$. Thus all these errors are reasonable, meaning that shear waves can be neglected in a first approximation.

# Appendix C

# Diagram of the computation field algorithm steps

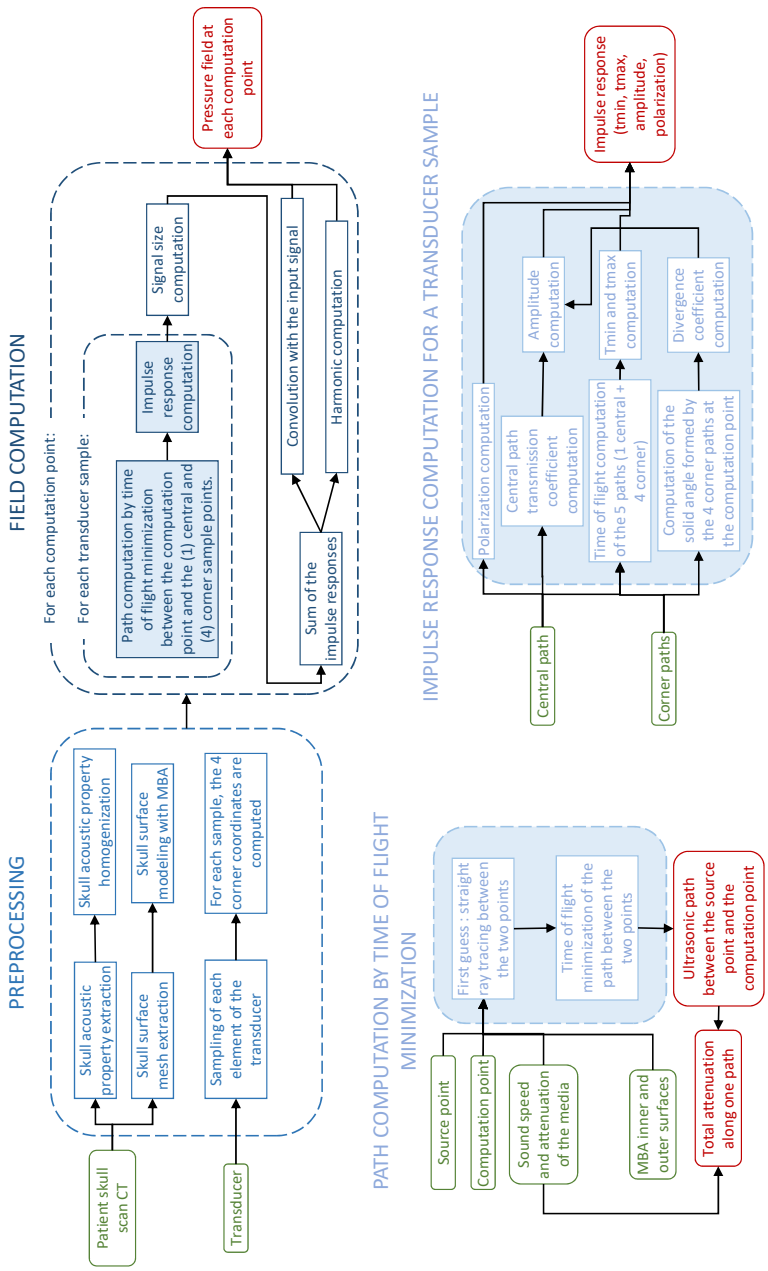


*Figure C.1: Diagram of the computation field algorithm steps (detailed in chapter 3)*

# Appendix D

# C++ code for impulse response sum

To add an impulse response of amplitude $A_{IR}$ (as computed in equation 3.16) and polarization $p$ to the final signal at index $k$, the following code is used:

```
const double A = rho3 / sL3;
const double B = rho3 * sL3 / sT3 / sT3;
const double C = A - 2 * B;

// Real displacement components
sig_dis_x_real[k] += A_IR.real * p.x;
sig_dis_y_real[k] += A_IR.real * p.y;
sig_dis_z_real[k] += A_IR.real * p.z;

// Imaginary displacement components
sig_dis_x_imag[k] += A_IR.imag * p.x;
sig_dis_y_imag[k] += A_IR.imag * p.y;
sig_dis_z_imag[k] += A_IR.imag * p.z;

// Real pressure components
sig_pres_S1_real[k] += A_IR.real * (p.x * p.x * A + p.y * p.y * C + p.z * p.z * C);
sig_pres_S2_real[k] += A_IR.real * (p.x * p.x * C + p.y * p.y * A + p.z * p.z * C);
sig_pres_S3_real[k] += A_IR.real * (p.x * p.x * C + p.y * p.y * C + p.z * p.z * A);

// Imaginary pressure components
sig_pres_S1_imag[k] += A_IR.imag * (p.x * p.x * A + p.y * p.y * C + p.z * p.z * C);
sig_pres_S2_imag[k] += A_IR.imag * (p.x * p.x * C + p.y * p.y * A + p.z * p.z * C);
sig_pres_S3_imag[k] += A_IR.imag * (p.x * p.x * C + p.y * p.y * C + p.z * p.z * A);
```

With rho3, sL3 and sT3 the density, longitudinal and transversal sound speeds of the material containing the transducer.

# Appendix E

# Comparison of SplineBeam and k-Wave pressure fields on benchmark configurations

In this appendix, all the pressure field comparisons between SplineBeam and k-Wave on the benchmark configurations proposed by Aubry et al. [10] are displayed. Boxplots comparing SplineBeam with k-Wave and the other solvers are also displayed.

## E.1 Water configurations

### E.1.1 Without attenuation

#### E.1.1.1 Spherically curved transducer

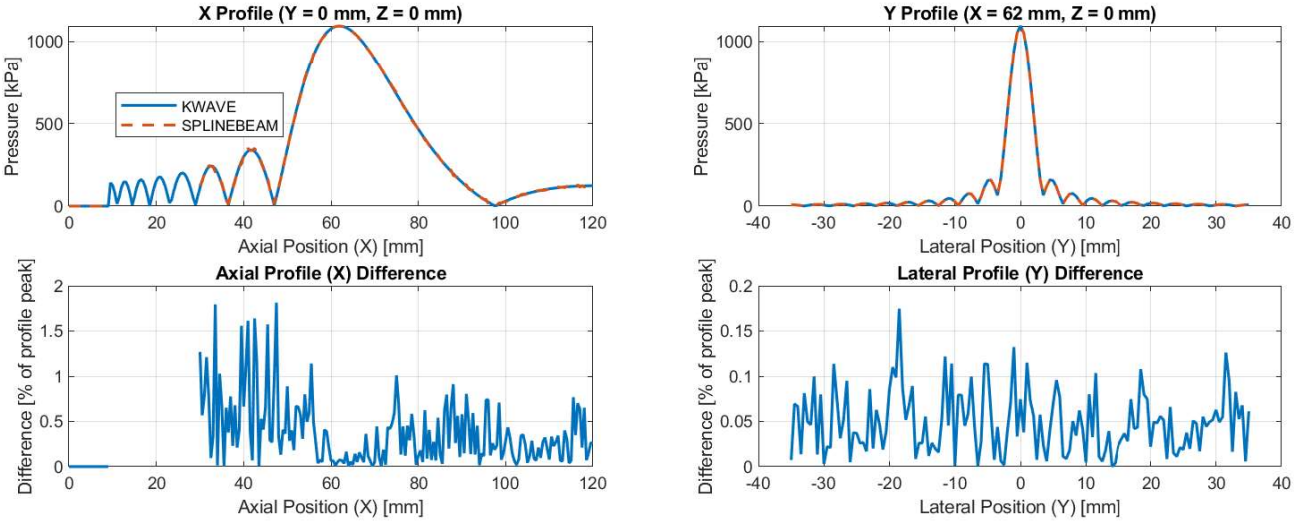


*Figure E.1: Comparison of SplineBeam and k-Wave pressure field profiles for configuration BM1-SC1*

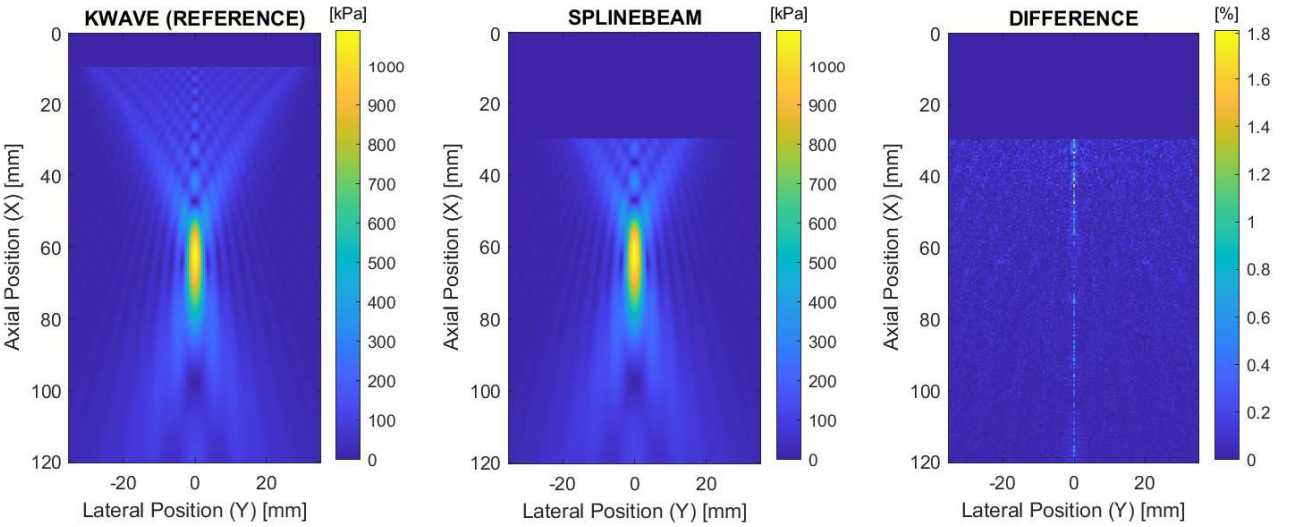


*Figure E.2: Comparison of SplineBeam and k-Wave pressure field XY planes for configuration BM1-SC1*

### E.1.1.2 Piston transducer

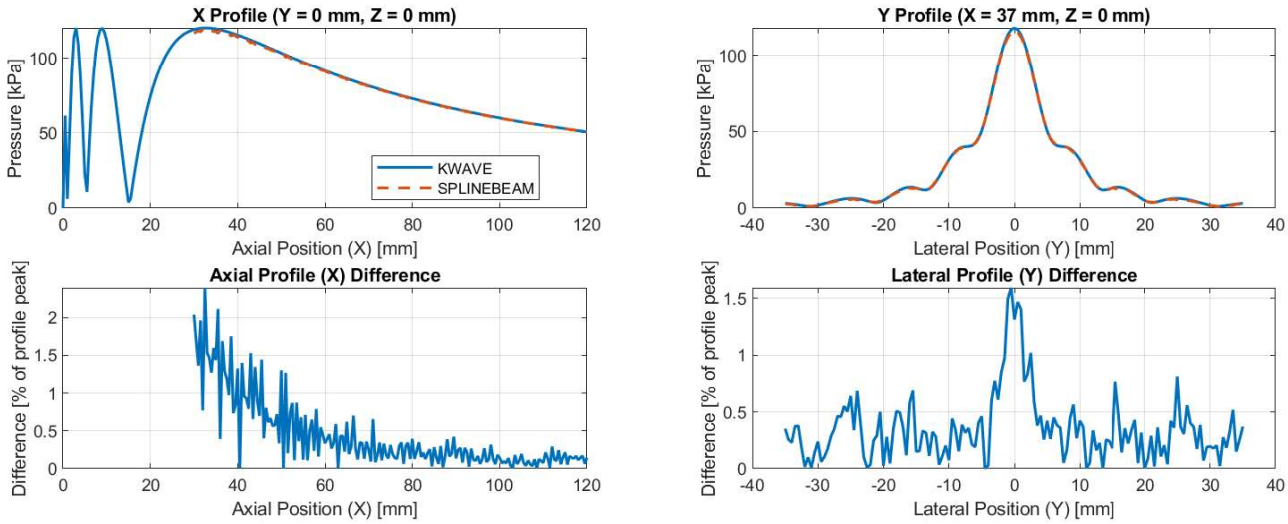


*Figure E.3: Comparison of SplineBeam and k-Wave pressure field profiles for configuration BM1-SC2*

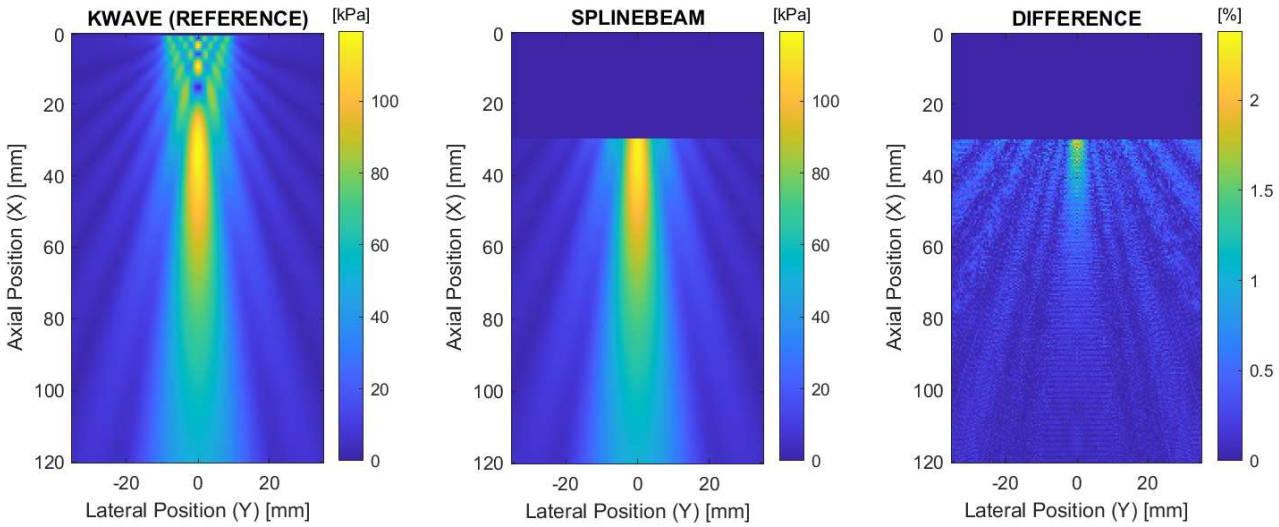


*Figure E.4: Comparison of SplineBeam and k-Wave pressure field XY planes for configuration BM1-SC2*

### E.1.2 With attenuation

#### E.1.2.1 Spherically curved transducer

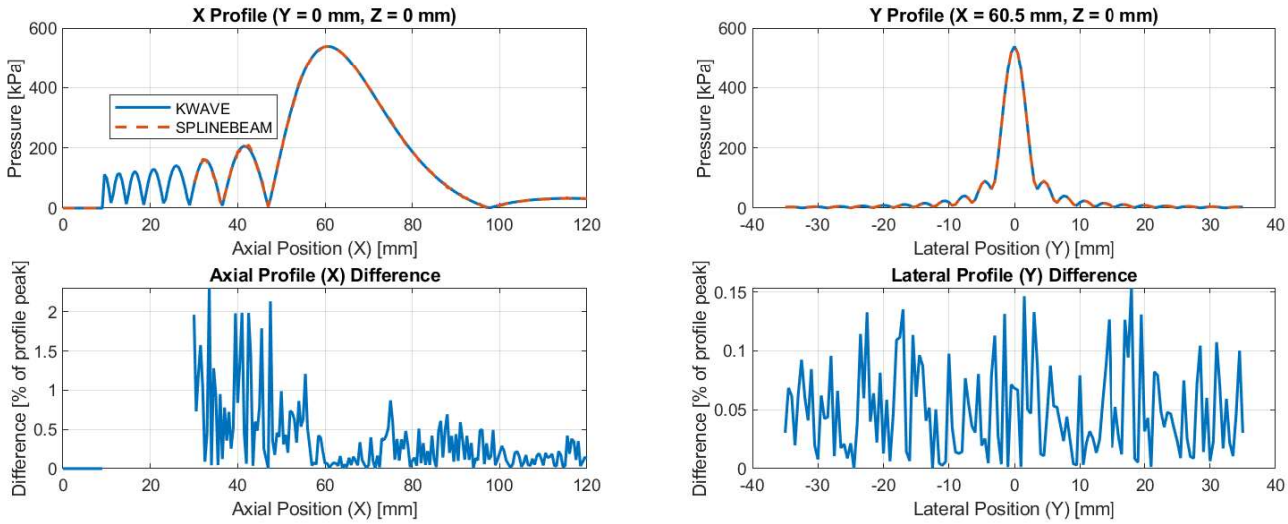


*Figure E.5: Comparison of SplineBeam and k-Wave pressure field profiles for configuration BM2-SC1*

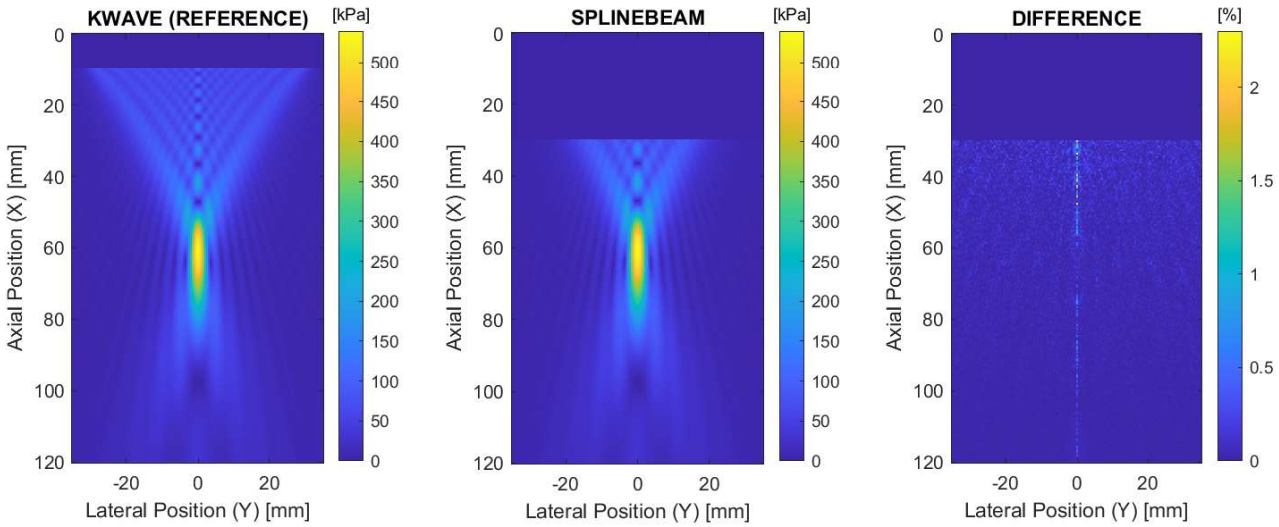


*Figure E.6: Comparison of SplineBeam and k-Wave pressure field XY planes for configuration BM2-SC1*

### E.1.2.2 Piston transducer

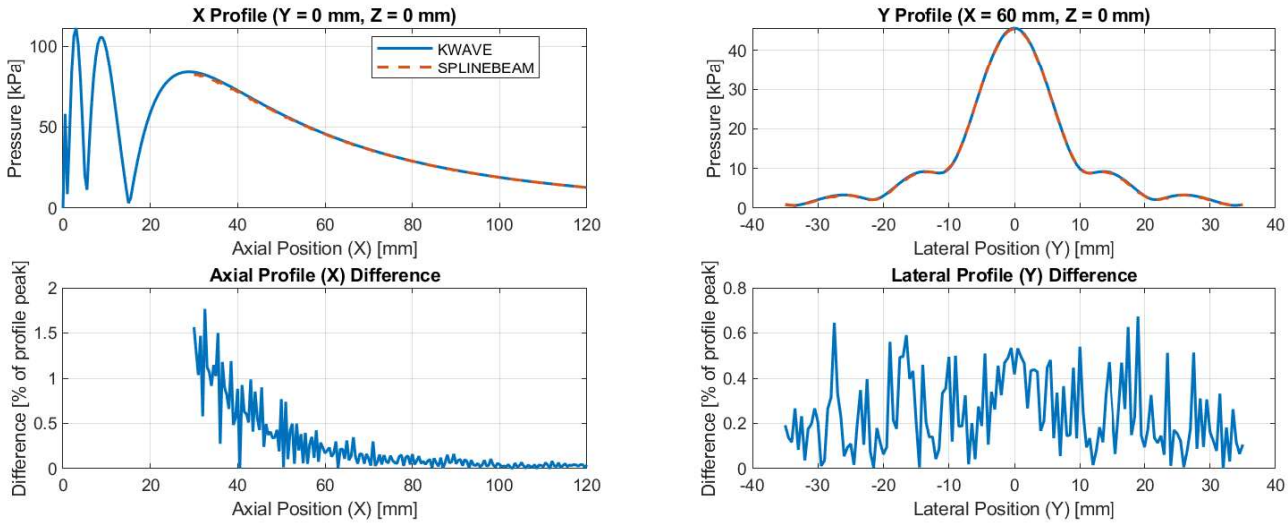


*Figure E.7: Comparison of SplineBeam and k-Wave pressure field profiles for configuration BM2-SC2*

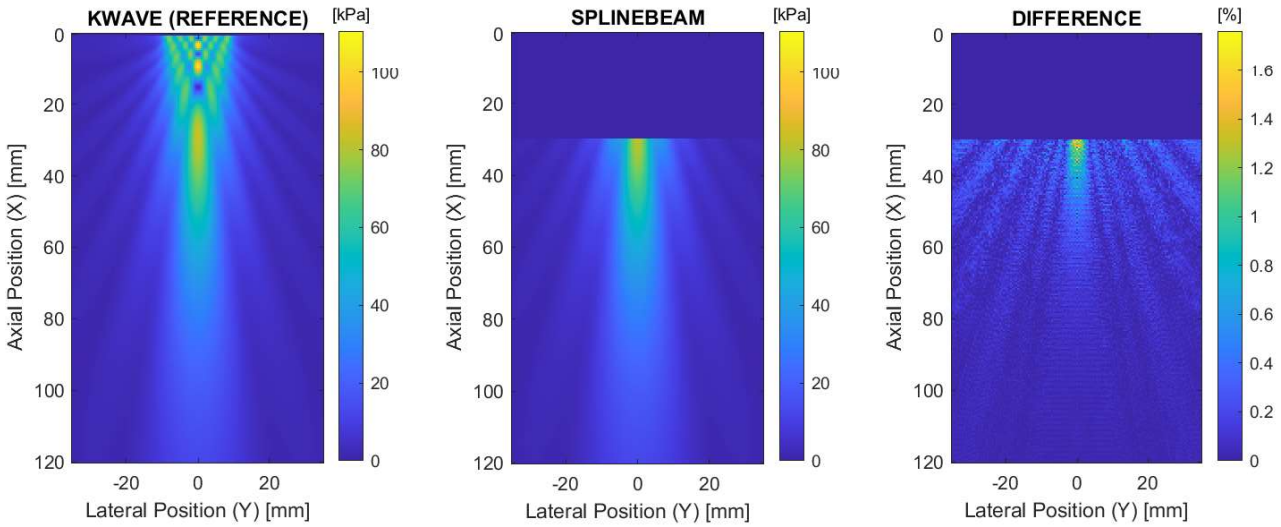


*Figure E.8: Comparison of SplineBeam and k-Wave pressure field XY planes for configuration BM2-SC2*

## E.2 Analytical shape configurations

### E.2.1 Planar layer of cortical bone

#### E.2.1.1 Spherically curved transducer

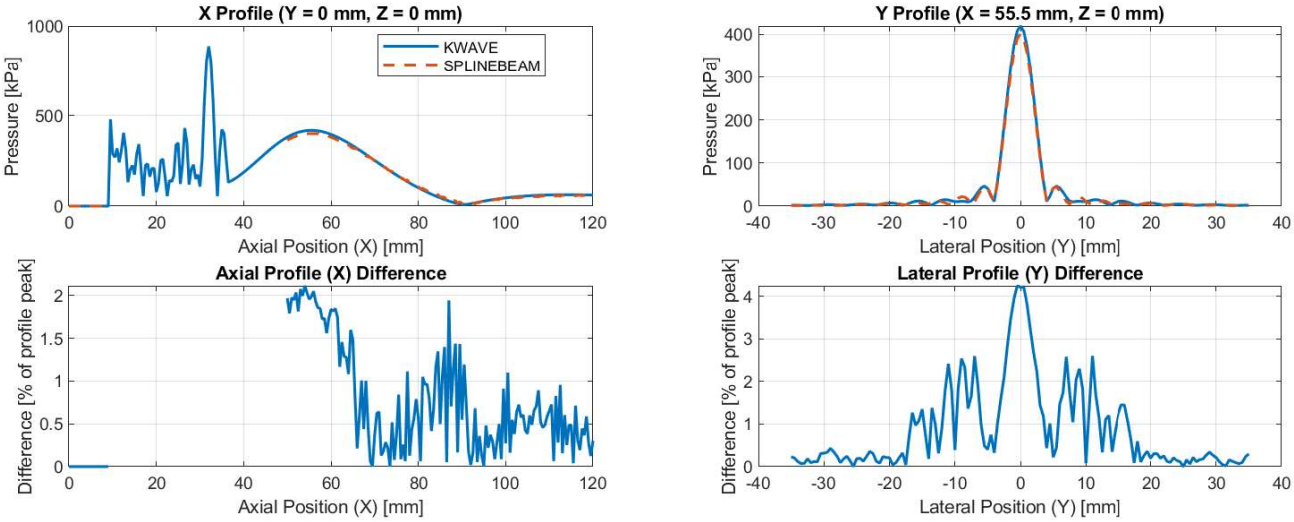


*Figure E.9: Comparison of SplineBeam and k-Wave pressure field profiles for configuration BM3-SC1*

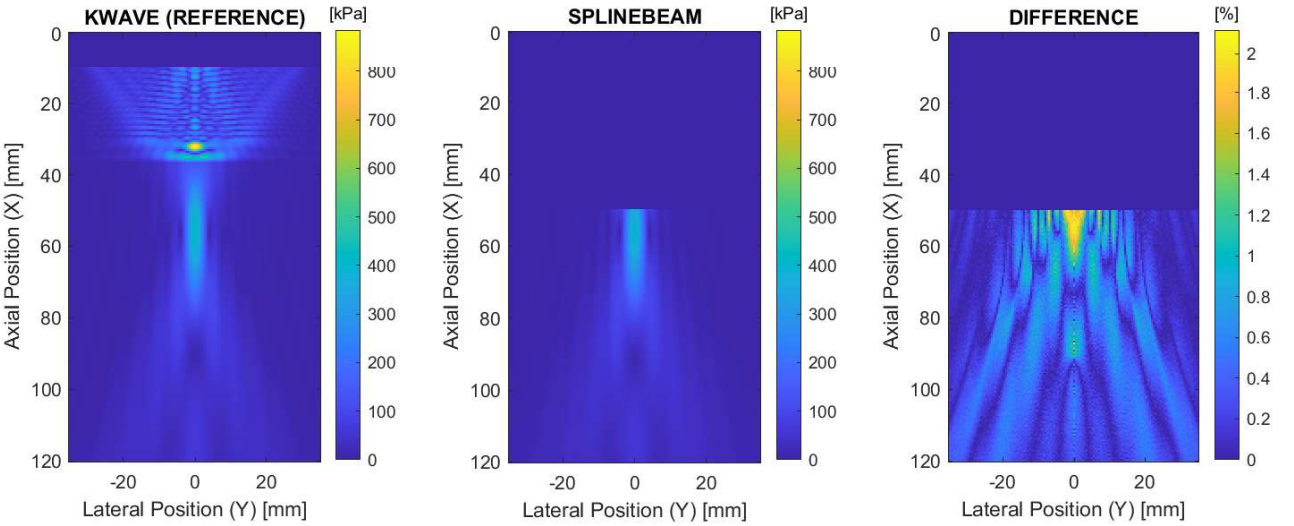


*Figure E.10: Comparison of SplineBeam and k-Wave pressure field XY planes for configuration BM3-SC1*

### E.2.1.2 Piston transducer

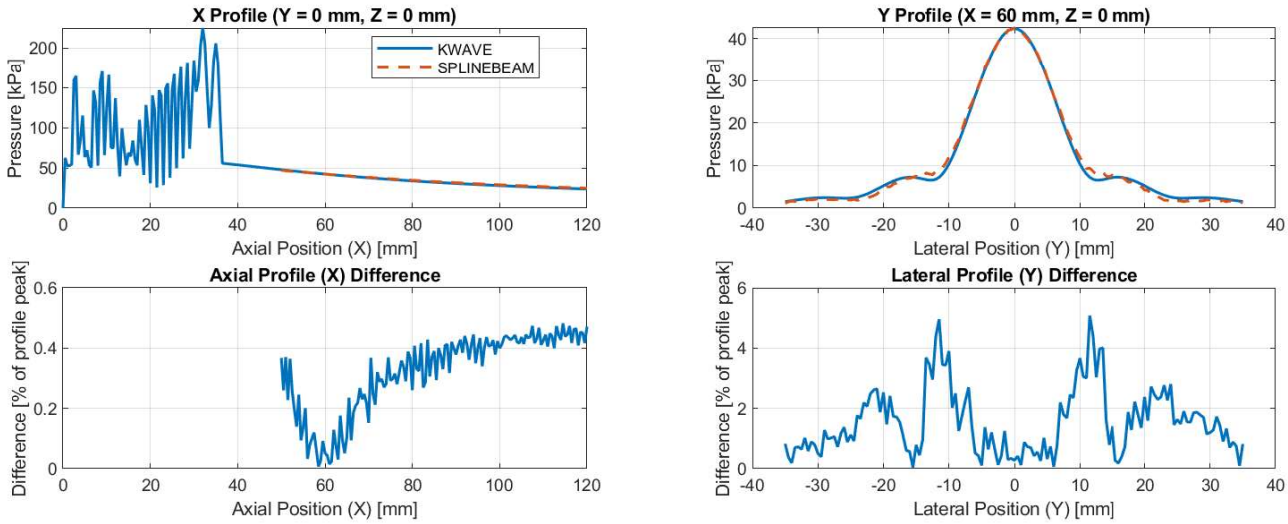


*Figure E.11: Comparison of SplineBeam and k-Wave pressure field profiles for configuration BM3-SC2*

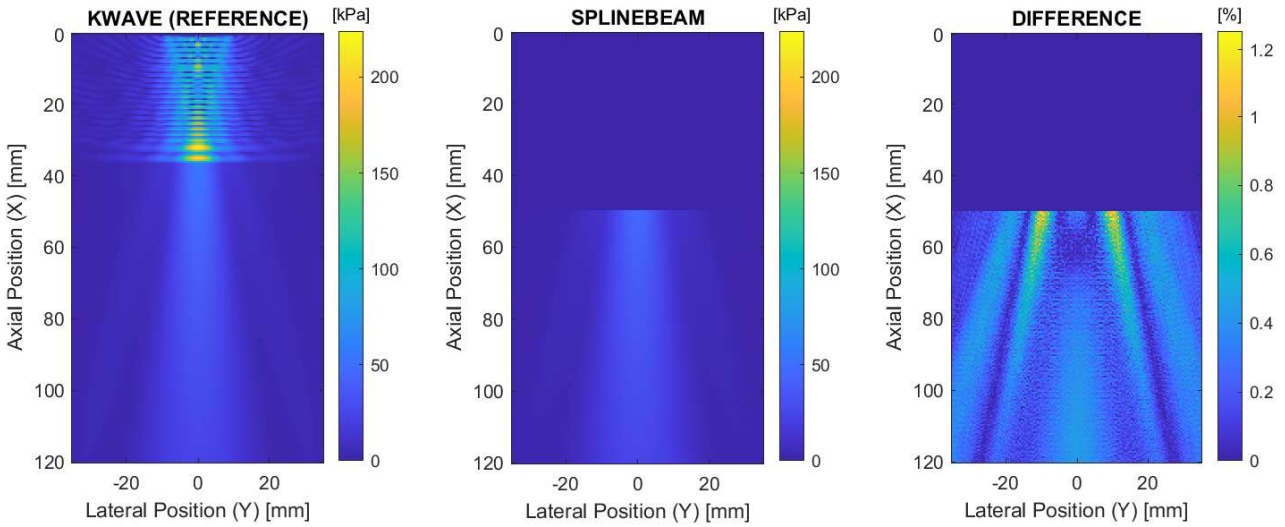


*Figure E.12: Comparison of SplineBeam and k-Wave pressure field XY planes for configuration BM3-SC2*

### E.2.2 Spherical layer of cortical bone

#### E.2.2.1 Spherically curved transducer

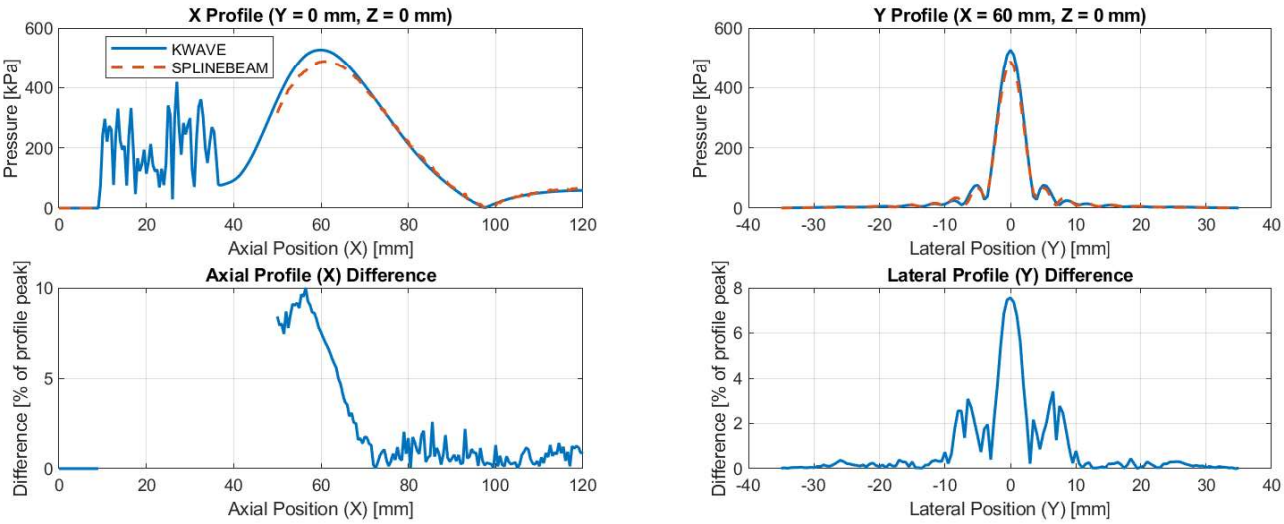


*Figure E.13: Comparison of SplineBeam and k-Wave pressure field profiles for configuration BM5-SC1*

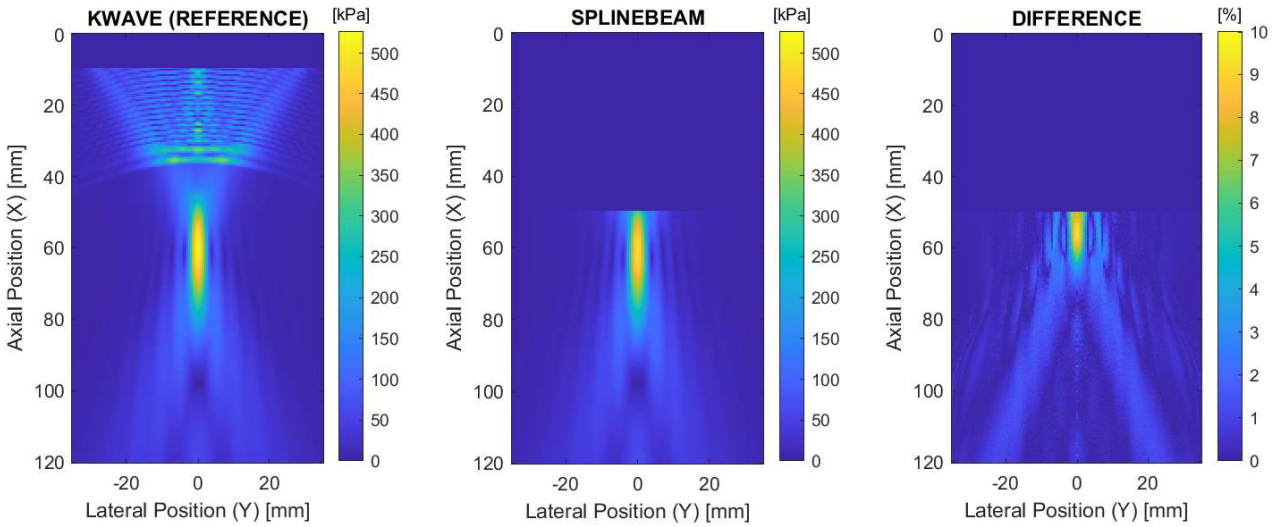


*Figure E.14: Comparison of SplineBeam and k-Wave pressure field XY planes for configuration BM5-SC1*

### E.2.2.2 Piston transducer

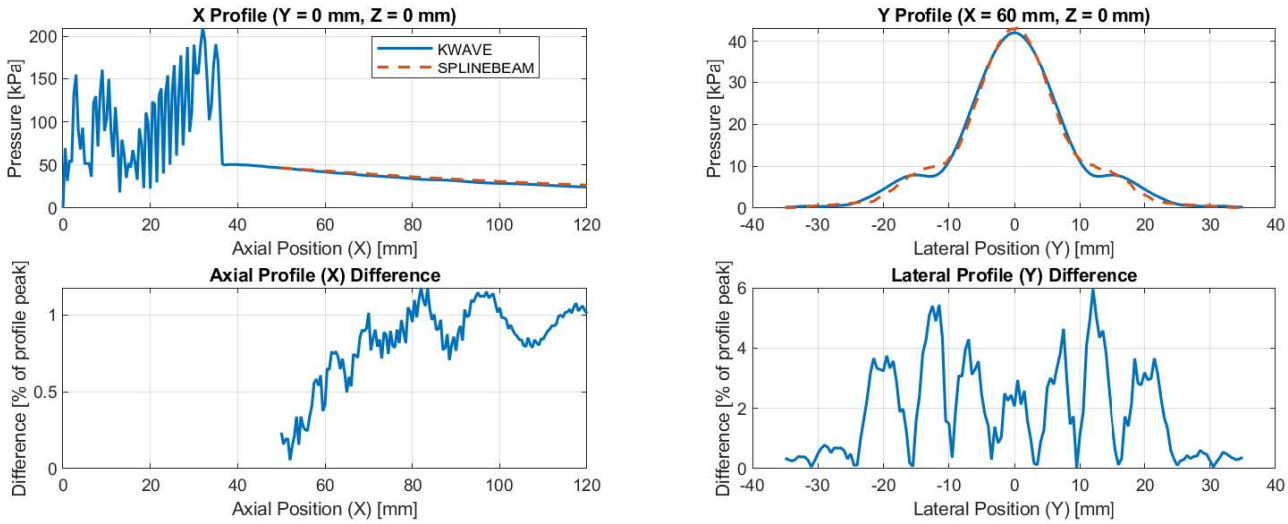


*Figure E.15: Comparison of SplineBeam and k-Wave pressure field profiles for configuration BM5-SC2*

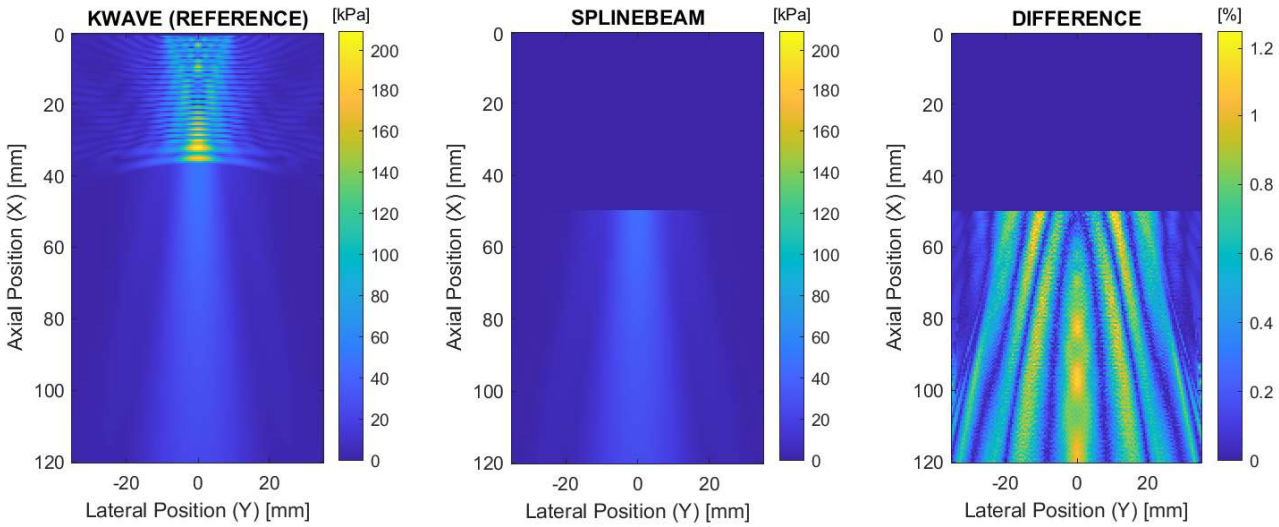


*Figure E.16: Comparison of SplineBeam and k-Wave pressure field XY planes for configuration BM5-SC2*

## E.3 Skull configurations

### E.3.1 Skull inside water and target in visual cortex

#### E.3.1.1 Spherically curved transducer

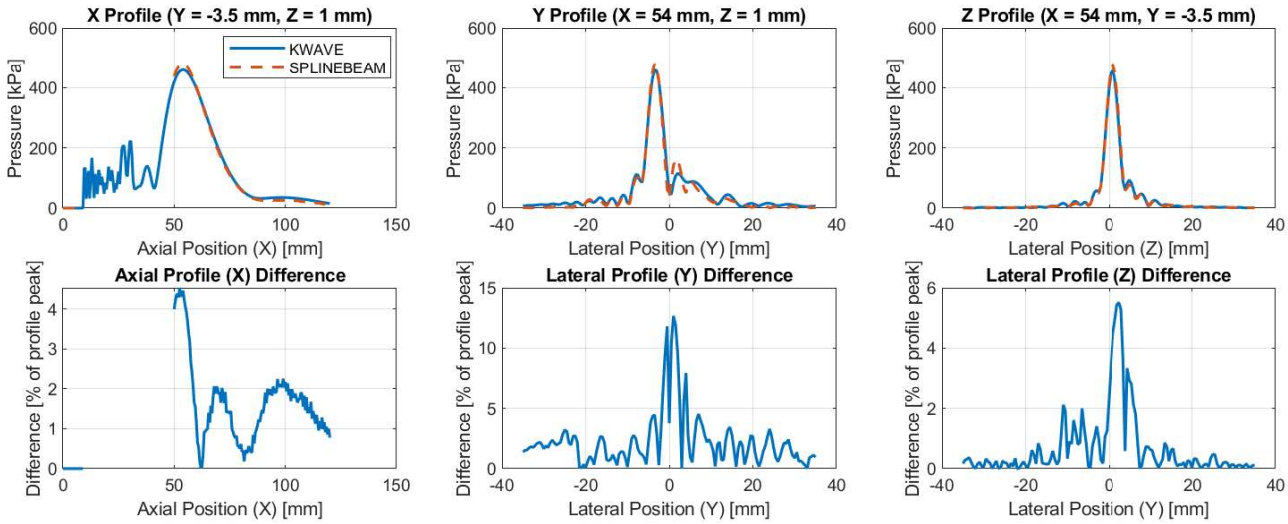


*Figure E.17: Comparison of SplineBeam and k-Wave pressure field profiles for configuration BM7-SC1*

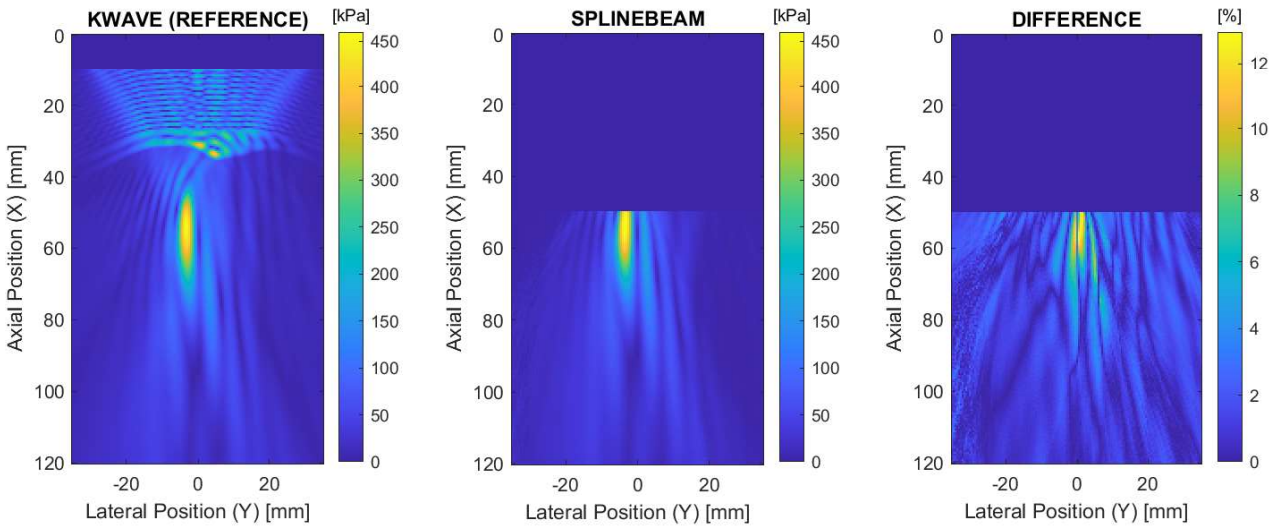


*Figure E.18: Comparison of SplineBeam and k-Wave pressure field XY planes for configuration BM7-SC1*

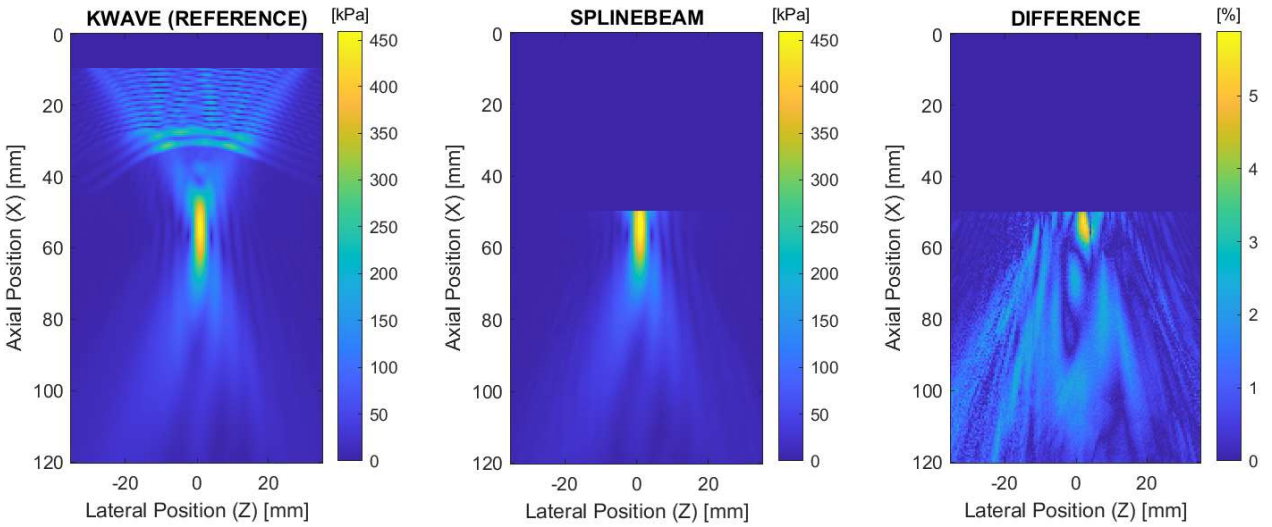


*Figure E.19: Comparison of SplineBeam and k-Wave pressure field XZ planes for configuration BM7-SC1*

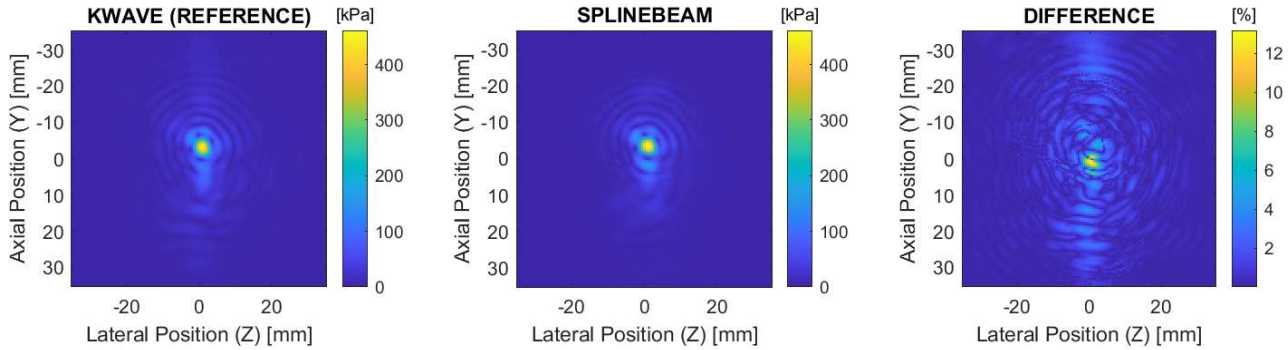


*Figure E.20: Comparison of SplineBeam and k-Wave pressure field YZ planes for configuration BM7-SC1*

### E.3.1.2 Piston transducer

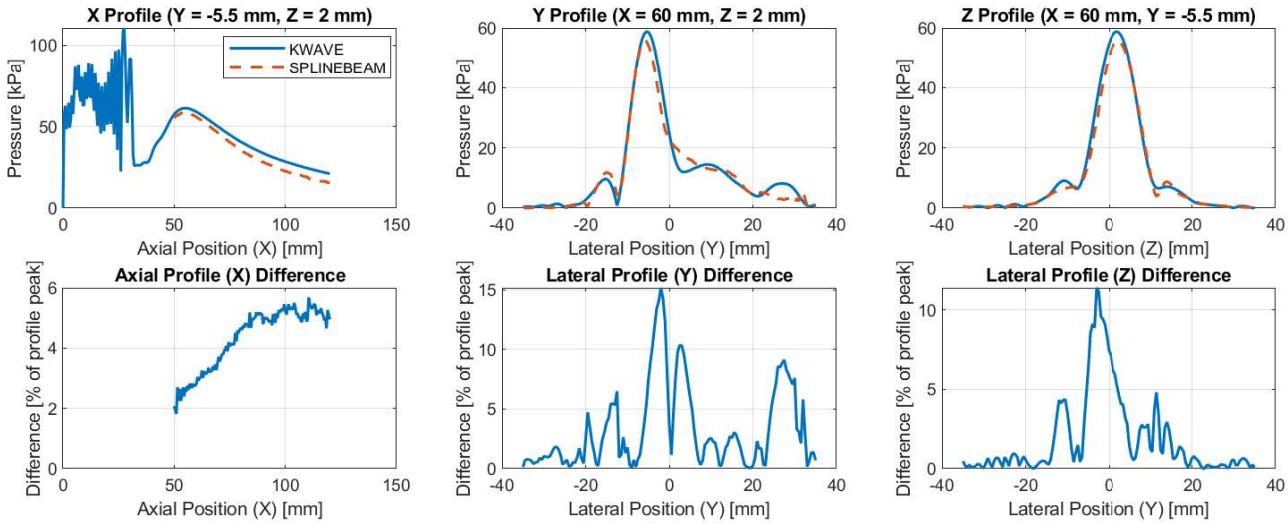


*Figure E.21: Comparison of SplineBeam and k-Wave pressure field profiles for configuration BM7-SC2*

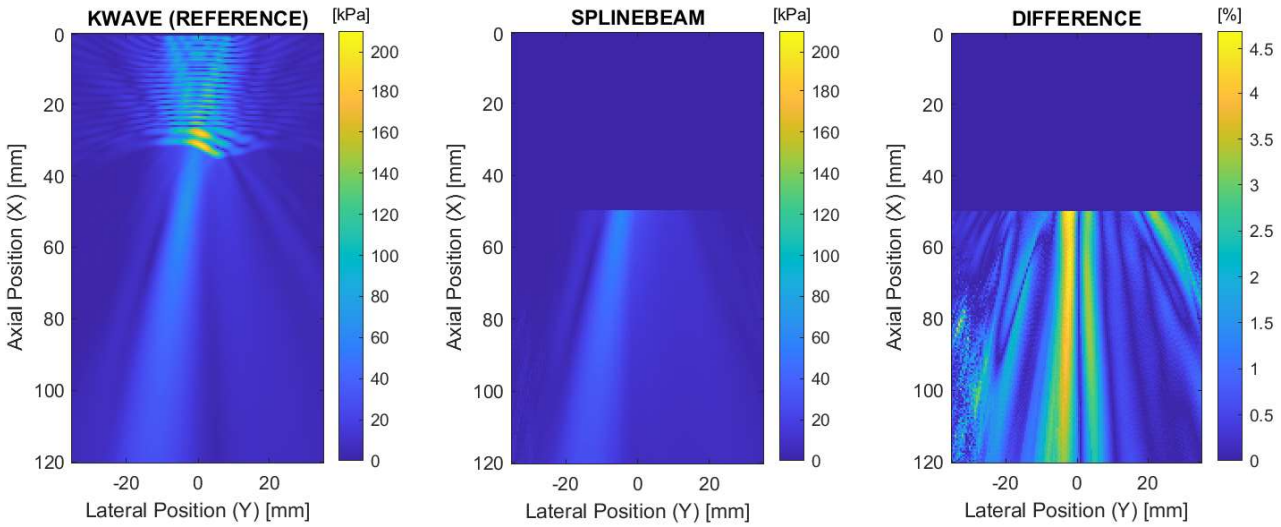


*Figure E.22: Comparison of SplineBeam and k-Wave pressure field XY planes for configuration BM7-SC2*

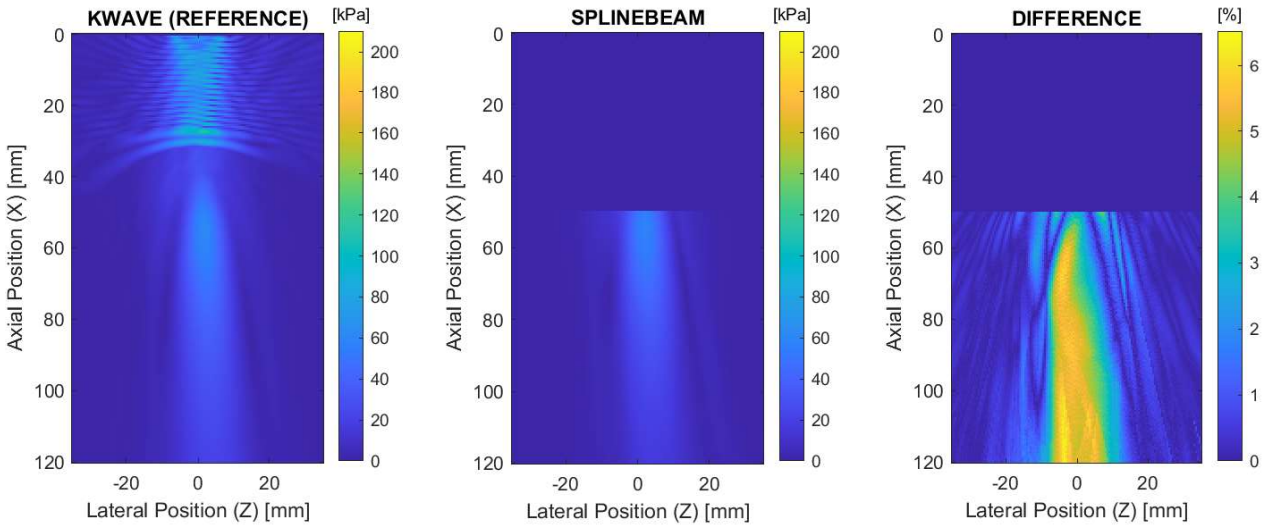


*Figure E.23: Comparison of SplineBeam and k-Wave pressure field XZ planes for configuration BM7-SC2*

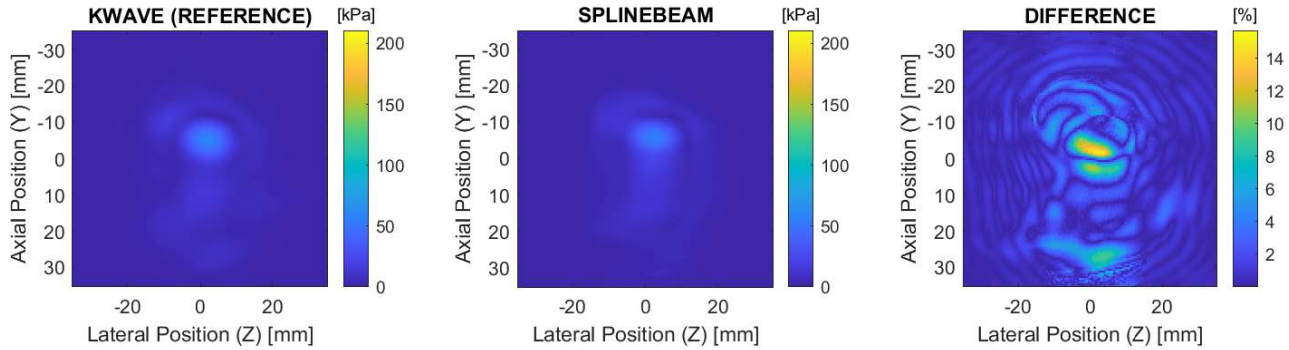


*Figure E.24: Comparison of SplineBeam and k-Wave pressure field YZ planes for configuration BM7-SC2*

### E.3.2 Skull with brain and target in visual cortex

#### E.3.2.1 Spherically curved transducer

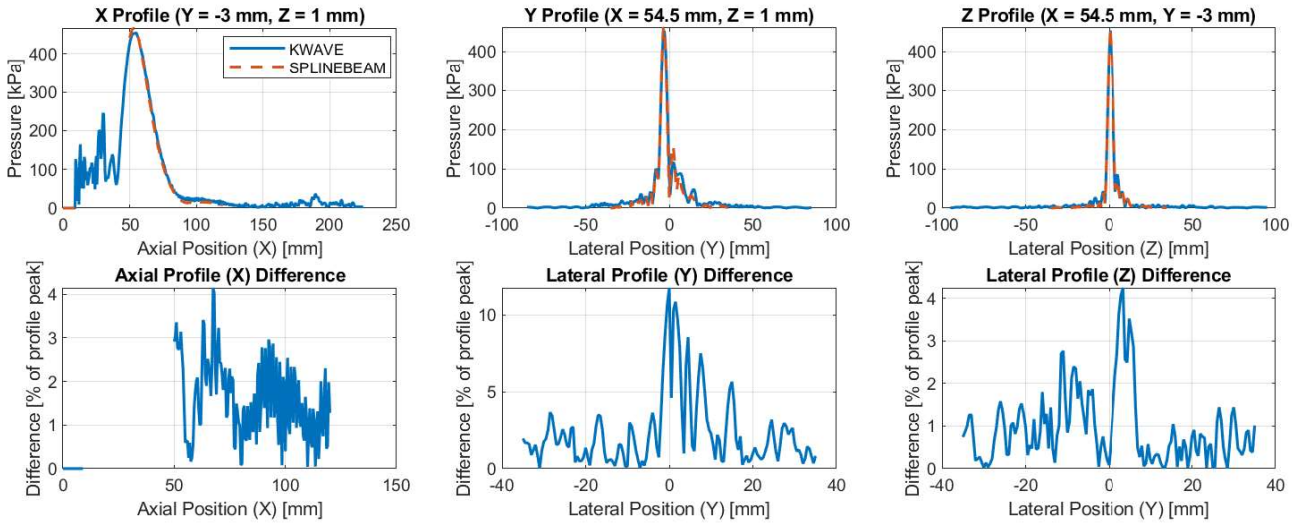


*Figure E.25: Comparison of SplineBeam and k-Wave pressure field profiles for configuration BM8-SC1*

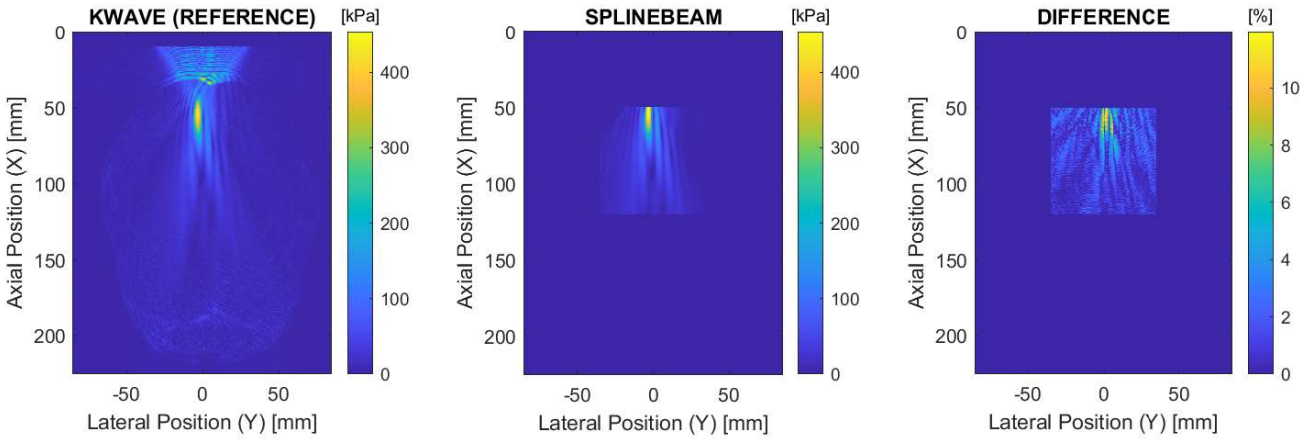


*Figure E.26: Comparison of SplineBeam and k-Wave pressure field XY planes for configuration BM8-SC1*

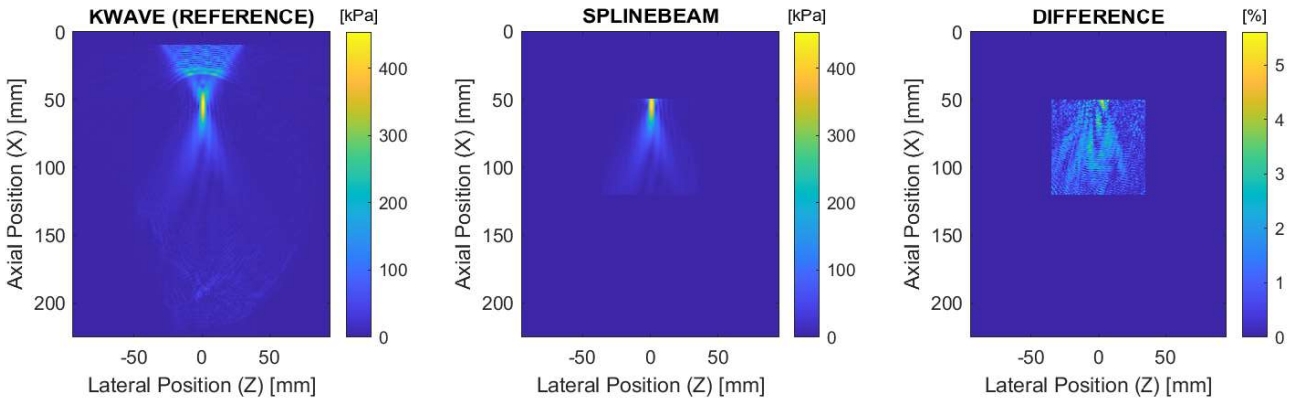


*Figure E.27: Comparison of SplineBeam and k-Wave pressure field XZ planes for configuration BM8-SC1*

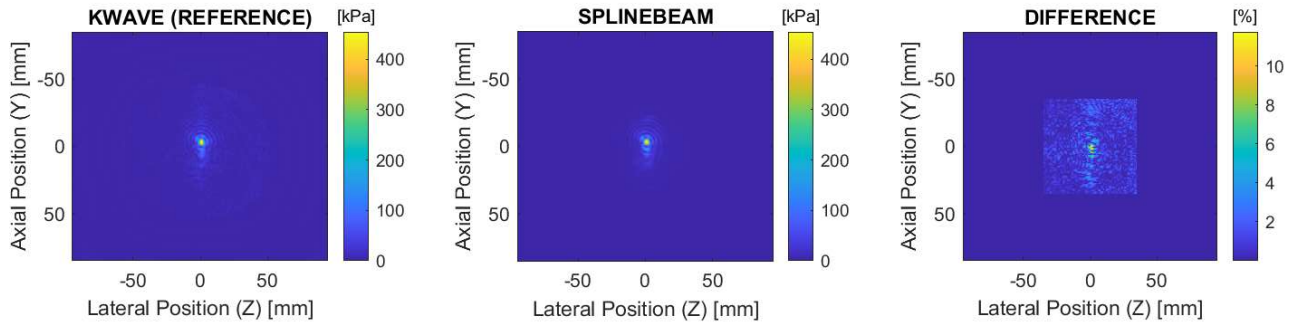


*Figure E.28: Comparison of SplineBeam and k-Wave pressure field YZ planes for configuration BM8-SC1*

### E.3.2.2 Piston transducer

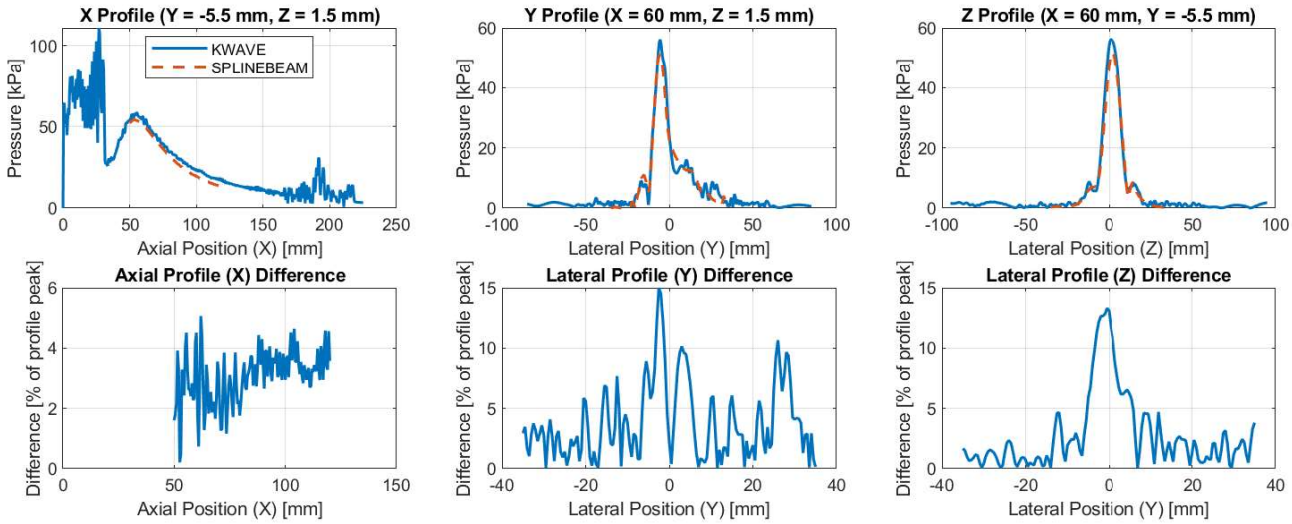


*Figure E.29: Comparison of SplineBeam and k-Wave pressure field profiles for configuration BM8-SC2*

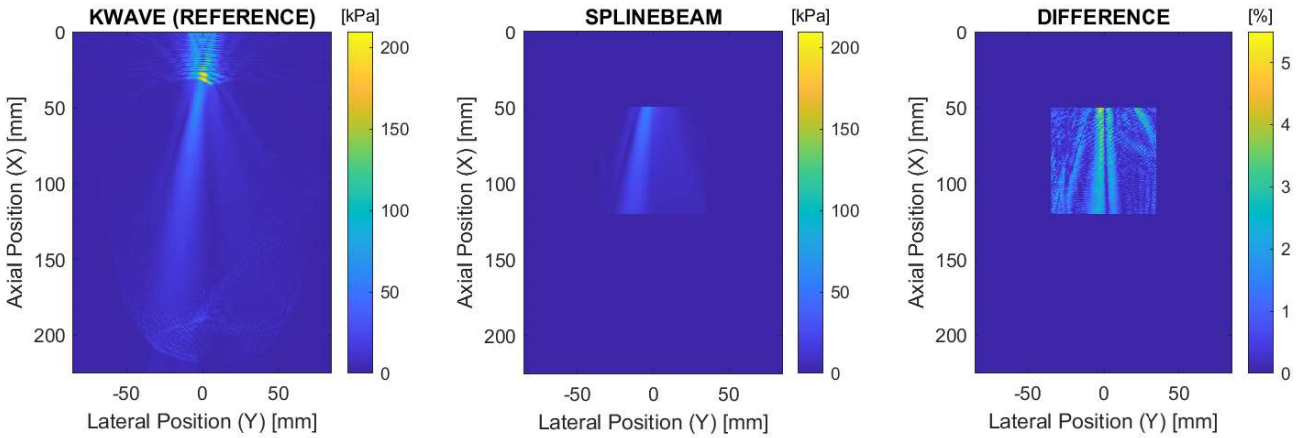


*Figure E.30: Comparison of SplineBeam and k-Wave pressure field XY planes for configuration BM8-SC2*

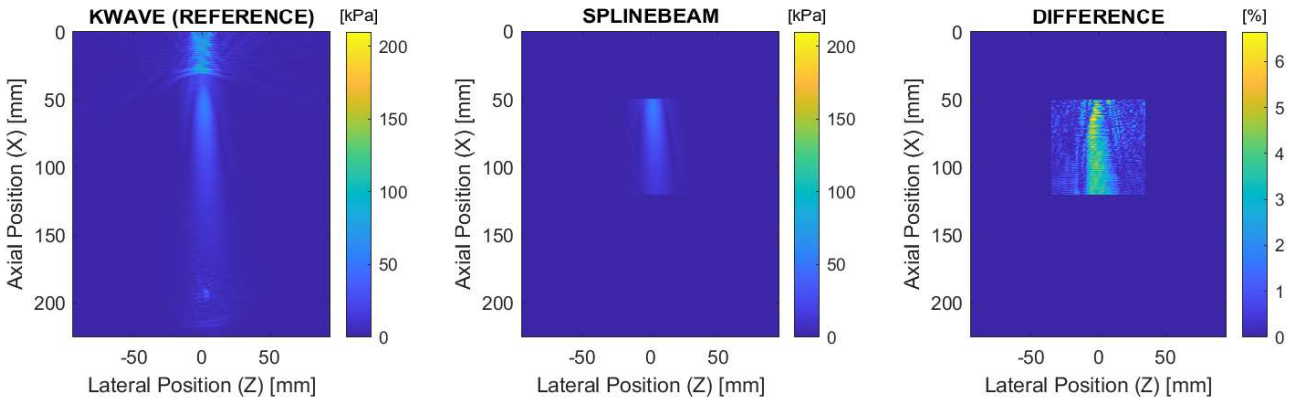


*Figure E.31: Comparison of SplineBeam and k-Wave pressure field XZ planes for configuration BM8-SC2*

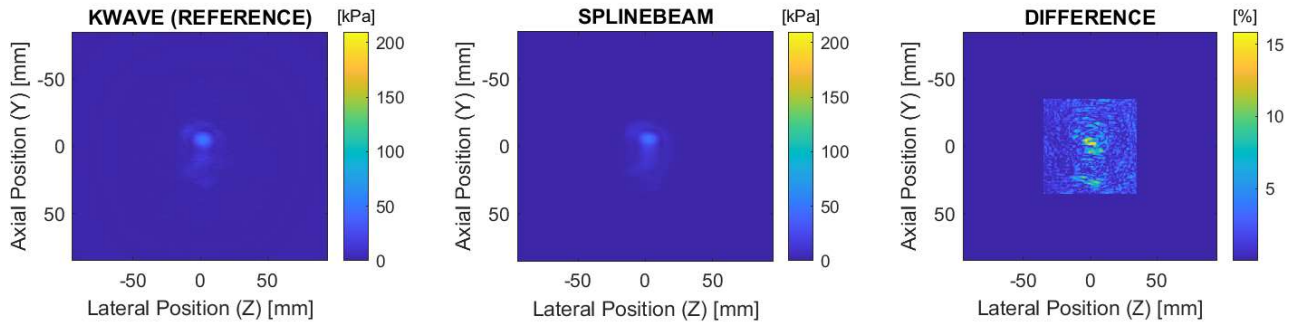


*Figure E.32: Comparison of SplineBeam and k-Wave pressure field YZ planes for configuration BM8-SC2*

### E.3.3 Skull with brain and target in motor cortex

#### E.3.3.1 Spherically curved transducer

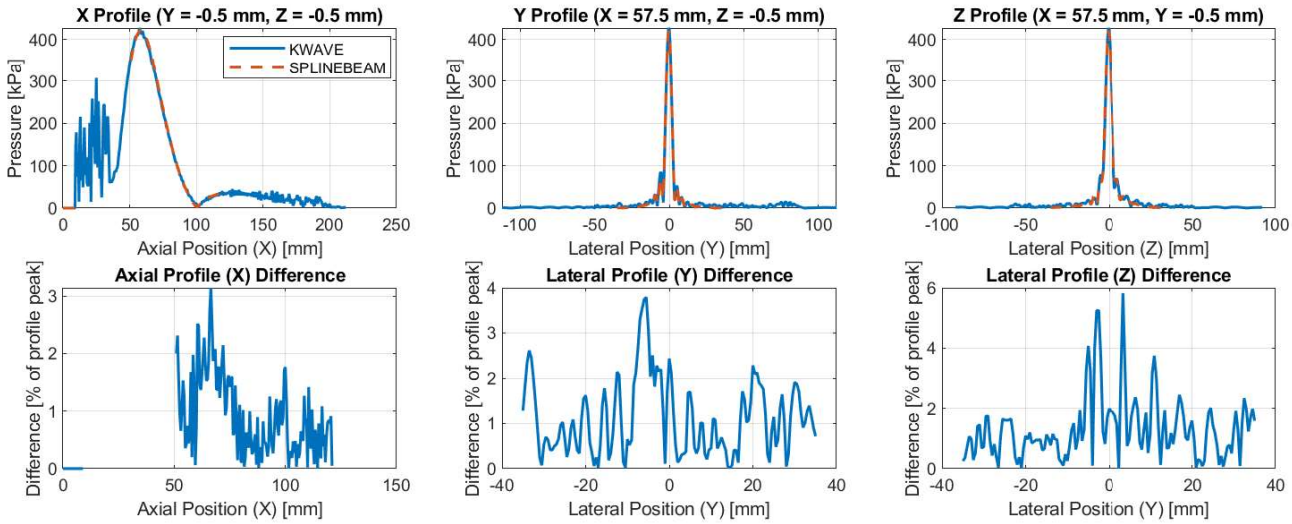


*Figure E.33: Comparison of SplineBeam and k-Wave pressure field profiles for configuration BM9-SC1*

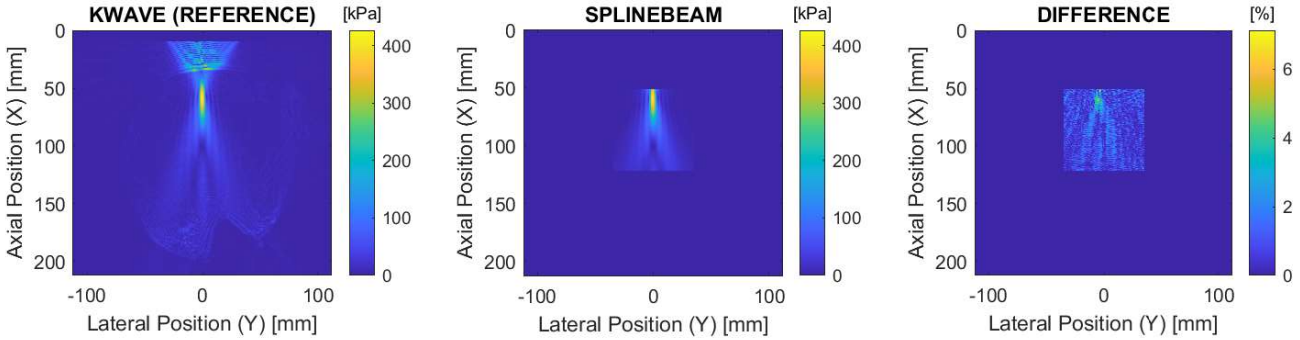


*Figure E.34: Comparison of SplineBeam and k-Wave pressure field XY planes for configuration BM9-SC1*

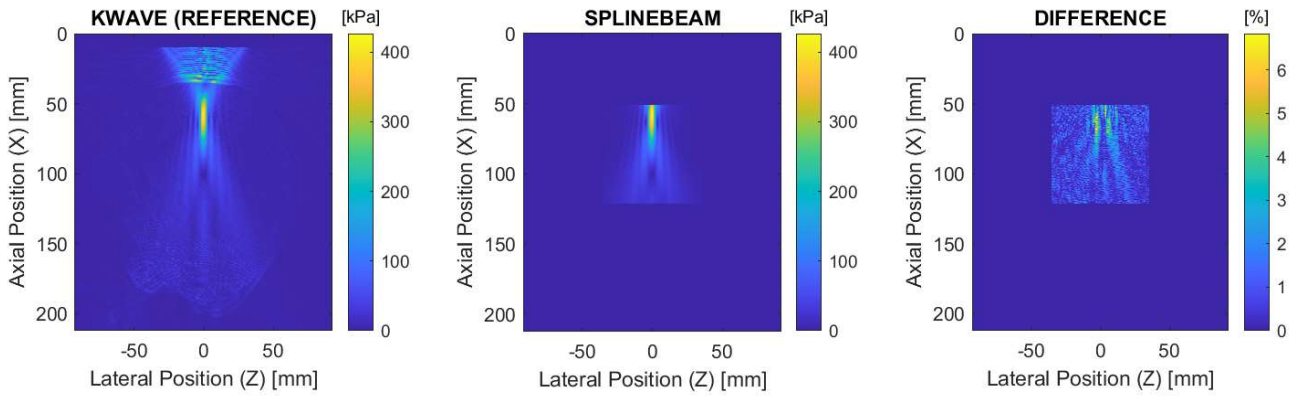


*Figure E.35: Comparison of SplineBeam and k-Wave pressure field XZ planes for configuration BM9-SC1*

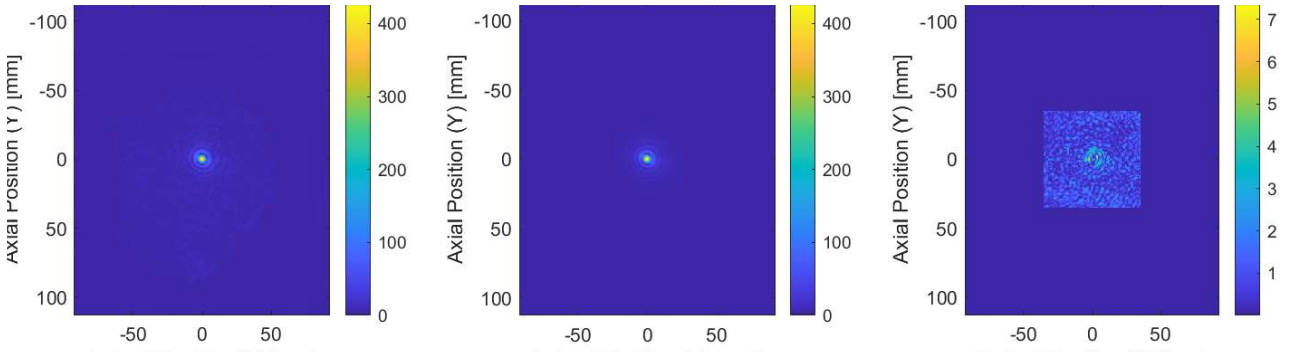


*Figure E.36: Comparison of SplineBeam and k-Wave pressure field YZ planes for configuration BM9-SC1*

### E.3.3.2 Piston transducer

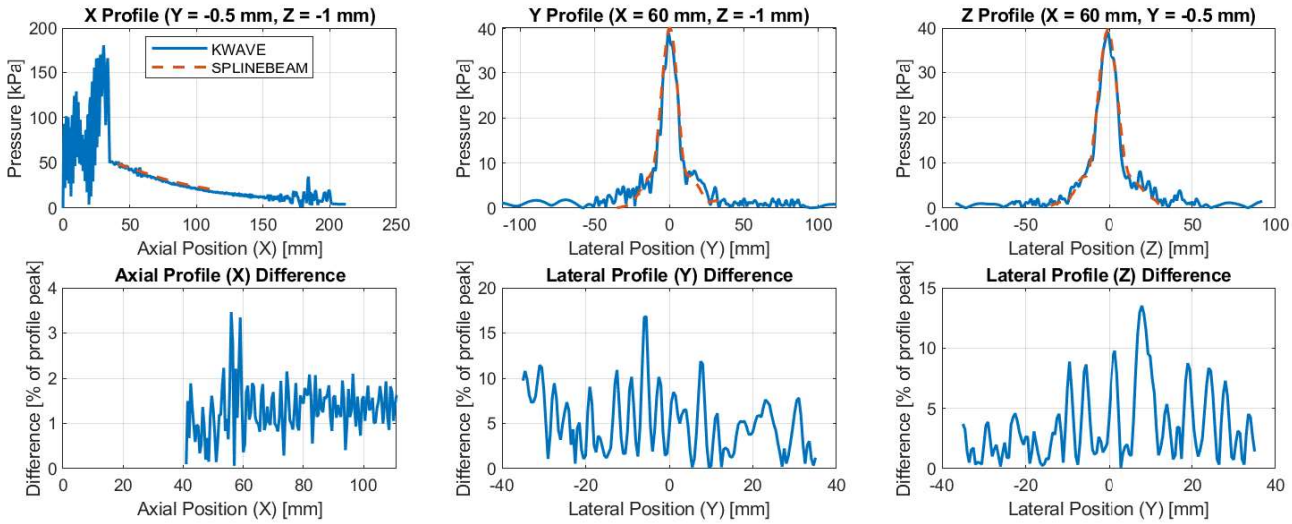


*Figure E.37: Comparison of SplineBeam and k-Wave pressure field profiles for configuration BM9-SC2*

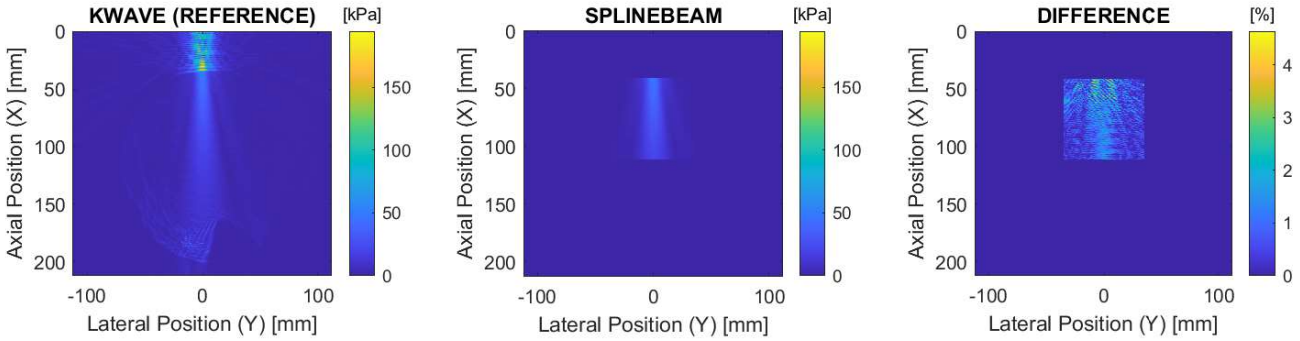


*Figure E.38: Comparison of SplineBeam and k-Wave pressure field XY planes for configuration BM9-SC2*

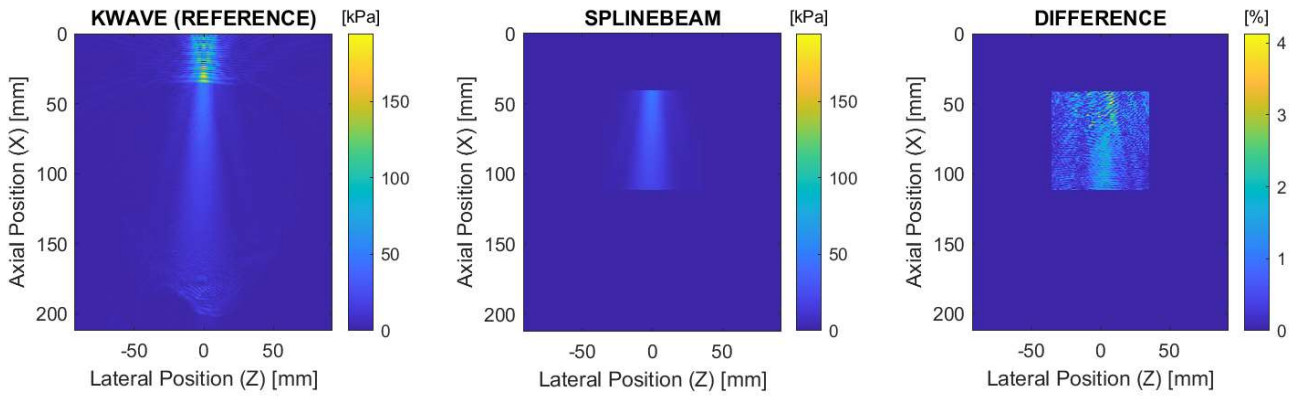


*Figure E.39: Comparison of SplineBeam and k-Wave pressure field XZ planes for configuration BM9-SC2*

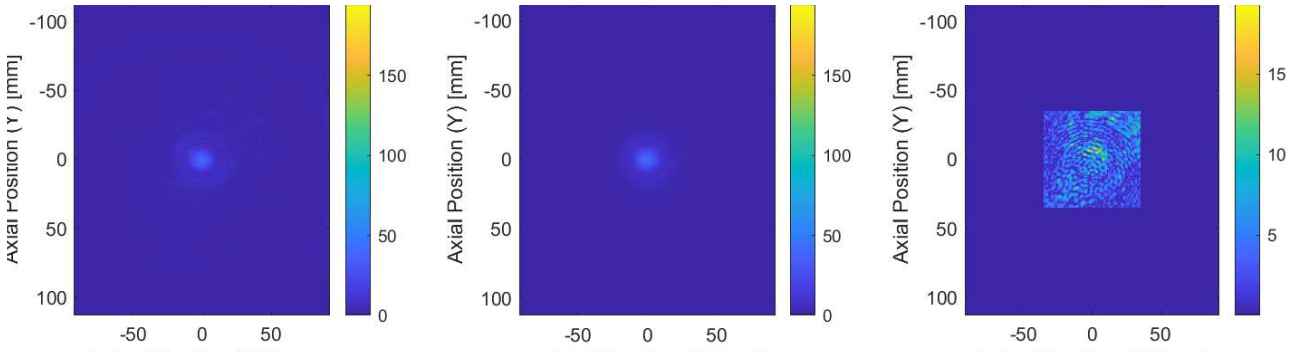


*Figure E.40: Comparison of SplineBeam and k-Wave pressure field YZ planes for configuration BM9-SC2*

## E.4 All solvers versus k-Wave

### E.4.1 Configurations

#### E.4.1.1 Focal position error

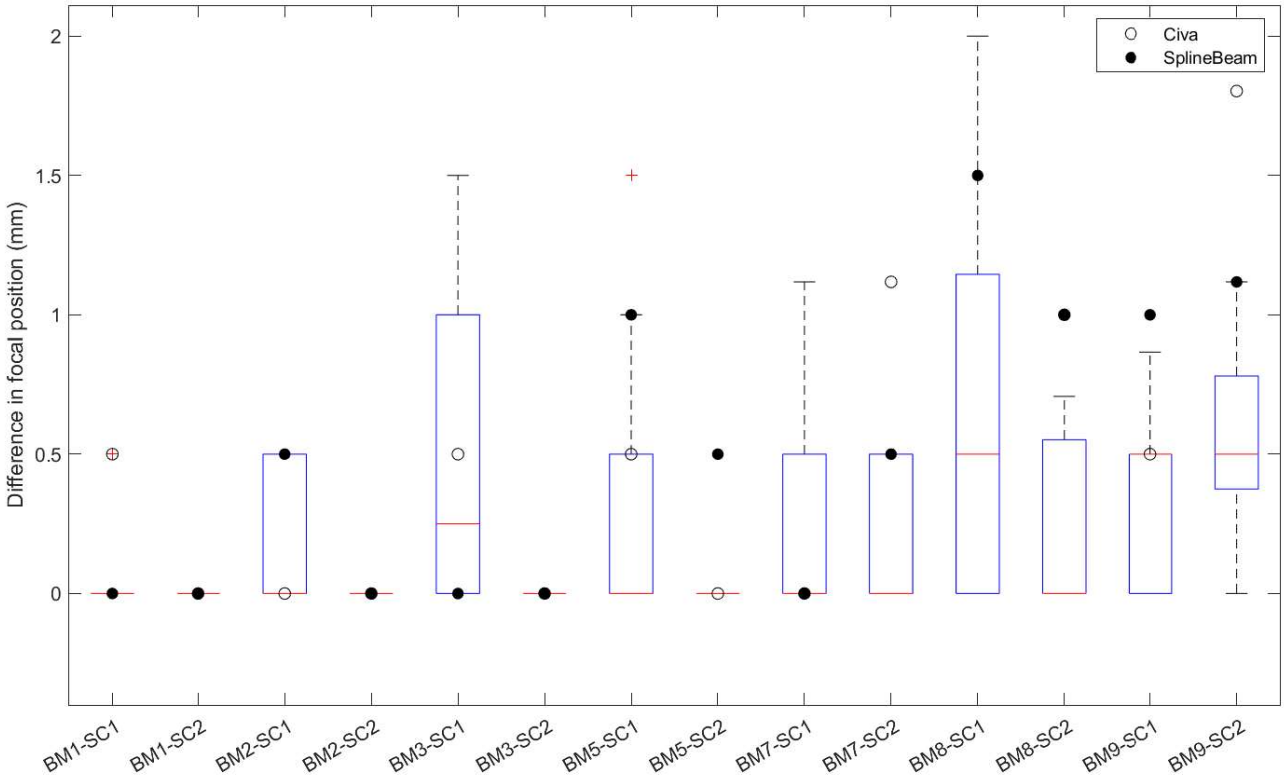


*Figure E.41: Configuration boxplots of focal position error relative to k-Wave*

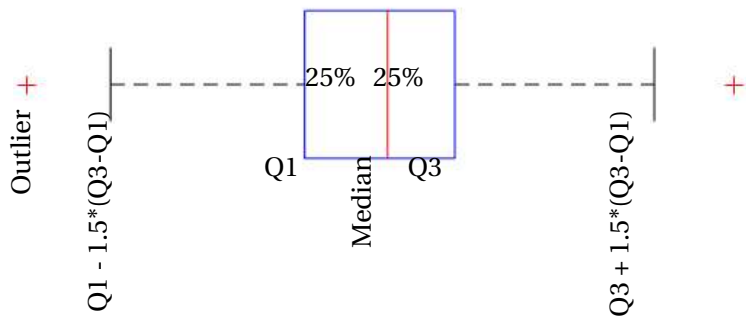


*Figure E.42: Different parts of a boxplot*

### E.4.1.2 Focal pressure error

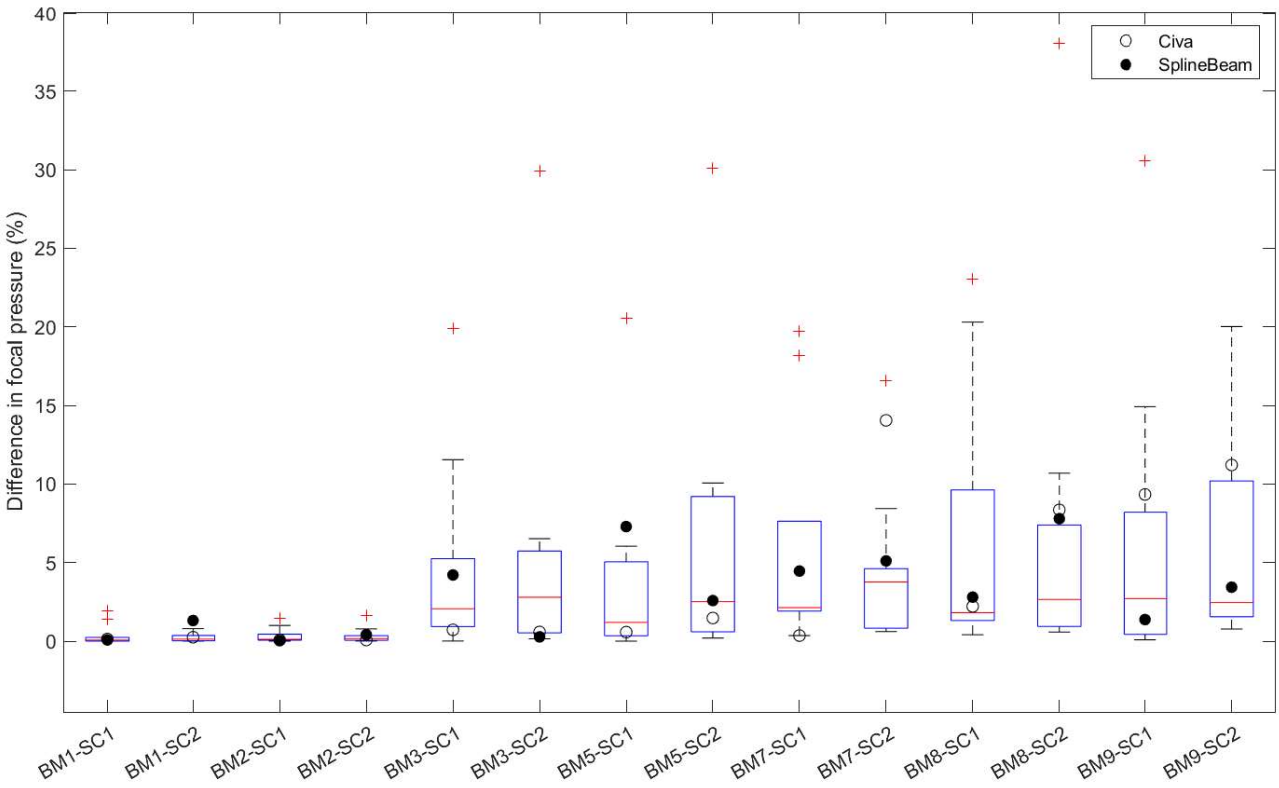


*Figure E.43: Configuration boxplots of focal pressure error relative to k-Wave*

### E.4.2 Solvers

#### E.4.2.1 Focal position error

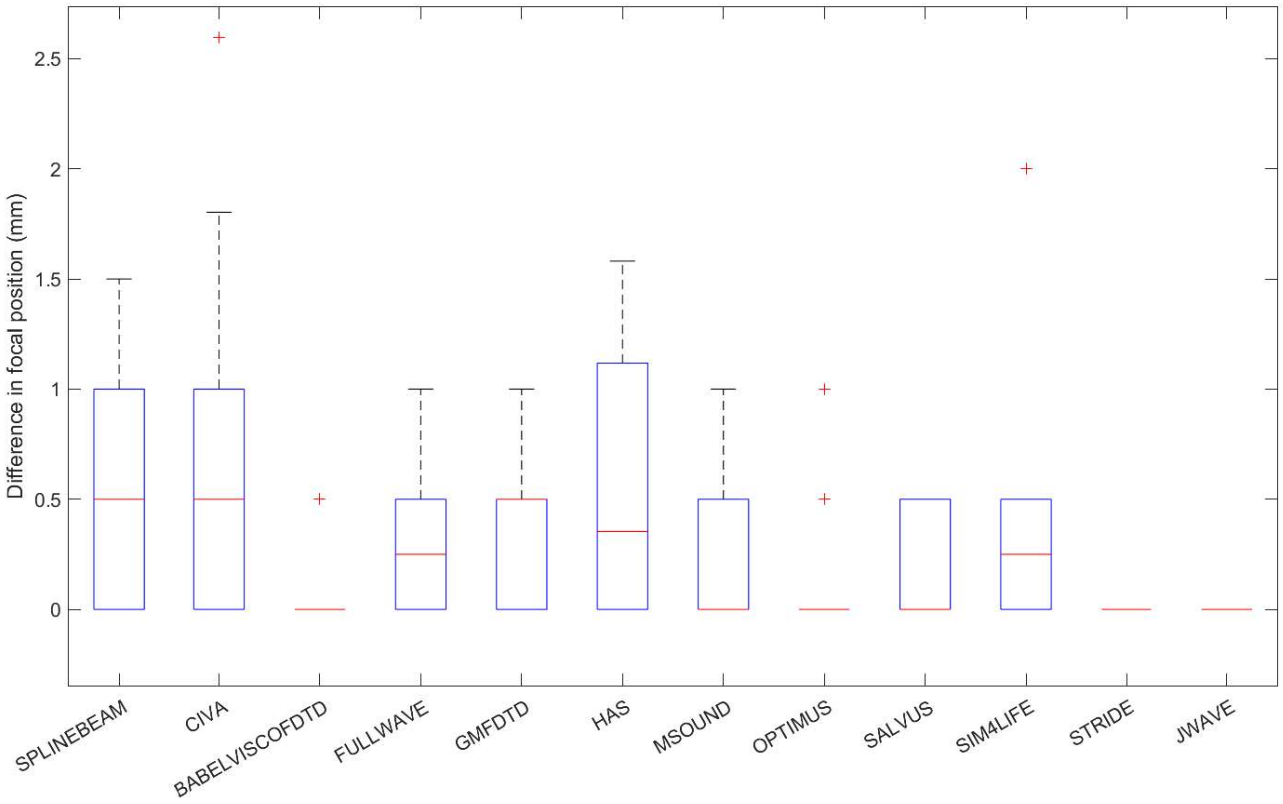


*Figure E.44: Solver boxplots of focal position error relative to k-Wave*

### E.4.2.2 Focal pressure error

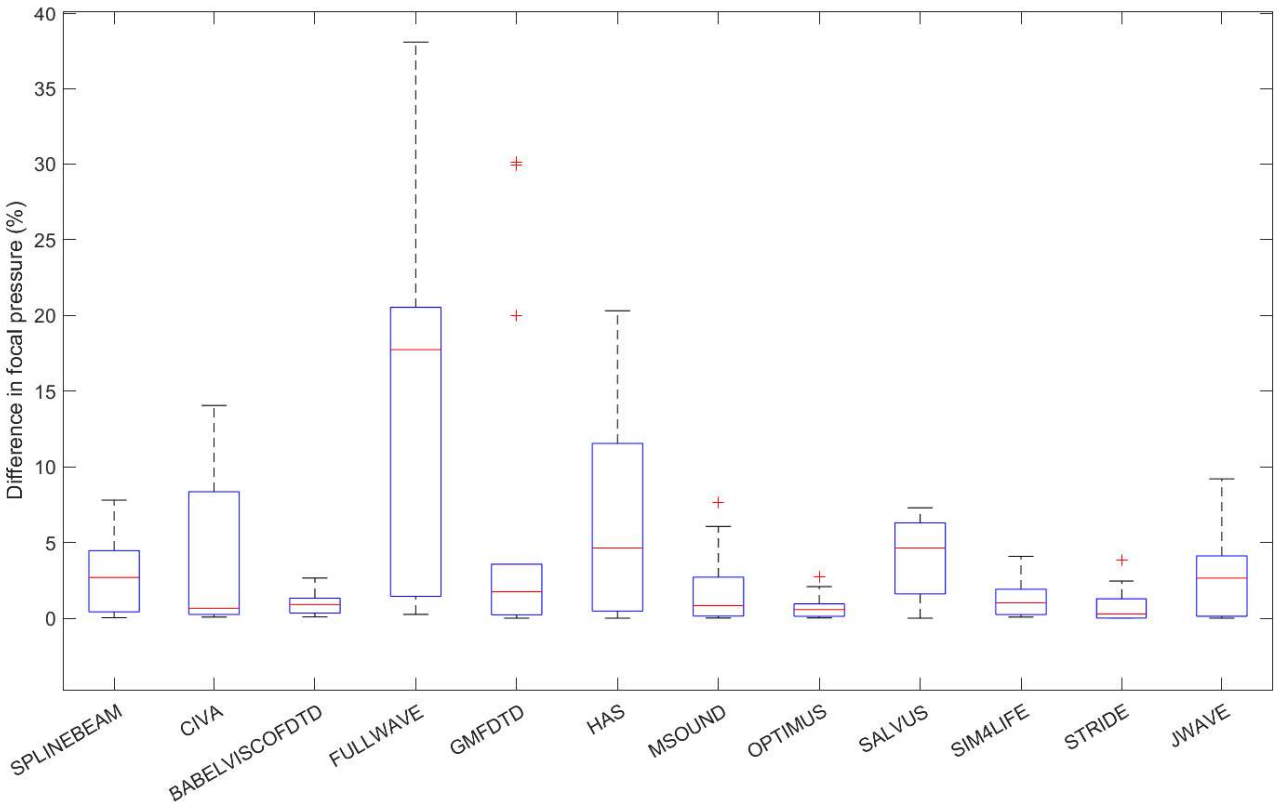


*Figure E.45: Solver boxplots of focal pressure error relative to k-Wave*

## E.5 All solvers versus SplineBeam

### E.5.1 Configurations

#### E.5.1.1 Focal position error

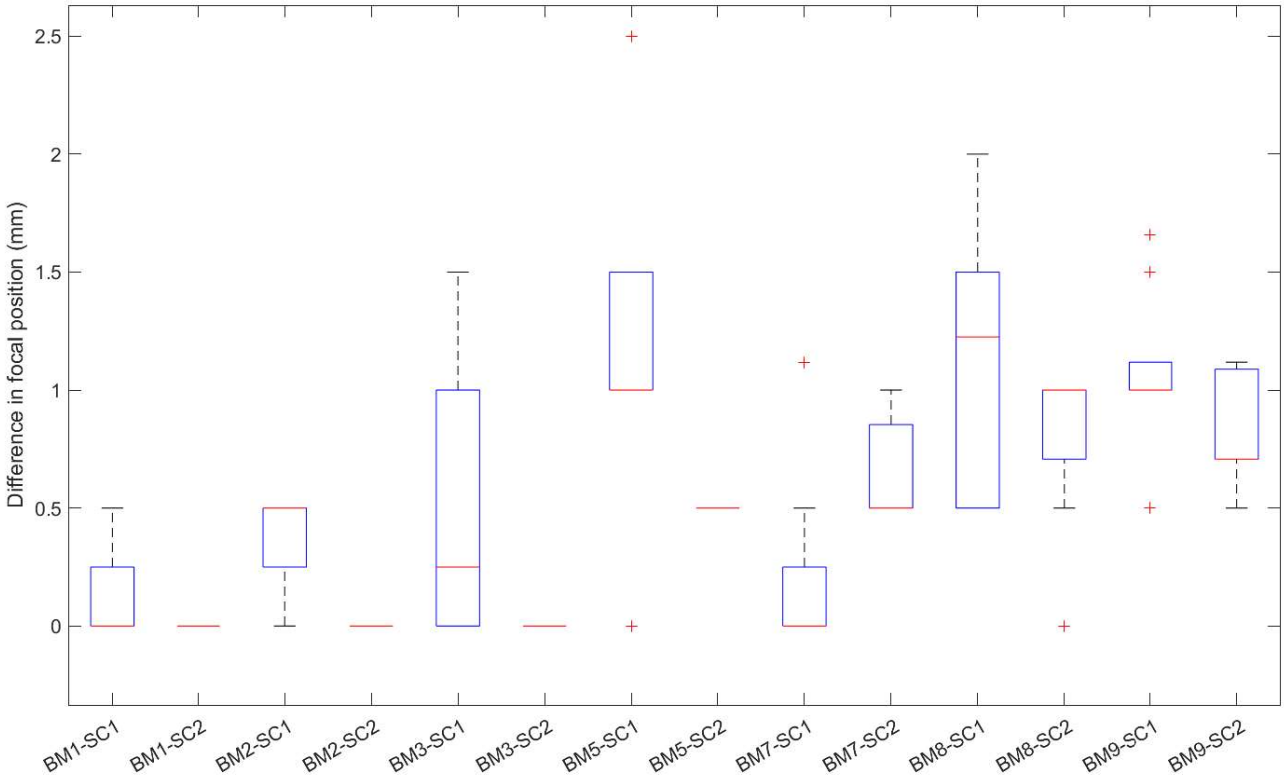


*Figure E.46: Configuration boxplots of focal position error relative to SplineBeam*

### E.5.1.2 Focal pressure error

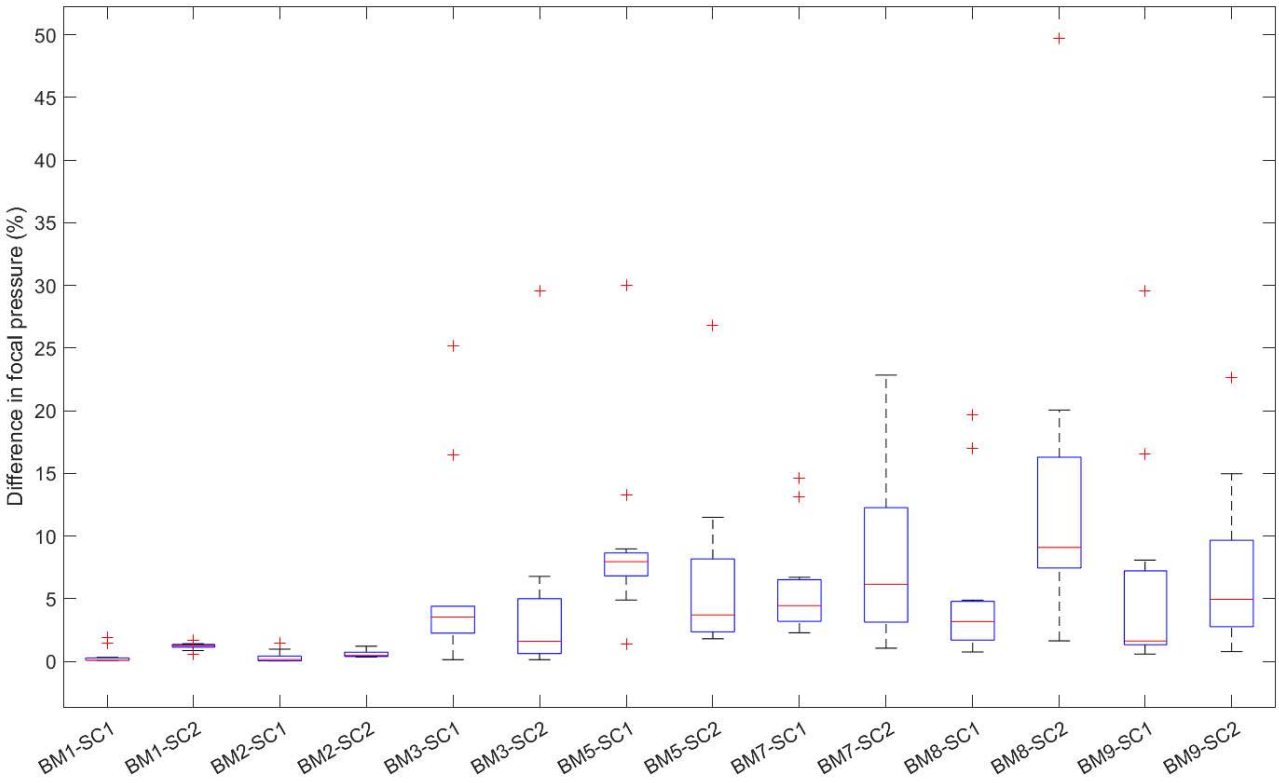


*Figure E.47: Configuration boxplots of focal pressure error relative to SplineBeam*

### E.5.2 Solvers

#### E.5.2.1 Focal position error

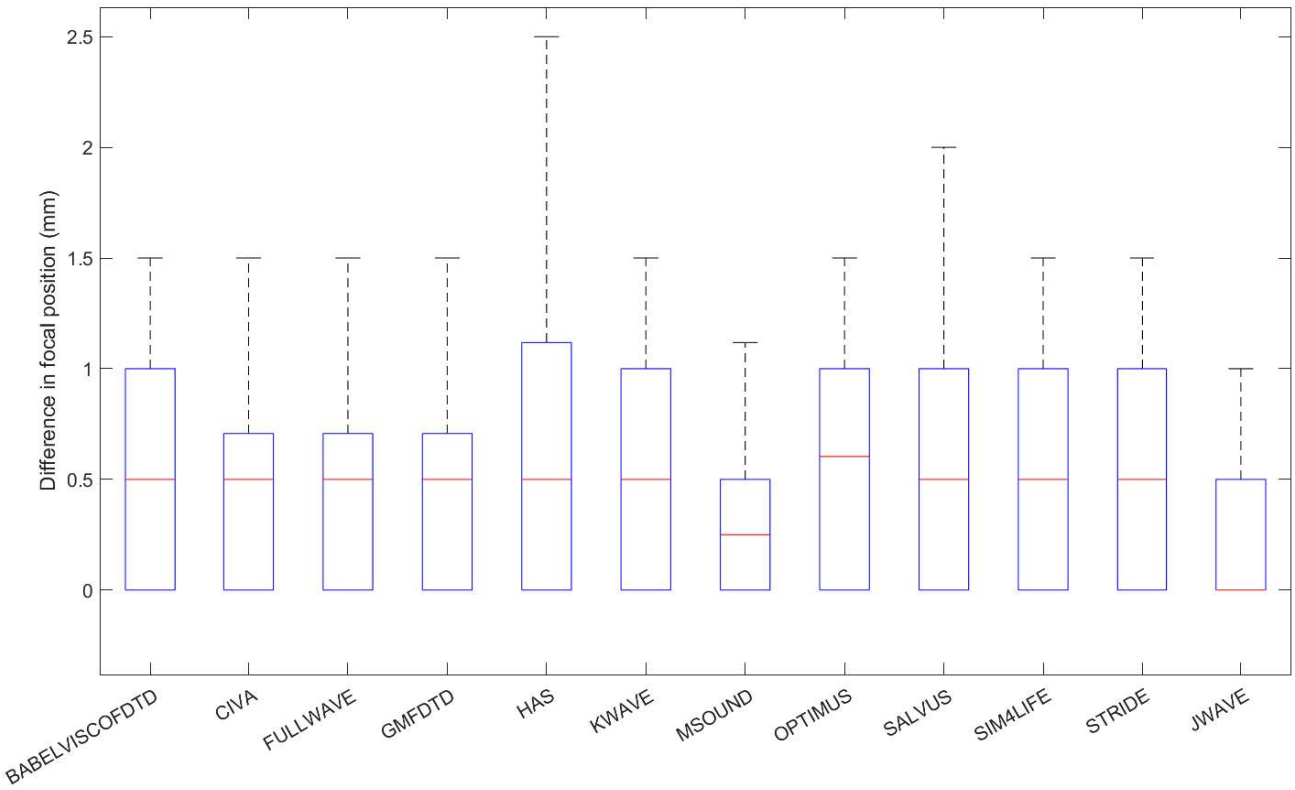


*Figure E.48: Solver boxplots of focal position error relative to SplineBeam*

#### E.5.2.2 Focal pressure error

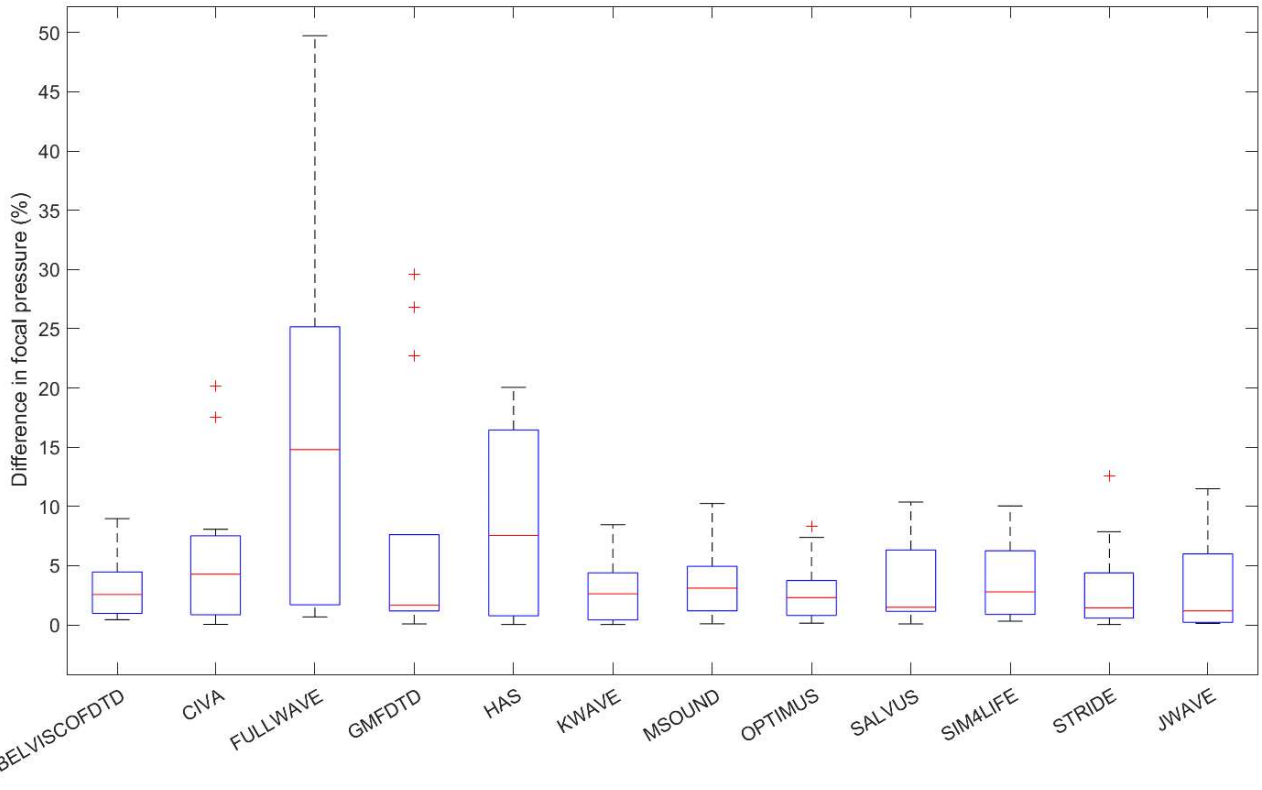


*Figure E.49: Solver boxplots of focal pressure error relative to SplineBeam*

# Bibliography


[1] Byung Gook Lee, Joon Jae Lee, and Jaechil Yoo. An efficient scattered data approximation using multilevel B-splines based on quasi-interpolants. *Proceedings of International Conference on 3-D Digital Imaging and Modeling, 3DIM*, pages 110–117, 2005.

[2] Marsac et al. Ex vivo optimisation of a heterogeneous speed of sound model of the human skull for non-invasive transcranial focused ultrasound at 1 MHz. *International Journal of Hyperthermia*, 33(6):635–645, 2017.

[3] James L B Robertson. The effects of image homogenisation on simulated transcranial ultrasound propagation. *Phys. Med. Biol*, 2018.

[4] Attali et al. Three-layer model with absorption for conservative estimation of the maximum acoustic transmission coefficient through the human skull for transcranial ultrasound stimulation. *Brain stimulation*, 16(1):48–55, jan 2023.

[5] Ryan M. Jones and Kullervo Hynynen. Comparison of analytical and numerical approaches for CT-based aberration correction in transcranial passive acoustic imaging. *Physics in Medicine and Biology*, 61(1):23–36, nov 2015.

[6] S. Lloyd. Least squares quantization in pcm. *IEEE Transactions on Information Theory*, 28(2):129–137, 1982.

[7] Nicolas Gengembre and Alain Lhémery. Pencil method in elastodynamics: Application to ultrasonic field computation. *Ultrasonics*, 38(1):495–499, 2000.

[8] Jorge Nocedal and Stephen J. Wright. *Numerical Optimization*. Springer, New York, NY, USA, 2e edition, 2006.

[9] Royer Daniel, Dieulesaint Eugène, Gennes Pierre-Gilles de, Daniel Royer, and Gennes Pierre-Gilles de. *Ondes élastiques dans les solides . Tome 1, Propagation libre et guidée / Daniel Royer,..., Eugène Dieulesaint,... ; préface de Pierre-Gilles de Gennes*. Enseignement de la physique. Masson, Paris, DL 1996.

[10] Aubry et al. Benchmark problems for transcranial ultrasound simulation: Intercomparison of compressional wave models. *The Journal of the Acoustical Society of America*, 152(2):1003–1019, feb 2022.

[11] Matthias Reinhard, Andreas Hetzel, Sebastian Krüger, Stefan Kretzer, Jochen Talazko, Sargon Ziyeh, Johannes Weber, and Thomas Els. Blood-brain barrier disruption by low-frequency ultrasound. *Stroke*, 37(6):1546–1548, jun 2006.

[12] Emily White. *Focused Ultrasound Foundation State of the Field Report 2021*. 2021.

[13] Timothy Wagner, Antoni Valero-Cabre, and Alvaro Pascual-Leone. Noninvasive human brain stimulation. *Annual review of biomedical engineering*, 9:527–565, 2007.

[14] J.-F. Aubry, M. Tanter, M. Pernot, J.-L. Thomas, and M. Fink. Experimental demonstration of noninvasive transskull adaptive focusing based on prior computed tomography scans. *The Journal of the Acoustical Society of America*, 113(1):84–93, 2003.

[15] Yun Jing, F. Can Meral, and Greg T. Clement. Time-reversal transcranial ultrasound beam focusing using a k-space method. *Physics in Medicine and Biology*, 57(4):901–917, 2012.

[16] Bradley E. Treeby, Jakub Budisky, Elliott S. Wise, Jiri Jaros, and B. T. Cox. Rapid calculation of acoustic fields from arbitrary continuous-wave sources. *The Journal of the Acoustical Society of America*, 143(1):529–537, jan 2018.

[17] Jiang et al. Numerical Evaluation of the Influence of Skull Heterogeneity on Transcranial Ultrasonic Focusing. *Frontiers in Neuroscience*, 14, apr 2020.

[18] Adamos Kyriakou, Esra Neufeld, Beat Werner, Gábor Székely, and Niels Kuster. Full-wave acoustic and thermal modeling of transcranial ultrasound propagation and investigation of skull-induced aberration correction techniques: a feasibility study. *Journal of therapeutic ultrasound*, 3(1):11, jul 2015.

[19] Bancel et al. Comparison between ray-tracing and full-wave simulation for transcranial ultrasound focusing on a clinical system using the transfer matrix formalism. *IEEE Transactions on Ultrasonics, Ferroelectrics, and Frequency Control*, 2021.

[20] Robert Andrew Drainville, Sylvain Chatillon, David Moore, John Snell, Frederic Padilla, and Cyril Lafon. A simulation study on the sensitivity of transcranial ray-tracing ultrasound modeling to skull properties. *The Journal of the Acoustical Society of America*, 154(2):1211–1225, 08 2023.

[21] H. Chouh, G. Rougeron, S. Chatillon, J. C. Iehl, J. P. Farrugia, and V. Ostromoukhov. High performance ultrasonic field simulation on complex geometries. *AIP Conference Proceedings*, 1706(1):050002, 02 2016.

[22] Célestine Angla, Benoit Larrat, Jean Luc Gennisson, and Sylvain Chatillon. Transcranial ultrasound simulations: A review. *Medical Physics*, 50(2):1051–1072, feb 2023.

[23] Scott Almquist, Dennis L. Parker, and Douglas A. Christensen. Rapid full-wave phase aberration correction method for transcranial high-intensity focused ultrasound therapies. *Journal of Therapeutic Ultrasound*, 4(1), dec 2016.

[24] Célestine Angla, Benoit Larrat, Jean Luc Gennisson, and Sylvain Chatillon. Improved skull bone acoustic property homogenization for fast transcranial ultrasound simulations. *Proceedings of the 20th Anglo-French Physical Acoustics Conference, to be published in the J. Phys.: Conf. Ser., submitted.*

[25] Jun Yasuda, Hideki Yoshikawa and Hiroki Tanaka. Phase aberration correction for focused ultrasound transmission by refraction compensation. *Japanese Journal of Applied Physics*, 58(SG):SGGE22, 2019.

[26] Jeffrey B. Wang, Tommaso Di Ianni, Daivik B. Vyas, Zhenbo Huang, Sunmee Park, Niloufar Hosseini-Nassab, Muna Aryal, and Raag D. Airan. Focused ultrasound for noninvasive, focal pharmacologic neurointervention. *Frontiers in Neuroscience*, 14, 2020.

[27] Guillaume Maimbourg, Alexandre Houdouin, Thomas Deffieux, Mickael Tanter, and Jean François Aubry. 3D-printed adaptive acoustic lens as a disruptive technology for transcranial ultrasound therapy using single-element transducers. *Physics in Medicine and Biology*, 63(2), 2018.

[28] Jean-Luc Gennisson and Sylvain Chatillon. ECHOBRAIN: Aberration correction in transcranial ultrasonic imaging using CT data and simulation-based focusing algorithms. *The Journal of the Acoustical Society of America*, 148:2485, 2020.

[29] W. Jeffrey Elias, Diane Huss, Tiffini Voss, Johanna Loomba, Mohamad Khaled, Eyal Zadicario, Robert C. Frysinger, Scott A. Sperling, Scott Wylie, Stephen J. Monteith, Jason Druzgal, Binit B. Shah, Madaline Harrison, and Max Wintermark. A pilot study of focused ultrasound thalamotomy for essential tremor. *The New England journal of medicine*, 369(7):640–648, aug 2013.

[30] Thomas Deffieux and Elisa Konofagou. Numerical study of a simple transcranial focused ultrasound system applied to blood-brain barrier opening. *IEEE Transactions on Ultrasonics, Ferroelectrics, and Frequency Control*, 57(12):2637–2653, 2010.

[31] Jerel K. Mueller, Leo Ai, Priya Bansal, and Wynn Legon. Numerical evaluation of the skull for human neuromodulation with transcranial focused ultrasound. *Journal of Neural Engineering*, 14(6), 2017.

[32] Yanqiu Zhang, Hao Zhang, Ting Pan, and Xiqi Jian. Simulation of Standing Wave Reduction in HIFU Transcranial Tumors Therapy. *IEEE International Ultrasonics Symposium, IUS*, 2019-Octob:552–555, 2019.

[33] Cecile Baron, Jean François Aubry, Mickael Tanter, Stephen Meairs, and Mathias Fink. Simulation of Intracranial Acoustic Fields in Clinical Trials of Sonothrombolysis. *Ultrasound in Medicine and Biology*, 35(7):1148–1158, 2009.

[34] Gianmarco Pinton, Jean Francois Aubry, Mathias Fink, and Mickael Tanter. Numerical prediction of frequency dependent 3D maps of mechanical index thresholds in ultrasonic brain therapy. *Medical Physics*, 39(1):455–467, 2012.

[35] Can Barlş Top, P. Jason White, and Nathan J. McDannold. Nonthermal ablation of deep brain targets: A simulation study on a large animal model. *Medical Physics*, 43(2):870–882, 2016.

[36] Tae Young Park, Ki Joo Pahk, and Hyungmin Kim. Method to optimize the placement of a single-element transducer for transcranial focused ultrasound. *Computer Methods and Programs in Biomedicine*, 179, oct 2019.

[37] Ryuta Narumi, Kosuke Matsuki, Shigeru Mitarai, Takashi Azuma, Kohei Okita, Akira Sasaki, Kiyoshi Yoshinaka, Shu Takagi, and Yoichiro Matsumoto. Focus control aided by numerical simulation in heterogeneous media for high-intensity focused ultrasound treatment. *Japanese Journal of Applied Physics*, 52(7 PART 2), 2013.

[38] Xin Ding, Yizhe Wang, Qian Zhang, Wenzheng Zhou, Peiguo Wang, Mingyan Luo, and Xiqi Jian. Modulation of transcranial focusing thermal deposition in nonlinear HIFU brain surgery by numerical simulation. *Physics in Medicine and Biology*, 60(10):3975–3998, 2015.

[39] Jérôme Gâteau, Laurent Marsac, Mathieu Pernot, Jean Francois Aubry, Mickaël Tanter, and Mathias Fink. Transcranial ultrasonic therapy based on time reversal of acoustically induced cavitation bubble signature. *IEEE Transactions on Biomedical Engineering*, 57(1):134–144, 2010.

[40] ELISA E. KONOFAGOU FABRICE MARQUET, YAO-SHENG TUNG. FEASIBILITY STUDY OF A CLINICAL BLOOD–BRAIN BARRIER OPENING ULTRASOUND SYSTEM. *Nano Life*, (1):309–, 2010.

[41] Nathan McDannold, P. Jason White, and Rees Cosgrove. An element-wise approach for simulating transcranial MRI-guided focused ultrasound thermal ablation, sep 2019.

[42] Nathan McDannold, P. Jason White, and Rees Cosgrove. Predicting skull lesions after clinical transcrani-al MRI-guided focused ultrasound with acoustic and thermal simulations. *arXiv*, 39(10):3231–3239, 2020.

[43] Steven A. Leung, Taylor D. Webb, Rachelle R. Bitton, Pejman Ghanouni, and Kim Butts Pauly. A rapid beam simulation framework for transcranial focused ultrasound. *Scientific Reports*, 9(1), dec 2019.

[44] Sijia Guo, Jiachen Zhuo, Guang Li, Dheeraj Gandhi, Mor Dayan, Paul Fishman, Howard Eisenberg, Elias R. Melhem, and Rao P. Gullapalli. Feasibility of ultrashort echo time images using full-wave acoustic and thermal modeling for transcranial MRI-guided focused ultrasound (tcMRgFUS) planning. *Physics in Medicine and Biology*, 64(9), apr 2019.

[45] Aki Pulkkinen, Yuexi Huang, Junho Song, and Kullervo Hynynen. Simulations and measurements of transcranial low-frequency ultrasound therapy: Skull-base heating and effective area of treatment. *Physics in Medicine and Biology*, 56(15):4661–4683, aug 2011.

[46] Guillaume Bouchoux, Ravishankar Shivashankar, Todd A. Abruzzo, and Christy K. Holland. In silico study of low-frequency transcranial ultrasound fields in acute ischemic stroke patients. *Ultrasound in Medicine and Biology*, 40(6):1154–1166, 2014.

[47] Urvi Vyas, Pejman Ghanouni, Casey H. Halpern, Jeff Elias, and Kim Butts Pauly. Predicting variation in subject thermal response during transcranial magnetic resonance guided focused ultrasound surgery: Comparison in seventeen subject datasets. *Medical Physics*, 43(9):5170–5180, aug 2016.

[48] Mark Hayner and Kullervo Hynynen. Numerical analysis of ultrasonic transmission and absorption of oblique plane waves through the human skull. *The Journal of the Acoustical Society of America*, 110(6):3319–3330, 2001.

[49] G. T. Clement and K. Hynynen. A non-invasive method for focusing ultrasound through the human skull, apr 2002.

[50] G. T. Clement, P. J. White, and K. Hynynen. Enhanced ultrasound transmission through the human skull using shear mode conversion. *The Journal of the Acoustical Society of America*, 115(3):1356–1364, 2004.

[51] Xiangtao Yin and Kullervo Hynynen. A numerical study of transcranial focused ultrasound beam propagation at low frequency. *Physics in Medicine and Biology*, 50(8):1821–1836, 2005.

[52] Samuel Pichardo and Kullervo Hynynen. Treatment of near-skull brain tissue with a focused device using shear-mode conversion: A numerical study. *Physics in Medicine and Biology*, 52(24):7313–7332, dec 2007.

[53] Stephen M. Smith, Mark Jenkinson, Mark W. Woolrich, Christian F. Beckmann, Timothy E.J. Behrens, Heidi Johansen-Berg, Peter R. Bannister, Marilena De Luca, Ivana Drobnjak, David E. Flitney, Rami K. Niazy, James Saunders, John Vickers, Yongyue Zhang, Nicola De Stefano, J. Michael Brady, and Paul M. Matthews. Advances in functional and structural MR image analysis and implementation as FSL. *NeuroImage*, 23 Suppl 1(SUPPL. 1), 2004.

[54] Samuel Pichardo, Vivian W. Sin, and Kullervo Hynynen. Multi-frequency characterization of the speed of sound and attenuation coefficient for longitudinal transmission of freshly excised human skulls. *Physics in Medicine and Biology*, 56(1):219–250, 2010.

[55] Daniel Pajek and Kullervo Hynynen. The design of a focused ultrasound transducer array for the treatment of stroke: A simulation study. *Physics in Medicine and Biology*, 57(15):4951–4968, aug 2012.

[56] Ryan M. Jones, Meaghan A. O'Reilly, and Kullervo Hynynen. Transcranial passive acoustic mapping with hemispherical sparse arrays using CT-based skull-specific aberration corrections: A simulation study. *Physics in Medicine and Biology*, 58(14):4981–5005, jul 2013.

[57] Tae Young Park, Ki Joo Pahk, and Hyungmin Kim. A novel numerical approach to stimulation of a specific brain region using transcranial focused ultrasound. *Proceedings of the Annual International Conference of the IEEE Engineering in Medicine and Biology Society, EMBS*, 2018-July:3697–3700, 2018.

[58] G. Wilson Miller, Matthew Eames, John Snell, and Jean François Aubry. Ultrashort echo-time MRI versus CT for skull aberration correction in MR-guided transcranial focused ultrasound: In vitro comparison on human calvaria. *Medical Physics*, 42(5):2223–2233, may 2015.

[59] P. J. White, G. T. Clement, and K. Hynynen. Longitudinal and shear mode ultrasound propagation in human skull bone. *Ultrasound in Medicine and Biology*, 32(7):1085–1096, 2006.

[60] Francis A. Duck. *Physical properties of tissue : a comprehensive reference book*. Academic Press, 1990.

[61] J. Y. Rho, M. C. Hobatho, and R. B. Ashman. Relations of mechanical properties to density and CT numbers in human bone. *Medical Engineering and Physics*, 17(5):347–355, jul 1995.

[62] Christopher W. Connor, Greg T. Clement, and Kullervo Hynynen. A unified model for the speed of sound in cranial bone based on genetic algorithm optimization. *Physics in Medicine and Biology*, 47(22):3925–3944, 2002.

[63] Guillaume Bouchoux, Kenneth B. Bader, Joseph J. Korfhagen, Jason L. Raymond, Ravishankar Shivashankar, Todd A. Abruzzo, and Christy K. Holland. Experimental validation of a finite-difference model for the prediction of transcranial ultrasound fields based on CT images. *Physics in Medicine and Biology*, 57(23):8005–8022, 2012.

[64] Samuel Pichardo, Carlos Moreno-Hernández, Robert Andrew Drainville, Vivian Sin, Laura Curiel, and Kullervo Hynynen. A viscoelastic model for the prediction of transcranial ultrasound propagation: Application for the estimation of shear acoustic properties in the human skull. *Physics in Medicine and Biology*, 62(17):6938–6962, 2017.

[65] James Robertson, Eleanor Martin, Ben Cox, and Bradley E. Treeby. Sensitivity of simulated transcranial ultrasound fields to acoustic medium property maps. *Physics in Medicine and Biology*, 62(7):2559–2580, 2017.

[66] Fabrice Marquet, Mathieu Pernot, Jean Francois Aubry, Gabriel Montaldo, Mickael Tanter, and Mathias Fink. Non-invasive transcranial ultrasound therapy guided by CT-scans. *Annual International Conference of the IEEE Engineering in Medicine and Biology - Proceedings*, pages 683–687, 2006.

[67] F. J. Fry and J. E. Barger. Acoustical properties of the human skull. *Journal of the Acoustical Society of America*, 63(5):1576–1590, 1978.

[68] Kyungho Yoon, Wonhye Lee, Phillip Croce, Amanda Cammalleri, and Seung Schik Yoo. Multi-resolution simulation of focused ultrasound propagation through ovine skull from a single-element transducer. *Physics in Medicine and Biology*, 63(10), may 2018.

[69] M. B. Tavakoli. The effect of bone structure on ultrasonic attenuation and velocity. *Ultrasonics*, 30(6):389–395, 1992.

[70] Emmanuel Bossy, Frédéric Padilla, Françoise Peyrin, and Pascal Laugier. Three-dimensional simulation of ultrasound propagation through trabecular bone structures measured by synchrotron microtomography. *Physics in Medicine and Biology*, 50(23):5545–5556, 2005.

[71] Guillaume Haïat, Frédéric Padilla, Françoise Peyrin, and Pascal Laugier. Variation of ultrasonic parameters with microstructure and material properties of trabecular bone: A 3D model simulation. *Journal of Bone and Mineral Research*, 22(5):665–674, 2007.

[72] Gianmarco Pinton, Jean Francois Aubry, Emmanuel Bossy, Marie Muller, Mathieu Pernot, and Mickael Tanter. Attenuation, scattering, and absorption of ultrasound in the skull bone. *Medical Physics*, 39(1):299–307, 2012.

[73] Omid Yousefian, Yasamin Karbalaeisadegh, and Marie Muller. Frequency-dependent analysis of ultrasound apparent absorption coefficient in multiple scattering porous media: application to cortical bone. *Physics in Medicine and Biology*, 66(3):35026, feb 2021.

[74] Taylor D. Webb, Steven A. Leung, Pejman Ghanouni, Jeremy J. Dahl, Norbert J. Pelc, and Kim Butts Pauly. Acoustic Attenuation: Multifrequency Measurement and Relationship To CT and MR Imaging. *IEEE Transactions on Ultrasonics, Ferroelectrics, and Frequency Control*, 3010(c):1–16, 2020.

[75] Max Wintermark, Nicholas J. Tustison, William J. Elias, James T. Patrie, Wenjun Xin, Nicholas Demartini, Matt Eames, Suna Sumer, Benison Lau, Alan Cupino, John Snell, Arik Hananel, Neal Kassell, and Jean Francois Aubry. T1-weighted MRI as a substitute to CT for refocusing planning in MR-guided focused ultrasound. *Physics in Medicine and Biology*, 59(13):3599–3614, jul 2014.

[76] Taylor D. Webb, Steven A. Leung, Jarrett Rosenberg, Pejman Ghanouni, Jeremy J. Dahl, Norbert J. Pelc, and Kim Butts Pauly. Measurements of the Relationship between CT Hounsfield Units and Acoustic Velocity and How It Changes with Photon Energy and Reconstruction Method. *IEEE Transactions on Ultrasonics, Ferroelectrics, and Frequency Control*, 65(7):1111–1124, 2018.

[77] J. F. Aubry, L. Marsac, M. Pernot, B. Robert, A. L. Boch, D. Chauvet, N. Salameh, L. Souris, L. Darasse, J. Bittoun, Y. Martin, C. Cohen-Bacrie, J. Souquet, M. Fink, and M. Tanter. High intensity focused ultrasound for transcranial therapy of brain lesions and disorders. *IRBM*, 31(2):87–91, 2010.

[78] Nan Wu, Guofeng Shen, Xiongfei Qu, Hao Wu, Shan Qiao, Enmin Wang, Yazhu Chen, and Han Wang. An efficient and accurate parallel hybrid acoustic signal correction method for transcranial ultrasound. *Physics in Medicine and Biology*, 65(21), 2020.

[79] Urvi Vyas and Douglas Christensen. Ultrasound beam simulations in inhomogeneous tissue geometries using the hybrid angular spectrum method. *IEEE Transactions on Ultrasonics, Ferroelectrics, and Frequency Control*, 59(6):1093–1100, 2012.

[80] F. Marquet, M. Pernot, J. F. Aubry, G. Montaldo, L. Marsac, M. Tanter, and M. Fink. Non-invasive transcranial ultrasound therapy based on a 3D CT scan: Protocol validation and in vitro results. *Physics in Medicine and Biology*, 54(9):2597–2613, 2009.

[81] Guillaume Maimbourg, Julien Guilbert, Thomas Bancel, Alexandre Houdouin, Guillaume Raybaud, Mickael Tanter, and Jean Francois Aubry. Computationally Efficient Transcranial Ultrasonic Focusing: Taking Advantage of the High Correlation Length of the Human Skull. *IEEE Transactions on Ultrasonics, Ferroelectrics, and Frequency Control*, 67(10):1993–2002, 2020.

[82] Antonio Stanziola, Simon R. Arridge, Ben T. Cox, and Bradley E. Treeby. A Helmholtz equation solver using unsupervised learning: Application to transcranial ultrasound. *Journal of Computational Physics*, page 110430, may 2021.

[83] L. Marsac, D. Chauvet, B. Larrat, M. Pernot, B. Robert, M. Fink, A. L. Boch, J. F. Aubry, and M. Tanter. MR-guided adaptive focusing of therapeutic ultrasound beams in the human head. *Medical Physics*, 39(2):1141–1149, feb 2012.

[84] Meaghan A. O'Reilly, Ryan M. Jones, Gabriel Birman, and Kullervo Hynynen. Registration of human skull computed tomography data to an ultrasound treatment space using a sparse high frequency ultrasound hemispherical array. *Medical Physics*, 43(9):5063–5071, 2016.

[85] Chen Jiang, Yunqing Li, Boyi Li, Chengcheng Liu, Feng Xu, Kailiang Xu, and Dean Ta. Ray Theory-Based Transcranial Phase Correction for Intracranial Imaging: A Phantom Study. *IEEE Access*, 7:163013–163021, 2019.

[86] Roger Hill and Samir M.A. El-Dardiry. A theory for optimization in the use of acoustic emission transducers. *Journal of the Acoustical Society of America*, 67(2):673–682, 1980.

[87] S.R. Haqshenas, P. Gélat, E. van 't Wout, T. Betcke, and N. Saffari. A fast full-wave solver for calculating ultrasound propagation in the body. *Ultrasonics*, 110:106240, 2021.

[88] N. Gengembre. Pencil method for ultrasonic beam computation. 2003.

[89] Pauline Agou. *Conception de la partie acoustique d'un dispositif médical pour l'ouverture transitoire de la barrière hémato-encéphalique par ultrasons focalisés transcraniens et sa validation préclinique*. PhD thesis, 2022.

[90] Gaelle Thomas. *Développement de solutions d'assistance robotique pour l'ouverture de la barrière hémato-encéphalique par ultrasons focalisés*. PhD thesis, 2021.